Studies on the physical structure, properties and operation of ionic liquid electrosprays in the pure-ion mode

by

Ximo Gallud Cidoncha

Submitted to the Department of Aeronautics and Astronautics
in partial fulfillment of the requirements for the degree of
Doctor of Philosophy in Aeronautics and Astronautics
at the
MASSACHUSETTS INSTITUTE OF TECHNOLOGY
September 2023

Author . . . .
Department of Aeronautics and Astronautics
June 28, 2023

Certified by . . . .
Paulo C. Lozano
M. Alemán-Velasco Professor of Aeronautics and Astronautics
Thesis Supervisor

Certified by . . . .
Elaine Petro
Assistant Professor, Cornell University
Thesis Committee Member

Certified by . . . .
Manuel Martínez-Sánchez
Professor Emeritus of Aeronautics and Astronautics
Thesis Committee Member

Certified by . . . .
Jaume Peraire
H.N. Slater Professor in Aeronautics and Astronautics
Thesis Committee Member

Accepted by . . . .
Jonathan How
R.C. Maclaurin Professor of Aeronautics and Astronautics
Chairman, Graduate Program Committee

Studies on the physical structure, properties and operation of ionic liquid electrosprays in the pure-ion mode

by

Ximo Gallud Cidoncha

Submitted to the Department of Aeronautics and Astronautics
on June 28, 2023, in partial fulfillment of the
requirements for the degree of
Doctor of Philosophy in Aeronautics and Astronautics

Abstract

Electrosprays operating in the pure-ion mode exhibit compelling characteristics for micropropulsion, such as the ability to achieve high specific impulses with high efficiency. Liquid metal and ionic liquid-based electrospray sources are the most well-established types that operate in this mode. Understanding the emission physics of ionic liquids has proven challenging due to their distinct differences from liquid metals, which impose limitations on the stability and current throughput of these sources. Notably, the minor role of space charge, lower surface tension coefficient, and limited conductivity of ionic liquids appear to significantly impact their operational range, restricting them to a narrow set of extracting potentials, requiring sufficient hydraulic impedance, and limiting the range of meniscus sizes to the micrometer scale. The latter constraint poses observational challenges that limit their experimental study.

Electrohydrodynamic numerical modeling has been instrumental in understanding the operational conditions of these sources, although existing models have not been able to reproduce normal experimental situations. The primary contribution of this thesis is the efficient implementation of an electrohydrodynamic model for ionic liquid electrosprays in the pure-ion mode, which can be experimentally validated, and that aims to explore electrode geometrical effects, the current and the stability of ionic liquid pure-ion electrospray menisci. The model takes into account the specific geometry of the sources and reveals emitted current ranges where the pure-ion regime can be sustained. Current bounds are wider at very small meniscus sizes ($<$10 μm), lower critical field for emission, and higher electrical conductivity. The model unveils a potentially universal range of electric fields local to the meniscus which in the limit of high impedance, axially symmetric configuration, and negligible space charge, it can be extended to the stable cone-jet mode. This range begins at the extinction voltage, where in the limit of negligible reservoir pressure, a conical geometry reminiscent of the Taylor cone is postulated and extends until the electric field near the electrode holding the meniscus reaches an electric pressure approximately twice the surface tension of a sphere with the same radius as the meniscus for the geometries tested. The specific value depends weakly on the geometrical details of the sustaining electrodes. Experimental efforts reveal that this limit likely corresponds to a bifurcation into two emitting menisci.

Further observations from the model indicate that the emitted current is likely independent of electric conductivity and the critical field for emission, similar to liquid metal ion sources. The modeling suggests that the flow rate emitted is primarily determined by upstream conditions of the flow, and in specific cases involving small meniscus sizes and low beam perveance, space charge becomes a factor. These upstream conditions encompass the local pressure, influenced solely by hydraulic impedance, surface tension coefficient, meniscus radius and reservoir pressure, as well as the local electric field near the meniscus anchoring point to the electrode, and not any coefficient with sole relevance in the emission region.

Preliminary validation efforts conducted in this thesis suggest a moving meniscus, where the radius and impedance properties of emitting pure-ion menisci may not remain constant during current-voltage excursions in porous emitters.

Thesis Supervisor: Paulo C. Lozano
Title: M. Alemán-Velasco Professor of Aeronautics and Astronautics

Acknowledgments

I want to dedicate this thesis to my parents Reyes and Juan, for their unconditional love traveling thousands of kilometers apart: *venga que ya tienes la gotita (the meniscus)*! Aquesta tesi no hagués pogut ser sense vosaltres. Vos estime.

I am profoundly grateful to Prof. Lozano for his guidance and mentorship. His commitment to creating an empowered and more democratic space has been a constant source of inspiration for me. From Paulo, I have learned many things, but perhaps the most vital ones that have shaped me during these thesis years are the importance of falling in love with a research problem, and the art of infusing each challenge you face with the potential for personal growth and self-discovery. Thank you Paulo for your unwavering patience even in my thousandth mistake, for shaping my mind, for your wisdom and brilliance, and for letting me work with you on this beautiful project.

I would like to thank Prof. Elaine Petro for her brilliance, friendship, and advice. Elaine is a role model for me, intellectually and personally. Elaine's words *persevere!* are always in my mind.

I would like to thank Prof. Martínez-Sánchez, Prof. Peraire and Prof. Higuera for their geniality and vision, especially in the moments when I was stuck.

Thank you SPLers Maddie, Mia, Matt, Gustav, Jon, Saba, Hannah, Charity, Oliver, Colin and Regina for your support, for your wittiness and patience in teaching me how to do experiments. No experiment of this thesis would have been possible without you.

Thank you so much, Spiros, for the synthesis of the ionic liquids in this thesis, and for opening my mind to the wonderful and difficult world of chemistry.

Thank you so much to the US Air Force Office of Scientific Research, MathWorks, and La Caixa Foundation for believing in me and funding the research in this thesis.

I am indebted to my mentees and collaborators Garrett, Ruth, Sebastian, and Rafid, you could not imagine how much have I learned from you.

Thank you Jordi, Junkal, Tiara, Aina and Xavi for your sensible and smart advice, for your warmth, and for making home the best place to stay, for being my adoptive family in Cambridge. I would not have imagined a better life abroad without you.

I would like to thank all my family in Valencia for their unwavering love and support throughout this journey. Their encouragement, humor, and delicious homemade treats provided much-needed relief during intense research moments at home. Thank you for being a constant source of joy in my life, both inside and outside the realm of thesis writing.

I could not have imagined this thesis journey without my favorite Ohio State University person Ramon. Thank you for being there every time, listening to me, and giving me wonderful advice. Thank you Julia for inspiring me with your passion for living, and compassion and for teaching me the value of believing in myself.

Thank you Albeta, Hele, Joan, Mar, Vallivana, Karen, Luis, Alberto, Jorge for your warmth, for your vision, humor, for being there everytime. You are my chosen family in Spain: when I am asked about what home is for me, you are most of the answer.

Contents

Chapter 1

Introduction

1.1 Electrospraying: The pure ion mode

Electrospraying is a technique to extract charged particles from electrically-conductive liquid surfaces using strong electric fields. This technique can be implemented in various configurations, but most commonly consists of an electrode in the form of a capillary tube, where fluid flows across from a reservoir. A potential difference is then applied between the liquid and a downstream electrode, thus polarizing the liquid exposed at the end of the tube.

A fluid meniscus is formed in the cavity between the electrodes. The surface of the meniscus adopts a geometrical shape that results from the balance of electric, surface tension, and hydrodynamic stresses. These forces depend on the applied potential, fluid flow rate, electrode configuration, and liquid properties. A general view of a typical electrospray setup can be seen in figure 1-1.

Electrospray sources can operate in various emission regimes. The most widely known is the cone-jet mode [18], where the meniscus has a conical shape near the contact line with the tube or Taylor cone [128], and transitions into a fast-moving liquid jet close to the cone apex [142]. The jet surface is inherently unstable and eventually breaks into droplets due to field-enhanced capillary instabilities [104]. The cone-jet mode has been widely studied in terms of its governing physics and the resulting spray structure [32, 52], from which scaling laws have been derived for metrics such as the jet width, electric current output, and the size and mass per unit charge of resulting droplets [50, 33].

When the fluid flow rate is reduced at constant conductivity, the characteristic dimension that controls the size of the jet and resulting droplets decreases, making the electric field, particularly in the cone-jet transition region and the jet termination

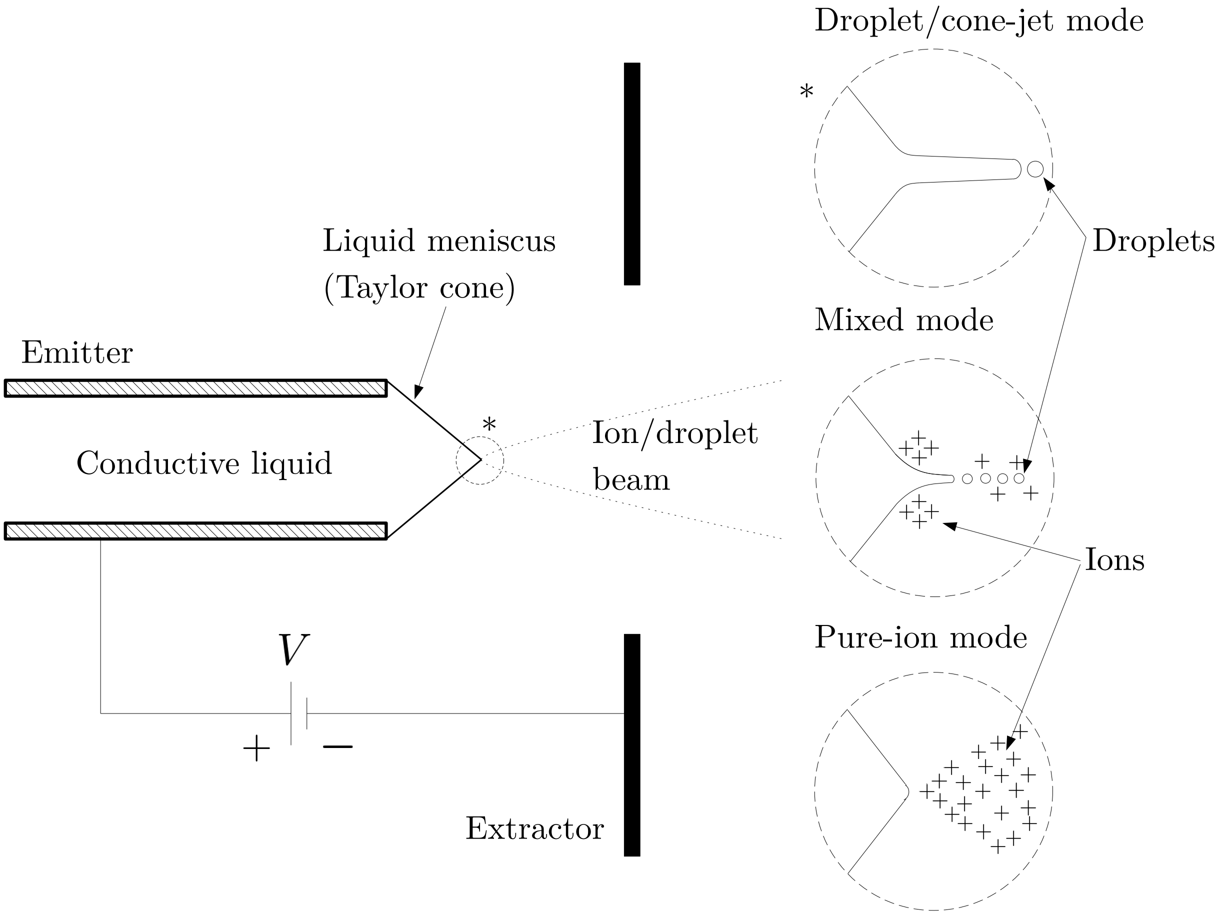

Figure 1-1: General electrospray setup with the three typical emission modes. Ions are depicted with a + sign, and droplets with an o sign. Ion emission in the mixed mode typically starts at the neck of the jet and at the apex, where the electric field is maximized.

[45, 44], to become sufficiently large to trigger direct ion evaporation from the charged interface [67]. The simultaneous ion evaporation from a cone-jet electrospray defines a second operational mode, characterized by the production of a mixed ion-droplet beam [93].

Under certain empirical conditions, namely a sufficiently high hydraulic impedance, a further reduction of the fluid flow rate results in the pure emission of ions, characterized by the absence of any droplet current. While no direct visual observation of a stable meniscus in this mode is available, it is likely that the jet is quenched and ion emission occurs from a closed surface at the meniscus apex. According to cone-jet scaling laws [33], the fluid flow rate corresponding to this regime is too low to support the formation of a stable jet.

The electrospray pure-ion evaporation mode is observed to exist only for a limited set of liquids, namely liquid metals [125] and ionic liquids [107, 81], and perhaps for some concentrated sulfuric acid solutions [93]. In addition to its interesting phenomenology, the pure ionic regime has recently gained significant attention for its potential applications in high-performance electric space propulsion [76, 106], Focused Ion Beams (FIB) for etching and deposition [145, 95, 127] or ion microscopy [77, 121].

1.1.1 Ionic liquid ion sources

Ionic liquids are a type of molten salts that remain liquid at relatively low temperatures, including room temperature, and sometimes much lower [137, 41, 84]. Unlike conventional simple salts, ionic liquids are formed by complex molecular ions, which are poorly coordinated in part due to their asymmetric nature, and therefore require significantly lower temperatures to organize into a solid structure. However, also as in conventional salts, strong ionic interactions between their molecules result in extraordinarily low vapor pressures, allowing them to be exposed to a vacuum in their liquid state, practically without evaporation.

Ionic liquid ion sources (ILIS) are of special interest because they can be made of numerous combinations of organic molecules tailored to the specific requirements of each application [99].

Similar to liquid metal ion sources (LMIS), the process governing the ion emission for ILIS is a highly non-linear activated process, which is usually modeled in a similar way to classical field-enhanced thermionic emission, where a critical electric field is required to reach a state of substantial ion evaporation. In this theory, ions are extracted from the closed meniscus interface, where the ion extracting work function $E_a = \Delta G - G(E_n^v)$ is reduced from the ion pure free energy of solvation ΔG due to the action of a very strong field perpendicular to the meniscus interface E_n^v, generally around a critical value E^*, defined as when $\Delta G \sim G(E_n^v)$.

In the limit of a planar interface geometry, the value of $G(E_n^v)$ and E^* can be approximated using an image charge hump argument [89]:

$$G(E_n^v) = \sqrt{\frac{q^3 E_n^v}{4\pi\varepsilon_0}} \tag{1.1}$$

$$E^* = \frac{4\pi\varepsilon_0 \left(\Delta G\right)^2}{q^3} \tag{1.2}$$

Where q is the charge of the ion evaporated, and ε_0 is the dielectric permittivity of vacuum. The value of the solvation energy ΔG and corresponding critical field for emission E^* is not very well known for ionic liquids. Some numerical simulations [144] and experimental efforts with organic solvent mixtures [64] suggest the values of ΔG lie in between 1 - 1.7 eV for ionic liquids, which would yield values for E^* on the order of 0.7-2 V/nm. The local current density emitted normal to the interface j_n^e yields:

$$j_n^e = Ae^{-\frac{E_a}{k_B T}} \tag{1.3}$$

Where A is the activation rate constant, k_B is the Boltzmann constant, and T is the temperature of the ionic liquid. The activation rate constant A is generally the product of the number of atoms per unit area N that are at risk of being evaporated, times the average charge per unit atom q and k_F, or a rate-constant [36]:

$$A = qNk_F \tag{1.4}$$

In the ILIS case, the number of charges per unit area qN at risk of being evaporated is identified as the interfacial charge, $qN = \sigma$. In the thermodynamic equilibrium limit, the rate of evaporation k_F is dependent on the temperature of the ionic liquid $k_F = \frac{k_B T}{h}$, therefore the A yields:

$$A = \frac{\sigma k_B T}{h} \tag{1.5}$$

Where h is the Planck constant. The current density normal to the interface is then written as [67]:

$$j_n^e = \frac{\sigma k_B T}{h} \exp\left(\frac{-\Delta G}{k_B T}\left(1 - \sqrt{\frac{q^3 E_n^v}{4\pi\varepsilon_0}}\right)\right) \tag{1.6}$$

The fact that the critical field governs the entirety of ion emission is normally considered a reference for other scaling parameters to follow. For instance, it appears reasonable to assume that the characteristic length scale of the emission size follows the radius of curvature of a spherical cap subject to an electric stress governed by E^* in the vacuum and E^*/ε_r in the liquid [21]:

$$r^* = \frac{4\gamma}{\varepsilon_0 {E^*}^2} \frac{\varepsilon_r}{\varepsilon_r - 1} \tag{1.7}$$

Where γ is the surface tension coefficient. In the limit where $\varepsilon \gg 1$ then $r^* = \frac{4\gamma}{\varepsilon_0 {E^*}^2}$. Other common scalings consider the current emitted by an ionic liquid as established by the conductive transport to the surface in a region with a size that scales with r^*. Given that charges are not fully relaxed at this scale, an internal field that scales with E^*/ε appears, thus driving a current density:

$$j^* = \kappa E^*/\varepsilon_r \tag{1.8}$$

Where κ is the electrical conductivity of the liquid. The current is then determined by the area of the emission region, which is also reasonable to assume that scales with the area of the spherical cap $A = 2\pi {r^*}^2$:

$$I^* \approx j^* A = \frac{32\pi\kappa\gamma^2\varepsilon_r}{\varepsilon_0^2 {E^*}^3 \left(\varepsilon_r - 1\right)^2} \tag{1.9}$$

Unlike LMIS, where space charge seems to play a primordial role to enhance the stability of the meniscus by shielding the effects of external electric perturbations, ILIS space charge effects are less relevant, which presumably makes the stability of the source more susceptible to the specific properties of the working ionic liquid [54], or emitter geometry [13]. Experimental challenges have hindered a clear understanding of ILIS, especially the role of these key geometrical operating parameters or others such as the external electric field [74, 96], liquid temperature [81], and other physical tip characteristics relevant to passive-type sources, such as the size of the inlet pores [27], electrode shape or hydraulic impedance of the feeding material [13] and material dielectric properties [22]. Among these challenges is the current lack of non-destructive techniques to resolve the small scales of ILIS menisci ($\sim$ 1-5 μm) to interrogate the system in situ, e.g., to capture the shape of the interface profile, the nature of fluid interactions with the tip and the characteristics of internal creeping flow while confirming that the source is operating in the pure ionic mode, for example through simultaneous mass spectrometry of the beam. Electron microscopy

[130] has been attempted to observe the small menisci; however, the electron beam interacts strongly with the charged surface making these observations uncertain at best.

The lack of empirical evidence, emphasizes the relevance of studying these liquid structures through numerical simulations. A validated numerical model would be a desirable tool in the design of these pure ion sources, as it will help transition to a physics-based design paradigm from the current trial-and-error approach.

1.2 Technical Gap

1.2.1 Experimental heuristics for ionic liquids

The pure-ion regime for ionic liquids has remained elusive in the experimental literature. Most of the efforts carried out so far for the design of tips in the pure-ion regime make choices of geometrical parameters, working liquids, and operational conditions that often follow heuristic results, and are constrained by the availability and feasibility of fabrication techniques.

The physical explanation behind these heuristic results, if there exists, may be incomplete and even misleading in some cases. Examples of these explanations and the related knowledge gap are enumerated below:

- **The pure ionic regime is achieved at low flow rates, usually when the non-dimensional flow parameter** $\eta = \sqrt{\frac{\rho\kappa Q}{\gamma\varepsilon_r\varepsilon_0}} \ll 1$. [1] In other words, there is a limit flow rate above which the pure ion regime cannot be sustained [81, 107]. Flow rates in the pure-ionic regime are generally much smaller than in the cone-jet mode. What are the hydrodynamic phenomena that cause these limitations? Is this mostly caused by a limitation on the ion evaporation time scales (in relation to other time scales, e.g., charge relaxation time)? Is it an insufficient surface tension to sustain the higher fields on the order of E^* needed to extract more ions?

- **The pure ionic regime is only sustained in sources with high enough hydraulic impedance.** Early experiments showed that the pure ion regime was achievable for externally wetted porous tips for ionic liquids that used to emit in the droplet mode in capillaries [81, 75], which typically have less

---

[1] ρ is the density of the liquid, κ is the electrical conductivity, γ is the surface tension coefficient, ε_r is the dielectric permittivity constant, ε_0 is the dielectric permittivity of vacuum, and Q is the flow rate.

hydraulic impedance. The fact was corroborated for several tips with different curvature radii and impedances [13], where the pure ion regime was only achieved for the tips having a high impedance factor, namely with curvature radii smaller than 80 μm. A natural question to ask is if the role of hydraulic impedance is only a convenient way to limit the flow to the ranges where the pure ion emission is allowed (see previous item); or whether it has more implications for the flow structure that favor ion evaporation, as for instance, a higher damping coefficient for any current perturbation.

- **The pure ion regime is only permissible for a single, presumably axially-symmetric meniscus under a narrow gap of operational voltages.** Precise operational voltages are often reported with little detail, especially the characterization of the source at the instability limits. For instance, Castro [13] reports a stable range of $\sim 2225 - 2425$ V for a 50 μm emitter. Unfortunately, no discussion of any time of flight measurements or current behavior was reported after 2425 V. Lozano [81] notices stable operational ranges between $\sim 1600 - 2000$ V in the negative mode for a 20 μm emitter. In that study, Lozano observes current saturation followed by erratic vanishing behavior after 2000 V. What characterizes this current saturation? Is this purely related to the saturation of the feeding conditions of the flow downstream? Could this be related perhaps to a maximum flow rate that can be sustained in the pure-ionic mode, before other mode appears (droplet emission, dripping)? Lozano also observes current fluctuations under 1600 V. The latter phenomenon is similar to what is observed in liquid metals [1] and is associated with poor liquid supply due to insufficient electric traction. Other studies [96] report stability ranges between 1600-2000 V ending at a presumably bifurcation of the meniscus. What are the conditions that enhance a possible bifurcation of the meniscus as opposed to current saturation and the possible appearance of other electrospraying modes?

- **Higher temperatures enhance pure ion emission.** There are three physical phenomena relevant to pure-ion emission where temperature plays a major role. Firstly, higher temperature will increase the mobility of the ionic species, and its conductivity as a consequence. Secondly, most ionic liquids exhibit the Walden rule [113], where the product of their conductivity and viscosity remains correlated, or nearly constant. If the conductivity increases due to a temperature enhancement, the viscosity may experience an inversely proportional decay, which can help improve flow transport through a reduced hydraulic impedance (see second item in this list). Thirdly, the barrier for thermionic evaporation may be lowered due to a higher temperature, which could have enhanced the charge emission process at the same voltages. These three aspects may have explained the increase in the pure-ionic current observed by studies such as Lozano [81] or Romero-Sanz [106]. Any uncoupling of these phenomena is very challenging experimentally, therefore it is not clear which of these played a major role in this current enhancement effect.

- **The pure ionic regime is better achieved in ionic liquids with high conductivity. Conductivity enhances the current emitted.** Garoz *et al.* concluded this after observing that the pure ion regime was not achieved for capillary emitters using ionic liquids with very limited conductivity (below 0.36 S/m) [54]. However, Garoz's results were contrasted by the findings of Castro *et al.* [14], where liquids with as low as 0.26 S/m exhibited pure ion characteristics for externally wetted tips of higher impedance, yet at the expense of lower current throughput. The unnoticed part of this experiment is that the poorly conducting ionic liquids tended to have a larger viscosity due to the Walden rule, which may have explained the decrease in current emission. This could have misled the conclusions of the paper about poor liquid conductivity limiting current extraction. Additionally, it seems plausible to think that any leading order dependence of the current with conductivity must vanish for highly conducting liquids. The most obvious example is the fact that liquid metal ion sources extract around 50 times the current of ionic liquids, despite having 6 orders of magnitude higher conductivity than ionic liquids. What is the exact role of conductivity in pure-ion electrospraying? Is the higher conductivity of liquid metals a key factor that explains the higher currents observed for these sources as opposed to ionic liquids?

- **Space charge effects are of limited importance for ionic liquid ion sources in the pure-ion regime, at the single source level.** The relevance of space charge is one of the key differences between liquid metal and ionic liquid ion sources [19]. Unlike ionic liquids, the large current densities emitted in liquid metals screen the electric fields to leading order. In other words, the electric field is highly dependent on the magnitude of the space charge. This has inspired the use of the Child-Langmuir law [82] as a reference for the current density in the emission region. Space charge limitations were thought to be one of the reasons why liquid metals exhibit a cusp protrusion in the emission region. If the extracted current density is limited by space charge, then higher current excursions are only explained with an extended area of emission, in this case in the form of a cusp. The space charge limitation assumption cannot be made in the case of lower current throughput ionic liquid ion sources, where the Ohmic model for conduction ($j \sim \kappa \frac{E^*}{\varepsilon_r}$) is often taken as reference for current density [63, 20] (see previous point). In this case, the current is thought to be limited by an insufficient charge transport to the interface. Any influence of space charge in the current emitted was also questioned by Castro [13], where it was found not to be affecting current output significantly.

It is believed that space charge also helps the stabilization of the meniscus in liquid metals [34], since it damps external perturbations of the electric field downstream. For the same reason, emission properties (e.g., current) are more independent from the external geometry [20] in terms of how amplified is the field near the emission region. The key assumption is to believe that the emission properties of the meniscus are strongly influenced by the shape of the electric fields in the emission region. This is rather intuitive since emission is only possible if these are around E^*. As mentioned earlier, the experimental evidence about the importance of the source hydraulic impedance suggests this is at least, an incomplete story.

In many ways, detailed empirical determination of these heuristics becomes intractable given the vast number of parameter combinations that are possible. In these cases, modeling becomes a powerful tool to approach these problems. Previous electrohydrodynamic models have been able to replicate many of the experimental trends observed in the operation of pure-ion sources. Yet, a specific physical explanation for these trends remains a challenging endeavor, especially since electrospraying is a highly coupled multi-physical problem with a lot of degrees of freedom, and observed phenomena may emerge from many elementary physics at the same time (e.g, current extraction may be a byproduct of having sufficient curvature, interfacial charge relaxation, high enough electric fields ...). In the next subsection, the most relevant electrohydrodynamic models of pure-ion electrospray emission are reviewed.

1.2.2 Literature review of numerical models

Early simulations of ion sources: Liquid metals

The early models of ion sources consider a fully conductive liquid metal subject to the action of a very strong electric field [71]. The equilibrium shape of the liquid metal is computed as a result of a balance between the surface tension stress, liquid pressure, and electric stress. The electric stress is computed by taking into account the space charge surrounding the emission region of the liquid metal meniscus. The space charge is computed by integrating the trajectory of the ions with the initial conditions determined by the position of the free interface and the current density. Due to the fact that the equilibrium interface is itself a byproduct of the space charge affecting the electric stress, multiple iterative modifications to the interface are needed for achieving a consistent field distribution that balances the surface tension and originates a total current compatible with the space charge model.

The early models of liquid metal ion sources were limited by their consideration of the equilibrium shape as a prescribed cusp model that exhibited a Taylor angle upstream and regarded the emission region as a spherical cap. The rigidity of this model may have precluded any fully consistent equilibrium interface computation since differences between the surface tension and electric stresses were up to 30% in some parts of the meniscus interface.

Some updates to this model were performed to include flow impedance and a free upstream angle [37, 39], which yielded close results to the current-voltage and current-to-cusp-length curves obtained experimentally.

Higuera [62] includes the ion evaporation recoil terms in the stress balance, resolves the full axisymmetric flow structure in the meniscus, and computes the equilibrium shapes and current-voltage characteristics more consistently. However, the consistency in the computation of the equilibrium shapes is at the expense of a simplified space charge model, which assumes a space charge limited ion beam with a parabolic current density profile. Nevertheless, the dynamics observed are in agreement with existing experimental and theoretical results, where steady ion evaporation is seen to occur in a narrow interval of electric fields. In agreement with previous models, the equilibrium interface from which ions evaporate resembles a cap at the end of a jet-like protrusion that grows linearly with the voltage. Higuera analyzes the meniscus behavior when taking into account the pressure drop induced during the evaporation process. The author finds this pressure is stabilizing and grows linearly with voltage. If this effect is not taken into account or is weakly present at low voltages, no steady solutions are found, and either oscillating behavior of the meniscus interface or drop formation is observed.

Still, all these efforts in the literature of liquid metal ion sources were limited by the computational capabilities of the time, and only simulate a very narrow region close to the emitting cusp. All past work neglects any geometrical effects from the tips and assumes boundary conditions mostly taken from the Taylor cone solution.

1.2.3 Accounting for limited conductivity: Ionic liquids

The fully conducting models described earlier needed to be updated to account for ionic liquids with limited conductivity.

Analogously to the cone-jet case, the electric charge is not fully relaxed near the emission region, and the meniscus behaves as a dielectric, thus departing from the equipotential case of liquid metals. This can be seen if inserting the jump condition for the electric field along the meniscus interface

$$\sigma = \varepsilon_0 E_n^v - \varepsilon_0 \varepsilon_r E_n^l = \varepsilon_0 E_n^v - \varepsilon_0 \varepsilon_r j_n^e / \kappa \tag{1.10}$$

in equation 1.6, where the latter equality has been obtained assuming a pure conductive charge transport near the emission region. With some algebraic manipulation, it can be shown that:

$$\frac{\sigma}{\varepsilon_0 E_n^v} = \frac{1}{1 + \frac{t_e}{t_m} \exp\left(\frac{-\Delta G}{k_B T}\left(1 - \sqrt{\frac{E}{E^*}}\right)\right)} \tag{1.11}$$

where $t_e = \frac{\varepsilon_0 \varepsilon_r}{\kappa}$ is the charge relaxation time, and $t_m = \frac{h}{k_B T}$ is the characteristic kinetic emission time. If the surface charge is fully relaxed (the meniscus is equipotential, and the electric field in the liquid is 0), then $\frac{\sigma}{\varepsilon_0 E_n^v} \approx 1$. This can be seen when we take the limit where the electrical conductivity $\kappa \to \infty$, and therefore $t_e \to 0$, and the exponential term in the denominator of eq. 1.11 vanishes. In the emission region $E \approx E^*$, and eq. 1.11 yields:

$$\frac{\sigma}{\varepsilon_0 E_n^v} \approx \frac{1}{1 + \frac{t_e}{t_m}} \tag{1.12}$$

For characteristic values of $\varepsilon_r = 15$, and $\kappa = 1$ S/m, $T \sim 300$ K, eq. 1.12 yields $\frac{\sigma}{\varepsilon_0 E_n^v} \approx 0.0012$, which illustrates the expected depletion of surface charge ($\sigma \to 0$) for ionic liquid pure-ion menisci.

In the cone-jet literature, many simulation frameworks have been developed based on the Taylor-Melcher leaky dielectric model [110], which have been successful in validating how emission properties and characteristic length scales are accurately represented by universal scaling laws [92, 61, 47, 59, 23, 51]. However, these models were not fully developed to capture the onset of pure ion evaporation from a closed interface. In other words, interfacial charge transport is governed by the activated ion evaporation process and therefore the need for special numerical techniques added to the standard Taylor-Melcher leaky dielectric model to capture its behavior[2]. First efforts introducing surface charge transport for pure ionic emission include the work

---

[2] As an example of this behavior, consider the characteristic depletion of surface charge illustrated in eqs. 1.11 and 1.12.

of Higuera [63], who simulated an ionic liquid drop attached to a flat conducting plate. Equilibrium meniscus shapes were obtained by sequentially solving the Laplace field equation outside and inside the droplet (no space charge was considered) with the activated emission condition derived by Iribarne and Thomson [67]. Electric and surface tension stresses were placed as boundary conditions for a Stokes flow solver. By using the interfacial velocity distributions coming from Stokes flow and a second-order Runge-Kutta temporal integration method, Higuera propagated the interface along time steps towards the equilibrium solution.

Higuera considered two cases. In the first case of constant meniscus volume, the author was able to sketch out the concept of starting voltage seen in the I-V (current vs voltage) traces, which is experimentally observed [74]. The current increase with the electric field yielded a linear behavior before it got unstable at a particular electric field. The same scaling relationship is reported by a number of empirical studies and it is believed to be due to the limits in conductive charge transport within ionic liquids [76, 81, 26].

In the second case, Higuera considered an external reservoir capable of pumping fluid with pressure p_0 towards the meniscus, and the pressure drop that occurs because of friction of the fluid with the channel walls that connect the reservoir to the external electrodes (hydraulic impedance). The non-dimensional total current emitted versus non-dimensional field was shown to be very dependent on p_0 and the hydraulic impedance coefficient, yielding currents with abnormal dissimilar behavior (up to 3 orders of magnitude difference for relatively similar values of p_0 and hydraulic impedance coefficient).

Regardless of the limitations of Higuera's model, the author was able to depict the notion of a maximum external field, which suggests that purely ionic emission might only be permissible within a narrow band of stability. The numerical variability for the current in the second case as a function of p_0 and the hydraulic impedance coefficient points out the importance of upstream conditions in determining emission behavior, which is in agreement with experimental work.

Coffman [19] updated Higuera's model by removing volumetric constraints, by including a substantial fraction of the liquid feeding system in the computational domain and by introducing Ohmic heating effects, which were predicted to play an important role in the current output.

Coffman's free volume generalization of the problem initialized by Higuera took three main input parameters, namely the electric field downstream E_0, a characteristic meniscus size r_0, and a hydraulic impedance coefficient C_R. The author's model unveiled a set of sharper families of emitting equilibrium shapes that sustained pure ion evaporation for high values of E_0. These solutions exist under a specific set of conditions, namely limited ranges of external E_0 and meniscus dimension r_0 ($1 \sim 5$ μm). These ranges would expand if sufficient hydraulic impedance is provided.

Coffman was able to reproduce the constant volume solutions of Higuera (no feeding channel) and categorize them in a set of solutions of particularly small size ($r_0 \sim 250$ nm), a low capillary number, and a high dielectric constant. This combination of parameters yielded equilibrium solutions that were practically hydrostatic and with a depleted distribution of surface charge in such a way that the evaporation process was generally decoupled from the balance between the surface tension and the electric stresses.

This extended Higuera's solutions to a higher range of electric fields with stable solutions for relatively large meniscus sizes at sufficient hydraulic impedance, which were reported to exist experimentally by Castro [13] and Romero-Sanz [107]. Coffman reported an increase in the electric field stability range for higher hydraulic impedance and an inverse proportionality relationship between the hydraulic impedance and total emitted current. The trade-off between the stability increase and the reduction in current throughput was found to be in agreement with Lozano's experimental findings [81].

Owing to the size of the problem (more than 10 independent non-dimensional numbers and 5 variables), lack of computational power, and the constraints imposed by commercial solvers (mesh resolution limitations, no parallelization), Coffman *et al.* [20] only report a moderate exploration of the region of stability as a function of the aforementioned input parameters, does not investigate Ohmic heating effects on stability and current emission, neglect volumetric charge effects due to temperature gradients, and couple the hydraulic impedance coefficient to the meniscus size. The latter point is especially critical, since many of the observations that led Coffman to conclude that static stability is increased at smaller radii for constant non-dimensional hydraulic impedances (coefficient C_R), are obscured by the fact that C_R itself is directly proportional to the meniscus radius ($\propto r_0^{5/2}$). In other words, for a given *dimensional*, or *experimental* hydraulic impedance Z, the C_R would have had to increase over the radius up to $r_0^{5/2}$, but was kept constant instead.

More recently, the work by Gallud and Lozano [42] leverages Coffman's model and extends it to include free charges in the bulk liquid originated by variable conductivity coefficients, presenting the results for a hydraulic impedance coefficient independent of the meniscus size. More importantly, this work provides a detailed exploration of the static stability regions and their interdependence on relevant metrics, such as menisci contact angles with the flat electrode and total current emitted. Based on these extensions, it appears that upper stability limits are a result of two competing phenomena. The first one is given by the maximum current output that a static evaporating meniscus can provide, while the second responds to a maximum electric pressure a meniscus can withstand before no static solutions can be found. The bifurcation of a static meniscus could be a possible outcome of this situation, which is reminiscent of what is experimentally observed in this type of ion sources [96, 97]. Numerical results suggest that this presumed bifurcation may represent a universal limit for all working liquids experiencing pure-ion emission with negligible space charge.

Gallud's results also indicate that an accurate resolution of the aforementioned limits of stability cannot be provided without considering energy effects. In this regard, simulations show how heated menisci can typically access a higher range of stable electric fields through the increase of electrical conductivity near the emission region.

1.2.4 The stability issue

Quantitative estimations of key outputs, such as current or stability for specific electrode geometries and ionic liquid parameters, continue to pose challenges within the technical domain. In the context of pure-ion meniscus models, the issue of stability has been approached using an ill-posed methodology in the works of Gallud [42] and Coffman [20]. Here, the absence of *physical* stability in these menisci under certain input parameters is attributed to the *numerical* instability or convergence limitations inherent in the employed numerical methods used for solving the models.

The selected numerical method in these works lacks the required robustness as it relies on a combined operator decomposition and fixed point iterative schemes. Such methods may fail to converge to solutions that exhibit higher stiffness under certain input parameters, even though these solutions may indeed exist, and be stable.

Furthermore, the fixed point iterative approach only defines stability up to the existence of a static solution. It is possible for static solutions to exist, but small infinitesimal perturbations can lead the equilibrium shape to transition into other oscillatory regimes.

To address both of these concerns, it is advantageous to decouple the analysis of *physical* stability from *numerical* stability. One approach involves examining the linear response of a simulated solution when subjected to small arbitrary perturbations [60]. This approach entails computing firstly the Jacobian of the system, which possesses substantially better convergence properties for computing the static solution; and secondly, computing a linear eigenvalue decomposition of the system's dynamics around the static solution.

By adopting this analysis, a clearer understanding of the meniscus behavior and its stability characteristics can be achieved, regardless of the numerical method's convergence properties. The difficulty in these cases arises from the computation of the Jacobian, which may be of particular difficulty to obtain in the cases where the domain of simulation is itself part of the desired solution.

1.2.5 Geometrical extensions

Most of the existent models focused their effort on addressing multiphysical complexity and meniscus-scale disparity (emission typically happens at a region smaller than 1% of the meniscus size for ionic liquids, and 0.1% for liquid metals), at the expense of geometrical simplifications. For this reason, these electrohydrodynamic models could only be regarded under qualitative scrutiny.

Geometry effects could be important: they are the key to any accurate description of the local fields surrounding the meniscus during its normal operation. This limitation has precluded any reliable experimental validation of current-throughput characteristics, at least for ionic liquid ion sources, where there is the additional scale disparity between the meniscus itself ($\sim 5\ \mu$m) and the scale of the electrodes that defines the electric problem (~ 1 mm).

Understanding the parameter and geometrical space where pure-ion emission could exist could open many other liquid formulations that so far have been neglected or unknown by the electrospray community, which has mostly chosen and designed operational conditions (tip geometry, extracting potential, tip material, and porosity, impedance, working fluids, etc) using heuristic knowledge (e.g, trial and error).

Chapter 2

Thesis objectives and contributions

The primary objectives of this thesis encompass the following:

1. Update existent electrohydrodynamic models [21] to:
    - **Represent the dynamics** of pure-ion menisci under realistic geometrical domains and best **alignment with experimental conditions** (including the extractor and axially-symmetric tip profile).
    - Include all physical phenomena associated with ion emission, namely the plume and **space charge effects**. Results show that space charge effects could **influence substantially the morphology** of the meniscus, but affect the current only in specific cases of **low perveance** and **very small meniscus sizes**.
2. Formulate a **Jacobian-based numerical approach** to overcome numerical challenges for the exploration of the model.
3. Assessment of the physical parameters that significantly influence two key aspects:
    - The **magnitude of current** emitted by ionic liquid ion sources. Results reveal that the magnitude of the current **follows existent theories for LMIS** in the limit of high hydraulic impedance and negligible space charge, and not physical scalings local to the emission region.
    - The **stability** of the meniscus. The stability is evaluated under the existence of static solutions, and under dynamics governed by small perturbations, albeit under simplified assumptions. Results reveal **a limited**

set of currents and hard limits on extracting fields where pure ion emission may be possible.

4. Conducting **preliminary experimental validation** of the developed model to assess its fidelity and reliability in capturing the essential features of pure-ion menisci, thereby enhancing confidence in its predictive capabilities.

Chapter 3

Physical model

In this chapter, we present the model proposed to solve the search of equilibrium and small perturbation dynamics of menisci in the pure ionic regime.

3.1 Geometry description

We consider two different geometries of the computational domain. The geometries depart from the ones considered by Higuera [63], Coffman [21] and Gallud [42] and include a curved electrode, or a capillary emitter. One of the geometries aims to represent actual experimental conditions used in our carbon emitters (figure 3-1). The size of the tip is also microscopic ($\sim 100\ \mu$m height), and is attached to a flat conductive substrate (Γ_D^v). The tip is axially symmetric and is situated at some distance d with respect to a hollow extractor plate Γ_E. The profile is given by the Scanning Electron Microscopy image of the tip used for each experiment. The flat hollow cylinder that serves as an extractor grid has thickness z_{el} with an internal hole radius r_h, and an aperture angle α. The simulation domain extends z_{up} above the extractor electrode.

The tip is truncated at its apex to accommodate a fluid channel of radius r_0 (see amplification of the square with a star in figure 3-1, represented in figure 3-2). A meniscus is pinned at the rim of the extruded channel and free to adopt any angle with the electrode. The channel is filled with ionic liquid ($\boldsymbol{\Omega}^l$), whose interface Γ_M separates the liquid from the vacuum domain ($\boldsymbol{\Omega}^v$). A fluid reservoir at pressure p_r feeds liquid into the channel, and is not treated computationally. The fluid enters the computational domain at Γ_I, which is at a distance $z_p = r_0$ from the rim of the truncation, as if it were the outlet of a fully developed pipe flow (Hagen-Poiseuille paraboloidal flow). Due to the locality of the problem, and in most parts of this thesis, it is convenient to use a reduced computational domain centered in this region, which is more local to the meniscus and allows a more generalizable description of the influence of the electric field on the meniscus (see figure 3-3). In this reduced computational domain, the tip is modeled as an (infinite) hyperboloid of revolution, which is also extruded to accommodate a meniscus in the same way as described in figure 3-2. The hyperboloid of revolution model is a very useful parametrization of the tip because it admits an analytical solution of the Laplace equation when the extractor is an infinite flat plate via the prolate spheroidal coordinate system [85], and consequently, an analytical estimation of the electric fields local to where the meniscus pins. The reduced domain of simulation only has a vertical dimension z_{sim} and is truncated at some distance r_{sim} and d^* from the apex of the hyperboloidal tip, where the potential is barely modified by the structure of the meniscus. The analytical solution for the potential in the infinite hyperboloidal and extractor plate case is imposed as a boundary condition on the limits of the computational domain (Γ_{EXT} in figure 3-3). The details of the boundary conditions for the potential structure will be explained in section 3.3.

Under this coordinate system (see figure 3-3), the radial r_{tip} and axial z_{tip} coordinates transform to a parameter set of confocal hyperboloids w and corresponding orthogonal ellipsoids v that follow the equations below:

$$w = \frac{1}{a}\left(\sqrt{r_{tip}^2 + \left(z_{tip} + \frac{a}{2}\right)^2} - \sqrt{r_{tip}^2 + \left(z_{tip} - \frac{a}{2}\right)^2}\right) \tag{3.1}$$

$$v = \frac{1}{a}\left(\sqrt{r_{tip}^2 + \left(z_{tip} + \frac{a}{2}\right)^2} + \sqrt{r_{tip}^2 + \left(z_{tip} - \frac{a}{2}\right)^2}\right) \tag{3.2}$$

The hyperboloid chosen as the tip geometry is defined as $w = w_0$ and the surface $w = 0$ is the extractor plate. The distance between the focal point F of the hyperboloids and the extractor plate, or surface where $w = 0$ is $\frac{a}{2}$. We can express the reference geometrical parameter a and the value of the hyperboloid parameter w_0 as a function of the radius of curvature R_c of the hyperboloid $w = w_0$ at its apex and the distance between this apex and the extractor surface $w = 0$:

$$a = 2d\sqrt{1 + \frac{R_c}{d}} \tag{3.3}$$

$$w_0 = \left(\sqrt{1 + \frac{R_c}{d}}\right)^{-1/2} \tag{3.4}$$

where:

$$R_c = \frac{\left(1 + \left(\frac{dz_{tip}}{dr_{tip}}\right)^2\right)^{\frac{3}{2}}}{\frac{d^2 z_{tip}}{dr_{tip}^2}} \tag{3.5}$$

The cases where we use this simplified geometry will be explicitly mentioned during this thesis. The origin of the coordinate system coordinates for the validity of eqs. 3.1, 3.2 and 3.5 (that is $r_{tip} = 0$, $z_{tip} = 0$) is not the same as the one considered for the whole model ($r = 0$, $z = 0$). The former is the one considered in reference [85], and it is used in this thesis exclusively to describe the shape of the hyperboloid of revolution (see the top of figure 3-3). The latter is the general origin of coordinates used in this thesis, and it is centered locally in the meniscus base by convenience (see figure 3-2, inside the meniscus). Finally, in the capillary case we consider the domain sketched in figure 3-4. The thickness of the capillary wall is 0 (the inner radius is equal to the outer radius r_0). When we use the reduced computational domain, we simulate the domain spanned by z_{sim} and r_{sim}, where $r_h = 0$.

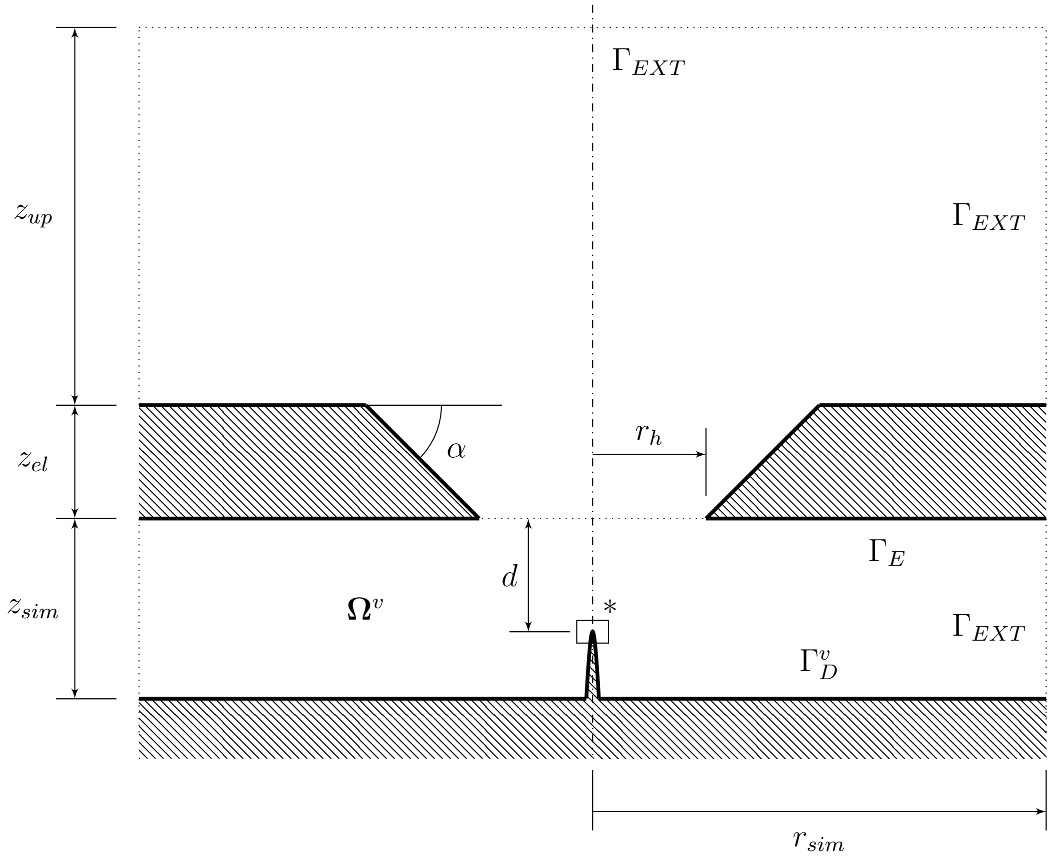

Figure 3-1: Computational domain of the electrohydrodynamic simulation model. The computational domain coincides with the actual experimental arrangement.

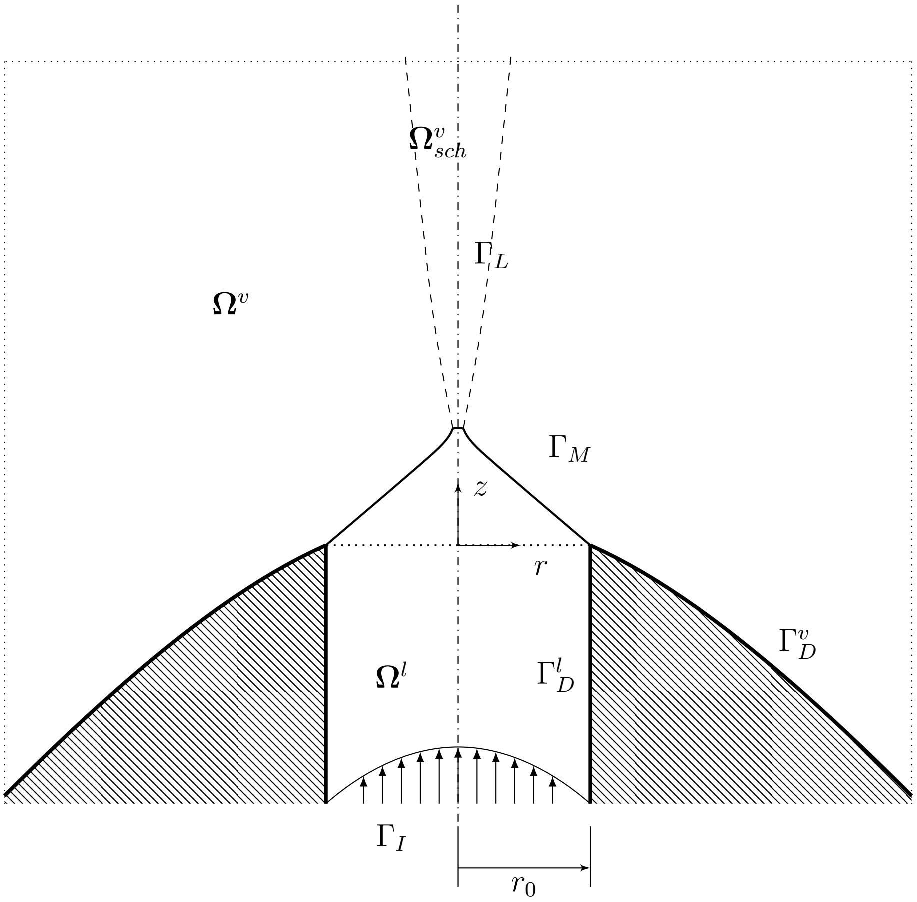

Figure 3-2: Zoomed computational domain where the truncation of the tip accommodates the inlet fluid channel.

3.2 Model equations

This section presents the electrohydrodynamic model, which incorporates several advancements compared to the Coffman model [21]. Notable differences include the inclusion of space charges in both the bulk liquid, necessary to account for conductivity gradients resulting from temperature variations, and the vacuum region, where a plume model is introduced. Additionally, the model features an uncoupled definition of hydraulic impedance from meniscus size, enabling a more comprehensive examination of its impact on current behavior. Moreover, dynamic terms are incorporated into the model, enhancing its ability to capture time-dependent phenomena.

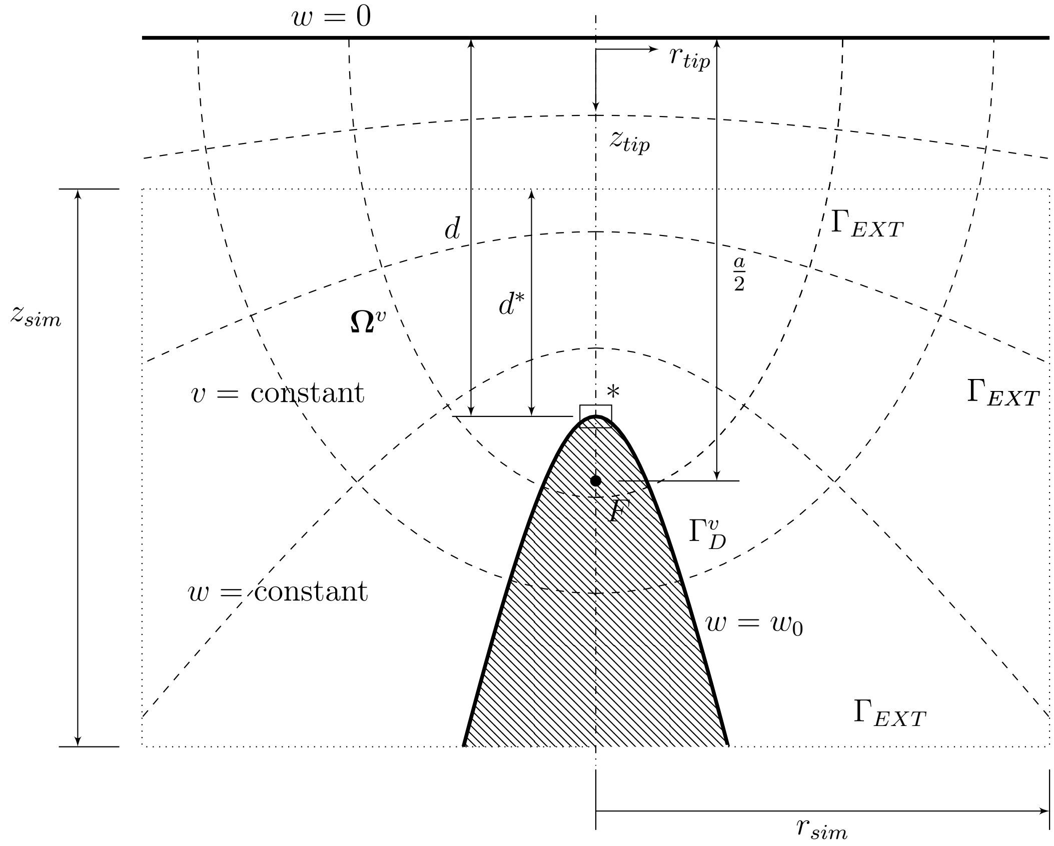

Figure 3-3: Reduced computational domain with prolate spheroidal tips. The reduced computational domain does not consider the geometry of the extractor electrode and cuts the computational domain at a shorter Γ_{EXT} than in figure 3-1. The *computational* distance d^* may be smaller than the physical distance between the hyperboloidal tip and the extracting electrode plane d, although the physical distance effect is correctly implemented via boundary conditions of the potential at Γ_{EXT}.

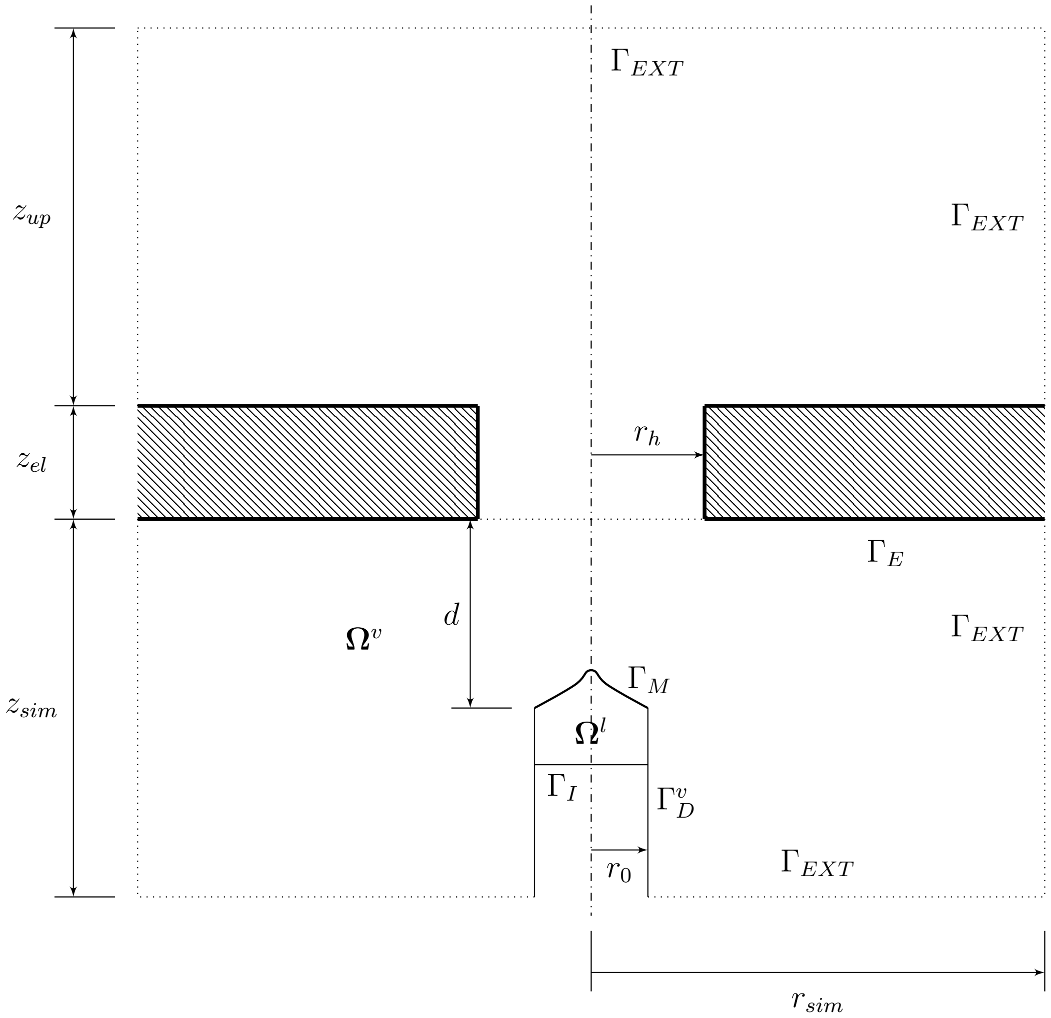

Figure 3-4: Computational domain of the electrohydrodynamic simulation model for the capillary case. The computational domain coincides with the actual experimental arrangement as well. The inner radius coincides with the outer diameter and it is equal to r_0.

However, it is important to note that the dynamic problem analysis is limited in this study and will primarily focus on the small perturbation analysis of the meniscus in chapter 9 of this thesis. Comprehensive analysis of the dynamic aspects will be addressed in future research endeavors.

3.2.1 Electric field equations

Consider the ionic liquid meniscus subject to an electric potential bias V with respect to an extracting electrode. The incompressible liquid flows along $\mathbf{\Omega}^l$ towards the vicinity of the emission region r^* when forced by the electric stresses acting on the surface. The electric stresses are calculated by solving the Poisson equation (or Laplace, when space charge effects are not relevant) and charge conservation equations in the vacuum and liquid domains. The Poisson equation in the vacuum and liquid domains can be expressed as:

$$\nabla \cdot (\varepsilon_0 \mathbf{E}) = -\varepsilon_0 \nabla^2 \phi = \rho_{sch} \qquad \text{in} \qquad \mathbf{\Omega}^v \tag{3.6}$$

$$\nabla \cdot (\varepsilon_0 \varepsilon_r \mathbf{E}) = -\varepsilon_0 \varepsilon_r \nabla^2 \phi = \rho_{sch} \qquad \text{in} \qquad \mathbf{\Omega}^l \tag{3.7}$$

Where $\mathbf{E} = -\nabla\phi$ is the electric field, ρ_{sch} is the space charge originated by the evaporated current in the vacuum domain, and the charge density in the bulk fluid, ε_0 is the dielectric permittivity of vacuum, and ε_r is the relative dielectric permittivity of the ionic liquid.

The electric field jump equation on the interface domain can be expressed as:

$$\varepsilon_0 E_n^v - \varepsilon_0 \varepsilon_r E_n^l = \sigma \qquad \text{on} \qquad \Gamma_M \tag{3.8}$$

Where σ is the surface charge density along the meniscus interface Γ_M, $E_n^v = \mathbf{E}^v \cdot \mathbf{n}$ is the electric field component normal to the interface evaluated in the vacuum $\mathbf{\Omega}^v$. Analogously for the component evaluated in $\mathbf{\Omega}^l$, $E_n^l = \mathbf{E}^l \cdot \mathbf{n}$.

3.2.2 Bulk charge conservation equation

The charge conservation equation is defined for the bulk liquid as:

$$\frac{\partial \rho_{sch}}{\partial t} + \nabla \cdot (\kappa(T)\mathbf{E} + \rho_{sch}\mathbf{u}) = 0 \qquad \text{in} \qquad \mathbf{\Omega}^l \tag{3.9}$$

Eq. (3.9) contains two terms associated to the conductive ($\mathbf{j}_{cond} = \kappa(T)\mathbf{E}$) and convective ($\mathbf{j}_{conv} = \rho_{sch}\mathbf{u}$) bulk charge transport, where $\mathbf{u}$ is the bulk velocity of the fluid. While considered in this thesis, the bulk convective charge transport is generally small and can be usually neglected. This can be seen if we take the characteristic conductive current density $j^* \sim \kappa E^*/\varepsilon_r$ when considering a fully depleted[1] interfacial charge σ, a characteristic fluid speed at this region $u \sim \frac{I}{2\pi {r^*}^2 \rho \frac{q}{m}}$, and a characteristic space charge in the bulk liquid ρ_{sch} that, if relevant, would be affecting the bulk liquid electric field through Poisson equation in the same fully depleted interfacial charge situation $\rho_{sch} \sim \varepsilon_0 \varepsilon_r E^l/r^* \sim \varepsilon_0 E^*/r^*$:

$$\frac{j_{cond}}{j_{conv}} \sim \frac{\kappa E^*}{\varepsilon_r \rho_{sch} u} \sim \frac{\kappa 2\pi {r^*}^3 \rho \frac{q}{m}}{\varepsilon_0 \varepsilon_r I} \tag{3.10}$$

where I is the total current emitted.

For typical physical parameters of ionic liquids, namely $I \sim 300$ nA, $\rho \sim 1200\ \frac{\text{kg}}{\text{m}^3}$, $q/m \sim 5 \cdot 10^5\ \frac{\text{C}}{\text{kg}}$, $r^* \sim 20$ nm, $\kappa = 1$ S/m, $\varepsilon_r \sim 10$, the ratio in eq. 3.10 yields $\frac{j_{cond}}{j_{conv}} \sim 570 \gg 1$.

If the convective charge transport is neglected in eq. 3.9, and under steady conditions, an expression can be obtained for ρ_{sch} as a function of the electric field in $\mathbf{\Omega}^l$ by inserting eq. 3.9 in eq. 3.7. This yields:

$$\rho_{sch} = \frac{-\varepsilon_0 \varepsilon_r \nabla \kappa(T) \cdot \mathbf{E}}{\kappa(T)} \tag{3.11}$$

The conductivity is assumed to depend exponentially on temperature for ionic liquids, as usually described by means of the Vogel-Tammann-Fulcher (VTF) equation [119, 10][2]:

$$\kappa(T) = \kappa_0 \exp\left(\frac{B_\kappa \left(T - T_0\right)}{\left(T - T_{\kappa 0}\right)\left(T_0 - T_{\kappa 0}\right)}\right) \tag{3.12}$$

Where κ_0 is the conductivity of the liquid at a reference temperature T_0, and B_κ and T_{κ_0} are constants.

Notice from eq. 3.11 that the breakup of quasi-neutrality is usually originated by spatial gradients in conductivity. The dependency of the conductivity with temperature (eq. 3.12) combined with temperature gradients in the bulk fluid originate

---

[1] As discussed in chapter 1, depleted surface charge means $\sigma \approx 0$ at the apex of the meniscus, as opposed to relaxed surface charge, where $\sigma \approx \varepsilon_0 E_n^v$. In the emission region, the meniscus behaves as a perfect dielectric when σ is depleted, and as a conductor when σ is relaxed.

[2] The VTF equation is usually written as $\kappa = A \exp \frac{-B}{(T - T_{\kappa_0})}$ in the literature, where A is a constant. We have scaled it by introducing κ_0 in such a way that $\kappa\left(T_0\right) = \kappa_0$ for convenience (e.g., $A = \kappa_0 \exp \frac{B}{T_0 - T_{\kappa_0}}$).

this space charge.

Ohmic model for charge conduction

The Ohmic model considered in this thesis is not technically correct: there is a breakup of bulk quasi-neutrality due to gradients in temperature, the liquid is exposed to high electric fields, and ionic liquids are not dilute solutions, therefore the linear response of the current density with the electric field inside the liquid may not be accurate.

Even in the highly diluted case, if neglecting the convective charge transport, a better approximation to the current density vector at higher electric fields would be:

$$\mathbf{j} = \kappa(T, \mathbf{E}, \rho_{sch})\mathbf{E} - D\nabla\rho_{sch} \tag{3.13}$$

Where D is a characteristic diffusion coefficient of the ionic liquid, and $\kappa\left(T, \mathbf{E}, \rho_{sch}\right)$ is an "effective" conductivity that may depend on the electric field itself, the space charge, and the temperature. An order of magnitude estimation yields that the conductive charge transport is much more relevant than the diffusive:

$$\frac{\kappa E^* r^*}{\varepsilon_r D \rho^*_{sch}} \sim 4.52 \cdot 10^4 \gg 1 \tag{3.14}$$

Where $\rho^*_{sch} \sim \frac{\varepsilon_0 \Delta\kappa E^*}{\kappa r^*}$ from eq. 3.11 evaluated in the fully depleted interfacial charge condition near the emission region $E \sim E^*/\varepsilon_r$, and r^* is the characteristic emission region dimension from eq. 1.7. For eq. 3.14, we have used values of $\kappa \sim 1$ S/m, $E^* \sim 1$ V/nm, $\varepsilon_r \sim 10$, $r^* \sim 20$ nm, conductivity increases about $\Delta\kappa \sim 1$ S/m for the estimated changes in temperature in the emission region of $\Delta T \sim 15°$ C [19] and [EMIm][BF$_4$]. The single-fluid diffusion coefficient D is estimated from a characteristic combined self-diffusion coefficient ($D \sim D_{anion} + D_{cation}$), for the case of [EMIm][BF_4] $D \sim 10^{-10}$ m^2/s [90].

Acknowledging this limitation, we use the Ohmic model $\mathbf{j}_{cond} = \kappa(T)\mathbf{E}$ neglecting diffusive transport, in the absence of a better model for the conductivity of ionic liquids in the single fluid electrohydrodynamic formulation that we are adopting in this thesis.

3.2.3 Interfacial charge conservation

The conservation of interfacial charge in this electrohydrodynamic can be expressed in a very similar way to the equations describing interfacial conservation of surfactants [132, 120, 70, 140]:

$$\frac{\partial \sigma}{\partial t} + \nabla_S \cdot (\sigma \mathbf{u}) = \kappa\left(T\right) E_n^l - j_n^e \qquad \text{on} \qquad \Gamma_M \tag{3.15}$$

Eq. 3.15 balances the temporal growth of surface charge (first term of the left-hand side), to the interfacial charge convection (second term of the left-hand side), the conductive current density entering the interface (first term of the right-hand side), and the evaporated current density (second term of the right-hand side). The operator $\nabla_S \cdot$ appearing in the convective charge transport expression is the surface divergence operator (see [56]).

Blyth [9] and van Gaalen [132] provide a useful axially symmetric evaluation of the left-hand side of eq. 3.15 as:

$$\frac{\partial \sigma}{\partial t} - \frac{\partial h}{\partial t}\mathbf{z} \cdot \nabla_S \sigma + \nabla_S \cdot (\sigma \mathbf{u} \cdot \mathbf{t}) + 2H\sigma \mathbf{u}_i \cdot \mathbf{n} = \kappa\left(T\right) E_n^l - j_n^e \tag{3.16}$$

Where $h = h(r,t)$ is the height of the meniscus control points, in other words, it is a function that describes the vertical coordinate of the interface, $\mathbf{z}$ is the unit vector pointing in the vertical direction, ∇_S is the surface gradient operator, or the gradient in the tangential direction [110, 56], $\mathbf{u}_i$ is the velocity of the interface and H is the average curvature of the interface. The function h and the velocity of the interface $\mathbf{u}_i$ are related by the following kinematic condition:

$$\frac{\partial h}{\partial t} = \mathbf{u}_i \cdot \mathbf{z} - \frac{\partial h}{\partial r}\mathbf{u}_i \cdot \mathbf{r} = \mathbf{u}_i \cdot \mathbf{n}\sqrt{1 + \left(\frac{\partial h}{\partial r}\right)^2} \tag{3.17}$$

Where $\mathbf{r}$ is the unit vector pointing in the radial (cylindrical) direction. The intuition behind eq. 3.17 is explained as follows from figure 3-5. Consider a displacement in some time span Δt of the interface $h(r,t)$. The points describing the interface of the meniscus will be displaced over this Δt some horizontal distance Δr and vertical distance Δz along the normal direction $\mathbf{n}$ of the same interface. Then, the vertical location of the interfacial point at $r + \Delta r$, $t + \Delta t$ will be:

$$h\left(r + \Delta r, t + \Delta t\right) = h\left(r, t\right) + \Delta z \tag{3.18}$$

If we Taylor expand eq. 3.18 we get:

$$h\left(r, t\right) + \frac{\partial h}{\partial r}\Delta r + \frac{\partial h}{\partial t}\Delta t = h\left(r, t\right) + \Delta z \tag{3.19}$$

Rearranging, dividing by Δt and taking the limit when Δt, Δr, Δz are infinitesimally small yields:

$$\frac{\partial h}{\partial r}\frac{dr}{dt} + \frac{\partial h}{\partial t} = \frac{dz}{dt} \tag{3.20}$$

Which is equation 3.17 if we substitute $\frac{dr}{dt}$, $\frac{dz}{dt}$ by the vector elements of the interface velocity $\mathbf{u}_i \cdot \mathbf{r}$, $\mathbf{u}_i \cdot \mathbf{z}$, respectively. The boundary conditions for h are the pinning condition:

$$h = 0 \qquad \text{on} \qquad r = r_0 \tag{3.21}$$

and the axially symmetric meniscus condition at the apex:

$$\frac{\partial h}{\partial r} = 0 \qquad \text{on} \qquad r = 0 \tag{3.22}$$

According to equation 3.21, it becomes evident that the current model does not account for the lateral movements of the meniscus along the electrode profile. This limitation is particularly significant since it overlooks the potential dynamic disturbances that could cause the meniscus to become unpinned from its anchoring site.

The normal $\mathbf{n}$ and tangential $\mathbf{t}$ vectors to the interface can be expressed as a function of the meniscus height function:

$$\mathbf{n} = \begin{pmatrix} -\frac{\partial h}{\partial r} / \sqrt{1 + \left(\frac{\partial h}{\partial r}\right)^2} \\ \\ 1 / \sqrt{1 + \left(\frac{\partial h}{\partial r}\right)^2} \end{pmatrix} \tag{3.23}$$

$$\mathbf{t} = \begin{pmatrix} 1 / \sqrt{1 + \left(\frac{\partial h}{\partial r}\right)^2} \\ \\ \frac{\partial h}{\partial r} / \sqrt{1 + \left(\frac{\partial h}{\partial r}\right)^2} \end{pmatrix} \tag{3.24}$$

The average curvature of the meniscus can be expressed as:

$$H = \frac{1}{2}\nabla \cdot \mathbf{n} \tag{3.25}$$

It can be shown that eq. 3.16 can be rearranged in intrinsic coordinates as:

$$\frac{\partial \sigma}{\partial t} = \frac{\partial h}{\partial t}\mathbf{z} \cdot \nabla_S \sigma - \frac{1}{r}\frac{\partial \left(\mathbf{u} \cdot \mathbf{t}\, \sigma r\right)}{\partial s} - 2H\sigma \mathbf{u}_i \cdot \mathbf{n} + \kappa\left(T\right) E_n^l - j_n^e \tag{3.26}$$

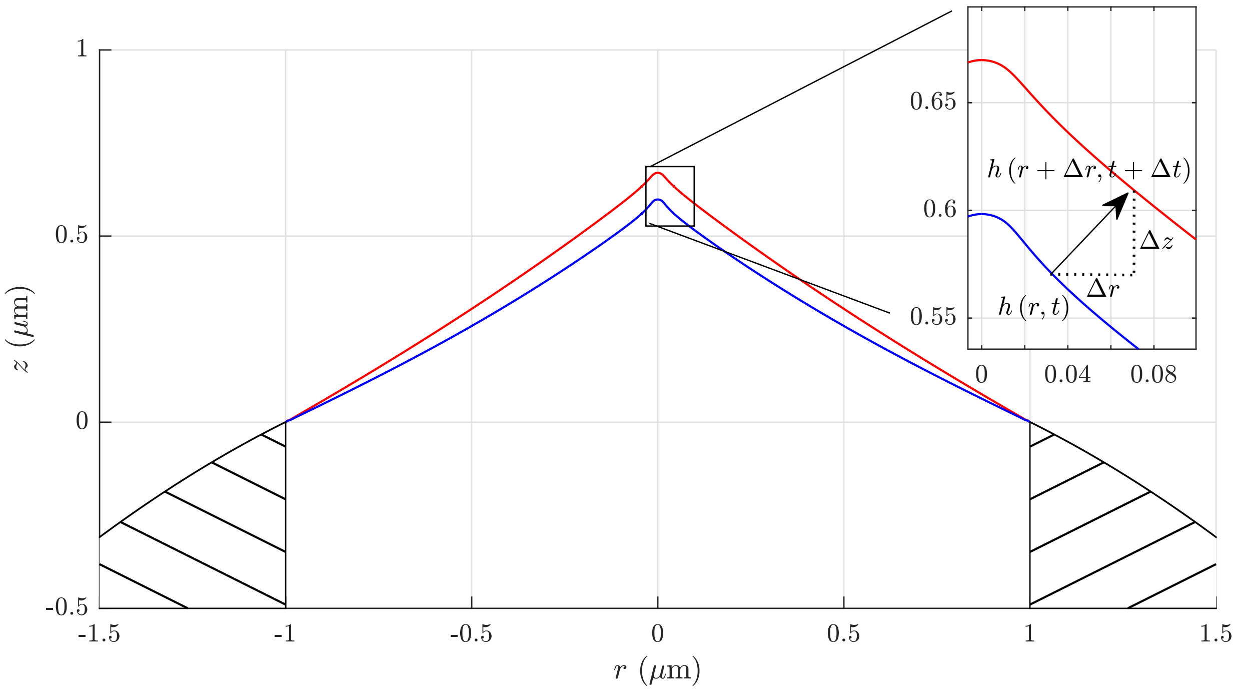

Figure 3-5: Meniscus interface displacement during a finite Δt. The radius of the sample meniscus is $r_0 = 1$ μm. The limit where $\Delta t \to 0$ is taken to derive the interfacial kinematic condition in eq. 3.17.

Where s is the arc-length coordinate of the meniscus interface:

$$\frac{\partial}{\partial s} = \frac{1}{\sqrt{1 + \left(\frac{\partial h}{\partial r}\right)^2}} \frac{\partial}{\partial r} \tag{3.27}$$

The term of the left-hand side of eq. 3.26 corresponds to the local variation of surface charge at a specific point along the meniscus interface h. The first term of the right-hand side is needed so that the local variation references the meniscus interface velocity in the vertical direction. In other words, that same meniscus control points *observe* the local surface charge variation (see [140]). The second term of the right-hand side is the convective variation of interface surface charge. This term was also derived and included by Coffman [19]. The third term represents variations of interfacial charge density by the deformation of the interface itself, for this reason it depends on the curvature H and the interfacial velocity $\mathbf{u}_i$. Eq. 3.26 is the one that will be used in our numerical scheme described in chapter 4.

3.2.4 Kinetic law for particle evaporation

The kinetic law for particle evaporation at the interface (eq. 1.6) is used to relate the evaporated current density j_n^e to the electric field normal to the meniscus interface. As we mentioned in chapter 1 this yields for ionic liquids:

$$j_n^e = \frac{\sigma k_B T}{h} \exp\left(-\frac{\Delta G - G(E_n^v)}{k_B T}\right) \tag{3.28}$$

3.2.5 Fluid dynamics

The dynamics of the fluid are described by the incompressible Navier-Stokes equations:

$$\nabla \cdot \mathbf{u} = 0 \qquad \text{in} \qquad \mathbf{\Omega}^l \tag{3.29}$$

$$\rho \left(\frac{\partial \mathbf{u}}{\partial t} + (\mathbf{u} \cdot \nabla)\,\mathbf{u}\right) = \nabla \cdot (\tau_f + \tau_e) \quad \text{in} \quad \mathbf{\Omega}^l \tag{3.30}$$

Where ρ is the ionic liquid density, τ_f is the viscous fluid stress tensor, and τ_e is the Maxwell stress tensor.

The fluid stress tensor can be arranged in this form:

$$\tau_f = -p\mathbf{I}_n + 2\mu\mathbf{e} = -p\mathbf{I}_n + \mu\left(\nabla\mathbf{u} + \nabla\mathbf{u}^T\right) \tag{3.31}$$

Where p is the bulk pressure, $\mathbf{I}_n$ is the identity tensor of order n (in the axially symmetric implementation of this problem, $n = 2$), μ is the viscosity of the fluid and $\mathbf{e} = \frac{1}{2}\left(\nabla \mathbf{u} + \nabla \mathbf{u}^T\right)$ is the strain rate tensor.

The viscosity is modeled also by means of the Vogel-Tammann-Fulcher (VTF) equation [91, 53]:

$$\mu(T) = \mu_0 \exp\left(\frac{-B_\mu\left(T - T_0\right)}{\left(T - T_{\mu 0}\right)\left(T_0 - T_{\mu 0}\right)}\right) \tag{3.32}$$

Where μ_0, B_μ and $T_{\mu 0}$ are constants.

The Maxwell stress tensor τ_e has the following form:

$$\tau_e = \varepsilon_0 \mathbf{E} \otimes \mathbf{E} - \frac{1}{2}\varepsilon_0\left(\mathbf{E} \cdot \mathbf{E}\right)\mathbf{I}_n \tag{3.33}$$

Where $\otimes$ indicates tensor product or dyadic product. The divergence of the Maxwell stress tensor (eq. 3.33) yields:

$$\nabla \cdot \tau_e = \rho_{sch} \mathbf{E} \tag{3.34}$$

3.2.6 Interfacial mass conservation

The equation for the mass evaporated at the interface yields:

$$\rho\ \left(\mathbf{u} - \mathbf{u}_i\right) \cdot \mathbf{n} = \rho^v\ \left(\mathbf{u}^v - \mathbf{u}_i\right) \cdot \mathbf{n} = \frac{j_n^e}{\frac{q}{m}} \quad \text{on} \quad \Gamma_M \tag{3.35}$$

Where ρ and $\mathbf{u}$ are the density and the net velocity inside the liquid, $\mathbf{u}_i$ is the velocity of the interface (see eq. 3.17), and ρ^v and $\mathbf{u}^v$ are the ion density and net velocity of the emitted ions in the vacuum right after they go past the interface. The last equality can be extracted from the equivalence between charge and mass of the ions evaporated, and represents the mass flux of ions going across the interface. In the single fluid picture that we are adopting in this thesis, the charge-to-mass ratio of the ions q/m represents the average of all species emitted i:

$$\frac{I}{\frac{q}{m}} = \sum_i \frac{I_i}{\frac{q_i}{m_i}} \tag{3.36}$$

Where I is the total current emitted:

$$I = \int_{\Gamma_M} j_n^e \, d\Gamma_M \tag{3.37}$$

3.2.7 Interfacial momentum conservation

For a given stress tensor τ, the stress that acts on any point along the meniscus interface is $\tau \cdot \mathbf{n}$. In our axially-symmetric implementation of this problem, $\tau \cdot \mathbf{n}$ is a 2-component vector indicating the value of this stress in the directions $\mathbf{r}$ and $\mathbf{z}$. The projection of this stress in the normal and tangential directions along the meniscus interface is then $\mathbf{n} \cdot \tau \cdot \mathbf{n}$ and $\mathbf{t} \cdot \tau \cdot \mathbf{n}$, respectively. Acknowledging this, and assuming a negligible interface mass, velocity, and evaporated ion pressure and viscosity, the momentum conservation equations in the normal and tangential direction to the interface Γ_M are respectively [62]:

$$\mathbf{n} \cdot \left(\tau_e^v - \tau_e^l - \tau_f\right) \cdot \mathbf{n} - \gamma \nabla \cdot \mathbf{n} = \frac{j_n^e}{\frac{q}{m}} \left(\mathbf{u} - \mathbf{u}^v\right) \cdot \mathbf{n} = \frac{\left(j_e^n\right)^2 (1-\beta)}{\rho \left(\frac{q}{m}\right)^2} \quad \text{on} \quad \Gamma_M \tag{3.38}$$

$$\mathbf{t} \cdot \left(\tau_e^v - \tau_e^l - \tau_f\right) \cdot \mathbf{n} + \frac{\partial \gamma}{\partial s} = \frac{j_n^e}{\frac{q}{m}} \left(\mathbf{u} - \mathbf{u}^v\right) \cdot \mathbf{t} = 0 \quad \text{on} \quad \Gamma_M \tag{3.39}$$

Where τ_e^l, τ_e^v are the electric stress tensors in the liquid and vacuum (e.g., the evaluation of the electric stress tensor in eq. 3.33 in either vacuum or liquid regions of the domain). The second term on the left-hand side of eq. 3.38 is the surface tension stress, where γ is the surface tension coefficient, and $\nabla \cdot \mathbf{n} = 2H$ is two times the average curvature of the interface (see eq. 3.25). The term on the right-hand side of eqs. 3.38 and 3.39 is the "recoil term" or the difference between the momentum flux in the normal and tangential directions carried by the evaporated ions and the ions arriving at the interface from the liquid. In the normal direction, this term can be simplified by inserting equation 3.35 in 3.38 to yield the third equality, where β is the ratio between the fluid and gas phase densities of the ionic liquid:

$$\beta = \frac{\rho}{\rho^v} \tag{3.40}$$

The theory of evaporation and electrically-assisted ion evaporation is a state-of-the-art research problem. In particular, this thesis does not intend to resolve the Knudsen layer [117] at the interface level or the rapid decay in density between the liquid and gas phases. We believe that relating this decay to the presence of an image charge hump and the structure of the electric field at such a scale is a very interesting research question out of the scope of this thesis. Still, in order to preserve physical consistency, we formulate the interfacial equations as a function of this arbitrary value of β.

In the tangential direction, we impose a no-slip condition at the interface and consider that $(\mathbf{u} - \mathbf{u}^v) \cdot \mathbf{t} = 0$.

The term $\frac{\partial \gamma}{\partial s}$ is the Marangoni stress in eq. 3.39, and is caused by gradients of surface tension. The gradients of surface tension are originated due to gradients in temperature along the meniscus interface:

$$\gamma = \gamma\left(T\right) = \gamma_0 \left(1 - B_\gamma \left(T - T_0\right)\right) \tag{3.41}$$

Where B_γ is a constant coefficient.

3.2.8 Energy transport equation

The temperature in the meniscus is governed by the energy transport equation balancing Ohmic and viscous dissipation with conductive and convective transport of heat:

$$\rho c_p \left(\frac{\partial T}{\partial t} + \mathbf{u} \cdot \nabla T\right) = \kappa_T \nabla^2 T + \frac{\mathbf{j} \cdot \mathbf{j}}{\kappa\left(T\right)} + \Phi \quad \text{in} \quad \boldsymbol{\Omega}^v \tag{3.42}$$

Where c_p and κ_T are the heat capacity and thermal conductivity of the ionic liquid respectively and Φ is the viscous dissipation power per unit volume for an incompressible fluid. The viscous dissipation term takes the following form:

$$\Phi = 2\mu e_{ij}^2 \tag{3.43}$$

Where e_{ij}^2 indicates summation over all the elements of the strain rate tensor to the square power.

3.2.9 Interfacial energy conservation

If we neglect the *accumulation* of energy at the interface, the thermal conductivity and viscosity in the vacuum, the work done by the electric, viscous stresses and surface tension, and the difference of kinetic energies between the ions evaporated and solvated in the fluid, the energy conservation equation at the interface yields:

$$\frac{j_n^e}{\frac{q}{m}} \Delta h = -\left(\kappa_T \nabla T\right) \cdot \mathbf{n} \quad \text{on} \quad \Gamma_M \tag{3.44}$$

Where Δh represents the enthalpy change per unit mass of the ions from the liquid to the gas phase. The enthalpy change is effectively implemented as:

$$\Delta h = c_p \left(T_{out} - T\right) + l_H \tag{3.45}$$

Where l_H is the enthalpy of vaporization or latent heat per unit mass, and T_{out} is the temperature at which ions leave. Recent research from fragmentation dynamics [87] suggests that the temperature at which the ions leave from electrospray sources is substantially higher than that in the bulk liquid, which is likely originated due to molecular processes occurring during ion emission.

3.2.10 Plume model

In this thesis, the plume will be only solved in steady conditions. In chapter 9 where we solve the small perturbation dynamics of the meniscus, space charge in the vacuum domain is neglected. We also neglect the pressure of the ions and we assume a pure convective transport of ions driven by the electric field as:

$$\rho^v \left(\mathbf{u}^v \cdot \nabla\right) \mathbf{u}^v = \rho_{sch} \mathbf{E} \quad \text{in} \quad \boldsymbol{\Omega}^v \tag{3.46}$$

and a mass conservation equation as:

$$\nabla \cdot \left(\rho^v \mathbf{u}^v\right) = 0 \quad \text{in} \quad \boldsymbol{\Omega}^v \tag{3.47}$$

Notice that the charge conservation equation can also be cast as:

$$\nabla \cdot \left(\rho^v_{sch} \mathbf{u}^v\right) = 0 \quad \text{in} \quad \boldsymbol{\Omega}^v \tag{3.48}$$

as it should be from the equivalence of mass and charge of the ions traveling through the plume (only in $\boldsymbol{\Omega}^v$):

$$\rho^v_{sch} = \frac{q}{m} \rho^v \quad \text{in} \quad \boldsymbol{\Omega}^v \tag{3.49}$$

Notice that if we multiply the left-hand side and right-hand side of eq. 3.46 by $\mathbf{u}^v$ rearrange terms, and use eqs. 3.49 and 3.47 we can get to:

$$\nabla \cdot \left(\left(\frac{q}{m} \phi + \frac{\mathbf{u}^v \cdot \mathbf{u}^v}{2} \right) \rho^v \mathbf{u}^v \right) = 0 \tag{3.50}$$

which is the traditional energy conservation equation for beam optics of charged particles.

3.3 Boundary conditions

The fluid enters the computational domain as a fully developed pipe flow (Hagen-Poiseuille) at the inlet (Γ_I). This condition can be represented accurately by constant pressure and zero viscous stress boundary conditions:

$$\begin{aligned} \mathbf{n} \cdot \tau_f \cdot \mathbf{n} = -p = -\left(p_r - \Delta p\right) \qquad & \text{on} \qquad \Gamma_I \\ \mathbf{t} \cdot \tau_f \cdot \mathbf{n} = 0 \qquad & \text{on} \qquad \Gamma_I \end{aligned} \tag{3.51}$$

Where p_r is the pressure at the reservoir and $\Delta p = \frac{I}{\rho \frac{q}{m}} Z$ is the pressure drop caused by the hydraulic impedance Z of the channel, or a characteristic impedance of the geometry.

The fluid does not slip on the walls of the channel, thus:

$$\mathbf{u} = 0 \qquad \text{on} \qquad \Gamma_D^l \tag{3.52}$$

The boundary conditions for the electric problem are:

$$\begin{aligned} \phi = V \qquad & \text{on} \qquad \Gamma_I \cup \Gamma_D^l \cup \Gamma_D^v \\ \phi = 0 \qquad & \text{on} \qquad \Gamma_E \\ -\nabla\phi \cdot \mathbf{n} = 0 \qquad & \text{on} \qquad \Gamma_L^v \cup \Gamma_L^l \cup \Gamma_{EXT} \end{aligned} \tag{3.53}$$

When the reduced computational domain in figure 3-3 is used instead, the boundary conditions for the electric problem are:

$$\begin{aligned} \phi = V \qquad & \text{on} \qquad \Gamma_I \cup \Gamma_D^l \cup \Gamma_D^v \\ \phi = V \frac{\text{arctanh } w}{\text{arctanh } w_0} \qquad & \text{on} \qquad \Gamma_L^v \cup \Gamma_L^l \cup \Gamma_{EXT} \end{aligned} \tag{3.54}$$

Where $\phi = V \frac{\text{arctanh } w}{\text{arctanh } w_0}$ is the solution of the Laplace problem in prolate spheroidal coordinates as if there was not any meniscus.

The rest of the boundary conditions for the energy transport problem are:

$$T = T_0 \quad \text{on} \quad \Gamma_D^l \cup \Gamma_I . \tag{3.55}$$

where the reference temperature T_0 is the temperature on the wall of the fluid channel.

For the space charge at the fluid inlet:

$$\rho_{sch} = 0 \quad \text{on} \quad \Gamma_I \tag{3.56}$$

and at the meniscus interface:

$$\begin{aligned} \rho^v_{sch} &= \frac{q}{m}\frac{\rho}{\beta} \quad && \text{on} \quad \Gamma_M \\ \mathbf{u}^v \cdot \mathbf{n} = \beta \mathbf{u} \cdot \mathbf{n} &= \frac{\beta j^e_n}{\rho \frac{q}{m}} \quad && \text{on} \quad \Gamma_M \\ \mathbf{u}^v \cdot \mathbf{t} &= \mathbf{u} \cdot \mathbf{t} \quad && \text{on} \quad \Gamma_M \end{aligned} \tag{3.57}$$

3.4 Non-dimensionalization

As a summary, tables 3.1 and 3.2 show the set of non-dimensional equations fulfilled in the bulk and interface domains respectively. The reference parameters for the non-dimensionalization are the contact line radius (r_0) for the length scale; for the pressure and the stresses, the capillary pressure of a sphere of such radius $\tau_0 = \frac{2\gamma_0}{r_0}$; for the electric fields, the corresponding $E_c = \sqrt{\frac{4\gamma_0}{r_0 \varepsilon_0}}$ whose electric pressure balances τ_0; the current density by $j_c = \kappa_0 E_c$; velocities by the capillary velocity $u_c = \gamma_0/\mu_0$; temperatures by a reference value T_0, electrical conductivity by the conductivity of the liquid κ_0 at the reference temperature T_0 (similarly for the viscosity, and surface tension); time is made non-dimensional by a characteristic capillary time $t_c = r^*/u_c$, where r^* is the characteristic size of the emission region as in eq. 1.7.

These non-dimensional variable definitions are compiled for the reader in table 3.3. A relevant non-dimensional number in this thesis comes from the non-dimensional form of the boundary conditions in eq. 3.51. This yields:

$$\begin{aligned} \mathbf{n} \cdot \hat{\tau}_f \cdot \mathbf{n} = -\left(\hat{p}_r - \hat{I} C_R\right) = -\left(\hat{p}_r - \hat{I} \frac{\kappa_0 E_c r_0^3 Z}{2\gamma_0 \rho \frac{q}{m}}\right) \qquad && \text{on} \qquad \Gamma_I \\ \mathbf{t} \cdot \hat{\tau}_f \cdot \mathbf{n} = 0 \qquad && \text{on} \qquad \Gamma_I \end{aligned} \tag{3.58}$$

The coefficient C_R captures the drop of pressure that is originated per unit of non-dimensional current $\hat{I} = \int_{\Gamma_M} \hat{\mathbf{j}} \cdot \mathbf{n} \, d\Gamma_M$ and can also be written in two forms:

$$C_R = \frac{\kappa_0 E_c r_0^3 Z}{2\gamma_0 \rho \frac{q}{m}} = \hat{R}^{\frac{5}{2}} \frac{\kappa_0 E^* {r^*}^3 Z}{2\gamma_0 \rho \frac{q}{m}} = \hat{R}^{\frac{5}{2}} \hat{Z} \tag{3.59}$$

Equation name	Equation	Domain
Maxwell-Poisson	$\hat{\nabla} \cdot \left(\varepsilon_r \hat{\mathbf{E}}\right) = \hat{\rho}_{sch}$	$\mathbf{\Omega}^l \cup \mathbf{\Omega}^v$
Maxwell-Faraday	$\hat{\nabla} \times \hat{\mathbf{E}} = 0 \rightarrow \hat{\mathbf{E}} = -\hat{\nabla}\hat{\phi}$	$\mathbf{\Omega}^l \cup \mathbf{\Omega}^v$
Charge conservation	$\frac{\partial \hat{\rho}_{sch}}{\partial \hat{t}} + \hat{\nabla} \cdot \left(\varepsilon_r \frac{t_c}{t_e} \hat{\kappa} \hat{\mathbf{E}} + \frac{1}{\hat{R}} \hat{\rho}_{sch} \hat{\mathbf{u}}\right) = 0$	$\mathbf{\Omega}^l$
Mass conservation	$\hat{\nabla} \cdot \hat{\mathbf{u}} = 0$	$\mathbf{\Omega}^l$
Momentum conservation	$\frac{\partial \mathbf{u}}{\partial \hat{t}} + \frac{1}{\hat{R}} \left(\hat{\mathbf{u}} \cdot \hat{\nabla}\right) \hat{\mathbf{u}} = 2 \left(\frac{Oh}{\hat{R}}\right)^2 \left(\hat{\nabla} \cdot \hat{\tau}_f + 2\hat{\rho}_{sch} \hat{\mathbf{E}}\right)$	$\mathbf{\Omega}^l$
Energy conservation	$\frac{\partial \hat{T}}{\partial \hat{t}} + \frac{1}{\hat{R}} \hat{\mathbf{u}} \cdot \hat{\nabla} \hat{T} = \frac{\hat{\nabla}^2 \hat{T}}{Pe \hat{R}^2} + \frac{\varepsilon_r t_\mu}{\hat{R} t_e} \hat{\kappa} \hat{\mathbf{E}} \cdot \hat{\mathbf{E}} + \frac{t_\mu}{2 \hat{R}^2 t_c} \hat{\mu} \hat{e}_{ij}^2$	$\mathbf{\Omega}^l$
Fluid stress tensor	$\hat{\tau}_f = -\hat{p} \mathbf{I}_n + \frac{\hat{\mu}}{2} \left(\hat{\nabla} \hat{\mathbf{u}} + \hat{\nabla} \hat{\mathbf{u}}^T\right)$	$\mathbf{\Omega}^l$
Steady vacuum momentum conservation	$\left(\hat{\mathbf{u}} \cdot \hat{\nabla}\right) \hat{\mathbf{u}} = \Theta \sqrt{\hat{R}}\, \hat{\mathbf{E}}$	$\mathbf{\Omega}^v$
Steady vacuum charge conservation	$\hat{\nabla} \cdot (\hat{\rho}_{sch}^v \hat{\mathbf{u}}) = 0$	$\mathbf{\Omega}^v$

Table 3.1: Dimensionless bulk equations.

Where $\hat{Z} = \frac{Z}{Z^*}$, $Z^* = \frac{2\gamma_0 \rho \frac{q}{m}}{\kappa_0 E^* {r^*}^3}$ is the non-dimensional value of the tip hydraulic impedance Z.

The remaining dimensionless numbers are compiled in table 3.4, where a physical interpretation is also provided, when possible, as a function of the properties of the ionic liquids, and the characteristic velocities and times of the problem summarized in table 3.5.

Equation Name	Equation
Charge conservation	$\frac{\partial\hat{\sigma}}{\partial\hat{t}} + \frac{1}{\hat{R}}\hat{\nabla}_S \cdot (\hat{\sigma}\hat{\mathbf{u}}) = \varepsilon_r \frac{t_c}{t_e}\left(\hat{\kappa}\hat{E}_n^l - \hat{j}_n^e\right)$
Surface charge jump condition	$\hat{\sigma} = \hat{E}_n^v - \epsilon_r \hat{E}_n^l$
Equality of tangential components of the electric field	$\hat{E}_t^v = \hat{E}_t^l$
Kinetic law for charge evaporation (ionic liquids)	$\hat{j}_n^e = \frac{\hat{\sigma}\hat{T}t_e}{\varepsilon_r t_m}\exp\left(-\frac{\psi}{\hat{T}}\left(1 - \hat{R}^{-\frac{1}{4}}\sqrt{\hat{E}_n^v}\right)\right)$
Equilibrium of stresses in the tangential direction	$\frac{\hat{\mu}}{2}\ \mathbf{t}\cdot\left(\hat{\nabla}\hat{\mathbf{u}} + \hat{\nabla}\hat{\mathbf{u}}^T\right)\cdot\mathbf{n} = 2\ \hat{\sigma}\hat{E}_t + \frac{1}{2}\frac{\partial\hat{\gamma}}{\partial\hat{s}}$
Equilibrium of stresses in the normal direction	$-\hat{p} + \frac{\hat{\mu}}{2}\ \mathbf{n}\cdot\left(\hat{\nabla}\hat{\mathbf{u}} + \hat{\nabla}\hat{\mathbf{u}}^T\right)\cdot\mathbf{n} = \hat{E}_n^{v^2} - \varepsilon_r\hat{E}_n^{l^2} +$ $(\varepsilon_r - 1)\,\hat{E}_t^2 - \hat{\gamma}\hat{H} - C_\beta\ \left(\hat{j}_n^e\right)^2(1-\beta)$
Mass conservation of ions evaporated	$\frac{\partial\hat{f}}{\partial\hat{t}} = \left(\frac{\varepsilon_r C_m}{\hat{R}^{3/2}}\hat{j}_n^e - \frac{1}{\hat{R}}\hat{\mathbf{u}}\cdot\mathbf{n}\right)\sqrt{1 + \left(\frac{\partial\hat{f}}{\partial\hat{r}}\right)^2}$
Energy conservation	$\frac{\varepsilon_r C_m \hat{R}^{1/2}}{Pe}\hat{j}_n^e\left(\hat{T}_{out} - \hat{T} + \hat{l}_H\right) = -\hat{\nabla}\hat{T}\cdot\mathbf{n}$

Table 3.2: Dimensionless interfacial equations.

Variable name	Dimensionless form	Reference value
Length	$\hat{r} = \frac{r}{r_0}$, $\hat{z} = \frac{z}{r_0}$	r_0
Pressures and stresses	$\hat{p} = \frac{p}{p_c}$, $\hat{\tau} = \frac{\tau}{p_c}$	$p_c = \frac{2\gamma_0}{r_0}$
Electric fields	$\hat{\mathbf{E}} = \frac{\mathbf{E}}{E_c}$	$E_c = \sqrt{\frac{4\gamma_0}{\varepsilon_0 r_0}}$
Voltage	$\hat{\phi} = \frac{\phi}{\phi_c}$	$\phi_c = E_c r_0$
Surface charge	$\hat{\sigma} = \frac{\sigma}{\sigma_c}$	$\sigma_c = \varepsilon_0 E_c$
Volumetric charge	$\hat{\rho}_{sch} = \frac{\rho_{sch}}{\rho_c}$	$\rho_c = \frac{\varepsilon_0 E_c}{r_0}$
Current density	$\hat{\mathbf{j}} = \frac{\hat{\mathbf{j}}}{j_c}$	$j_c = \kappa_0 E_c$
Total emitted current	$\hat{I} = \frac{I}{I_c}$	$I_c = j_c r_0^2$
Velocity	$\hat{\mathbf{u}} = \frac{\mathbf{u}}{u_c}$	$u_c = \gamma_0/\mu_0$
Temperature	$\hat{T} = \frac{T}{T_0}$	T_0
Time	$\hat{t} = \frac{t}{t_c}$	$t_c = \frac{r^*}{u_c}$
Electrical conductivity	$\hat{\kappa} = \frac{\kappa}{\kappa_0}$	κ_0
Viscosity	$\hat{\mu} = \frac{\mu}{\mu_0}$	μ_0
Surface tension	$\hat{\gamma} = \frac{\gamma}{\gamma_0}$	γ_0

Table 3.3: Dimensionless reference values for the dependent and independent variables (r,z,t).

Number	Value	Description
ψ	$\frac{\Delta G}{k_B T_0}$	Ratio of solvation energy ΔG and characteristic thermal molecular energy $k_B T_0$ at the reference temperature
C_β	$\frac{2\kappa_0^2}{\rho\varepsilon_0\left(\frac{q}{m}\right)^2}$	Characteristic recoil number
Pe	$\frac{\kappa_T}{u_c r^* \rho c_p}$	Péclet number (ratio between thermal diffusivity and *capillary* convective transport of heat)
Oh	$\frac{\mu_0}{\sqrt{\rho\gamma_0 r^*}}$	Ohnesorge number (ratio between viscous and geometric average of capillary and inertial forces)
C_m	$\frac{u^*}{u_c}$	Ratio between the characteristic velocity in the emission region and the capillary velocity
Θ	$\frac{u_{ion}^2}{u_c^2}$	Space charge strength (ratio between ion evaporation kinetic energy, and capillary kinetic energy)
$\hat{R}$	$\frac{r_0}{r^*}$	Meniscus dimensionless radius
β	$\frac{\rho^v}{\rho}$	Ratio between density in the gas phase and density in the liquid phase
$\hat{Z}$	$\frac{Z}{Z^*}$	Dimensionless hydraulic impedance
$\hat{l}_H$	$\frac{l_H}{c_p T_0}$	Dimensionless latent heat

Table 3.4: Dimensionless numbers.

Reference symbol	Reference value	Description
u_c	$\frac{\gamma_0}{\mu_0}$	Capillary velocity
u_{ion}	$\sqrt{\frac{q}{m}E^* r^*}$	Ion characteristic space charge velocity
u^*	$\frac{\kappa_0 E^*}{\varepsilon_r \rho \frac{q}{m}}$	Ion characteristic emission region velocity
t_c	$\frac{r^*}{u_c} = \frac{r^* \mu_0}{\gamma_0}$	Capillary time in the emission region
t_e	$\frac{\varepsilon_0 \varepsilon_r}{\kappa_0}$	Charge relaxation time
t_μ	$\frac{4\mu_0}{\rho c_p T_0}$	Viscous thermal dissipation time
t_m	$\frac{h}{k_B T_0}$	Kinetic emission time
Z^*	$\frac{2\gamma_0 \rho \frac{q}{m}}{\kappa_0 E^* {r^*}^3}$	Characteristic impedance

Table 3.5: Reference times, velocities and impedance.

Chapter 4

Numerics

This section proposes a finite element method to resolve the non-dimensional steady electrohydrodynamic system described in chapter 3.

4.1 A finite element formulation for the electrohydrodynamic model

The finite element formulation follows the strategy described by Basaran [7] and Suvorov [124], and is extended to handle small dynamic perturbations by Herrada and Montanero [60].

4.1.1 Overview

The method implemented solves the set of non-dimensional equations described in section 3 to get the solution for the following variables vector: $\{\hat{\phi}, \hat{\rho}_{sch}, \hat{T}, \hat{\mathbf{u}}, \hat{p}, \hat{\sigma}\}$, together with the meniscus steady equilibrium coordinates as a function of the properties of the ionic liquid, and a geometry input represented in the physical domains $\mathbf{\Omega}^v$ and $\mathbf{\Omega}^l$. In dimensionless terms, the physical independent variables $(\hat{r}, \hat{z})$ are defined in $\mathbf{\Omega}^v$, $\mathbf{\Omega}^l$. The main difference with other mesh updating procedures for the solution of flows involving capillary phenomena [47, 42, 21] is that the information of the meniscus coordinates is not contained in the coordinates of the mesh, but in an auxiliary function $\hat{y}$ that represents a *map* of the meniscus vertical coordinate to a fixed reference vacuum domain $\mathbf{\Omega}^v_{(\eta,\xi)}$, and liquid domain $\mathbf{\Omega}^l_{(\eta,\xi)}$. The method, then, involves a change of coordinates where $(\hat{r}, \hat{z})$ are mapped to a new set of independent coordinates (η, ξ) defined in $\mathbf{\Omega}^v_{(\eta,\xi)}$ and $\mathbf{\Omega}^l_{(\eta,\xi)}$. This method allows including

the transformation between $\mathbf{\Omega}^v$ and $\mathbf{\Omega}^v_{(\eta,\xi)}$, and between $\mathbf{\Omega}^l$ and $\mathbf{\Omega}^l_{(\eta,\xi)}$ (i.e., function $\hat{y}$) as a part of the solution process. This transformation is given by the equilibrium conditions. Details of this process will be given in the following sections of this chapter.
All the equations presented in tables 3.1 and 3.2 are solved in this fixed domain. Figure 4-1 shows the mapped numerical domain. In this map, a point A on the physical meniscus interface Γ_M is mapped vertically to $A_{(\eta,\xi)}$ on a flat fixed interface $\Gamma_{M_{(\eta,\xi)}}$ square. The way we do this map is by representing the set of vertical coordinates $\hat{z}$ of the physical domain in the function $\hat{y}$ defined in the reference domain. Another way to say it: if the meniscus is mapped to the flat surface $\Gamma_{M_{(\eta,\xi)}}$ ($\eta \in [0,1]$, $\xi = 0$), the value of $\hat{y}$ will be exactly the equilibrium shape of the meniscus function on $\Gamma_{M_{(\eta,\xi)}}$ ($\hat{y} = \hat{h}$).

What about the other regions of the physical domain that are not the meniscus interface? How are they mapped to the fixed reference domain?

Ideally, we would define an algebraic function that would map the rest of the points of $\mathbf{\Omega}^v$ and $\mathbf{\Omega}^l$ to $\mathbf{\Omega}^v_{(\eta,\xi)}$ and $\mathbf{\Omega}^l_{(\eta,\xi)}$ given the value of $\hat{y}$ on $\Gamma_{M_{(\eta,\xi)}}$. This is what Basaran [7], Herrada and Montanero [60], and Suvorov [124] do with other simpler electrified capillary systems. The particularity of the problem solved in this thesis is that the domain is considered to be the best axially symmetric approximation to the tip profile feeding the meniscus, which contains usually small ripples and undulations not easily describable by functions (see the actual carbon tip in figure 8-5 in chapter 8, and the axially symmetric mesh figure 8-4 in the same chapter). This particular aspect restricts the meniscus coordinate maps to be numerical maps, instead of maps described by an algebraic function. The irregularities of the domain also restrict the scheme of our numerical model to follow traditional finite element schemes with convergence of at most order $k+1$, where k is the order of the polynomial basis functions. In Herrada and Montanero [60], the simplicity of the domains considered makes their problems solvable by methods of spectral convergence. These numerical maps are essentially obtained by solving a Laplace equation for $\hat{y}$ in the reference domains $\mathbf{\Omega}^v_{(\eta,\xi)}$ and $\mathbf{\Omega}^l_{(\eta,\xi)}$, where $\hat{y} = \hat{z}$ in the external boundaries of the domain. The details will be described in the following sections.

Due to the high hyperbolicity of the space charge problem (eqs. 3.46, 3.47), the space charge equations in the vacuum domain are solved separately. Consistency between the main system of equations and the space charge system of equations will be achieved by an outer iteration loop.

This method is beneficial over mesh iterative methods in multiple aspects:

1. It removes computational time spent on mesh updating.

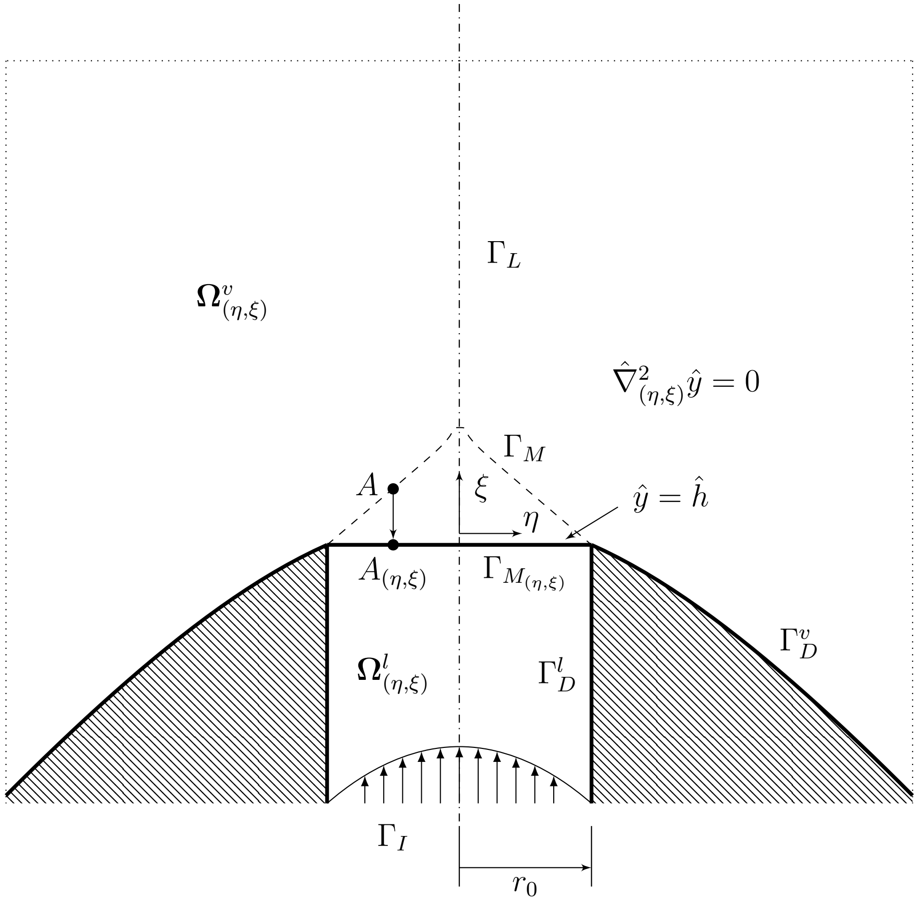

Figure 4-1: Fixed mapped computational domain to a square. The meniscus coordinates are embedded in function $\hat{y}$, and all equations are solved with respect to the fixed domain.

2. It allows the inclusion of the meniscus profile coordinates in the solution process, thus allowing the implementation of more efficient solution algorithms such as the Newton method, because now, we can easily compute the sensitivity of the variables to changes in the physical domain, precisely through this auxiliary variable $\hat{y}$ that represents the vertical coordinate in the fixed reference domain.

3. It allows the implementation of implicit time marching schemes, which are generally more stable under longer time steps.

4. It allows a natural way of decomposing the dynamics of the problem in its oscillation modes, thus allowing a more accurate estimation of stability (dynamic stability).

With the drawback of the fact that now, all the equations are highly non-linear, because they are transformed to apply in the fixed numerical domain. While the benefits of the model greatly outweigh the drawbacks, this method is also more memory expensive, because it adds another solution variable $\hat{y}$, and in order to access higher convergence regimes, all equations have to be solved at the same time (no operator decomposition).

The details of this transformation and formulation of the main problem in the fixed domain[1] can be read in the annex section B.1.

4.2 Space charge system

4.2.1 Overview

The solution of equations 3.46 and 3.47 is obtained using a *hybrid* approach. The Lagrangian version of eq. 3.46 is integrated using a standard Runge-Kutta method of order 4 to get the emitted ions velocity map in the vacuum $\hat{\mathbf{u}}^v$.

Essentially, what we mean in saying Lagrangian is that the velocity field is integrated in the same way as finding the velocity and position of a particle departing from the meniscus interface in free fall through the potential field $\hat{\phi}$, which we have obtained in solving the equations presented in the latter section. The position of the particles is collected together with the velocity field, and it is used afterward to build a *space charge* mesh. Then, the velocity field is distributed in the nodes of the mesh, whose coordinates are defined by the particle's position points. Finally, as a

---

[1] All the equations except those governing the space charge in the vacuum domain $\boldsymbol{\Omega}^v$.

sort of post-process, the divergence operator is applied to this velocity field to get the space charge in the vacuum $\hat{\rho}^v_{sch}$. Details of each step are described as follows.

4.2.2 Equations in the transformed domain

The first equation that is solved in this space charge solution algorithm is eq. 3.46 in its steady state non-dimensional form:

$$\left(\hat{\mathbf{u}}^v \cdot \hat{\nabla}\right) \mathbf{u}^v = \Theta \, \hat{\mathbf{E}} \tag{4.1}$$

The equation above 4.1 can be put in the Lagrangian form:

$$\frac{D\hat{\mathbf{u}}^v}{Dt} = \Theta \, \hat{\mathbf{E}} \tag{4.2}$$

The intuitive *mathy* way to say this is that we changed from a coordinate system $(\hat{r}, \hat{z})$, to (t, ζ) where t is the actual traveling *time* of the ions:

$$\frac{\partial \hat{r}}{\partial t} = \hat{u}^v_r \tag{4.3}$$

$$\frac{\partial \hat{z}}{\partial t} = \hat{u}^v_z \tag{4.4}$$

And ζ is a parameter that is constant along the trajectory lines of the ions, namely:

$$\hat{\mathbf{u}}^v \cdot \hat{\nabla}\zeta = 0 \tag{4.5}$$

We can easily check the equivalence between 4.2 by applying the chain rule:

$$\frac{D\hat{\mathbf{u}}^v}{Dt} = \frac{\partial \hat{\mathbf{u}}^v}{\partial \hat{r}} \frac{\partial \hat{r}}{\partial t} + \frac{\partial \hat{\mathbf{u}}^v}{\partial \hat{z}} \frac{\partial \hat{z}}{\partial t} = \frac{\partial \hat{\mathbf{u}}^v}{\partial \hat{r}} \hat{u}^v_r + \frac{\partial \hat{\mathbf{u}}^v}{\partial \hat{z}} \hat{u}^v_z = \left(\hat{\mathbf{u}}^v \cdot \hat{\nabla}\right) \hat{\mathbf{u}}^v \tag{4.6}$$

Thus we have the system formed by eqs. 4.2, 4.3 and 4.4:

$$\begin{aligned} \frac{D\hat{\mathbf{u}}^v}{Dt} &= \Theta \, \hat{\mathbf{E}} \\ \frac{\partial \hat{\mathbf{r}}}{\partial t} &= \hat{\mathbf{u}}^v \end{aligned} \tag{4.7}$$

Where:

$$\hat{\mathbf{r}} = \begin{pmatrix} \hat{r} \\ \hat{z} \end{pmatrix} \tag{4.8}$$

System 4.7 can be transformed to the fixed domain (η, ξ) if we apply the chain rule as:

$$\frac{\partial \hat{\mathbf{r}}}{\partial t} = \begin{pmatrix} \frac{\partial \hat{r}}{\partial \eta}\frac{\partial \eta}{\partial t} + \frac{\partial \hat{r}}{\partial \xi}\frac{\partial \xi}{\partial t} \\ \frac{\partial \hat{z}}{\partial \eta}\frac{\partial \eta}{\partial t} + \frac{\partial \hat{z}}{\partial \xi}\frac{\partial \xi}{\partial t} \end{pmatrix} = \mathbf{K}\,\frac{\partial \boldsymbol{\eta}}{\partial t} \tag{4.9}$$

Where:

$$\boldsymbol{\eta} = \begin{pmatrix} \eta \\ \xi \end{pmatrix} \tag{4.10}$$

The final equations that we integrate for a constant ζ using explicit methods (Runge-Kutta order 4), for a given meniscus coordinate map $\hat{y}$ and electric field are:

$$\begin{aligned} \frac{D\hat{\mathbf{u}}^v}{Dt} &= \Theta\,\hat{\mathbf{E}}_{(\eta,\xi)} \\ \frac{\partial \boldsymbol{\eta}}{\partial t} &= \mathbf{K}^{-1}\hat{\mathbf{u}}^v \end{aligned} \tag{4.11}$$

After having an integrated velocity profile, we can now obtain the space charge map by solving equation 3.48 in the transformed domain as:

$$\hat{\nabla}_{(\eta,\xi)} \cdot \left(\eta\ \det(\mathbf{K})\hat{\rho}^v_{sch}\ \mathbf{K}^{-1}\hat{\mathbf{u}}^v\right) = 0 \tag{4.12}$$

4.3 Iterative process: equation linearization and the Newton method

In the traditional continuous Galerkin finite element framework (FEM), the domain is discretized into smaller, interconnected elements (roughly speaking, the "mesh") where the solution to a system of partial differential equations is approximated using piecewise continuous functions. The FEM solution to this system is computed in its weak formulation [24]. The weak form of the system of equations can be derived from the strong form (i.e., the original form of a partial differential equation that describes the relationship between the unknown functions $\mathbf{x}$ and its derivatives) by multiplying it by a set of arbitrary test functions (within a function space) $\mathbf{x}_{\mathcal{T}}$ and integrating it over the simulation domain. The test functions act as a weight that helps in reducing the order of the derivatives in the equation, making it more amenable to numerical computation. The trial functions represent the approximate solution to $\mathbf{x}$. Both trial and test functions are constructed as a linear combination of basis functions defined on each element and associated nodal values. The FEM then seeks to find the nodal values that minimize the error when the weak form of the equations that we want to solve is satisfied for each element. Importantly, the solution obtained using FEM resides in a subspace spanned by the class of test and trial functions (e.g, the solution is computed *for all* possible test functions in the function space of choice). The richer this space is in its basis function order, the better the convergence to the exact solution will be as the mesh is refined. By assembling the element-wise contributions, a system of algebraic equations is formed, which is then solved to obtain the numerical solution over the entire domain.

For our problem, let's say we have an initial guess of space charge map in the vacuum $\hat{\rho}^v_{sch}$ (it could be $\hat{\rho}^v_{sch} = 0$). The vector of errors in the system of the equations in their weak form described in the annex section B.1.3, and weighted by the test functions $\mathbf{x}_{\mathcal{T}}$ can all be expressed as:

$$\mathbf{F}\left(\mathbf{x};\mathbf{x}_{\mathcal{T}},\hat{\rho}^v_{sch}\right) = [f_1, f_2, f_3, ..., f_n] = \vec{0} \tag{4.13}$$

Where $\mathbf{x}$ is the set of variables solved in this thesis described in table B.1 and eq. B.43, and $[f_1,\ f_2,\ f_3,\ ...,f_n]$ are set of equations in the weak form described in the annex section B.1.3, such as the Poisson, Navier-Stokes equations, ... etc.

The system $\mathbf{F}\left(\mathbf{x};\mathbf{x}_{\mathcal{T}},\hat{\rho}^v_{sch}\right) = \vec{0}$ can be solved for all $\mathbf{x}_{\mathcal{T}}$ in the mixed finite element space of functions for all the variables (piecewise polynomial Lagrange elements of order shown in table B.1[2]) using the traditional Newton method to solve systems of non-linear equations. Here, we review the basic foundations.

Consider a guess of the solution $\mathbf{x}_i$. The guess is slightly away from the actual solution up to some $\delta\mathbf{x}_i$, namely:

$$\mathbf{F}\left(\mathbf{x}_i + \delta\mathbf{x}_i;\mathbf{x}_{\mathcal{T}},\hat{\rho}^v_{sch}\right) = \vec{0} \tag{4.14}$$

We can expand eq. 4.14 in Taylor series:

$$\mathbf{F}\left(\mathbf{x}_i + \delta\mathbf{x}_i;\mathbf{x}_{\mathcal{T}},\hat{\rho}^v_{sch}\right) = \mathbf{F}\left(\mathbf{x}_i;\mathbf{x}_{\mathcal{T}},\hat{\rho}^v_{sch}\right) + \mathcal{J}\left(\mathbf{x}_i;\mathbf{x}_{\mathcal{T}},\hat{\rho}^v_{sch},\delta\mathbf{x}_i\right) + O\left(\delta\mathbf{x}_i^2\right) \tag{4.15}$$

Where $\mathcal{J}\left(\mathbf{x}_i;\mathbf{x}_{\mathcal{T}},\hat{\rho}^v_{sch},\delta\mathbf{x}_i\right)$, is the Jacobian of the system evaluated at the guess of the solution $\mathbf{x}_i$. This term is formally the *Gateaux* derivative of $\mathbf{F}\left(\mathbf{x};\mathbf{x}_{\mathcal{T}},\hat{\rho}^v_{sch}\right)$ at

---

[2] The mathematical details of the function spaces used in this thesis are the standard for the traditional finite element methods in fluid mechanics, with some variables and Lagrange multipliers defined in restricted parts of the domain. We believe the function space mathematical formalism adds unnecessary wordiness for the purpose of this thesis, and we have omitted its details. For more information the reader may consult [133].

$\mathbf{x} = \mathbf{x}_i$ in the direction of $\delta\mathbf{x}_i$ (see [109]). Technically, this derivative is defined as:

$$\mathcal{J}\left(\mathbf{x}_i; \mathbf{x}_{\mathcal{T}}, \hat{\rho}^v_{sch}, \delta\mathbf{x}_i\right) = \lim_{\epsilon \to 0} \frac{d}{d\epsilon} \mathbf{F}\left(\mathbf{x}_i + \epsilon\delta\mathbf{x}_i; \mathbf{x}_{\mathcal{T}}, \hat{\rho}^v_{sch}\right) \tag{4.16}$$

The derivation of eq. 4.16 is large, and very prone to human computation errors. We found it useful to implement the solution of the equations in the open source finite element library FeNiCs, which includes an automatic differentiator [79, 3] to derive eq. 4.16 analytically for us. If we neglect the second order terms and assume $\mathbf{F}\left(\mathbf{x}_i + \delta\mathbf{x}_i; \mathbf{x}_{\mathcal{T}}, \hat{\rho}^v_{sch}\right) = 0$, we can find $\delta\mathbf{x}_i$ by solving the linear system 4.17:

$$\mathcal{J}\left(\mathbf{x}_i; \mathbf{x}_{\mathcal{T}}, \hat{\rho}^v_{sch}, \delta\mathbf{x}_i\right) = -\mathbf{F}\left(\mathbf{x}_i; \mathbf{x}_{\mathcal{T}}, \hat{\rho}^v_{sch}\right) \tag{4.17}$$

This Newton update will improve the guess for the root of $\mathbf{F}\left(\mathbf{x}_i; \mathbf{x}_{\mathcal{T}}, \hat{\rho}^v_{sch}\right)$ that we want to find. The guess can be improved iteratively using several Newton updates:

$$\mathbf{x}_{i+1} = \mathbf{x}_i + \delta\mathbf{x}_i \tag{4.18}$$

Until any of the termination conditions are met:

$$\|\mathbf{F}\left(\mathbf{x}_i; \mathbf{x}_{\mathcal{T}}, \hat{\rho}^v_{sch}\right)\|_2 < \text{abs. tol} \tag{4.19}$$

$$\frac{\|\mathbf{F}\left(\mathbf{x}_i; \mathbf{x}_{\mathcal{T}}, \hat{\rho}^v_{sch}\right)\|_2}{\|\mathbf{F}\left(\mathbf{x}_0; \mathbf{x}_{\mathcal{T}}, \hat{\rho}^v_{sch}\right)\|_2} < \text{rel. tol} \tag{4.20}$$

Where $\mathbf{F}\left(\mathbf{x}_0; \mathbf{x}_{\mathcal{T}}, \hat{\rho}^v_{sch}\right)$ refers to the evaluation of the error vector at the first initial guess $\mathbf{x}_0$. We use 10^{-10} as an absolute tolerance, and 10^{-8} as the relative[3]. After reaching the termination conditions in eq. 4.19 or 4.20, the system will not have reached equilibrium: the space charge system will generally not be consistent, since the solution vector $\mathbf{x}$ is changed from the initial guess, and the boundary conditions for the space charge problem depend on $\mathbf{x}$. It is necessary to solve again the space charge problem, and compute the equilibrium solution of the meniscus with the new boundary conditions. This process is repeated in an outer iteration loop until consistency is found.

Algorithm 1 Outer loop algorithm for solving meniscus equilibrium solutions with consistent space charge

```
procedure GetEquilibriumShape
    $\mathbf{x}_0, \hat{\rho}^v_{sch_0} \rightarrow$ GetInitialSolution    ▷ They can be from previous iteration
    $m = 1$
    $\mathbf{x}_1 \leftarrow$ NewtonAlgorithm($\mathbf{x}_0, \hat{\rho}^v_{sch_0}$)
    $\hat{j}^*_m = \hat{j}^e_{n_m}/C_1$
    while $\max_k \left| \frac{\left(\hat{j}^*_m\right)_k - \left(\hat{j}^e_{n_m}\right)_k}{\left(\hat{j}^e_{n_m}\right)_k} \right|$ do
        Solve system 4.11, with boundary conditions 4.21.
        Store velocities $\hat{\mathbf{u}}$ and positions $\boldsymbol{\eta}$.
        Build space charge mesh $\boldsymbol{\Omega}^v_{sch(\eta,\xi)}$ from $\boldsymbol{\eta}$.
        Interpolate $\hat{\mathbf{u}}$ to $\boldsymbol{\Omega}^v_{sch(\eta,\xi)}$.
        Solve 4.25 to get $\hat{\rho}^v_{sch}$ in $\boldsymbol{\Omega}^v_{sch(\eta,\xi)}$.
        Interpolate $\hat{\rho}^v_{sch}$ in $\boldsymbol{\Omega}^v_{sch(\eta,\xi)}$ to $\boldsymbol{\Omega}^v_{(\eta,\xi)}$.
        $\mathbf{x}_{m+1} \leftarrow$ NewtonAlgorithm($\mathbf{x}_m, \hat{\rho}^v_{sch_m}$)
        Get $\mathbf{E}_{(\eta,\xi)}$ from B.11.
        Get $\hat{j}^e_{n_{m+1}}$ from the dimensionless kinetic evaporation law in table 3.2.
        $\hat{j}^*_{m+1} = (1-\omega)\hat{j}^*_m + \omega\, \hat{j}^e_{n_{m+1}}$
        $m = m + 1$
    end while
end procedure
```

4.4 Outer iteration loop

We describe how to get a solution for the combined problem, including a space-charge solution in the vacuum $\hat{\rho}^v_{sch}$ consistent with the physical boundary conditions. The built iterative numerical procedure updates the space charge system in such a way that a given converged Newton iteration $\mathbf{x}_m$ changes minimally when updating the space charge with the new boundary conditions. The algorithm takes as an input an initial solution converged after a Newton iteration, considering an initial guess of the space charge $\hat{\rho}^v_{sch_0}$ that usually is $\hat{\rho}^v_{sch_0} = 0$ (line 2 of algorithm 1).

The current density of the ions that originates from this initial solution will probably be high enough to originate a space charge in the vacuum domain that is very high for the convergence of the algorithm. Since the initial conditions for the space charge problem are very sensititve to the electric field (through the exponential dependence of the Iribarne and Thomson equation 3.28), we need to slowly incorporate the ion flux to guarantee the convergence of the algorithm. For this reason, we need a guess of the current density in equilibrium with the space charge j^* that is significantly less than the initial current density given by the kinetic law for evaporation 3.28 (computed via the solution to vector $\mathbf{x}$). This initial guess is a small fraction of that corresponding to the current density $\hat{j}^e_{n_0}$ emitted (line 5, constant $C_1 \approx 10$ for the cases of low current (<150 nA), $C_1 \approx 100$ for the higher current cases).

Then when the difference between the maximum relative element-wise difference between of $\hat{j}^*_m$ and the total current emitted according to the kinetic evaporation law $\hat{j}^e_{n_m}$ is higher than some tolerance, start the iterative process (line 6).

In the m iteration, firstly, equation 4.11 is solved with a modified version of the space charge boundary conditions in eq. 4.21 (line 7 of algorithm 1):

$$\begin{aligned} \hat{\mathbf{u}}^v \cdot \mathbf{n} &= \frac{\varepsilon_r C_m \beta \hat{j}^*_m}{\sqrt{\hat{R}}} \\ \hat{\mathbf{u}}^v \cdot \mathbf{t} &= \hat{\mathbf{u}} \cdot \mathbf{t} \end{aligned} \tag{4.21}$$

Only the region where j^*_m is sufficiently high is integrated, this corresponds to the size of the emission region. The criterion below is what we consider sufficiently high:

$$j^*_m < 10^{-3} \max\left(j^*_m\right) \tag{4.22}$$

Where $\max\left(j^*_m\right)$ is the maximum value of the current density, which usually corre-

---

[3] The norm refers to the euclidean 2-norm of the assembled $\mathbf{F}\left(\mathbf{x}_i; \mathbf{x}_{\mathcal{T}}, \hat{\rho}^v_{sch}\right)$ error vector, once the equations have been discretized using the finite element scheme.

sponds to the value at the apex of the meniscus.

Integrating the velocity field beyond this region will generate negligible space charge. The time step that we used for the integration for each Runge-Kutta n step in eq. 4.11 that worked best as a compromise of a well-resolved plume vs. memory used is:

$$\Delta\hat{t}_n = \min\left(\max\left(C_2\frac{\hat{u}_{\xi_n}}{\hat{u}_{\xi_n}-\hat{u}_{\xi_{n-1}}}\Delta\hat{t}_{n-1},\ \Delta t_0\right),\ \Delta\hat{t}_{max}\right) \tag{4.23}$$

Where $C_2 \in (0.02, 0.04)$ is a constant that depends on the choice of density jump of the ions (β parameter). The gradient of space charge right at the meniscus interface is dramatically steep (see figure 5-11 in the next chapter 5), and the steepness depends on how fast ions are at the beginning of their flight. For smaller initial velocities of the ions (e.g, low β), one may be interested in the lower range of C_2 for an accurate resolution of the steep region. For $\beta = 200$ we used $C_2 = 0.02$. The *minmax* structure of the time-step in eq. 4.23 would take into account this fast acceleration of the ions, thus yielding a smaller time-step at the beginning of the ions' flight (close to $\Delta\hat{t}_0$), and a larger time-step at the end of the integrated plume (close to $\Delta\hat{t}_{max}$) with a transitory time step inbetween of $C_2\frac{\hat{u}_{\xi_n}}{\hat{u}_{\xi_n}-\hat{u}_{\xi_{n-1}}}\Delta\hat{t}_{n-1}$. The latter is an expression combining a reference value of the velocity magnitude of the ions at step n, $\hat{u}_{\xi_n}$, and its change from the previous iteration $\hat{u}_{\xi_n} - \hat{u}_{\xi_{n-1}}$ weighted by C_2. The reference value $\hat{u}_{\xi_n}$ is taken as the velocity of the ion departing from the apex of the meniscus in the ξ direction (mapped vertical direction). We used for $\Delta\hat{t}_{max} = 1.5 \cdot 10^{-6}$, and for Δt_0:

$$\Delta\hat{t}_0 = C_2\Theta\hat{u}_{\xi_0} \tag{4.24}$$

The plume is integrated up to where the space charge field almost vanishes at the axis of symmetry $\hat{\rho}^v_{sch_m} < 10^{-3}$. For a current of $\sim$ 150 nA, such as the one presented in figure 5-10 and the time step scheme of eq. 4.23, we need around 350 integration steps. With the solution of the velocity fields and positions of the Lagrangian particles, a fixed domain for the space charge is built $\mathbf{\Omega}^v_{sch(\eta,\xi)}$ (line 9). As an order of magnitude example for the reader, we need $350 \times 150 \approx 5 \cdot 10^4$ data points for each stored variable in the space charge mesh (positions η, ξ, and velocities $\hat{u}_\eta$, $\hat{u}_\xi$) in the above example. The 150 value is for the number of "particle" elements of the emission region that are integrated (e.g, those who fulfill the condition in eq. 4.22). After the mesh is built with the values of the velocity $\hat{\mathbf{u}}^v$, equation 4.11 is solved with finite element methods, using the following in the transformed domain (line 11):

$$\int_{\boldsymbol{\Omega}^v_{sch(\eta,\xi)}} \hat{\nabla}_{(\eta,\xi)} \cdot \left(\eta \ \det(\mathbf{K}_m)\hat{\rho}^v_{sch_m} \ \mathbf{K}_m^{-1}\hat{\mathbf{u}}^v\right) \ \hat{\rho}^v_{sch_\mathcal{T}} \ d\boldsymbol{\Omega}^v_{sch(\eta,\xi)} = 0 \tag{4.25}$$

Where $\hat{\rho}^v_{sch_\mathcal{T}}$ is a test function for $\hat{\rho}^v_{sch_m}$. The subscript m indicates the iteration number in algorithm 1. The results for $\hat{\rho}^v_{sch_m}$ are interpolated to the main domain (line 12), where the Newton iteration is performed again (line 13). An updated value of the current emitted $\hat{j}^e_{n_m}$ with the space charge field from the previous iteration can be computed with $\mathbf{E}_{(\eta,\xi)}$ (line 15). The new guess j^*_m is updated with the new $\hat{j}^e_m$ using a numerical relaxation process (adding a little bit of $\hat{j}^e_{n_m}$ in line 16), where ω is the addition fraction (normally $\omega \in (0.2, 0.5)$ depending on the current).
It is observed that after some iterations, $\hat{j}^*_m$ and $\hat{j}^e_{n_m}$ converge to the same solution (see figure 4-2 for an example of the convergence mechanics). Figure 4-3 shows the exponential decrease of the residual, which is expected from numerical relaxation schemes of the same type as that presented in line 16 of algorithm 1. A termination metric for the outer loop of $\max_k \left| \frac{\left(\hat{j}^*_m\right)_k - \left(\hat{j}^e_{n_m}\right)_k}{\left(\hat{j}^e_{n_m}\right)_k} \right| = 2.5 \cdot 10^{-3}$ is found to be empirically sufficient for the Newton algorithm termination conditions in eqs. 4.19 or 4.20 to hold right in the first iteration, where the subscript k represents the element-wise values along the emission region. If our discretization of $\hat{j}^e_{n_m}$, and $\hat{j}^*_m$ has K values discretized along the emission region, $k = 0$ refers to the value at the apex of the meniscus, and $k = K$ refers to the value at the contact line with the electrode.

4.4.1 Comments

We naively tried to solve the equations 4.1 and 4.12 together with the whole Jacobian system equations, as if the space charge $\hat{\rho}^v_{sch}$ in the vacuum and the ion velocities in vacuum were part of the whole solution vector $\mathbf{x}$, and the system did not converge. We believe that the lack of convergence was due to the high hyperbolicity of eq. 4.1, which seems to limit the applicability of our mapping strategy to solutions with space charge. Perhaps the fact that one does not know the limits of the space charge domain $\boldsymbol{\Omega}_{sch(\eta,\xi)}$ a-priori makes it harder to define a proper map, similar to the unit square approach that is adopted in this thesis for the meniscus. Furthermore, perhaps the space of functions (i.e, continuous piece-wise polynomial) is not powerful enough to handle the sharp gradients encountered in the solution of this system, namely, the discontinuities of the plume profile (presence of ions, vs. no presence of ions, or even possible overlaps in ions trajectories, which would cause double values for the velocity in the same mesh point). While solving a version of $\mathbf{F}(\mathbf{x}; \mathbf{x}_\mathcal{T}) = \vec{0}$ that contains $\hat{\rho}^v_{sch}$

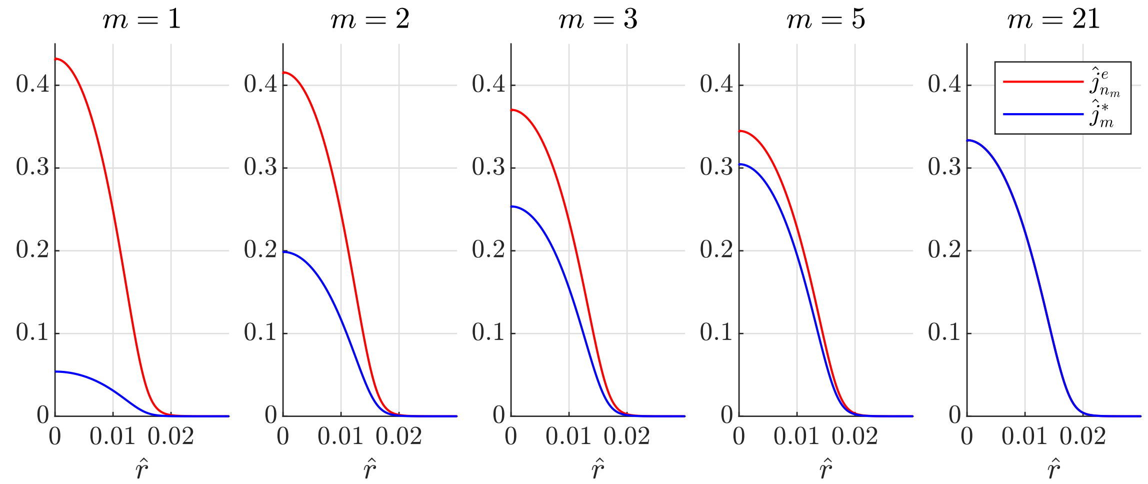

Figure 4-2: Difference between $\hat{j}^e_{n_m}$ and $\hat{j}^*_m$ across the outer iterative loop. The initial guess is $\hat{\rho}^v_{sch_0} = 0$ and $\mathbf{x}_0$ equal to the converged solution without space charge. The simulated data correpond to $\hat{R} = 84.4$, $\hat{Z} = 0.037$, $\hat{E}_{tip} = 0.82$. The simulated liquid properties are the same as described in section 5.1 of chapter 5.

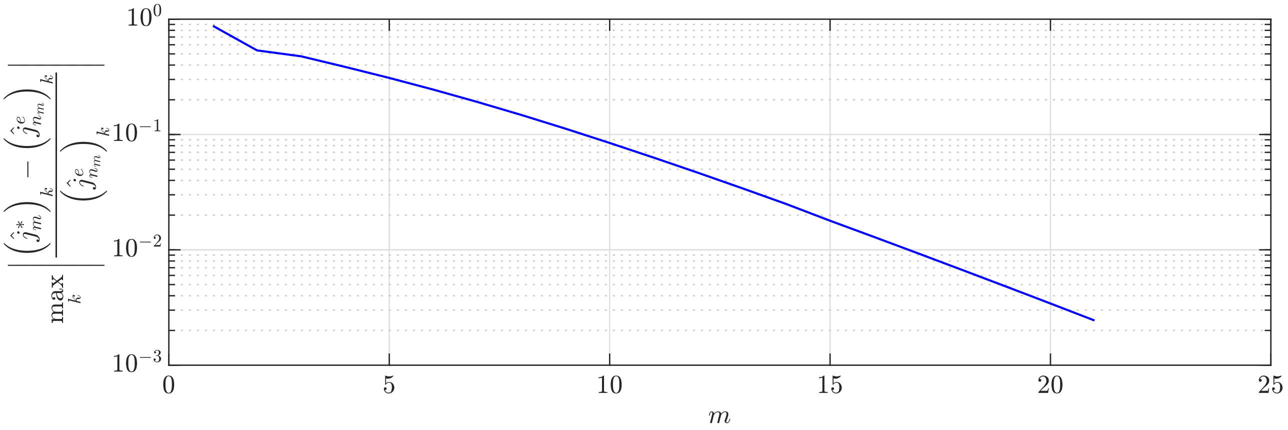

Figure 4-3: Residual decrease during outer loop iterations.

as a part of the solution with the Eulerian version of the equations may be possible, one must carefully study stabilization methods, artificial viscosity or perhaps a clever change of variables for 3.46 and 3.47, and evaluate if such methodology is better than the Lagrangian approach adopted in this thesis. In any event, the difficulties to solve these highly hyperbolic systems of equations are well-known in the literature on plasma physics, which usually adopts particle-in-cell methods using the Lagrangian version of 4.1.

4.5 Meshing

4.5.1 The meniscus and domain mesh

An example of mesh used in the mapped domain is shown in figure 4-4. The mesh used consists of irregularly arranged triangles (unstructured mesh) that reduce their size when approaching the emission region. This allows a good trade-off between the distribution of nodes in the domain and the computational effort. In the emission region, the mesh contains a refined structured section, (regularly placed triangles originated from partitioned rectangles), better suited for the analysis of sharp gradients. The size of the structured mesh spans about 2.5 times r^*/r_0. The structured mesh is built in such a way that it contains at least 250 subdivisions.

4.6 Validation

In this section, we validate the implementation of our new approach in the fixed domain with existing solutions of previously published models in planar geometry [42], without taking into account the space charge effects. Such models were validated already with existent solutions [21]. We compare the convergence of the fixed point iterative method in [42] and [21], to the new Jacobian-based method implemented in this thesis in figure 4-5 with the same initial guess. The initial guess is very far from the equilibrium solution, as can be seen in figure 4-6. The meniscus equilibrium conditions and initial shape are the same as the ones presented in Appendix E of Gallud [42].

Both methodologies are not directly comparable, since the convergence rates of the fixed point method depend on a parameter of numerical relaxation (β in [19]). Acknowledging this limitation, we try to illustrate the power of the new method by choosing a "hard" initial guess that only converged with a very small numerical relaxation parameter $\beta = 0.01$ for the fixed point iteration method (moving mesh,

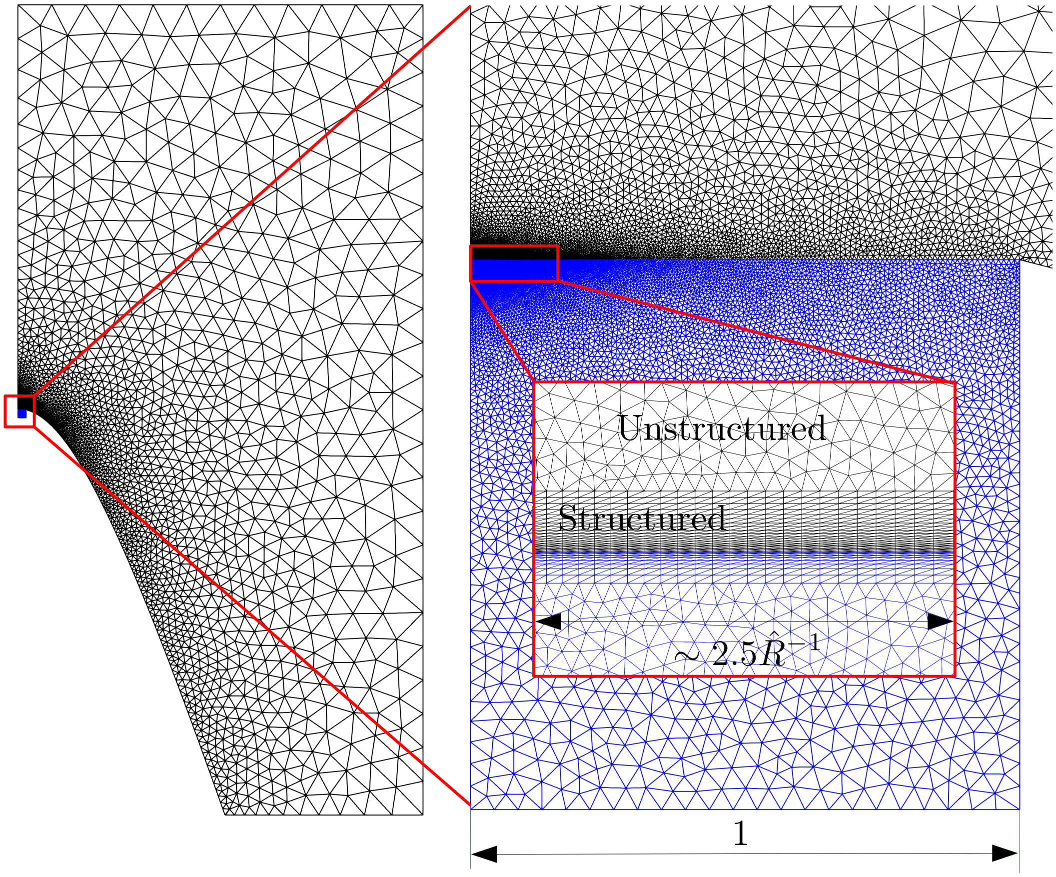

Figure 4-4: Example of mesh used in the solution of this problem for the reduced computational domain in figure 3-3. The model is axially-symmetric, therefore the mesh is formed by only one side of the domain. The blue-colored section is the mapped meniscus.

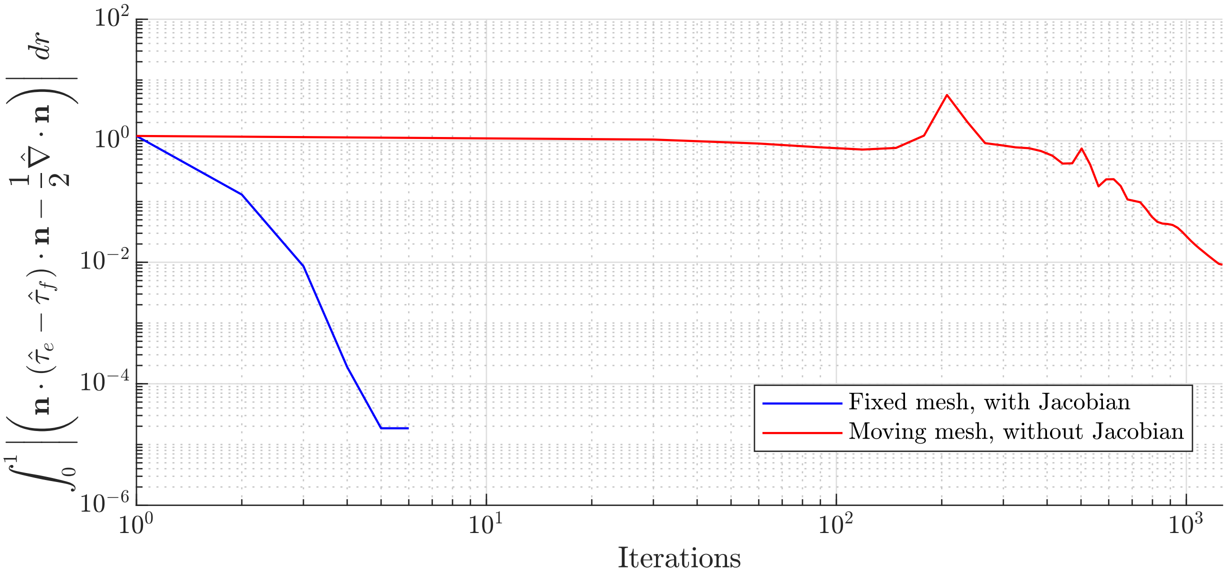

Figure 4-5: Comparison between the convergence of Jacobian-based approach algorithms (blue) and fixed point iterations (red) for the cases tested.

without Jacobian). We can see in figure 4-5 that the Jacobian-based method is faster: it converges in 5 iterations, even reaching quadratic error decay in the last iteration. The metric used for convergence is an integral of the dimensionless balance of stresses in the normal direction. The fixed point method with the moving mesh takes at least 300 initial iterations of warming-up before it is numerically conditioned to start converging. During this period, the equilibrium shapes exhibit large deformations (figure 4-6a), while for the Jacobian method, the equilibrium shapes across the iterative process lead directly to the converged solution (figure 4-6a). Even after the warming-up period, the fixed point iteration converges linearly at best. In figure 4-7 we can see how after converging, the two methods arrive to the same equilibrium shape (subfigure 4-7b), with the same distribution of stresses (subfigure 4-7a). The fixed point iteration with moving mesh needed a lower numerical relaxation parameter than $\beta = 0.01$ to go below the 10^{-2} error threshold after iteration 1286, therefore we stopped the computation there.

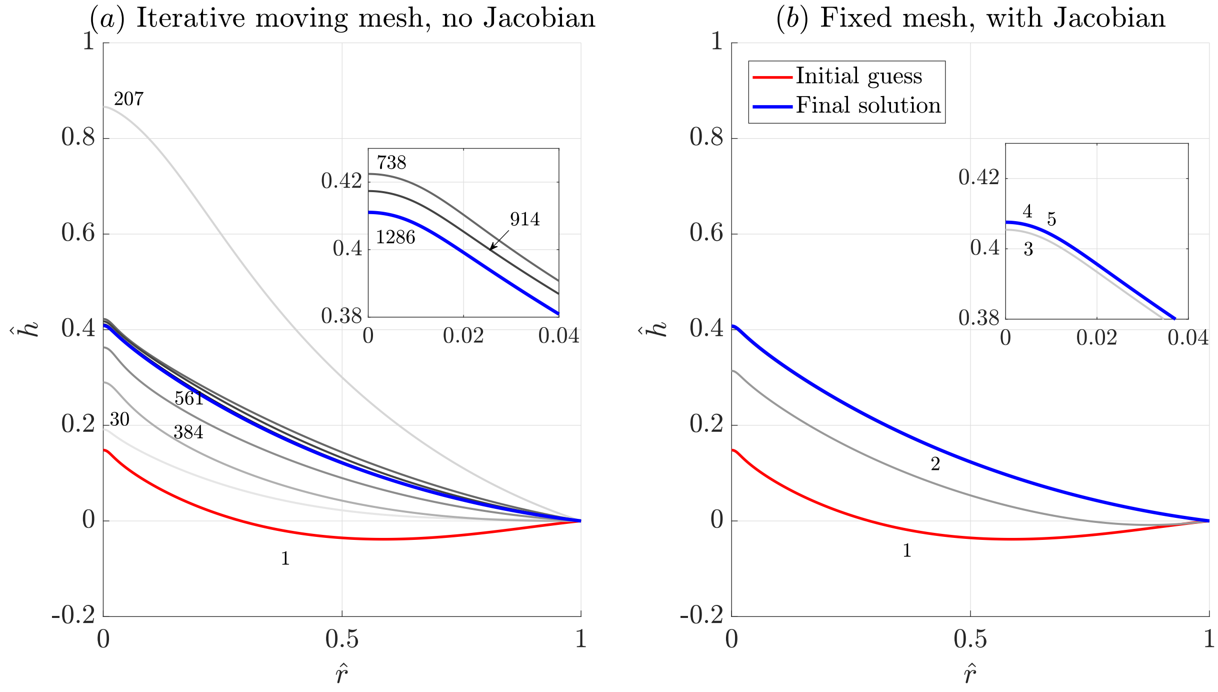

Figure 4-6: Equilibrium shapes across the iterative process. On the left, we show results with the fixed point iteration scheme without Jacobian. The fixed domain with Jacobian is shown on the left. Integer numbers indicate the number of iteration. For the case considered in this section, the fixed point iteration gets to a converged solution with 10^{-2} error norm in the normal stress balance in 1286 iterations (see figure 4-5), whereas the fixed mesh Jacobian-based approach gets to a solution with 10^{-4} error norm in the normal stress balance in just 5 iterations for the same initial guess.

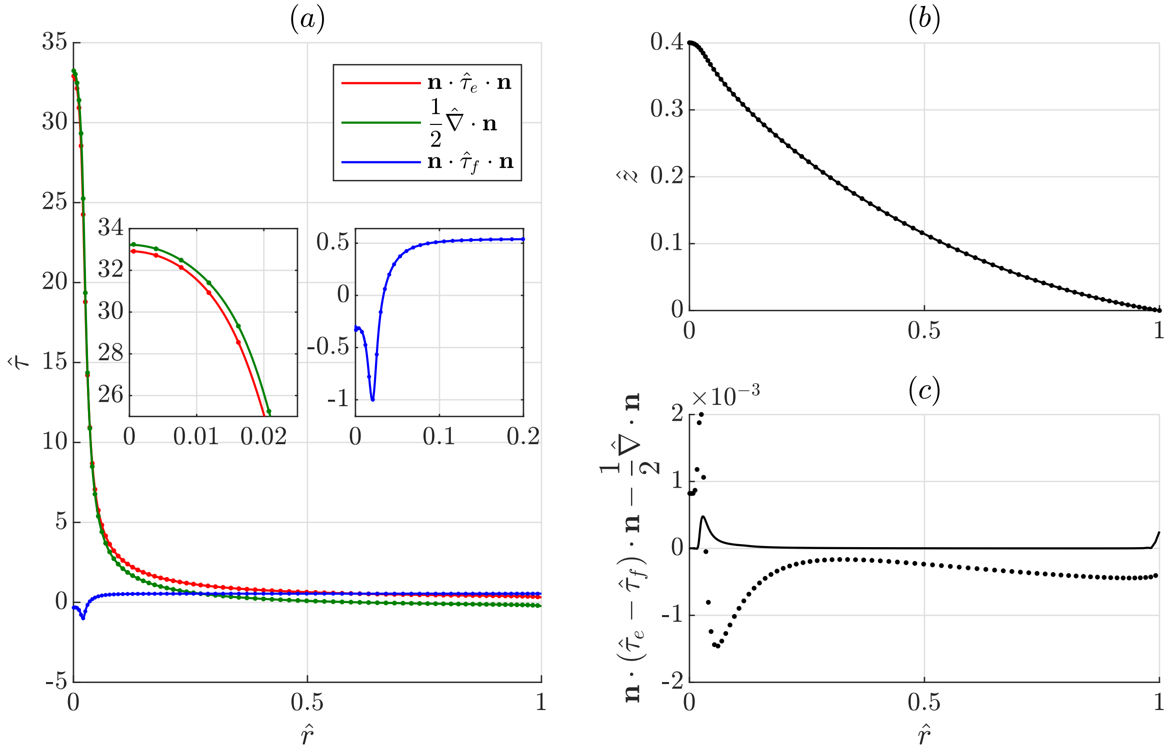

Figure 4-7: Subfigure a) shows the balance of dimensionless stresses in the normal direction for the converged solution in the fixed point iteration (moving mesh without Jacobian) (dotted points), and fixed mesh with Jacobian (solid lines). Sum of vacuum and liquid electric stresses are shown in red, surface tension stress in green and fluid stress in blue. Subfigure b) shows the equilibrium shapes, and subfigure c) shows the balance of stress residual in the normal direction for the converged solution in both methods. The Jacobian based approach yields an order of magnitude less error in the balance of stresses in approximately 3 orders of magnitude less iterations.

Chapter 5

Steady solutions, influence of the properties of the ionic liquids and space charge

In this chapter we present a general overview of the outputs of the model, and variations with respect to the parameters conductivity and critical field for emission. We also investigate the effects of space charge in the equilibrium shapes and the current.

5.1 Simulation parameters: the model ionic liquid [EMIm][BF$_4$] and geometrical setup

We use the geometry model described in figure 3-2 with parameters $\hat{z}_{sim} = 80$, $\hat{r}_{sim} = 40$, $\hat{d}^* = 40$[1], $a = 83.91$ and $w_0 = 0.953$ (corresponding to $R_c = 10\ \mu$m and $d = 100\ \mu$m).

The default operational parameters used are $q/m = 5.8 \cdot 10^5$ C/kg, $T_0 = 23$°C. The values of dimensionless $\hat{Z}$, $\hat{R}$, and potential will be mentioned for each analysis. The reservoir pressure is $p_r = 0$. We changed some physical and operational parameters in order to explore the dependencies of solutions. In these cases, the changed parameters will be explicitly mentioned. The default simulated physical properties of [EMIm][BF$_4$] used can be consulted in the annex (see annex section A), and they

---

[1] Notice that this is the computational domain distance, not the distance between the prolate spheroidal electrode and the tip.

Number	Value	$\Delta G = 1.1$ eV	$\Delta G = 1.15$ eV	$\Delta G = 1.2$ eV
ψ	$\frac{\Delta G}{k_B T_0}$	43.1	45.1	47.0
C_β	$\frac{2\kappa_0^2}{\rho\varepsilon_0\left(\frac{q}{m}\right)^2}$	$1.15 \cdot 10^{-3}$	$1.15 \cdot 10^{-3}$	$1.15 \cdot 10^{-3}$
Pe	$\frac{\kappa_T}{u_c r^* \rho c_p}$	2.67	3.19	3.79
Oh	$\frac{\mu_0}{\sqrt{\rho\gamma_0 r^*}}$	28.8	31.5	34.3
C_m	$\frac{u^*}{u_c}$	0.108	0.118	0.129
Θ	$\frac{u_{ion}^2}{u_c^2}$	$9.90 \cdot 10^6$	$9.04 \cdot 10^6$	$8.30 \cdot 10^6$
β	$\frac{\rho^v}{\rho}$	10^{-3}	10^{-3}	10^{-3}
$\hat{l}_H$	$\frac{l_H}{c_p T_0}$	1.38	1.38	1.38
$\hat{T}_{out}$	$\frac{T_{out}}{T_0}$	1.74	1.74	1.74

Table 5.1: Dimensionless numbers for three ΔG considered in this chapter.

originate the dimensionless parameters and dimensionless numbers found in tables 5.1 and 5.2:

5.2 Benchmark solution, and general outputs of the model.

We solved the model to obtain a benchmark solution of $V = 1360.5$ V, which yields $\hat{V} = V/\phi_c = 5.84$, $\hat{R} = 81.4$, $\hat{Z} = 0.0206$ and the parameters in tables 5.1 and 5.2 for $\Delta G = 1.1$ eV. As an overview for the reader, figure 5-1 shows the potential distribution for the whole computational domain (top), and locally at the meniscus level (bottom left) and emission region level (bottom right). From the figure, we can observe that the potential structure is mostly localized, with the prolate spheroidal potential being minimally affected by the presence of the meniscus. Moreover, the two plots at the bottom indicate that the meniscus is nearly equipotential, with a negligible loss of potential (up to 1.47%) compared to the electrode potential. Figure 5-2 shows the velocity field lines together with the electric field magnitude in the color plot. We can see how the Hagen-Poiseuille flow gets distorted by an eddy approximately half way from the inlet to the emission region. Subsequent simulations show that the size of the eddy is increased at lower flow rates. The flow contracts as it enters the emission region where the field lines of the velocity field

Reference symbol	Reference value	$\Delta G = 1.1$ eV	$\Delta G = 1.15$ eV	$\Delta G = 1.2$ eV
u_c	$\frac{\gamma_0}{\mu_0}$	1.23 m/s	1.23 m/s	1.23 m/s
u_{ion}	$\sqrt{\frac{q}{m} E^* r^*}$	$3.87 \cdot 10^3$ m/s	$3.70 \cdot 10^3$ m/s	$3.55 \cdot 10^3$ m/s
u^*	$\frac{\kappa_0 E^*}{\varepsilon_r \rho \frac{q}{m}}$	0.133 m/s	0.146 m/s	0.158 m/s
t_c	$\frac{r^*}{u_c} = \frac{r^* \mu_0}{\gamma_0}$	$2.50 \cdot 10^{-8}$ s	$2.09 \cdot 10^{-8}$ s	$1.76 \cdot 10^{-8}$ s
t_e	$\frac{\varepsilon_0 \varepsilon_r}{\kappa_0}$	$7.77 \cdot 10^{-11}$ s	$7.77 \cdot 10^{-11}$ s	$7.77 \cdot 10^{-11}$ s
t_μ	$\frac{4\mu_0}{\rho c_p T_0}$	$2.73 \cdot 10^{-10}$ s	$2.73 \cdot 10^{-10}$ s	$2.73 \cdot 10^{-10}$ s
t_m	$\frac{h}{k_B T_0}$	$1.62 \cdot 10^{-13}$ s	$1.62 \cdot 10^{-13}$ s	$1.62 \cdot 10^{-13}$ s
Z^*	$\frac{2\gamma_0 \rho \frac{q}{m}}{\kappa_0 E^* {r^*}^3}$	$1.95 \cdot 10^{21}$ Pa·s/m^3	$3.04 \cdot 10^{21}$ Pa·s/m^3	$4.64 \cdot 10^{21}$ Pa·s/m^3

Table 5.2: Reference times, velocities and impedance for three ΔG considered in this chapter.

terminate. The magnitude of the electric field in the emission region is about 8.3, which is on the order of the dimensionless critical field for this benchmark simulation ($\hat{E}_{crit} = \sqrt{\hat{R}} = 9.02$). The magnitude of the electric field at the base of the meniscus is close to the dimensionless amplified field from the prolate spheroidal geometry:

$$\left|\hat{E}_{base}\right| \approx \left|\frac{E_{tip}}{E_c}\right| = \frac{2V}{a\left(1 - w_0^2\right) \operatorname{arctanh}\left(w_0\right)} \sqrt{\frac{\varepsilon_0 r_0}{4\gamma_0}} \approx 0.82 \tag{5.1}$$

Figure 5-3 shows a temperature map of the emission region, where we can see how the emission region is heated, although very moderately. The temperature quickly decays to the base meniscus temperature away from the emission region, as expected due to the highly localized Ohmic effects in the emission region, where the electric field in the liquid is non-negligible.

Regarding the dimensionless space charge emanating from the meniscus in figure 5-4, we can highlight two aspects: the first one is the sharp decay due to the high acceleration of the particles right after emission ($\rho^v_{sch} \sim j^v/u^v$). The second one is the divergence angle of the plume right at its birth around $\sim 56°$ from the axis of symmetry. It is significantly wider than the semi-developed plume angle $\sim 14°$ (not shown in 5-4, albeit shown later in this chapter). Such wide angles in the early plume right after emission could be a potential threat for electrode impingement if highly solvated ions are subject to rapid fragmentation. The byproduct neutrals have low energy and once they are born from a fragmentation event, they are no longer subject to the electric field, since they are chargeless. As such, they travel in straight trajectories within the wider angle span, and could deposit in the extractor grids if the apertures are not wide enough [43]. Perhaps a practical design strategy is to use an aperture that provides an exit angle of at least 56°, as opposed to the current approach which is based on the (charged) plume measurements of a few degrees $\sim 18°$.

5.3 The current dependency on selected parameters

We explore the solution space by varying the electrical conductivity κ_0 and critical field for emission (through ΔG) from the benchmark solution.

5.3.1 The independence of the current on electrical conductivity

Figure 5-5 shows solutions for $\hat{V} = V/\phi_c = 5.84$, $\hat{R} = 81.4$, $\hat{Z} = 0.0411$ and the benchmark parameters for $\Delta G = 1.1$ eV in table except for the value of κ_0, which is scaled up almost 7 times, and down almost 2 times (numbers in tables 5.1 and 5.2 change accordingly). Figure 5-5a shows the dimensionless velocity of the ions normal to the meniscus interface. The velocity is scaled by the dimensionless area differential $\sqrt{1+\hat{h}'^2}$ to allow a fair comparison. Here $\hat{h}$ is the dimensionless interface profile equation (governed by the kinematic condition eq. 3.17), and $\hat{h}' = \frac{\partial \hat{h}}{\partial \hat{r}}$. The total current emitted is:

$$I = \rho \frac{q}{m}\, u_c r_0^2\, 2\pi \int_0^1 \hat{r}\; \hat{\mathbf{u}} \cdot \mathbf{n} \sqrt{1+\hat{h}'^2}\, d\hat{r} \tag{5.2}$$

Distribution of physical variables along the emission region and equilibrium menisci $\hat{r} = 0$ indicates axis of symmetry, $\hat{r} = 1$ indicates contact line pinning site. Notice that if the current were to depend on conductivity according to this model, it would appear in the term $\hat{\mathbf{u}} \cdot \mathbf{n}\sqrt{1+\hat{h}'^2}$, given the non-dimensionalization of this problem. This can be seen when looking at eq. 5.2: it does not contain any parameter dependence on electrical conductivity, since the capillary velocity term $u_c = \gamma_0/\mu_0$ only depends on the surface tension coefficient and viscosity at the reference temperature. We can see that this is not the case, and the term $\hat{\mathbf{u}} \cdot \mathbf{n}\sqrt{1+\hat{h}'^2}$ adjusts to variations in conductivity in such a way that the total emitted current does not change

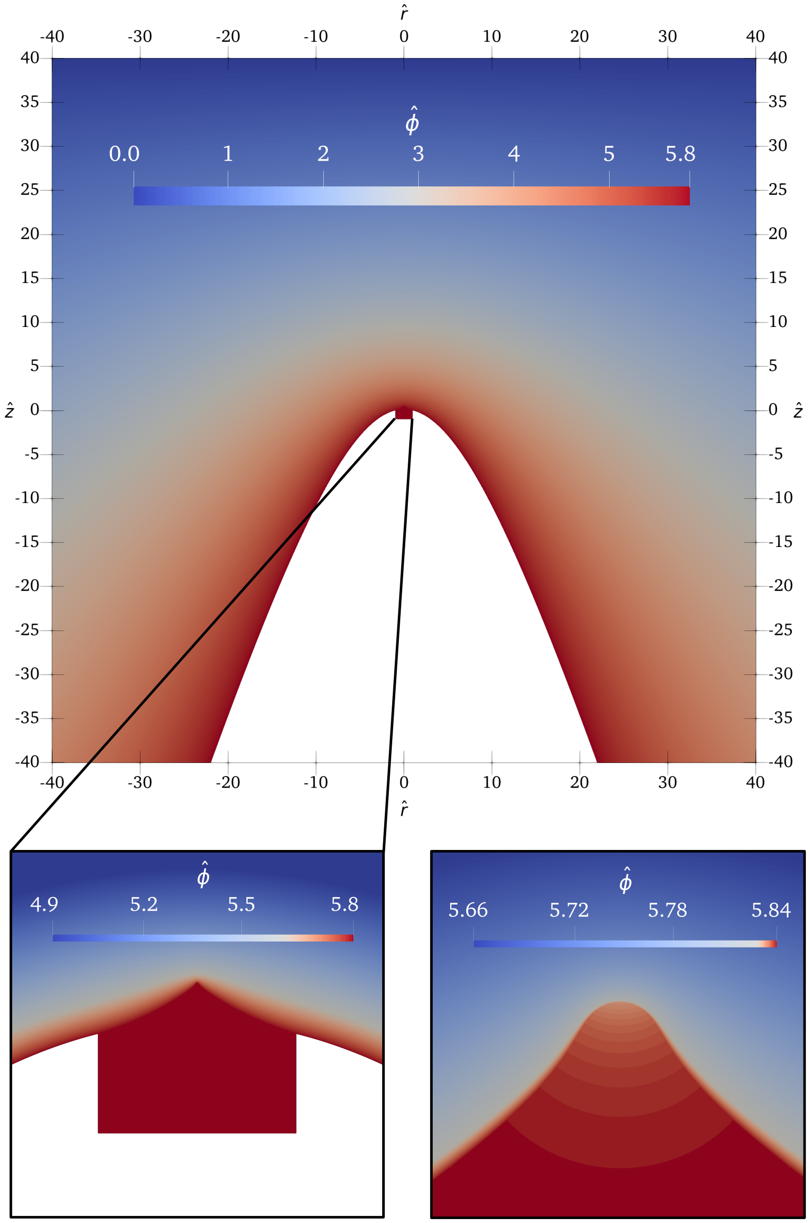

Figure 5-1: Dimensionless potential distribution near the meniscus. The meniscus is practically equipotential with Ohmic losses accounting for less than 2 %.

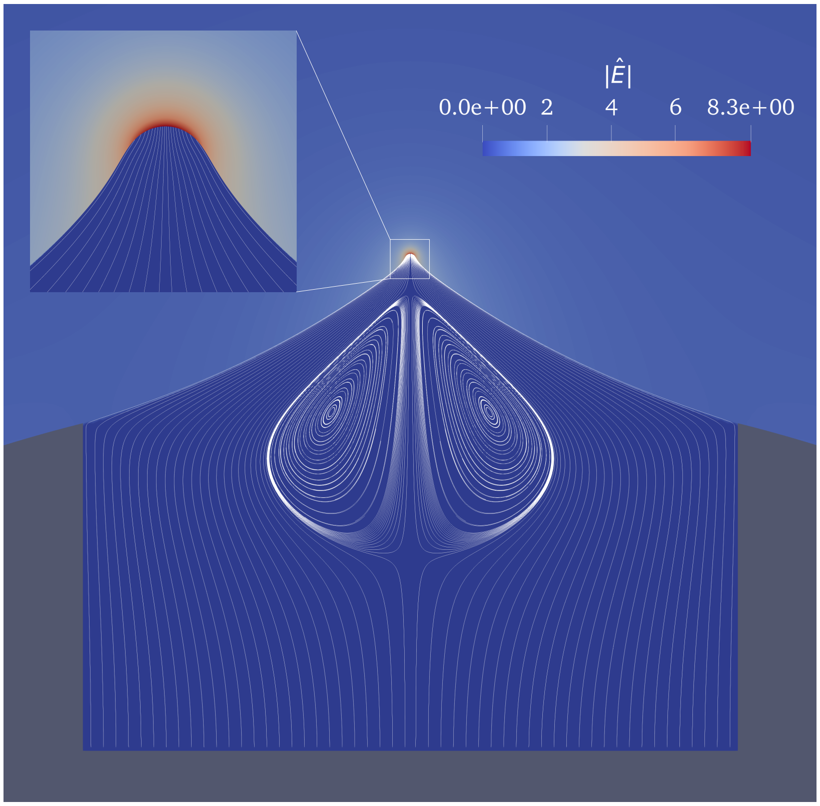

Figure 5-2: Dimensionless electric field modulus $\left|\hat{E}\right|$. Velocity field lines are shown in white. The zoomed panel shows the termination of the field lines in the liquid before starting evaporation, and magnitude of the electric field modulus close to the dimensionless critical field for evaporation.

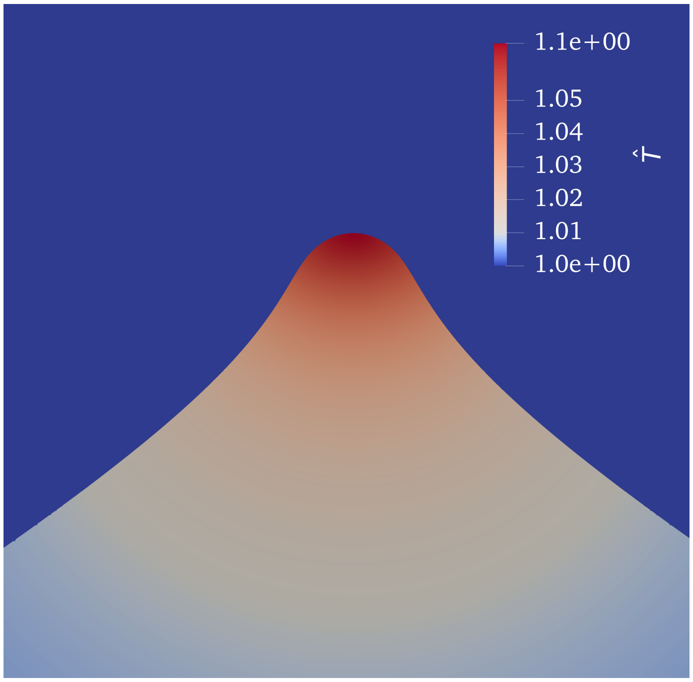

Figure 5-3: Dimensionless temperature map near the emission region.

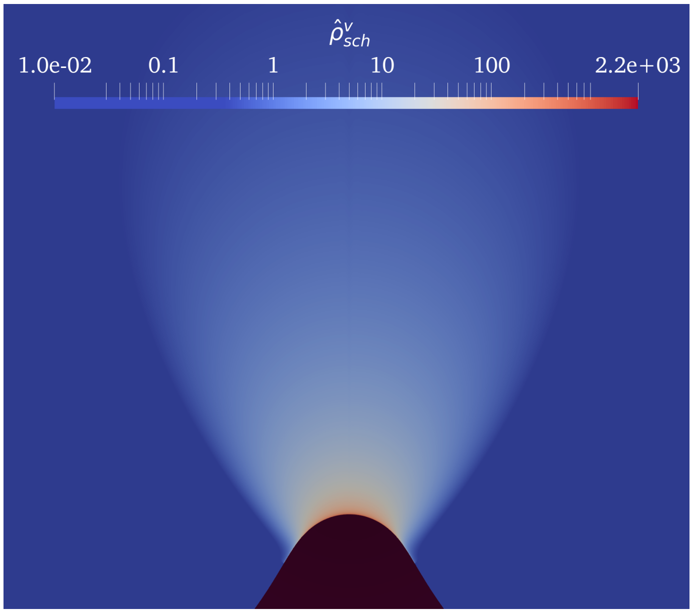

Figure 5-4: Dimensionless space charge map near the emission region. Meniscus apex is shown in black.

(the integral on equation 5.2 remains constant at $I = 315$ nA). The response of the meniscus to these conductivity variations is very subtle in shape, and highly localized in the emission region, as we can observe in figure 5-5b. The subtleness of this adaptation comes along with the fact that the kinetic law for evaporation (eq. 5.3) contains exponentials that are very sensitive to the electric field (slight variations in the electric field cause large variations in current density):

$$j_n^e = \frac{\sigma k_B T}{h} \exp\left(-\frac{\Delta G}{k_B T}\left(1 - \sqrt{\frac{E_n^v}{E^*}}\right)\right) \tag{5.3}$$

Therefore, the meniscus only has to adapt its curvature very slightly to adapt to the new emission region configuration at the new conductivity. Interestingly, the distribution of electric fields along the emission region does experience a significant change. This change spans from a practically relaxed surface charge in the case of high conductivity (dashed red line figure 5-5c) to a practically depleted surface charge configuration in the low conductivity case (dashed blue line in figure 5-5c). Equivalence between mass and charge evaporated makes the actual simulated current density scaled by the emission area differentials identical to the velocity of the ions in the fluid displayed in figure 5-5a (up to a constant). We can then argue by looking at both figure 5-5 and eq. 5.3 that if the current density remains practically constant upon large conductivity reductions (and consequently, the total current emitted), both, a higher normal electric field (figure 5-5c solid lines) and higher temperature along the meniscus must compensate for the depletion of charge (figure 5-5d). This temperature increase is due to the fact that lower conductivities enhance Ohmic dissipation in the meniscus ($\sim \mathbf{j} \cdot \mathbf{E}^l \sim \frac{j^2}{\kappa}$).

It is worth mentioning that, in this section, our focus lies on the variation of the electrical conductivity κ_0 as the sole parameter under consideration. This variation can be most easily carried out through simulation efforts, as the electrical conductivity of real ionic liquids strongly correlates with other parameters. In experimental efforts, it is very challenging to change electrical conductivity exclusively without affecting other parameters. For example, a higher electrical conductivity often corresponds to a lower viscosity or a higher charge-to-mass ratio of the ions. This correlation enables us to explain both the popular notion that ionic liquids with higher conductivity generally extract more current and the simulation results reported in this thesis, which demonstrate that conductivity plays a negligible role in the current emitted. A more in-depth discussion of this fact is provided in section 5.3.5.

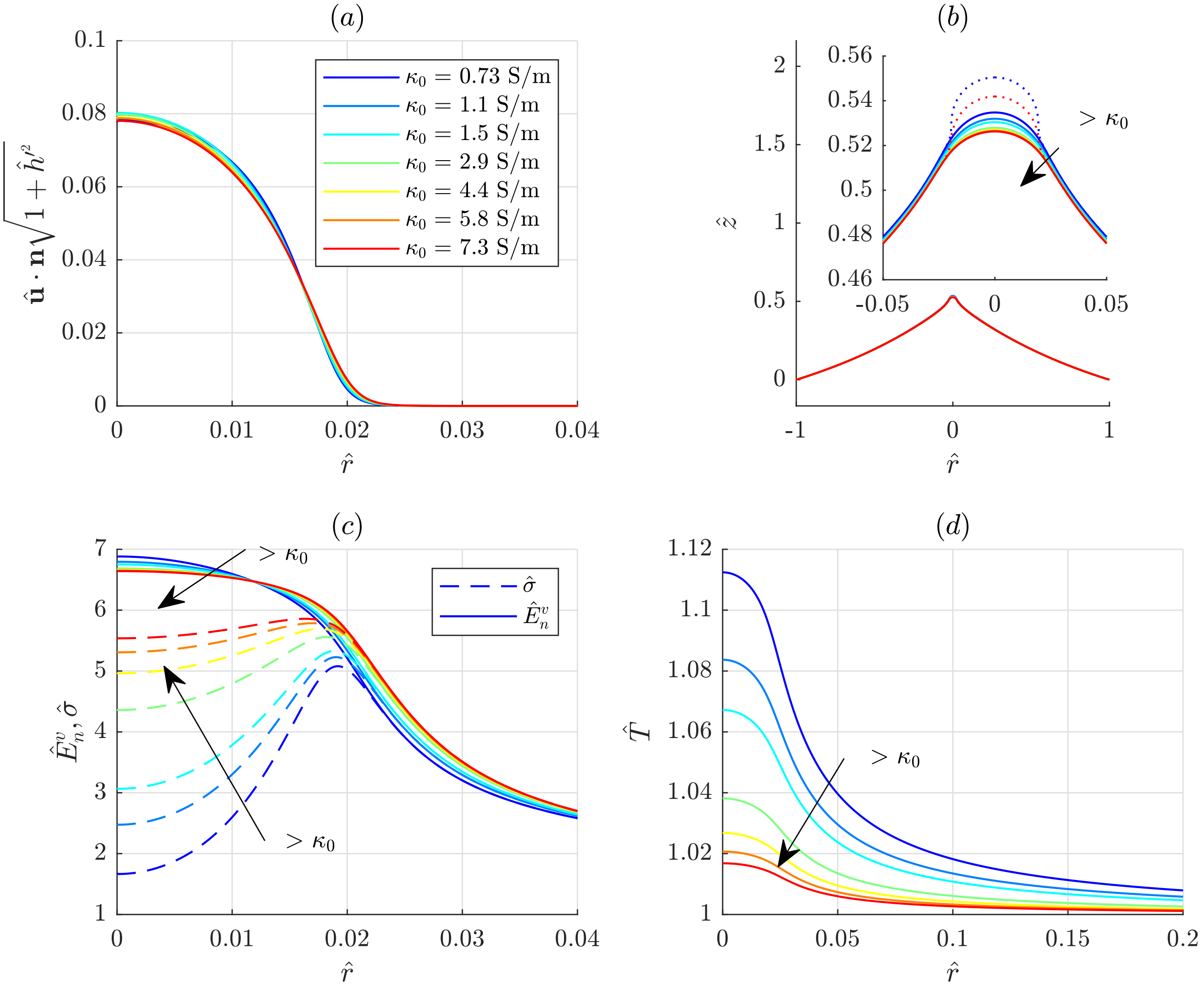

Figure 5-5: Analysis of the solutions for cases with varying electrical conductivity. a) Dimensionless distribution of normal velocities to the interface for different nominal conductivities. b) Meniscus shapes, structure of the emission region. The lowest conductivity (blue) and highest conductivity (red) contain an additional arc in dotted line whose magnitude is proportional to the velocity of the ions emitted. c) Dimensionless normal electric field on the vacuum side (solid) and surface charge (dashed). d) Dimensionless temperature.

5.3.2 The independence of the current on moderate changes in critical field

We report similar behavior when what we change is the critical field for emission in figure 5-6. The dimensionless numbers used are shown in tables 5.1 and 5.2. The value for the voltage used is $\hat{V} = V/\phi_c = 5.84$. We use a fixed dimensional impedance and radius for the simulations of $Z = 8 \cdot 10^{19}$ Pa s/m^3 and $r_0 = 2.5$ μm, which originate the following dimensionless numbers: for $\Delta G = 1.1$ eV, $\hat{R} = 81.4$ and $\hat{Z} = 0.0411$; for $\Delta G = 1.15$ eV, $\hat{R} = 97.3$ and $\hat{Z} = 0.0264$; for $\Delta G = 1.2$ eV, $\hat{R} = 115.3$ and $\hat{Z} = 0.0172$.

In this case, the balance of stresses is shown in subfigure 5-6a. Electric stresses are shown in red; surface tension stresses in green; fluid stress in blue and the recoil terms in black. We can see how most of the electric stress is compensated by the surface tension over the emission region. Over the conical base region of the meniscus, there is a balanced interplay between the hydrostatic pressure drop due to current evaporation, electrohydrodynamic stress and surface tension. From the fluid stress in figure 5-6, we can see its viscous nature in the sign change along the emission region (inviscid "Bernoulli" flow would show a purely negative pressure due flow acceleration). Similar to the conductivity case, we can see that the meniscus adapts very locally in the emission region to changes in critical field (figure 5-6b). Figure 5-6c) shows the influence of the ΔG on the emission region in increasing the scale of the electric stress ($E^* \sim \Delta G^2$), and narrowing its size ($r^* \sim \Delta G^{-4}$) yet, it does it in such a way that the total current emitted (eq. 5.2) does not change ($I = 159$ nA). We can see that while narrowing the size of the emission region, such an increase in critical field is followed by an increase of the electric field in the liquid, which at similar conductivities boosts current densities along the emission region, and Ohmic heating effects (figure 5-6d).

5.3.3 Space charge effects: the elongation of the meniscus

Figure 5-7 shows the equilibrium shapes of selected menisci at the same extracting field, ΔG and radius as in section 5.2, but different currents. The currents are modulated by decreasing the hydraulic impedance. We show the results obtained when considering space charge effects (black lines) and without considering space charge effects (blue lines). We can see that the general effect of space charge is to elongate the meniscus shapes. The elongation is not localized in the meniscus apex, as with the variations in conductivity or critical field, but is extended up to the meniscus base.

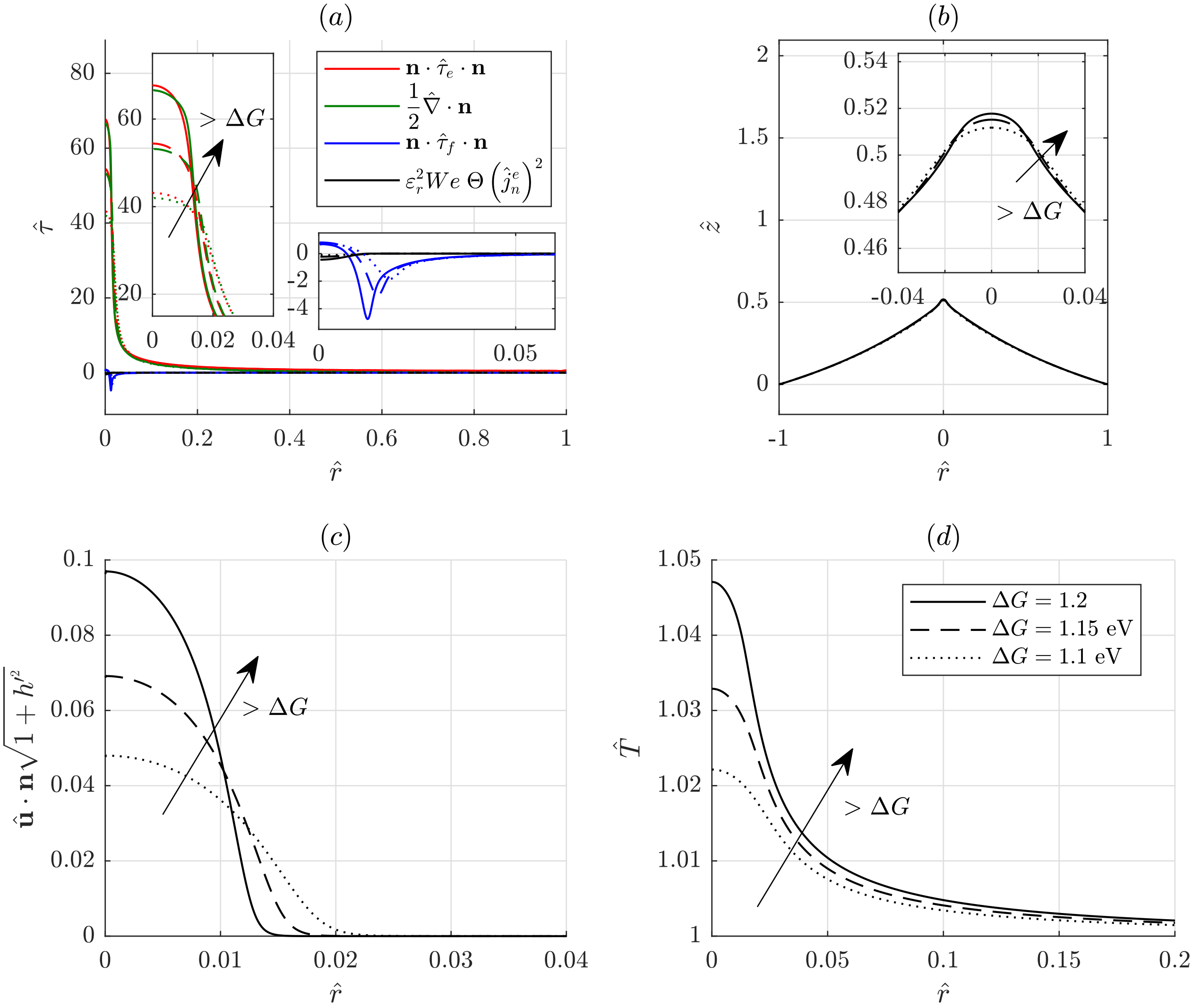

Figure 5-6: Analysis of the solutions for cases with varying critical field for emission. Dimensionless a) stress equilibrium distributions, b) meniscus shapes, c) distribution of normal velocities, and d) temperature along the meniscus interface.

The most interesting feature of this analysis is that this elongation is substantial, yet the meniscus adapts to the space charge screening of the electric field by "climbing up" or trying to sharpen its shape to amplify the electric field, to the extent that the total emitted current practically remains the same as the one without space charge.

This current seems to be dictated by the impedance for the cases tested. This can be seen in figures 5-8 a1, b1 and c1 for the three currents considered, where the velocity of the ions scaled by the area differential is shown. We can see this adaptation more clearly in this subfigure, where the meniscus compensates for the screening of the electric field by increasing the area of emission. This increase in the area of emission is slightly larger for the higher current case (subfigure a1), as intuitively expected. For the lower current case, both changes in the size of the emission region (subfigure c1) and meniscus elongation are less apparent. We can see also the effect of space charge on the distribution of electric fields normal to the interface, in subfigures 5-8 a2, b2 and c2. The electric fields are smoothed, or redistributed along the meniscus profile by lowering their value at the apex, but increasing their value at the end of the emission region if compared to the case without space charge. This general trend where the meniscus elongates with the action of space charge is very coherent to observations of liquid metal ion sources equilibrium shapes, where their shapes usually develop a cusped protrusion at the apex that elongates when the current (or space charge) is more intense [101]. Due to the substantially higher currents than ILIS, the liquid metal cusps are more elongated than what is shown in figure 5-7.

5.3.4 Space charge effects: influences on the current

Previous analyses have categorized the relevance of space charge against other physics by having only a look at its effects on the emission region r^* [21]. The results reported in the previous section show that that analysis may be true very locally, but can be misleading in the sense that it neglects the adaptability of the emission region to changes in current, which seems not to be defined by any emission parameter itself in the regimes that we are studying, but by the conditions of the flow upstream, namely the hydraulic impedance, and the meniscus radius.

In this regard, and given how space charge affects the geometry of the meniscus (e.g, not only local changes in the emission region), we believe there should be a parameter of scale that includes how space charge affects the field at the base of the cone, whose physics seem to govern the current emitted by the meniscus.

Models proposed by Puretz [102] and Mair [83] give a rough estimation of this dependency for liquid metal ion sources. They suggest that the current is dominated

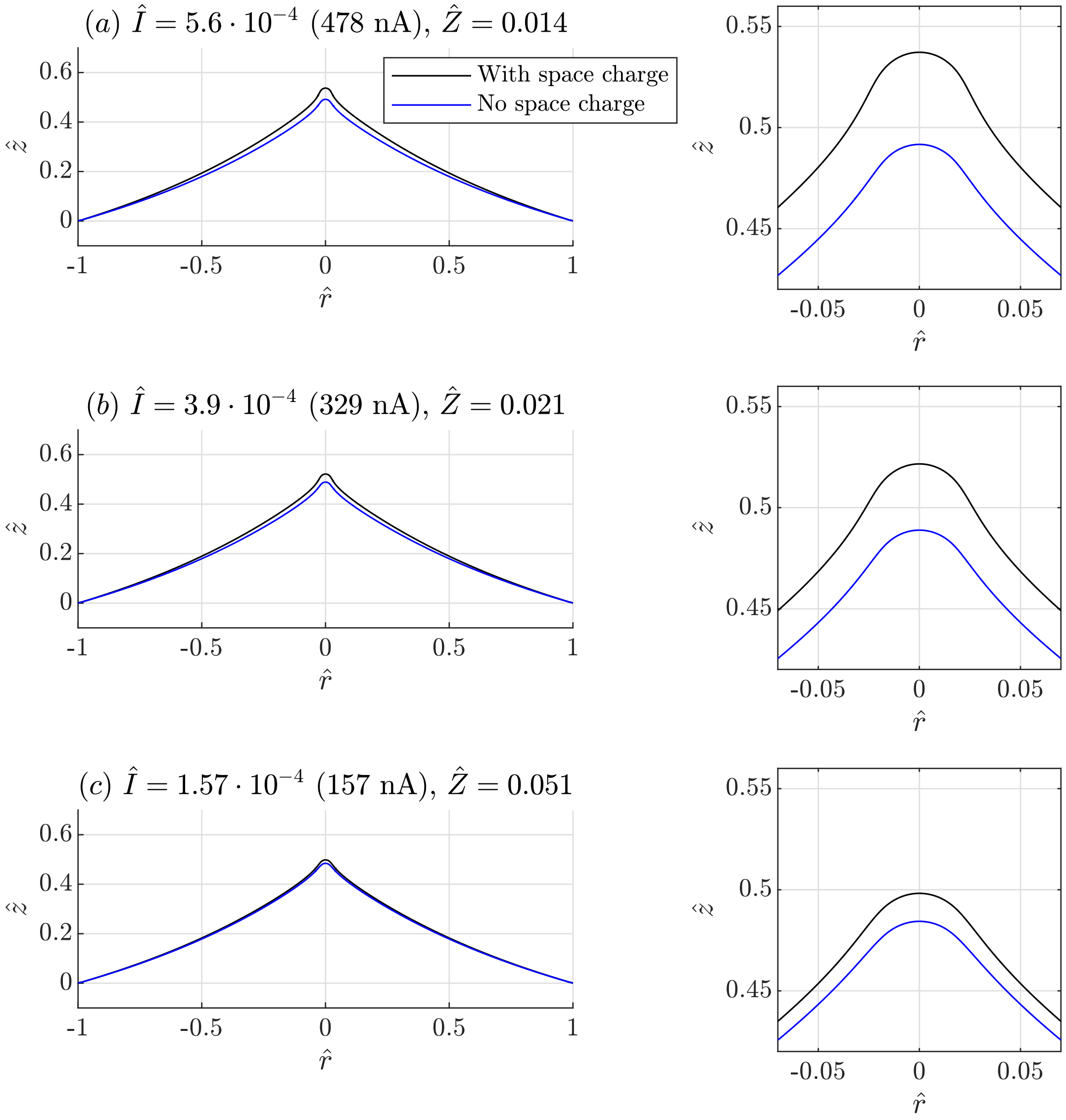

Figure 5-7: Space charge effects on the meniscus interface for three different currents. The figure shows equilibrium shapes for the full meniscus in the left column, and the correspondent zoom on the emission region on the right column.

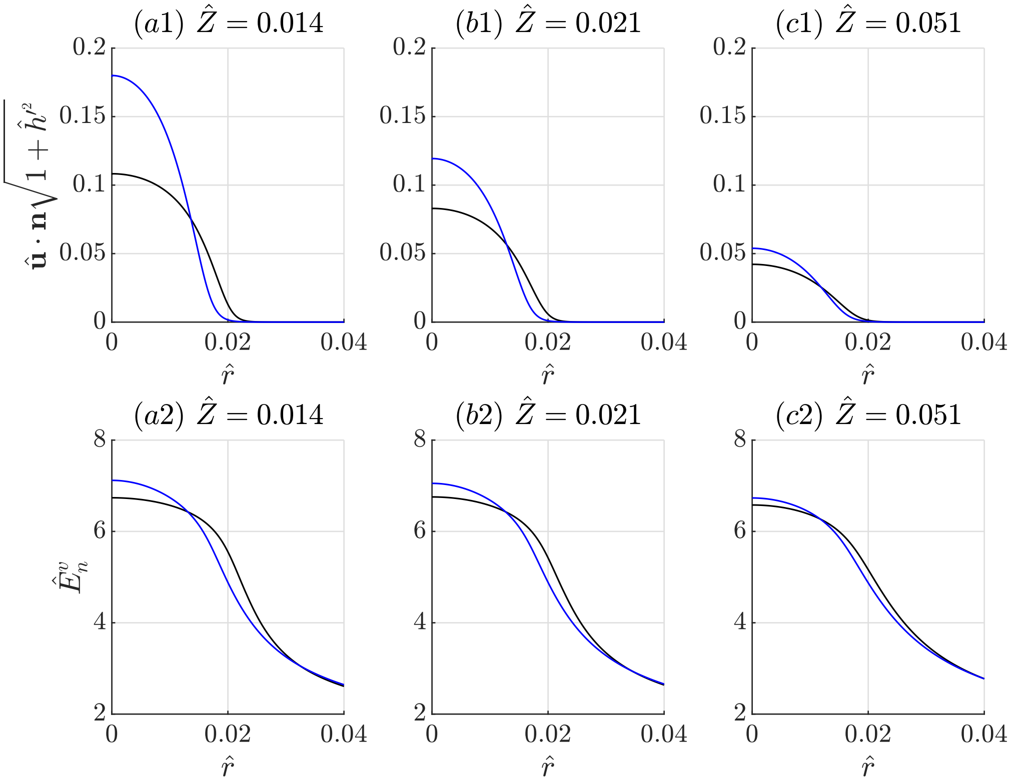

Figure 5-8: Space charge effects on the distribution of dimensionless velocities in the liquid and electric fields in the vacuum normal to the meniscus interface. Dimensionless velocity normal to the emission region scaled by the area differential in subfigures 1. Subfigures 2 show the distribution of normal electric fields in vacuum. The letter codes correspond to the same dimensionless impedance as in figure 5-7. Similar to figure 5-7, distributions considering space charge effects are shown in black. Distributions without space charge effects are shown in blue.

by the impedance if the drag force F_μ is much greater than the momentum flux brought to the extractor:

$$F_\mu \gg \frac{mv}{q} I \tag{5.4}$$

Where v is the velocity of the ions ($v \approx \sqrt{\frac{2qV}{m}}$). For the single fluid channel case implemented in this thesis, and assumed fully relaxed Hagen-Poiseuille flow, and a length of the line equal to L:

$$F_\mu = \int_S \mu \frac{\partial v_z}{\partial r}\, dS = \int_S \mu \frac{\partial v_z}{\partial r}\, dS = \frac{\Delta P}{L} \pi r_0^2 L = QZ\pi r_0^2 \tag{5.5}$$

where S indicates the cylindrical outer surface of the inlet channel. Inserting 5.5 in 5.4 and rearranging gives an expression for the impedance as:

$$Z \gg \frac{\rho}{\pi r_0^2} \sqrt{\frac{2q}{m} V} \tag{5.6}$$

Notice the dependence of eq. 5.6 with r_0, not with r^*: the bigger the meniscus, the smaller the impedance has to be for space charge effects to dominate the current emitted.

It is convenient to define a *characteristic space charge impedance*:

$$Z_{spch} = \frac{\rho}{\pi r_0^2} \sqrt{\frac{2q}{m} V} \tag{5.7}$$

And have a criterion to study the influence of the space charge on the current: if $Z/Z_{spch} \gg 1$, the current is dominated by the impedance, and when $Z/Z_{spch} \ll 1$ space charge effects become important. For the case considered in figures 5-7 and 5-8, $V \sim 1377$ V, $q/m \sim 5.8$ C/kg, $r_0 \sim 2.5$ μm, $\rho \sim 1240$ kg/m^3, the characteristic space charge impedance yields $Z_{spch} = 2.51 \cdot 10^{18}$ Pa s/m^3, which is much lower than the impedance simulated for the maximum current in figure 5-8a, $Z = 2.73 \cdot 10^{19}$ Pa s/m^3, $Z/Z_{spch} \sim 10$. Therefore according to this criterion, space charge will not dominate.

We further test the validity of eq. 5.6 for four additional example operating points in figure 5-9. Each of the operating points has a different meniscus radius, operates at a fixed voltage, and has the standard $q/m = 5.8 \cdot 10^5$ C/kg, and $\rho = 1240$ kg/m^3 considered in this chapter, the only parameter that we change for each point is the impedance Z, and consequently Z/Z_{spch}. Figure 5-9a shows the current obtained for the impedance sweep in the four operating points when considering space charge

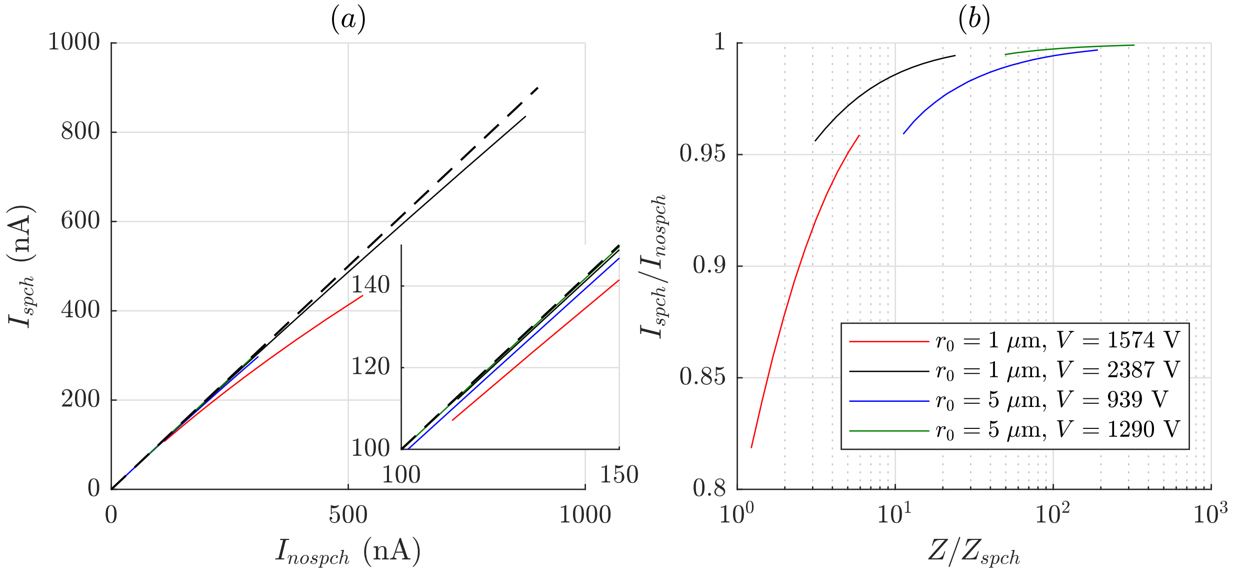

Figure 5-9: Comparison between current obtained without space charge and with space charge at selected operational points, and varying impedances.

(I_{spch}) as a function of that same current without space charge effects (I_{nospch}). If space charge effects are irrelevant, then $I_{spch} \approx I_{nospch}$, and the curves in 5-9a have all a slope 1 (this unit slope is shown in dashed black line). For the cases considered the only one that presents a relevant space charge influence is the smaller meniscus and lower voltage case, very close to the extinction voltage (red line). In figure 5-9b, the current decrease does not get larger than 20% in the cases where Z/Z_{spch} approaches to 1. We can see how in most of the cases, the current does not decrease further than 5% when considering space charge effects, as expected by the generally low perveance of ILIS beams, and such decrease is indeed correlated with the parameter Z/Z_{spch}. Figure 5-9b also suggests that Z_{spch} has a limitation as a yardstick to predict the influence of space charge effects in the current. We can see that for the same value of Z/Z_{spch}, there are still small differences of current decrease depending on the operational parameters of the meniscus. For the cases simulated, such differences may be due to geometrical aspects of the electrodes (for instance, at a given R_c, the *dimensionless* electrode geometry that the meniscus sees when $r_0 = 1\ \mu$m is different than the one at $r_0 = 5\ \mu$m), or a larger spreading of the beam at lower voltages. In any event, the cases presented in figure 5-9 are shown containing the maximum current that our algorithm could converge for. If that is considered as a criterion for estimating how close is the stability boundary for these menisci, we are in a position to say that space charge effects influence current up to a maximum of 20%, *and only* in cases of likely waning stability.

5.3.5 Discussion

The results presented in this section suggest that when $r^*/r_0 \ll 1$, ILIS current is likely given by parameters referencing upstream conditions of the flow (i.e, hydraulic impedance, reservoir pressure) and with slight space charge screening in very specific conditions (very small menisci, voltages close to extinction), and not by parameters of the liquid that play a relevant role close to the emission region (conductivity, critical field, or parameters considered in other studies, for instance higher temperature of the meniscus at constant viscosity [42] or varying dielectric permittivities [19]).

We believe there have been clear hints of this fact that in retrospect seem clear, but have been perhaps unnoticed. In addition to our simulation work presented earlier in this section, we provide two additional arguments in this thesis supporting this fact:

Argument 1: The liquid metal case

Liquid metal ion sources extract at most $0.5 - 1 \cdot 10^3$ times the amount of current that ionic liquid ion sources extract, despite having more than 6 orders of magnitude higher conductivity. Practically all literature on liquid metal ion sources develops current scalings without any parameter referencing the emission region [35, 37, 34, 36, 82, 83].

In fact, in chapter 6 we will see that when $Z/Z_{spch} \gg 1$ and $r^*/r_0 \ll 1$, the model presented here predicts that the current can be explained with an equation of the following structure:

$$I = \frac{2\gamma\rho}{r_0 Z}\frac{q}{m}\left(f\left(\hat{E}_{tip}, \Theta\right) + \frac{p_r r_0}{2\gamma}\right) \tag{5.8}$$

where $f\left(\hat{E}_{tip}, \Theta\right)$ is a dimensionless function of order 1 $\left(f\left(\hat{E}_{tip}, \Theta\right) \in [0, \sim 2]\right)$ that depends on parameters governing the geometry of the electrodes (Θ) and a dimensionless electric field local to the meniscus pinning site. This site is assumed to be at the apex of the tip in an axially symmetric configuration ($\hat{E}_{tip}$). The dimensionless electric field $\hat{E}_{tip}$ is essentially proportional to the voltage V applied and the specific geometric configuration of the electrodes. No conductivity κ, ε_r, E^*, or T appear in 5.8. In chapter 6, we will delve into a detailed study of the function in eq. 5.8, but as a brief introduction, we can compare eq. 5.8 for an indium emitter firing in a tungsten tip of curvature radius $R_c \sim 1\ \mu$m [101] ($T = 160$°C, $\rho \sim 7000$ kg/m^3, $q/m \sim 8.4 \cdot 10^5$ C/kg, $\gamma \sim 0.57$ N/m, $\mu \sim 0.0019$ Pa s), and an [EMIm][BF$_4$] emitter firing in a tungsten tip of curvature radius $R_c \sim 20\ \mu$m [81] ($T = 22°$ C, $\rho \sim 1240$ kg/m^3, $q/m \sim 5 \cdot 10^5$ C/kg, $\gamma \sim 0.048$ N/m, $\mu \sim 0.038$ Pa s) under similar meniscus radius:

$$\frac{I_{LMIS}}{I_{ILIS}} \approx \frac{\left(\frac{\gamma\rho}{Z}\frac{q}{m}\right)_{LMIS}}{\left(\frac{\gamma\rho}{Z}\frac{q}{m}\right)_{ILIS}} \approx \frac{\left(\frac{\gamma\rho}{\mu/R_c}\frac{q}{m}\right)_{LMIS}}{\left(\frac{\gamma\rho}{\mu/R_c}\frac{q}{m}\right)_{ILIS}} \approx 10^2 \tag{5.9}$$

Which is very close to the ratio of currents obtained experimentally in the referenced papers.

Argument 2: The stable cone-jet case

It is well established that at a given flow rate Q, the current emitted by a stable cone-jet follows the scaling law defined by Profs. Juan Fernández de la Mora (FdM) and Loscertales [33]:

$$I = f_{FdM}(\varepsilon_r)\sqrt{\frac{\gamma\kappa Q}{\varepsilon_r}} \tag{5.10}$$

Where $f_{FdM}\left(\varepsilon_r\right)$ is an empirical function that is approximately linear with ε_r, until it reaches a plateau around $\varepsilon_r \approx 20$. The current in eq. 5.10 has a dependence on conductivity. Interestingly, there is clear experimental evidence that when the flow rate Q is not actively controlled and emerges as a result of a matural balance between the electric, surface tension, hydrodynamic and hydraulic impedance stresses, the flor rate Q does not depend on the conductivity of the liquid [116, 108].

In fact, what confers the cone-jet current its characteristic square root dependence on the conductivity is the increase of specific charge q/m via the reduction of the electrical relaxation time, and the reduction of the droplet radius. This can be seen if considering Gañán-Calvo's [49] universal scaling law for the average surface charge σ_{drop} and the diameter d_{drop} of the emitted droplets:

$$\sigma_{drop} = 0.59\left(\varepsilon_0\gamma^2\rho\kappa^2\right)^{\frac{1}{6}} \tag{5.11}$$

$$d_{drop} = 2.9\ d_{drop_0}\sqrt{\frac{Q}{Q_0}} \tag{5.12}$$

where $d_{drop_0} = \left(\frac{\varepsilon_0^2\gamma}{\pi^2\rho\kappa^2}\right)^{\frac{1}{3}}$ is a characteristic diameter, $Q_0 = \frac{\varepsilon_0\gamma}{\rho\kappa}$ is a characteristic flow rate, γ is the surface tension of the liquid and ε_0 is the dielectric permittivity of vacuum. In this case,

$$\frac{q}{m} = \frac{\sigma_{drop}\mathcal{S}}{\rho\mathcal{V}} = \frac{\sigma_{drop}\pi d^2}{\rho\pi d^3/6} = \frac{2.62}{\rho}\sqrt{\frac{\gamma\kappa}{Q}} \tag{5.13}$$

where $\mathcal{S}$ and $\mathcal{V}$ are the surface and volume of the droplet, assumed here as spherical. Inserting equation 5.13 in the continuity equation for the current in eq. 5.14:

$$I = \rho\frac{q}{m}Q \tag{5.14}$$

yields the well established scaling for the current [33, 48]:

$$I \propto \sqrt{\gamma\kappa Q} \tag{5.15}$$

For ionic liquids, when the non-dimensional flow rate parameter η,

$$\eta = \sqrt{\frac{\rho\kappa Q}{\gamma\varepsilon\varepsilon_0}}, \tag{5.16}$$

is sufficiently low $\eta \ll 0.5$, and the normal electric field at the apex of the meniscus becomes similar to the critical field for ion evaporation E^*, the electrospray can operate in the pure ion regime, where the specific charge q/m is the highest that an electrospray can have: that corresponding to the discrete nature of the ionic molecules. This magnitude of q/m is obviously independent of the electric conductivity of the liquid: higher conductivity cannot increase it further. If the flow rate does not depend on conductivity, and neither does q/m in the pure ion regime, then by continuity neither does the current (5.14).

An explanation for experimental evidence supporting a leading order effect on the magnitude of the current

Many empirical studies have assumed a leading order effect of the conductivity in the current emitted by ILIS in the pure ion regime [106, 54, 80, 15, 75, 16], probably inspired by eq. 5.10 of electrospraying in the cone-jet regime. In summary, the popular notion is that ionic liquids with the highest electrical conductivities not only achieve the pure ionic regime more readily (as opposed to the mixed regime, in which a cone-jet produces droplets and ions in the plume), but more importantly, seem to produce the largest ion emission currents. This has served as a prescription recipe when looking for better ionic liquids: on top of the list are those that have the highest electrical conductivity when the objective is to maximize the emitted current, which is highly desirable for many applications, ranging from ion sources for space thrusters to microfabrication and analysis tools [106, 17, 127].

In addition, this has been rationalized theoretically by looking at the scaling arguments [63, 21] presented in the first chapter of this thesis (eq.1.9), where conductivity plays a central role:

$$I^* \approx j^* A = \frac{32\pi\kappa\gamma^2\varepsilon_r}{\varepsilon_0^2 E^{*3}\left(\varepsilon_r - 1\right)^2} \tag{5.17}$$

Scaling arguments like this, together with the interpretation of the empirical evidence, have fueled the notion that conductivity has a central role in the operation and performance of electrosprays in the pure ionic regime, more precisely through its effects on the magnitude of the emission current.

The numerical evidence presented in this thesis and the arguments that precede this section apparently contradict both the experimental interpretations, and the zeroth order of magnitude approximation in eq. 5.17. The argument that we can provide to reconcile the contradiction with experiments is that the effect of viscosity has been practically overlooked from any discussion in all those empirical studies, and this is especially important since viscosity is correlated precisely to electrical conductivity through the Walden mechanism [113]: higher conductivity ionic liquids usually have lower viscosity, which could definitely have explained their enhanced currents through a lower hydraulic impedance compared to the less conductive ones.

5.4 The plume

The plume of the ions of the benchmark solution in section 5.2 is shown in figure 5-10. The space charge contour plots take the form of a lobe. The current density approximately follows a Gaussian profile in polar coordinates. For example, see the normalized angular beam intensity in the additional axis on the right of figure 5-10[2]. For our computational capacity, we can only show a semideveloped plume, therefore the divergence angle for the current should be below the shown (14°) with a fully developed plume. We can see how the dimensionless space charge maximizes at the center of the beam ($\theta = 0°$), and decays approximately quadratically downstream in the domain in figure 5-11a. The space charge has a sharp decay at the beginning due to the high acceleration of the ions near the emission region. Notice that in the case where the initial velocity of the ions $\hat{\mathbf{u}}^v \cdot \mathbf{n}$ was taken to be 0, charge continuity

---

[2] Other authors identify this shape as supergaussian [98].

would require $\hat{\rho}^v_{sch}$ to tend to infinity right at the meniscus interface. The normalized potential drop can be seen in figure 5-11b. The low angular divergence of the plume makes it almost collapse to the Laplace potential drop corresponding to the prolate spheroidal coordinate system at the axis of symmetry, which is also a symptom of the fact that the meniscus is very far from being space charge limited, at no surprise.

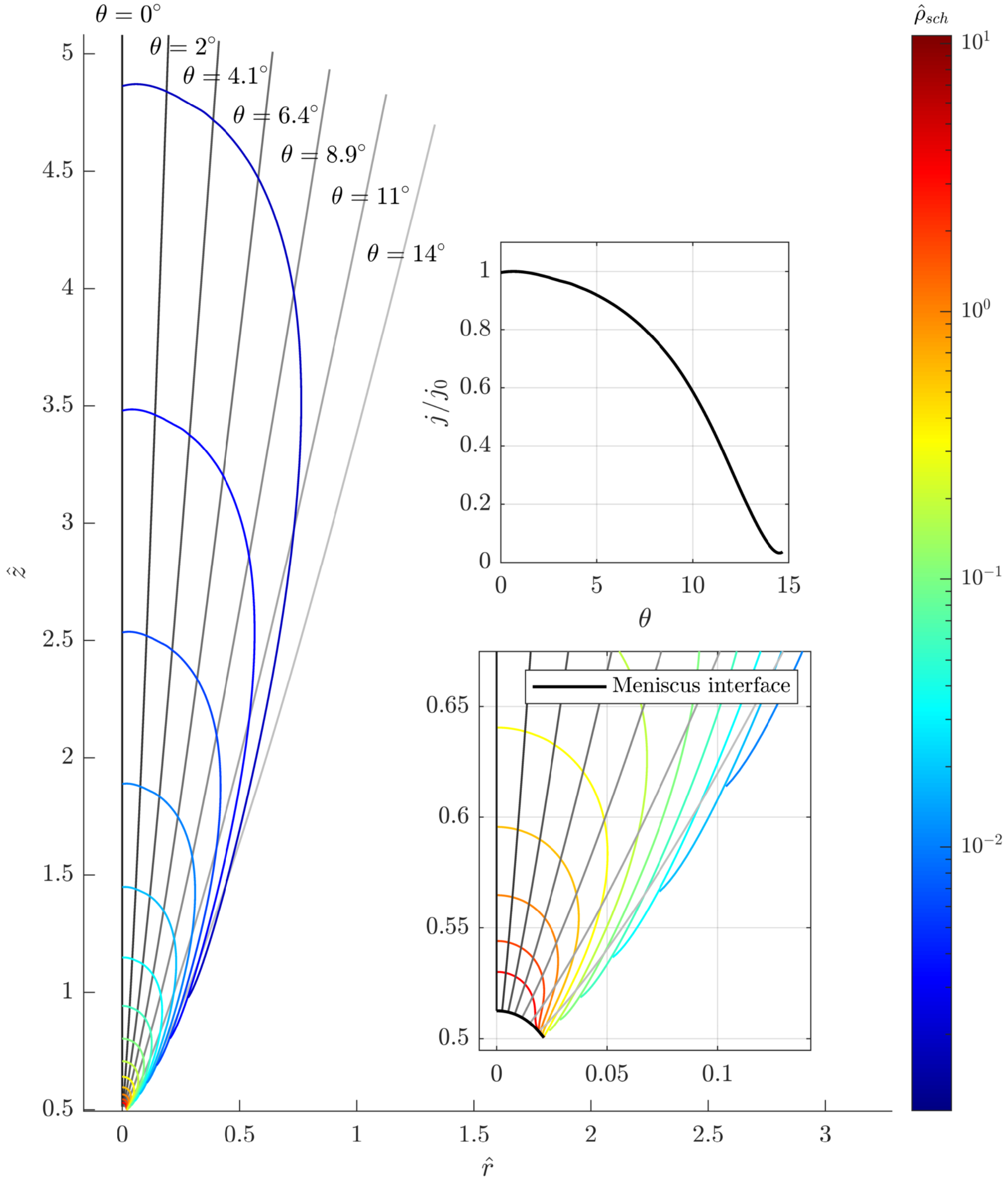

Figure 5-10: Space charge contour plots on the left. Results are shown with the integrated trajectory of particles in grey at different particle divergence angle θ. A zoomed panel is shown in the bottom right part of the figure. Top right figure shows a normalized current density j/j_0 plot evaluated at the end of the integrated region (end of the grey lines), where j_0 is the current density at the center of the plume. The plume is the same as shown in figure 5-4.

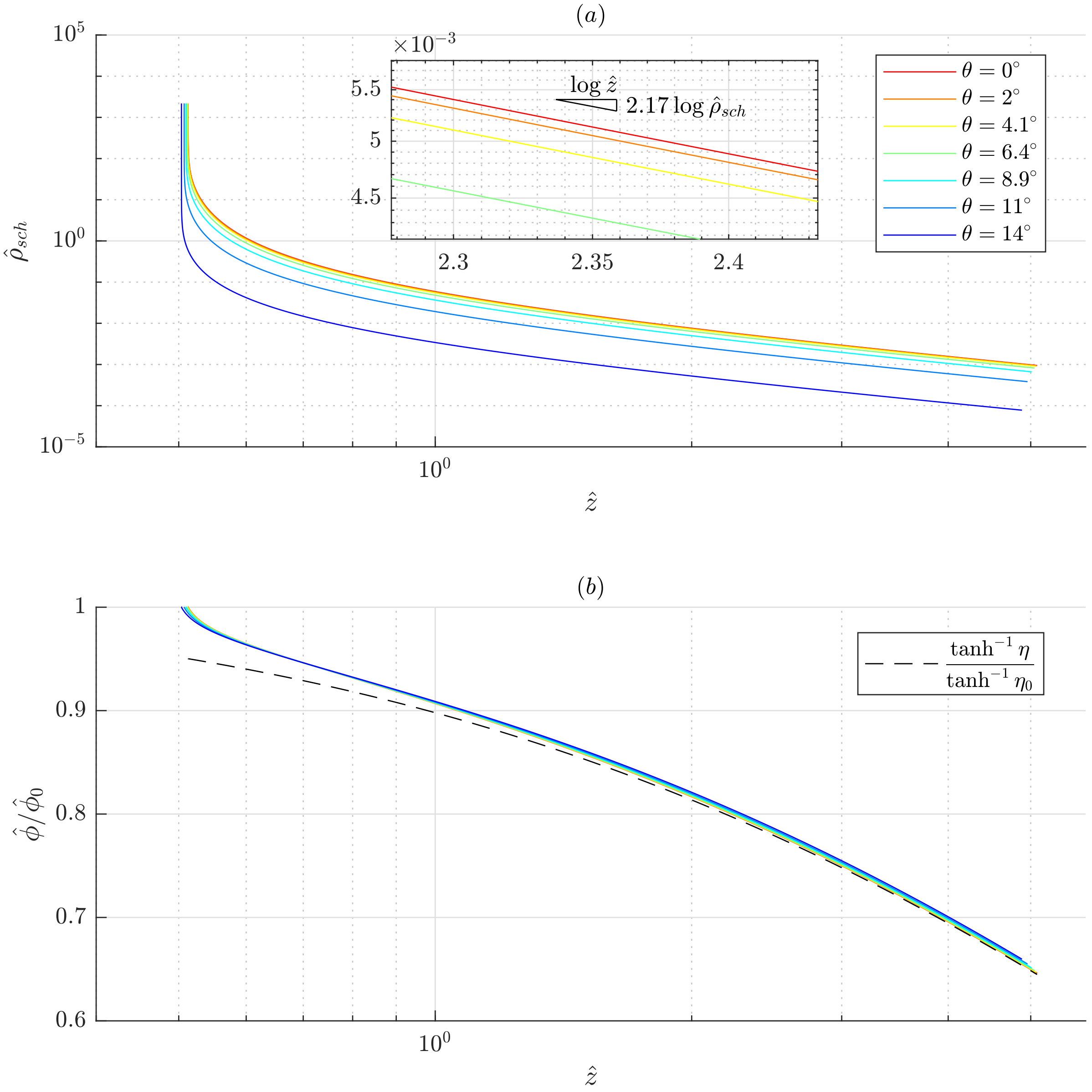

Figure 5-11: Space charge analysis in the physical domain as a function of the semideveloped plume divergence angle and axial coordinate in subfigure a). Subfigure b) shows the normalized potential in the domain as a function of the $\hat{z}$ coordinate.

Chapter 6

The current-voltage behaviour: insights from simulations

In this chapter we study the range of external potential/electric field parameters where we found a steady solution to the meniscus problem. We neglect space charge in this chapter. The way we neglect space charge is by directly considering $\hat{\rho}^v_{sch} = 0$ in the dimensionless Poisson equation for vaccuum, we also neglect the recoil term ($\beta = 1$ as in Coffman [21]). We also restrict the exploration to menisci with sizes r_0 much larger than the emission region size $r_0 \gg r^*$. The parameters used are described in the section below.

6.1 Simulation parameters for [EMIm][BF$_4$]

We use the parameters corresponding to [EMIm][BF$_4$] described in the annex section A with the default operating conditions of $\Delta G = 1.2$ eV, $q/m = 3.53$ C/kg, and $T_0 = 23$°C. The reservoir pressure is $p_r = 0$, except in the results of figures 6-8 and 6-10. These properties originate the dimensionless numbers and characteristic velocities, and timescales in tables 6.1 and 6.2.

6.2 Classification of solutions using the field $\hat{E}_{tip}$ as reference

It is useful to describe the range of voltages that yield a solution to this problem by referencing the electric field that the meniscus *sees*, or that is amplified by the geometry of the electrode at the meniscus level $\hat{E}_{tip}$. Such electric field is not trivial,

Number	Value	Default
ψ	$\frac{\Delta G}{k_B T_0}$	47.0
C_β	$\frac{2\kappa_0^2}{\rho\varepsilon_0\left(\frac{q}{m}\right)^2}$	$3.1 \cdot 10^{-3}$
Pe	$\frac{\kappa_T}{u_c r^* \rho c_p}$	3.79
Oh	$\frac{\mu_0}{\sqrt{\rho\gamma_0 r^*}}$	34.3
C_m	$\frac{u^*}{u_c}$	0.211
Θ	$\frac{u_{ion}^2}{u_c^2}$	No space charge
β	$\frac{\rho^v}{\rho}$	1 (No space charge)
$\hat{l}_H$	$\frac{l_H}{c_p T_0}$	1.38
$\hat{T}_{out}$	$\frac{T_{out}}{T_0}$	1.74

Table 6.1: Dimensionless numbers used in this chapter 6.

Reference symbol	Reference value	Default
u_c	$\frac{\gamma_0}{\mu_0}$	1.23 m/s
u^*	$\frac{\kappa_0 E^*}{\varepsilon_r \rho \frac{q}{m}}$	0.260 m/s
t_c	$\frac{r^*}{u_c} = \frac{r^* \mu_0}{\gamma_0}$	$1.76 \cdot 10^{-8}$ s
t_e	$\frac{\varepsilon_0 \varepsilon_r}{\kappa_0}$	$7.77 \cdot 10^{-11}$ s
t_μ	$\frac{4\mu_0}{\rho c_p T_0}$	$2.73 \cdot 10^{-10}$ s
t_m	$\frac{h}{k_B T_0}$	$1.62 \cdot 10^{-13}$ s
Z^*	$\frac{2\gamma_0 \rho \frac{q}{m}}{\kappa_0 E^* {r^*}^3}$	$2.83 \cdot 10^{21}$ Pa·s/m^3

Table 6.2: Reference times, velocities and impedance used in this chapter 6.

because it generally depends also on the meniscus itself: its pinning angle, shape, orientation with the electrode, etc. Therefore, quantifying the range of voltages where solutions exist is hard for all geometric possibilities. In this section, we have restricted ourselves to the study of three different geometries that are idealized but can be described by a few parameters, thus more amenable to study. In particular:

- A meniscus sitting on an **infinite hyperboloidal tip** of apex radius of curvature R_c, where the extractor is a solid flat plate coincident with the origin of a prolate spheroidal coordinate system (same as in figure 3-3). The geometric degrees of freedom are $\Theta = \{\frac{r_0}{R_c}, \frac{d}{r_0}\}$. We define the ratio r_0/R_c as the slenderness parameter, and $\frac{d}{r_0} = \hat{d}$ is the ratio comparing the distance between the tip of the hyperboloid and the extracting electrode and the meniscus size. For simplicity we consider $d = 100$ μm, and we study the dependency on r_0 and R_c.

  An estimation of the electric field local to the meniscus can be found in [85]:

  $$E_{tip} = \frac{2V}{a\left(1 - w_0^2\right)\operatorname{arctanh}\left(w_0\right)} \tag{6.1}$$

  where w_0 and a are given by eqs. 3.3, 3.4, described in chapter 3. In terms of the definitions in figure 3-3 for this geometry, we use $\hat{z}_{sim} = 80$, $\hat{r}_{sim} = 40$, and $\hat{d}^* = \min\{40, \hat{d}\}$, and the values of w_0 and a/r_0 corresponding to specific r_0/R_c and $\hat{d}$ simulation case.

- A meniscus sitting on a conducting plate, or **the planar case** where $R_c \to \infty$. This case was studied by Coffman [21] and Gallud [42], and does not have any geometric degrees of freedom.

  The electric field E_{tip} in the planar case can be considered a special case, or a limit when $R_c \to \infty$ in eq. 3.4, that is $w_0 \to 0$ in eq. 6.1:

  $$E_{tip} = \frac{2V}{a} = \frac{V}{d} \tag{6.2}$$

  For this geometry, we use $\hat{d}^* = 20$, $\hat{r}_{sim} = 20$ in a similar way as [42].

- A meniscus on a **capillary** geometry with a flat solid extractor where the capillary radius equals the meniscus radius. This problem has only one geometric degree of freedom: $\Theta = \{\frac{d}{r_0}\}$, and it is chosen according to variations in r_0, knowing that we consider $d = 100$ μm also for the capillary case.

We use the equation suggested by Ryan [108] for the electric field:

$$E_{tip} = \frac{V}{A_1 r_0 \ln\left(\frac{4d}{r_0}\right)} \tag{6.3}$$

Where the constant $A_1 = 0.37$. In terms of the definitions in figure 3-4 for this geometry, we use $\hat{z}_{sim} = 80\hat{d}$, $\hat{r}_{sim} = \hat{d}$, where $\hat{d}$ varies depending on the specific simulation case. A flat plate is considered as an extractor, thus $\hat{r}_h = 0$.

This electric field local to the meniscus can be non-dimensionalized by the reference field E_c used in this thesis:

$$\hat{E}_{tip} = \frac{E_{tip}}{E_c} = \frac{E_{tip}}{\sqrt{\frac{4\gamma_0}{\varepsilon_0 r_0}}} \tag{6.4}$$

There are two families of static solutions depending on the external values of $\hat{E}_{tip}$. The limit values of each region depend on the geometry of the electrodes and the reservoir pressure $\hat{p}_r$.

- **Region I** is found at low fields, it starts at $\hat{E}_{tip} = 0$ and ends at $\hat{E}_{tip} = \hat{E}^{I}_{tip_{max}}$. Solutions are characterized by having equilibrium shapes that resemble a hyperboloid shape, that increase their volume at increasing values of $\hat{E}_{tip}$ and do not emit (see figure 6-1a). These solutions are well studied in the literature [7], and are not discussed in this thesis. Solutions at the critical field $\hat{E}^{I}_{tip_{max}}$ exhibit a turning point [7], above which no solutions of this branch exist.

- **Region II** is found at higher fields and is characterized by conical-shaped sharper solutions that emit ions. Region **II** starts at $\hat{E}_{tip} = \hat{E}_{tip_0}$, and ends at $\hat{E}_{tip} = \hat{E}^{II}_{tip_{max}}$, where region **III** begins and a turning point is also found. The solver is able to find solutions after the turning point in region **II**, but these are unstable. The instability of solutions in region **III** will be discussed in the upcoming sections of this chapter. The solutions in region **II** decrease their volume at increasing values of $\hat{E}_{tip}$ (see figure 6-1b).

  The model unveils a non-dimensional equation that describes the current emitted by menisci in this region, given the assumptions of negligible space charge ($Z/Z_{spch} \gg 1$), and meniscus sizes much greater than the emission region size $\hat{R} \gg 1$.

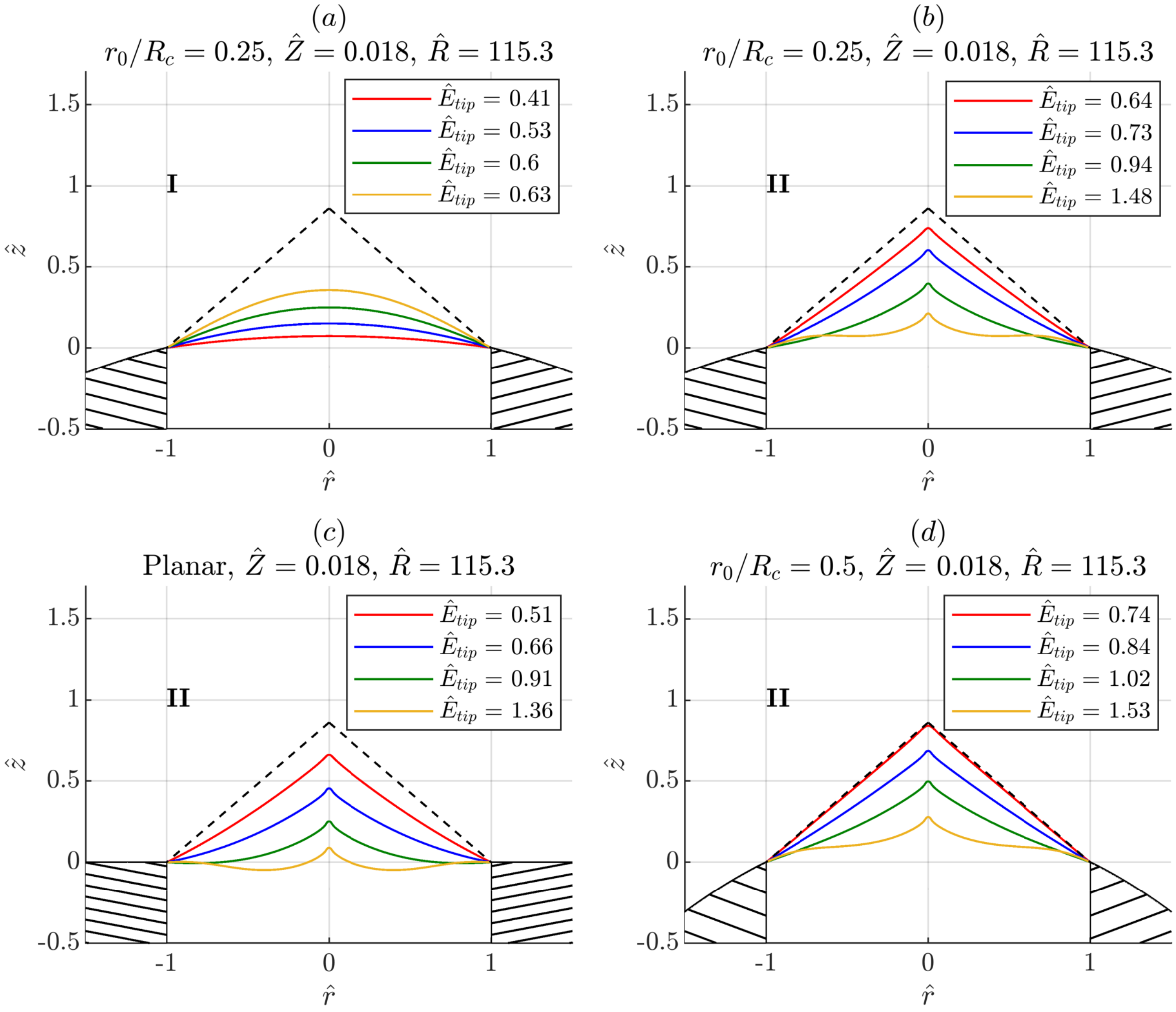

Figure 6-1: Solutions in region I non-emitting (a) and region II emitting (b) branches. Taylor cone is shown in dashed line for comparison. Solutions in region II for the planar case and a more slender case are shown in (c) and (d), respectively. We used a value of $\hat{d} = d/r_0 = 40$ for subfigures a), b) and d).

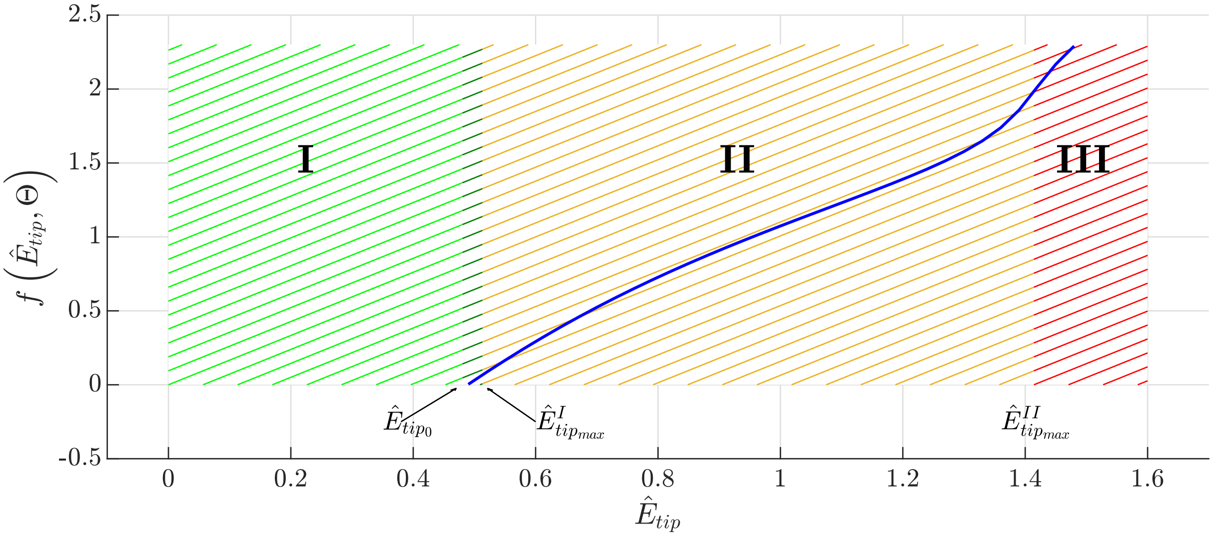

Figure 6-2: General diagram of solution existence. Two branches of solutions identified. Low field solutions in region I do not emit. High field solutions region II undergo emission characterized by a function $f\left(\hat{E}_{tip}, \Theta\right)$. The $f\left(\hat{E}_{tip}, \Theta\right)$ is shown in the figure for the case of planar geometry and $\hat{p}_r = 0$ in blue.

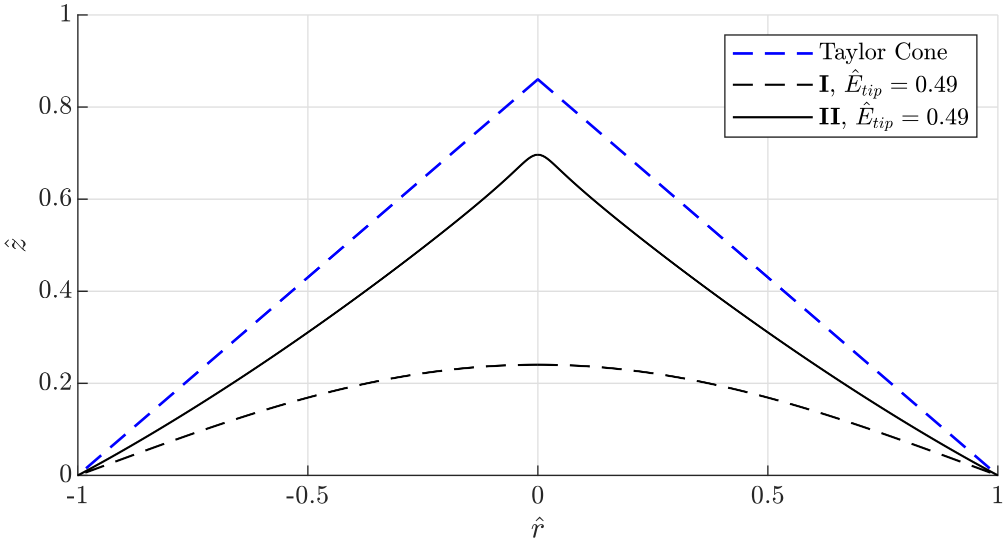

Figure 6-3: Equilibrium shapes in the overlap (hysteresis) region for the emitting case (solid) and non-emitting case (dotted). Taylor cone geometry is shown for cross-reference. Solutions plotted for the same conditions of $\hat{E}_{tip} = 0.49$. The simulations are obtained for the planar geometry, $\hat{R} = 115.3$, $\hat{Z} = 0.018$, $\hat{p}_r = 0$.

$$\hat{I} = \frac{f\left(\hat{E}_{tip}, \Theta\right) + \hat{p}_r}{\hat{Z}\hat{R}^{\frac{5}{2}}} \tag{6.5}$$

Where $f\left(\hat{E}_{tip}, \Theta\right)$ is a function that depends on the dimensionless electric field $\hat{E}_{tip}$, and a given geometry of the electrode Θ. This function contains information about the current that the meniscus emits as a function of the electric field that the meniscus *sees*, or that is amplified by the geometry of the electrode at the meniscus level. This function $f\left(\hat{E}_{tip}, \Theta\right)$ is plotted in figure 6-2, together with the limits of regions **I** (bright green in figure 6-2) and **II** (orange in figure 6-2) for the case of a planar substrate.

- **Overlap region**. In this overlap zone, solutions from region **I** or **II** are obtained depending on the initial guess provided to the solver. An example of the two equilibrium shapes obtained for the different solution branches is shown in figure 6-3. This hysteresis region is characterized by a current reduction when the electric field is decreased with a starting solution from the emitting region **II**. This hysteresis behavior is well documented experimentally for liquid metal ion sources [34], where the extinction voltage is typically smaller than the one needed for the onset of pure-ion emission. Current being very small at these field magnitudes undermines the relative importance of the hydrodynamic stress with respect to the surface tension and the electric stress. In this sense, the equilibrium shapes tend to resemble the canonical Taylor solution with negligible static pressure. The exact Taylor conical shape cannot generally be recovered with this setting due to the geometrical details of the electrodes, *except* when the electrodes are very close to a Taylor cone, and the boundary conditions of the potential correspond to those derived by Taylor [128]. We will see this fact in the next section 6.3.

6.3 The Zero-current solution, exact Taylor angle, and the slenderness effect on menisci

In this section, we explore the impact of deviating from the planar geometry and examine the equilibrium shapes in geometries with different slenderness at the reference point: the zero-current electric field, denoted as $\hat{E}_{tip_0}$. Figure 6-4 provides a visual representation of the general effect of increasing the slenderness of the geometry (or r_0/R_c), resulting in sharper equilibrium shapes. The dotted lines illustrate the electrode geometry, while the solid lines represent the equilibrium meniscus shape. It is notable that near the apex or emission region, the equilibrium shapes resemble Taylor cones. However, at the base of the meniscus, where the electric field is more influenced by the electrode geometry, the meniscus adopts a flatter structure depending on whether the angle between the electrode and the vertical axis ($\mathbf{z}$) is greater or smaller than the Taylor angle $\theta_T = 49.3°$. When $r_0/R_c = 0.5$ (blue line) configuration of extruded channel and electrode holding a meniscus is close to the Taylor angle, thus at extinction, the meniscus practically resembles the Taylor solution. This can also be seen in figure 6-1d.

Interestingly, when the electrode supporting the meniscus extends from the Taylor cone (black line in figure 6-4) and the boundary conditions of the domain at Γ_{EXT} precisely match those of the Taylor solution, the meniscus is practically an "exact" Taylor cone. These boundary conditions are:

$$\phi = a_0 Q_{1/2}\left(\cos\theta\right) r^{1/2} \tag{6.6}$$

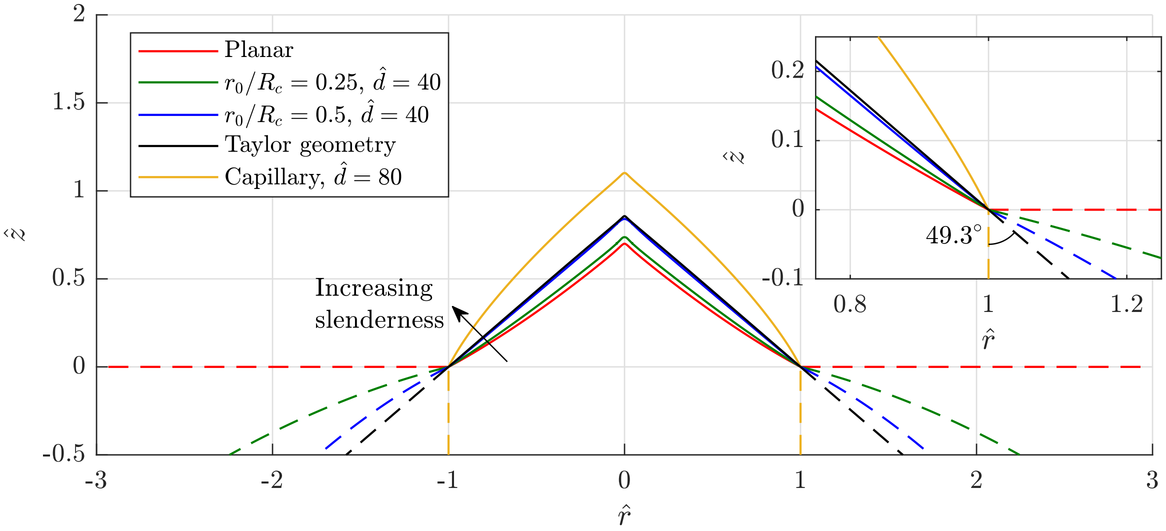

Figure 6-4: Equilibrium shapes at the Zero-current electric field for different slenderness parameter. Solid indicates meniscus shapes, and dashed indicates electrode shapes. Taylor cone geometry and equilibrium meniscus is shown in black color. Simulations done with $\hat{R} = 115.3$, $\hat{Z} = 0.018$, $\hat{p}_r = 0$.

Here, $Q_{1/2}$ represents the Legendre function of the second kind, θ is the polar angle in spherical coordinates with its origin at the apex of the Taylor conical solution, r is the distance to this apex and the constant a_0 is determined by [128]:

$$a_0^{-2} = 0.552\left(\varepsilon_0/\gamma\right)^{1/2} \tag{6.7}$$

It is important to note that the meniscus is not a perfect cone at the apex, as this would create a singular electric field. As the emission region commences, the "exact" Taylor cone exhibits a closed, nearly spherical cap that undergoes minimal evaporation.

At this point, readers may question how solutions of this nature can be obtained using our numerical approach, considering that the Taylor solution is inherently unstable [32]. In Chapter 9, we will delve into this matter and discover that solutions in close proximity to the Taylor cone are indeed unstable under infinitesimal arbitrary perturbations. However, the solutions presented here suggest the existence of static Taylor cone configurations with a closed interface at the apex.

6.4 The function $f\left(\hat{E}_{tip},\Theta\right)$ and its relation to the voltage-current behaviour

In this section, we present the shape of the function $f\left(\hat{E}_{tip},\Theta\right)$ for different geometries Θ as a function of a slenderness parameter r_0/R_c and $\hat{d}$. Since $\hat{E}_{tip}$ results from a mere amplification of the potential field applied to the emitter and extractor (see eqs. 6.1, 6.2, 6.3), describing $f\left(\hat{E}_{tip},\Theta\right)$ is analogous to describing the shapes of typical current-voltage curves (see eq. 6.5).

Figure 6-5a shows the shape of $f\left(\hat{E}_{tip},\Theta\right)$ for the planar meniscus, several values of r_0/R_c and the capillary case. The function $f\left(\hat{E}_{tip},\Theta\right)$ is generally monotonic, and grows sublinearly with $\hat{E}_{tip}$. We can see that when the radius of the meniscus starts becoming on the order of the radius of curvature of the tip, the function $f\left(\hat{E}_{tip},\Theta\right)$ experiences a shift towards higher $\hat{E}_{tip}$, and shortens the range of electric fields where $f\left(\hat{E}_{tip},\Theta\right)$ is defined. In the capillary case, $f\left(\hat{E}_{tip},\Theta\right)$ exhibits a more linear behaviour. The more slenderness r_0/R_c, the narrower the range where $f\left(\hat{E}_{tip},\Theta\right)$ exists.

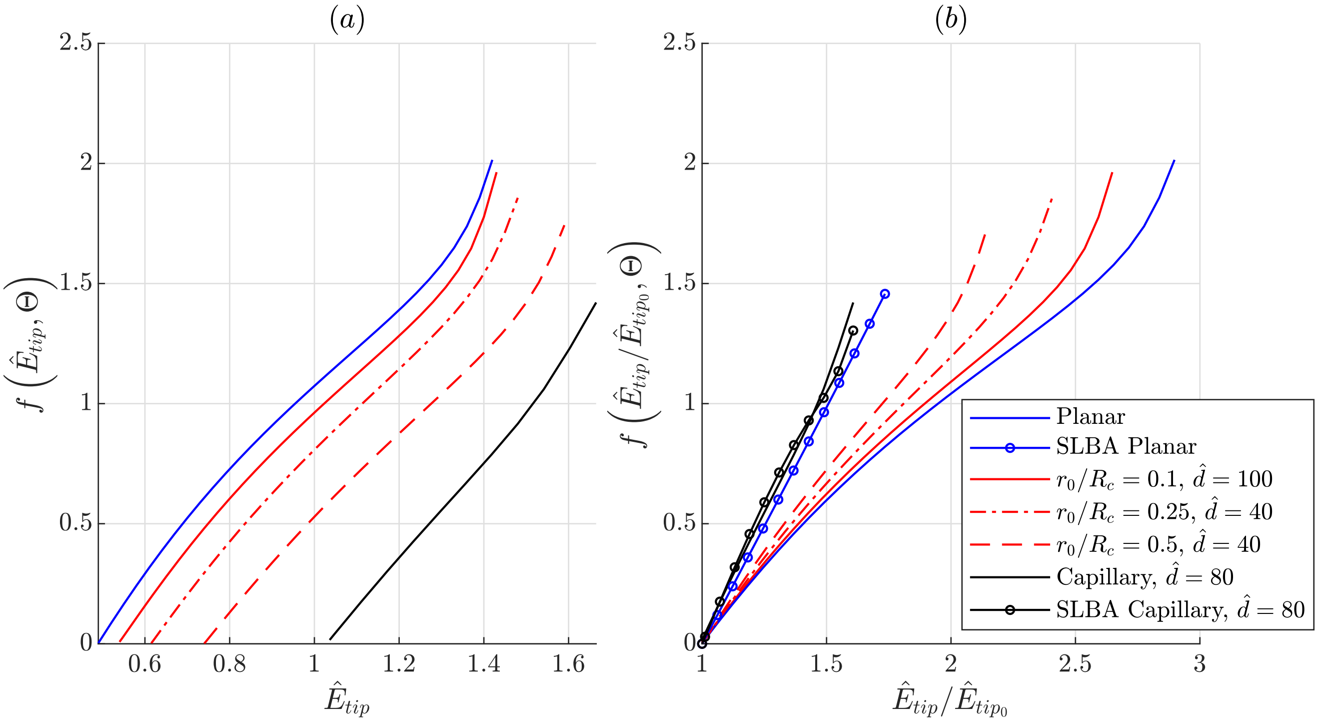

Figure 6-5: Expression of function $f\left(\hat{E}_{tip},\Theta\right)$ in a) for different slenderness parameters r_0/R_c and $\hat{d}$ in red, compared to the planar case in blue and the capillary case in black. The same function is shown in b) $f\left(\hat{E}_{tip}/\hat{E}_{tip_0},\Theta\right)$ as a function of the Zero-current field. Slender body approximations of $f\left(\hat{E}_{tip}/\hat{E}_{tip_0},\Theta\right)$ are shown with the markers for the planar (blue marker) and capillary (black marker) cases. Simulations done for $\hat{p}_r = 0$, results are independent from $\hat{Z}$ and $\hat{R}$ provided the assumptions described in the first paragraph of this beginning of this chapter.

Ideally, we would like to find a *universal* $f\left(\hat{E}_{tip}, \Theta\right)$ that only depends on the geometry of the electrodes as dictated by the amplification factors in eqs. 6.1, 6.2 and 6.3, or in other words, finding amplification factors that capture geometrical effects generally enough such that $f\left(\hat{E}_{tip}, \Theta\right) \approx f\left(\hat{E}_{tip}\right)$. However, this is not the case. This analysis reveals the limits of analytical approaches to these problems, and reinforces the usefulness of electrohydrodynamic simulations to accurately describe the amplified electric fields for each geometrical configurations.

6.4.1 The slender body approximation, and current-voltage curves relative to the zero-current voltage

One option that is typically used to better incorporate geometrical effects when expressing current-voltage behaviour is to express $f\left(\hat{E}_{tip}, \Theta\right)$ as a function of the non-dimensional extinction field, or the field of Zero-current. This is done for instance in the literature of liquid metal ion sources [82], that is $f\left(\hat{E}_{tip}/\hat{E}_{tip_0}, \Theta\right)$. From the results shown in figure 6-5b, we notice that this geometrical dependence is indeed better captured by including $\hat{E}_{tip_0}$: we can see that $f\left(\hat{E}_{tip}/\hat{E}_{tip_0}, \Theta\right) \sim f\left(\hat{E}_{tip}/\hat{E}_{tip_0}\right)$ for values of $r_0/R_c < 0.5$ and $\hat{E}_{tip}/\hat{E}_{tip_0} < 1.5$.

However, we need to mention that this $f\left(\hat{E}_{tip}/\hat{E}_{tip_0}, \Theta\right)$ is not more helpful to the designer than $f\left(\hat{E}_{tip}, \Theta\right)$, since it assumes that we know the Zero-current field $\hat{E}_{tip_0}$, which is generally dependent also on the geometry of the electrodes.

Additional insight can be obtained if we can compare our results for the geometrical dependence of the current-voltage behavior in terms of the theoretical framework developed for liquid metal ion sources [38]. In its most general form, a balance of forces that act axially (in the z direction) on the meniscus can be cast as:

$$g_E + g_\gamma + g_f = 0 \tag{6.8}$$

Where g_E is the axial electric stress force (including the space charge), g_γ is the surface tension force, and g_f is the hydrodynamic force. For simplicity, we assumed that $\hat{p}_r = 0$, and neglected the dynamic part of the fluid stress and recoil. We can get expressions for g_E, g_γ and g_f as:

$$g_E = \int_{\Gamma_M} \mathbf{z} \cdot \left(\tau_e^v - \tau_e^l\right) \cdot \mathbf{n} \, d\Gamma_M \tag{6.9}$$

$$g_\gamma = -2\pi r_0 \gamma \cos\varphi \tag{6.10}$$

$$g_f = -\frac{IZ\pi r_0^2}{\rho q/m} \tag{6.11}$$

Where the angle φ is the angle that the meniscus makes at the pinning point with respect to the $\mathbf{z}$ axis. At the point of Zero-current, the hydrodynamic force vanishes and we have:

$$g_{E_0} + g_{\gamma_0} = 0 \tag{6.12}$$

Subtracting 6.12 to 6.8 and factorizing we get:

$$g_{E_0}\left(\frac{g_E}{g_{E_0}} - 1\right) + g_{\gamma_0}\left(\frac{g_\gamma}{g_{\gamma_0}} - 1\right) + g_f = g_{\gamma_0}\left(\frac{g_\gamma}{g_{\gamma_0}} - \frac{g_E}{g_{E_0}}\right) + g_f = 0 \tag{6.13}$$

Substituting 6.9, 6.10 and 6.11 into 6.13 and simplifying, we can arrive at:

$$I = \frac{2\gamma\rho}{r_0 Z}\frac{q}{m}\cos\varphi_0\left(\frac{\int_{\Gamma_M}\mathbf{z}\cdot\left(\tau_e^v - \tau_e^l\right)\cdot\mathbf{n}\,d\Gamma_M}{\int_{\Gamma_M}\mathbf{z}\cdot\left(\tau_{e_0}^v - \tau_{e_0}^l\right)\cdot\mathbf{n}\,d\Gamma_M} - \frac{\cos\varphi}{\cos\varphi_0}\right) \tag{6.14}$$

Now, we can make further assumptions that 1) the space charge makes negligible modifications to the electric field stress, 2) the meniscus sits on a slender body[1], and 3) the meniscus is equipotential ($\tau_e^l \ll \tau_e^v$). Under such circumstances, according to Taylor and Van Dyke [129][2], the ratio of integrals depends very weakly on the details of the meniscus. A brief outline of Van Dyke's argument [129] is provided as follows. For axially-symmetric slender bodies of maximum radial dimension a, length L, distance to an extracting plate h and radial shape $R(x)$ (see figure 6-6), the total electric force F acting on the body is independent from $R(x)$ when $L \gg a$ and $L \sim h$, it yields:

$$F \approx \frac{4\pi\varepsilon_0 V^2}{\left(2\ln\left(L/a\right)\right)^2}\ln\frac{\left(2h+L\right)^2}{4h\left(h+L\right)}\left(1 + O\left(\frac{1}{\ln\left(L/a\right)}\right)\right) \tag{6.15}$$

---

[1] The slender body approximation holds when the axial dimension of the needle or capillary emitter (L in figure 6-6) is much larger than the radial dimension (a in figure 6-6). In this context, the slender body concept is the same as in aerodynamic theory, where the thickness of an aerodynamic profile is much smaller than its chord. For a fixed emitter length in this thesis, this occurs when $r_0/R_c \approx 1$, namely when the meniscus radius is on the order of the curvature radius of the emitter. The most slender case considered in this thesis is the capillary.

[2] The paper is originally written by Taylor, but contains an annex describing the slender body approximation by Van Dyke.

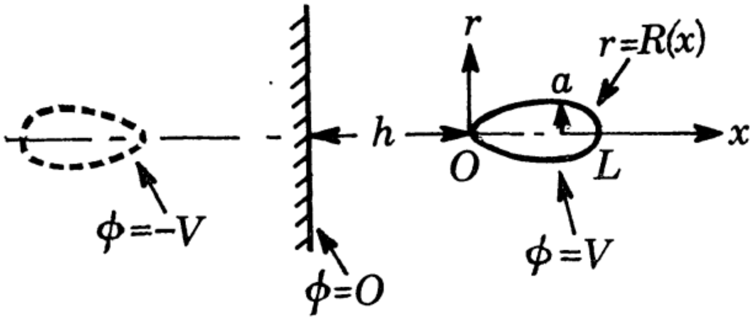

Figure 6-6: Geometry of the slender body considered by Van Dyke [129].

where the dependency on $R(x)$ is embedded in the term $O\left(\frac{1}{\ln(L/a)}\right)$.

Eq. 6.15 corresponds to eq. (A 16b) in [129], but we have added the extra term $4\pi\varepsilon_0$ to make eq. 6.15 dimensionally consistent with the international system units. In other words:

$$F \approx \frac{4\pi\varepsilon_0 V^2}{k_V} \tag{6.16}$$

where k_V is a dimensionless constant [38] that depends on geometrical parameters. This force has contributions for both the meniscus (Γ_M), and the emitter part (Γ_D^v). Let's say the emitter is a capillary. For a perfectly conducting (equipotential) meniscus and capillary this yields:

$$F = \int_{\Gamma_M} \mathbf{z} \cdot \tau_e^v \cdot \mathbf{n}\, d\Gamma_M + \int_{\Gamma_D^v} \mathbf{z} \cdot \tau_e^v \cdot \mathbf{n}\, d\Gamma_D^v \tag{6.17}$$

We can substitute eq. 6.17 in 6.16 to yield:

$$\int_{\Gamma_M} \mathbf{z} \cdot \tau_e^v \cdot \mathbf{n}\, d\Gamma_M \approx \frac{4\pi\varepsilon_0 V^2}{k_V} - \int_{\Gamma_D^v} \mathbf{z} \cdot \tau_e^v \cdot \mathbf{n}\, d\Gamma_D^v \tag{6.18}$$

The last term in the right-hand side of eqs. 6.17 and 6.18 only contains the back part of the emitter, because, for a conductive capillary, the side integral vanishes since the electric stress tensor is perpendicular to the axial vector **z**. If we assume that this part of the integral is negligible or proportional to $\varepsilon_0 V^2$, then:

$$\int_{\Gamma_M} \mathbf{z} \cdot \tau_e^v \cdot \mathbf{n}\, d\Gamma_M \approx \frac{4\pi\varepsilon_0 V^2}{k'_V} \tag{6.19}$$

where k'_V is another constant. The validity of eqs. 6.19, 6.16 and 6.15 is subject to the slender body approximation assumption. Under this circumstance, we can substitute eq. 6.19 in the ratio of integrals in 6.14:

$$\frac{\int_{\Gamma_M} \mathbf{z} \cdot \left(\tau_e^v - \tau_e^l\right) \cdot \mathbf{n}\, d\Gamma_M}{\int_{\Gamma_M} \mathbf{z} \cdot \left(\tau_{e_0}^v - \tau_{e_0}^l\right) \cdot \mathbf{n}\, d\Gamma_M} \approx \frac{\int_{\Gamma_M} \mathbf{z} \cdot \tau_e^v \cdot \mathbf{n}\, d\Gamma_M}{\int_{\Gamma_M} \mathbf{z} \cdot \tau_{e_0}^v \cdot \mathbf{n}\, d\Gamma_M} \approx \left(\frac{V}{V_0}\right)^2 = \left(\frac{\hat{E}_{tip}}{\hat{E}_{tip_0}}\right)^2 \tag{6.20}$$

to yield:

$$I_{SLBA} = \frac{2\gamma\rho}{r_0 Z}\frac{q}{m}\cos\varphi_0\left(\left(\frac{V}{V_0}\right)^2 - \frac{\cos\varphi}{\cos\varphi_0}\right) \tag{6.21}$$

where the subscript SLBA reads as *Slender Body Approximation*.

It may be interesting to see that when we get a dimensional form of the equation 6.5 coming from our simulation framework, in the case of negligible reservoir pressure $\hat{p}_r = 0$, we get:

$$I = \frac{2\gamma\rho}{r_0 Z}\frac{q}{m} f\left(\frac{\hat{E}_{tip}}{\hat{E}_{tip_0}}, \Theta\right) \tag{6.22}$$

We can equate $I = I_{SLBA}$ and get an explicit equation for $f\left(\frac{\hat{E}_{tip}}{\hat{E}_{tip_0}}, \Theta\right)_{SLBA}$ as:

$$f\left(\frac{\hat{E}_{tip}}{\hat{E}_{tip_0}}, \Theta\right)_{SLBA} = \cos\varphi_0\left(\left(\frac{\hat{E}_{tip}}{\hat{E}_{tip_0}}\right)^2 - \frac{\cos\varphi}{\cos\varphi_0}\right) = \cos\varphi_0\left(\left(\frac{V}{V_0}\right)^2 - \frac{\cos\varphi}{\cos\varphi_0}\right) \tag{6.23}$$

We can test how well 6.23 works in describing the current-voltage potential in figure 6-5b. The approximated $f\left(\frac{\hat{E}_{tip}}{\hat{E}_{tip_0}}, \Theta\right)_{SLBA}$ is superimposed to the simulated f for the capillary and planar cases. The approximated $f\left(\frac{\hat{E}_{tip}}{\hat{E}_{tip_0}}, \Theta\right)_{SLBA}$ is shown with the circle markers. We can clearly see that it only becomes very close to the simulated one in the most slender body that we can imagine: the capillary case. This is observed despite three limitations: 1) the fact that the slender body approximation has been derived for a finite body ($L \sim h$ in figure 6-6); 2) the boundary conditions considered for the simulations $\mathbf{E} \cdot \mathbf{n} = 0$ on Γ_{EXT} seem to correspond better to a semi-infinite capillary ($L \to \infty$ in figure 6-6) and 3) Van Dyke's slender body is "sufficiently smooth", which does not correspond to the possible sharp angle conditions that could arise in the contact line of the meniscus with the capillary at $r \approx r_0$. For the planar case, it yields an approximation substantially far from the simulated $f\left(\frac{\hat{E}_{tip}}{\hat{E}_{tip_0}}, \Theta\right)$

(close to 100% error).

We believe then that the SLBA is not a good fit for $f\left(\frac{\hat{E}_{tip}}{\hat{E}_{tip_0}}, \Theta\right)$ simulated in this problem. In fact, it can be inferred from direct transmission electron beam observations [101] that liquid metal ion sources form menisci with radii $r_0 \approx R_c$ where the slender body approximation may apply. In our case, we suggest departing from this approximation due to the particular small range of menisci sizes that are believed to enhance the stability of the pure-ion regime ($r_0/R_c < 1$). Some evidence will be seen in direct observations of quenched meniscus in chapter 10.

6.4.2 Connection to liquid metal ion source theory

Equation 6.21 bears a striking resemblance to the equation derived by Mair for liquid metal ion sources with impedance drag (see equation 12 in [83]):

$$I_{Mair} = \frac{3\pi\left(2q/m\right)^{1/2} r_0 \gamma \cos\varphi}{2V^{1/2}} \left(\left(\frac{V}{V_0}\right)^2 - 1\right)\left(1 + \frac{3}{4}\frac{Z}{Z_{spch}}\right)^{-1} \tag{6.24}$$

Where Z_{spch} is the same as the characteristic space charge introduced in chapter 5:

$$Z_{spch} = \frac{\rho}{\pi r_0^2}\sqrt{\frac{2q}{m}V} \tag{6.25}$$

If we consider the limit when the hydraulic impedance is high $Z \gg \frac{4}{3}Z_{spch}$, the similarity becomes more apparent:

$$I_{Mair} \approx \frac{2\gamma\rho}{r_0 Z}\frac{q}{m}\cos\varphi_0\left(\left(\frac{V}{V_0}\right)^2 - 1\right) \tag{6.26}$$

This equation is equivalent to the slender body approximation equation I_{SLBA} (eq. 6.21) under the condition that the contact line angle remains constant ($\varphi \approx \varphi_0$). Mair typically assumes this angle to be the Taylor angle $\varphi_0 = 49.3°$.

It's not surprising that the dimensional equation we obtain in this thesis, in the case where $\hat{p}_r = 0$ (eq. 6.22), is very similar to I_{Mair}.

The key difference lies in the pronounced "sucking-in" effect that the hydraulic impedance has on the equilibrium shapes, as well as the absence of a slender body assumption. These two factors are not accounted for in I_{Mair}, but they are captured by our function $f\left(\frac{\hat{E}_{tip}}{\hat{E}_{tip_0}}, \Theta\right)$.

We believe that the similarities between the two equations are a direct consequence of the fact that the significant differences between ILIS and LMIS, such as six orders of magnitude difference in electrical conductivity and one order of magnitude difference in E^*, do not play a substantial role in the emitted current according to the electrohydrodynamic model implemented in this thesis.

Based on the information given in this section, we can conclude that both ILIS and LMIS can be explained using **the same global force arguments**. However, the simplifications commonly made for LMIS, such as the slender body approximation and constant contact angle, are not generally applicable to ILIS. Instead, we could utilize the simulated function $f\left(\frac{\hat{E}_{tip}}{\hat{E}_{tip_0}}, \Theta\right)$ to account for the non-slenderness effect and deviations from the Taylor solution.

6.5 The dimensionless current $\hat{I}$

From eq. 6.5 we can see that the effect of changing the hydraulic impedance parameter $\hat{Z}$ is a mere scaling of $f\left(\hat{E}_{tip}, \Theta\right)$. The inverse relationship between current and impedance was stated by Coffman's simulation work [21] and generalized to a broader spectrum of geometries and electric fields in this thesis by referencing to $f\left(\hat{E}_{tip}, \Theta\right)$. This inverse proportionality scaling has not been derived with a rigorous analytical approach of the problem. This is a very interesting task, but very challenging to do due to the vast parameter dimensionality of the problem solved in this thesis. In fact, such observation comes from repeated simulations of menisci with a wide range of $\hat{Z}, \hat{R}^{5/2}$ and $\hat{p}_r$. It is then customary to show the numerical validity of these scalings.

Effect of varying $\hat{Z}\hat{R}^{5/2}$

In figure 6-7, we can observe simulated results on several values of $\hat{Z}$ and constant $\hat{R}$ for values of $r_0/R_c = 0.05$ and $\hat{d} = 100$ in subfigures 6-7 1a) and 1b). Subfigures 6-7 2a) and 2b) show the same plots for menisci involving two different dimensional radii of 2.5 μm ($\hat{R} = 115.3$, $\hat{d} = 40$) and 5 μm ($\hat{R} = 230.4$, $\hat{d} = 20$) but same $r_0/R_c = 0.5$. On the left (subfigures a), we have plotted the value of the non-dimensional current as a function of $\hat{E}_{tip}$. We can observe how the current decreases when increasing the dimensionless impedance $\hat{Z}$, as expected. When plotting the scaled dimensionless current as $\hat{I}\hat{Z}\hat{R}^{5/2} - \hat{p}_r = f\left(\hat{E}_{tip}, \Theta\right)$ (subfigures b), we can observe how the curves practically collapse as discussed. The case described in subfigures 2a) and 2b) is

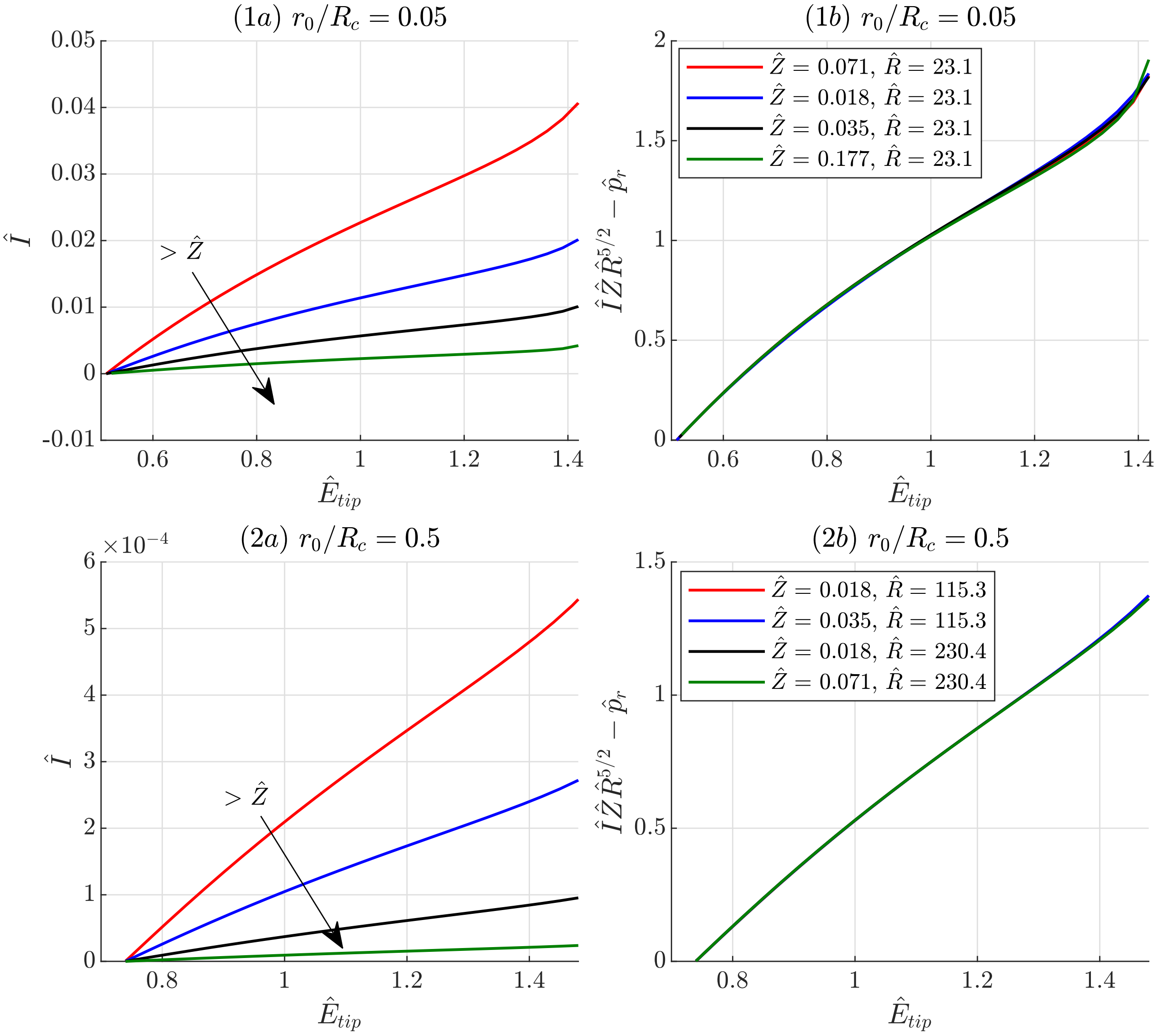

Figure 6-7: Effect of varying $\hat{Z}R^{5/2}$ for different slenderness parameters. Subfigures 1 on top have a fixed meniscus radius $\hat{R} = 23.06$ with a slenderness of $r_0/R_c = 0.05$, a fixed meniscus radius of curvature R_c, and $\hat{d} = 200$. Subfigures 2 on the bottom have alternative radii and dimensionless distances of $\hat{R} = 115.3$, $\hat{d} = 40$ and $\hat{R} = 230.4$, $\hat{d} = 20$ with a tip curvature radius that yields the same slenderness parameter of $r_0/R_c = 0.5$.

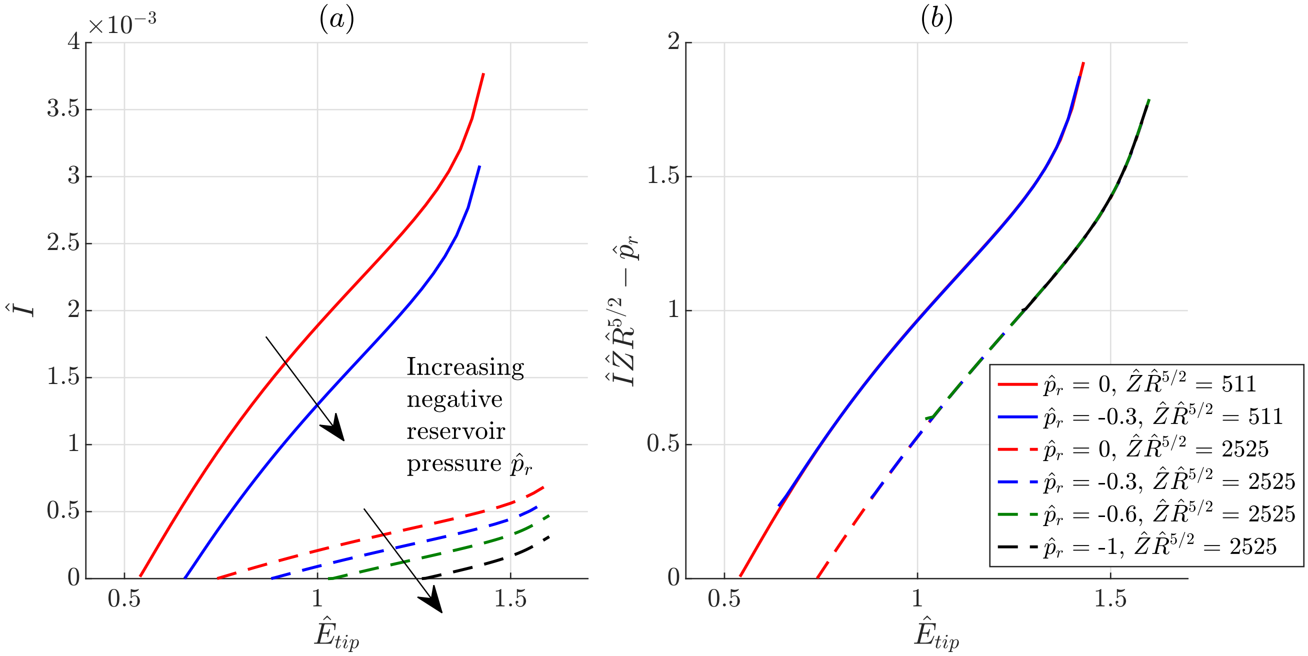

Figure 6-8: Dimensionless current behavior at different negative Laplace pressures for two different slenderness parameters in a). Subfigure b) shows the same curves plotted in a) collapsing when considering the scaling of $f\left(\hat{E}_{tip}, \Theta\right)$ instead. Solid curves correspond to $r_0/R_c = 0.1$ and $\hat{d} = 100$, dashed curves correspond to $r_0/R_c = 0.5$ and $\hat{d} = 40$.

especially interesting since the dimensionless value of $\hat{d}$ changes for the two radii simulated, yet the value of $f\left(\hat{E}_{tip}, \Theta\right)$ is barely changed, as seen by the collapse of the curves in 2b). This indicates that the function $f\left(\hat{E}_{tip}, \Theta\right)$ is mostly affected by r_0/R_c through Θ, and the dependency on $\hat{d}$ is less important, and well captured by the reference electric field $\hat{E}_{tip}$.

Effect of a negative pressure $\hat{p}_r$

Passive electrospray ion sources usually operate with slight negative reservoir pressure. This is most apparent in porous emitters, where in the case of semisaturation, the ionic liquid wets the porous material forming negative curvatures in the pores. In the case of perfect wetting material, we may infer a negative reservoir pressure equal to the capillary pressure of the pore radius $p_r = -\frac{2\gamma}{r_0}$. The effect of negative reservoir pressure (or Laplace pressure [27]) on the dimensionless current is a translation in the vertical direction, as observed in figure 6-8a. The effect of this shift is increasing the Zero-current dimensionless field $\hat{E}_{tip_0}$ and shortening the range of $\hat{E}_{tip}$ where the function $f\left(\hat{E}_{tip}, \Theta\right)$ is defined. In the limit case where the suction is equal to the perfect wetting case, the range where solutions exist is substantially reduced. When instead of plotting the current, we plot the function $f\left(\hat{E}_{tip}, \Theta\right) = \hat{I}\hat{Z}\hat{R}^{5/2} - \hat{p}_r$ at the different reservoir pressures $\hat{p}_r$ in figure 6-8, they collapse to the same curve at the corresponding slenderness parameter.

6.6 Upper field turning points

Experimentally, it is observed that when the electric field $\hat{E}_{tip}$ is increased further, pure-ion menisci either incur erratic behavior, or they **bifurcate** into two or more emission sites. It is reasonable to think that either outcome is a byproduct of an instability of the meniscus.

The standard method to assess the linear stability of a general steady flow involving capillary phenomena entails subjecting the flow to small arbitrary linear perturbations and examining the growth rate of these perturbations [60]. If any perturbation shows positive growth, the flow can be considered generally unstable since there exists at least one perturbation that will not be dampened by the flow's natural response to infinitesimal disturbances. Conversely, if all arbitrary perturbations are damped or exhibit negative growth rates, the flow can be deemed stable under small infinitesimal perturbations.

Selecting an appropriate perturbation is not a trivial task. For example, deforming the meniscus through a small bump at the apex and observing its time evolution would not be sufficiently general. Depending on the shape of the bump, the equilibrium shape may or may not return. To consider truly arbitrary perturbations, which encompass all possible shapes of bumps compatible with the function space employed in our numerical approach, often requires solving computationally expensive eigenvalue problems.

Nevertheless, in the realm of electrified droplets, it is well-known that equilibrium shapes of *static* capillary systems exhibiting "turning points" can indicate marginal stability, without the need for computing the eigenvalue decomposition of the meniscus dynamics under small perturbations.

Turning solutions in static electrified droplets can be observed, for instance, in equilibrium shapes that closely resemble the marginally stable position when varying a defining parameter (e.g., the externally applied potential) while featuring a small elongation proportional to the neutrally stable equilibrium shape in cases where the volume is fixed [7, 4, 5, 6]. In these studies, the elongation is manifested in a reverse direction aspect ratio growth of the equilibrium shapes. In other static capillary systems, such as liquid bridges, turning points manifest when changes in volume trends occur in response to variations in pressure [11] (e.g, $dV/dp = 0$).

Our problem involves a free volume, and is nearly hydrostatic, with significant flow movement primarily occurring at the apex, a narrow region of the meniscus domain. Even though the conditions of the menisci under study in this thesis are not fixed volume or fully static, we observe equilibrium shapes that do exhibit these characteristic turning points of the fully static capillary systems as we approach $\hat{E}_{tip}$ to $\hat{E}^{II}_{tip_{max}}$. As we have seen previously, equilibrium shapes in region **II** reduce their volume and aspect ratio when $\hat{E}_{tip}$ is increased. At some value of $\hat{E}_{tip}$, the trend reverses, and solutions start increasing their volume and aspect ratio. This phenomenon is shown in figure 6-9. The point where this happens marks the turning point, $\hat{E}^{II}_{tip_{max}}$, and the beginning of region **III**. In chapter 9, we will demonstrate that the equilibrium shapes obtained after these turning points in region **III** also yield menisci that are unstable under small perturbations. For the planar geometry, it is observed that the turning point occurs when [42]:

$$\frac{1}{2}\varepsilon_0 E_0^2 = 2\left(\frac{2\gamma}{r_0}\right) \tag{6.27}$$

where $E_0 = E_{tip} = V/d$. Equation 6.27 tells us that pure-ion emission in this regime cannot be sustained when the electric pressure created by the electrodes local to the meniscus anchoring location that holds the meniscus is greater than two times the capillary pressure of a sphere of the same radius as the meniscus.

This result is very weakly dependent on the hydraulic impedance Z and external reservoir pressure p_r.

For other geometries, equation 6.27 can be generalized to:

$$\frac{1}{2}\varepsilon_0 E_{tip}^2 = b_0\left(\frac{2\gamma}{r_0}\right) \tag{6.28}$$

which, for the prolate spheroidal geometry simulated cases in this thesis, b_0 is a constant very close to 2 ($b_0 \approx 2 - 2.25$), but certainly weakly dependent on the geometry of the electrodes, especially when $r_0 \sim R_c$. In dimensionless form, eq. 6.28

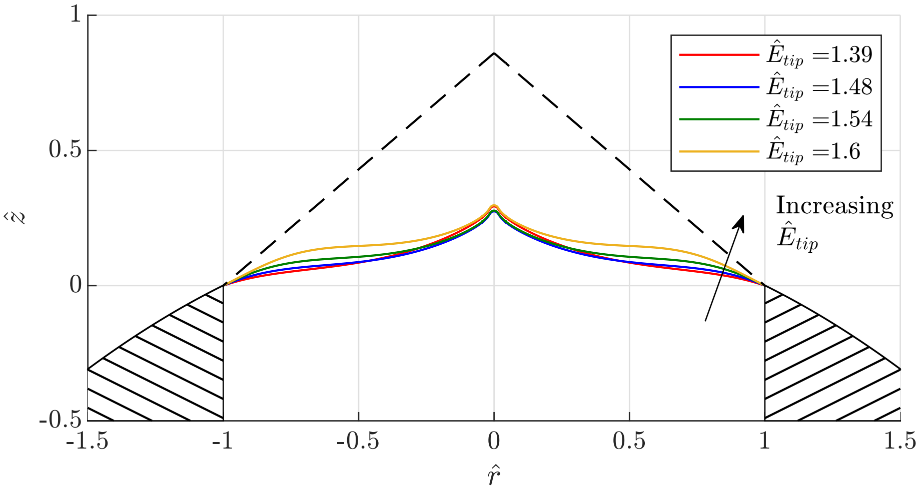

Figure 6-9: Equilibrium shapes of the simulated meniscus after the turning point. Shapes develop bumps near the contact line and increase their aspect ratio. Taylor cone is shown in dashed black. Simulated parameters are $\hat{R} = 115.3$, $\hat{Z} = 0.0353$ and $\hat{p}_r = 0$. Meniscus slenderness parameter is $r_0/R_c = 0.5$, and dimensionless distance $\hat{d} = 40$.

reads:

$$\hat{E}_{tip} = \hat{E}^{II}_{tip_{max}} = \sqrt{b_0} \tag{6.29}$$

In the planar case eq. 6.29 reads, $\hat{E}^{II}_{tip_{max}} = \sqrt{2} = 1.414$.

Figure 6-10 shows an additional example of this turning point behavior for four different menisci in a capillary setting, with three dimensionless distances and diverse reservoir pressures. We can see the aspect ratio of the equilibrium shapes at increasing values of dimensionless field in the emitting region **II** decreasing, until reaching the turning point, where the solutions start elongating. The value of the dimensionless field where the turning point happens $\hat{E}^{II}_{tip_{max}}$ does not change for the parameters tested as a function of $\hat{p}_r$ and it is close to $\sqrt{2}$, although the equilibrium shapes change slightly at higher $\hat{p}_r$. As seen in the previous section, higher $\hat{p}_r$ usually expands the region of dimensionless voltages where solutions can be found, but only at lower voltages. This can also be seen in the dashed line of figure 6-10.

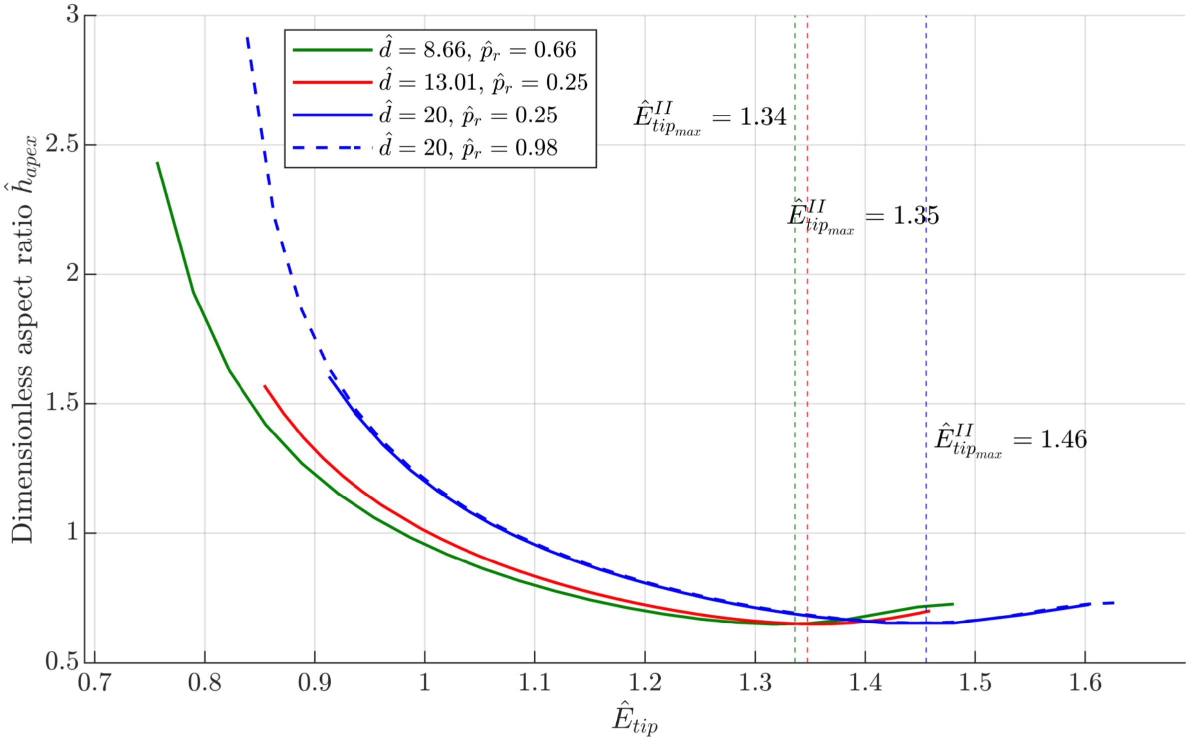

Figure 6-10: Aspect ratio vs. external field $\hat{E}_{tip}$ for capillary geometry at different dimensionless distances $\hat{d}$ and reservoir pressures $\hat{p}_r$. The dimensionless aspect ratio $\hat{h}_{apex}$ is the dimensionless height $\hat{h} = h/r_0$ of the meniscus apex. The value of the turning point corresponds to the minimum of this curve at $\hat{E}^{II}_{tip_{max}}$. This value is depicted with dashed lines. Simulation parameters are $\hat{R} = 69.15$ and $\hat{Z} = 0.177$.

6.7 The dominance of the upstream conditions of the flow and universality hypothesis: application to the stable cone-jet regime

To the author of this thesis' opinion, the rather simple result of equation 6.5 could be subject to some reflection. What the equation 6.5 suggests is that in the regime that we are studying (flow limited by impedance, negligible space charge), there may be *only one* dimensionless internal pressure that the meniscus can have when emitting in steady state for a given geometry and applied voltage, this meniscus pressure is:

$$\hat{p} = \hat{p}_r - \hat{I}\hat{Z}\hat{R}^{5/2} = -f\left(\hat{E}_{tip}, \Theta\right) \tag{6.30}$$

If such a result is independent of any emission region transport parameter as seen in chapter 5, does it really matter if we have a closed interface such as that in the pure-ion regime or a jet issued from the apex? Is it possible that this unique pressure could be a more general result from electrified menisci emitting in confined geometries limited by their impedance (e.g, including a stable cone-jet)? If this were true, what would happen when we have for example a flow rate controlled by a syringe pump? The equation suggests that in that case, the reservoir pressure, which contains the reaction pressure that the flow makes with the syringe pump, will adapt itself in such a way that $\hat{p}_r = f\left(\hat{E}_{tip}, \Theta\right) + \hat{I}\hat{Z}\hat{R}^{5/2}$. In this regard, if the pressure in 6.30 is a general result describing the operation regime of Taylor cones in a steady state limited by their impedance, then it may be reasonable to think that such Taylor cone will be also subject to the turning point described earlier at higher fields.

Even more interesting: since eq. 6.5 also gives us a closed expression for the flow rate as a function of $f\left(\hat{E}_{tip}, \Theta\right)$,

$$Q = \frac{2\gamma}{r_0 Z}\left(f\left(\hat{E}_{tip}, \Theta\right) + \frac{p_r r_0}{2\gamma}\right) \tag{6.31}$$

we could insert this expression in the well-established law derived by Fernández de la Mora (FdM) and Loscertales [33] to get an alternative expression for the current in the cone-jet mode in the regime that we are studying, where the flow rate is not prescribed by any controller but by a reservoir pressure p_r:

$$I = f_{FdM}(\varepsilon)\sqrt{\frac{\gamma\kappa Q}{\varepsilon_r}} = f_{FdM}(\varepsilon)\sqrt{\frac{2\gamma^2\kappa}{r_0 Z\varepsilon_r}\left(f\left(\hat{E}_{tip}, \Theta\right) + \frac{p_r r_0}{2\gamma}\right)} \tag{6.32}$$

The stable cone-jet then emerges as an interesting tool to examine the nature of the turning point, and the nature of function $f\left(\hat{E}_{tip}, \Theta\right)$ affecting the flow rate Q and the current I as shown in eqs. 6.31 and 6.32, respectively. We believe that the turning point nature and the flow rate equation (eq. 6.31) are applicable to both systems: the pure-ion and the cone-jet pure droplet regime.

In chapter 7, we will describe the experimental efforts that we did and the comparisons that we made with existing literature to test this hypothesis with the cone-jet regime. To provide advanced insight to the reader, we will show that under certain conditions, namely those considered in this thesis (axially symmetric menisci, and flow dominated by the impedance) **this upper field turning point could correspond to a meniscus bifurcation** in the cone-jet mode.

Chapter 7

Experiments with stable cone-jets, the flow rate-voltage behavior and meniscus bifurcation

In this chapter, we compare our simulation framework with existent literature results, and we perform self-made experiments to test the hypotheses in chapter 6 with regard to the stable cone-jet. In particular:

1. For the flow rate equation (eq. 6.31), we find existent published data that measure this flow rate as a function of the voltage and provide sufficient detail of the geometry that we can simulate in our framework. We did not have accurate enough instrumentation to test the flow rate in a self-made experiment. Results are reported in section 7.1.

2. For testing the turning point phenomenon, we do experimental efforts with an electrospray cone-jet of high hydraulic impedance, where the jet diameter is much smaller than the meniscus size. According to our simulation framework, the turning point is practically independent of the flow rate and the electrical conductivity, therefore, we did not measure their specific values. Results are reported in section 7.2.

7.1 A comparison with stable cone-jets: the function $f\left(\hat{E}_{tip}, \Theta\right)$

In this section we simulate the capillary setup cone-jet electrospray experimented by the works of Smith [115] and Ryan [108]. The geometrical setup is the same for the two works and can be easily represented by the diagram in figure 3-4. The experimental geometrical parameters reported are $d = 3$ mm, $r_h = 3$ mm, $z_{el} = 3$ mm. The simulated parameters are $\frac{r_{sim}}{r_h} = 6$, $\frac{z_{up}}{r_h} = 6$, $\frac{z_{sim}}{r_h} = 7$. The dimensionless parameters change, since the outer radius of the capillary r_0 changes. The lengths of the dimensionless domain are extended accordingly, for example $\hat{r}_{sim} = \frac{r_{sim}}{r_0} = \frac{r_{sim}}{r_h}\frac{r_h}{r_0}$. The main idea is to obtain the function $f\left(\hat{E}_{tip}, \Theta\right)$ using our simulation framework, and then check if our simulated $f\left(\hat{E}_{tip}, \Theta\right)$ fulfills eq. 6.31:

$$f\left(\hat{E}_{tip}, \Theta\right) = \frac{r_0 Z}{2\gamma} Q - \frac{p_r r_0}{2\gamma} \tag{7.1}$$

Where $Q = Q\left(\hat{E}_{tip}, \Theta\right)$ is the experimental data that Smith [115] and Ryan [108] report. Unfortunately, the reported data do not include the value of p_r. However, since p_r is constant (it is just a shift in the vertical direction, as shown in figure 6-8), we can instead compare the slopes of $f\left(\hat{E}_{tip}, \Theta\right)$, with the advantage that in the capillary case these slopes are practically constant (see figure 6-5). Differentiating in the left-hand side and right-hand side of eq. 7.1 and using the chain rule we have the following:

$$\frac{\partial f\left(\hat{E}_{tip}, \Theta\right)}{\partial \hat{E}_{tip}} = \frac{r_0 Z}{2\gamma} \frac{\partial Q}{\partial V} \frac{\partial V}{\partial \hat{E}_{tip}} \tag{7.2}$$

Note that in this case, the geometry has two additional degrees of freedom included in the set of parameters Θ: the dimensionless radius r_h and thickness z_{el} of the aperture extruded in the extractor plate ($\Theta = \frac{d}{r_0}, \frac{r_h}{r_0}, \frac{z_{el}}{r_0}$). We can get $\frac{\partial V}{\partial \hat{E}_{tip}}$ from the amplification factor in eq. 6.3:

$$\frac{\partial V}{\partial \hat{E}_{tip}} = A_1 r_0 \ln\left(\frac{4d}{r_0}\right) \sqrt{\frac{4\gamma_0}{r_0 \varepsilon_0}} \tag{7.3}$$

And we can substitute in eq. 7.2 to yield a final expression comparing the slopes of the simulated and experimental data:

$$\frac{\partial f\left(\hat{E}_{tip},\Theta\right)}{\partial \hat{E}_{tip}} = \frac{A_1 Z r_0^{3/2}}{\sqrt{\gamma\varepsilon_0}} \ln\left(\frac{4d}{r_0}\right)\frac{\partial Q}{\partial V} \tag{7.4}$$

We show the results from our analysis in table 7.1. We can observe that our simulation model is able to predict the sensitivity with good accuracy (less than 25%). For the simulations, we use [EMIm][BF$_4$] with the benchmark parameters described in section 6.1. It is worth mentioning that this analysis is significantly flawed, since we could not control the experimental results presented in table 7.1. This is especially important since the authors in [108] and [115] do not report flow rate error bounds, nor the exact meniscus radius r_0, which affects up to the 3/2 power the sensitivity of function $f\left(\hat{E}_{tip},\Theta\right)$, according to eq. 7.4. It is is assumed here that the meniscus pins at the outer radius of the emitter. A more controlled updated version of this experiment is needed to ensure the validity of this comparison.

Reference	Liquid	r_0 (mm)	γ (N/m)	Z (Pa s/m^3)	Experimental $\partial Q/\partial V$ (nL/s)	Average simulated $\partial f/\partial \hat{E}_{tip}$	Experimental from eq. 7.2 $\partial f/\partial \hat{E}_{tip}$	Deviation % from experimental
[108]	PC[a]	0.115	0.0412[122]	$3.80 \cdot 10^{13}$	16.4	2.57	2.19	17.2
[115]	TEG3[b]	0.127	0.0447[139]	$3.95 \cdot 10^{14}$	1.60	2.57	2.42	6.21
[115]	EG1	0.203	0.0488[2]	$1.75 \cdot 10^{14}$	2.65	2.35	3.08	23.6
	EG2						2.68	12.3
	EG3[c]						2.83	17.0

[a] Propylene carbonate doped with NaI $\kappa_0^{PC} = 0.003$ S/m. [b] Triethylene glycol doped with NaI $\kappa_0^{TEG3} = 0.0025$ S/m. [c] Ethylene glycol doped with NaI $\kappa_0^{EG1} = 0.23$ S/m, $\kappa_0^{EG2} = 0.027$ S/m and $\kappa_0^{EG3} = 0.0029$ S/m, respectively.

Table 7.1: Comparison between simulated $f\left(\hat{E}_{tip}, \Theta\right)$ and experimental cone-jet data from [108] and [115].

7.2 A comparison with stable cone-jets: turning points and the bifurcation of stable cone-jet menisci

7.2.1 Setup

We prepared a capillary electrospray cone-jet with two different blunt stainless steel needles of gauges 24 (Benecreat company, 38.1 mm tall, 0.565 mm outer diameter, 0.300 mm inner diameter) and 28 (Hamilton company, 50.8 mm tall, 0.362 mm outer diameter, 0.184 mm inner diameter). The two different gauges serve to create menisci of different radii. The needle is connected to a thin tube of 1.59 mm outer diameter, 0.03 mm inner diameter and 150 cm long which is attached to a 5 mL syringe that acts as a reservoir (Beckton Dickinson). The syringe hangs from a vertical support of variable height that serves to create a gravitationally induced pressure at the end of the syringe.

The needle is supported by a stainless steel standoff and is faced perpendicular to a porous stainless steel metallic plate (38.1 mm diameter, 1.59 mm thick, 5 μm particle absorbance). The metal plate is situated at $d = 2.33$ mm from the needle and is held by a linear stage. The center of the plate coincides with the center of the needle. The metallic needle is connected to an amplification circuit with a shunt resistor whose output voltage is proportional to the current emitted from the capillary. The amplified voltage is read by an oscilloscope. The plate is connected to a high-voltage power supply.

The setup is placed inside a fume hood at ambient pressure and monitored with a camera that points directly to the cone-jet meniscus.

The working liquids are mixtures of ethanol ($\gamma = 0.0218$ N/m, $\mu = 0.00104$ Pa s at 25°C) and ethylene glycol ($\gamma = 0.0486$ N/m, $\mu = 0.018$ Pa s at 25° C). The mixtures are slightly enriched with NaCl to ensure that when the liquid droplets impinge into the extractor, they have enough electrical conductivity so that the extracting plate remains equipotential.

The mixtures are listed in increasing order by their % molar weight in ethanol (in table 7.2). The mixtures are prepared in a beaker that has been cleaned for 5 min in deionized water, 5 min in isopropanol, and 5 min in acetone. After each experiment with each mixture, the line is cleaned with acetone and allowed to dry for 10 minutes. Different syringe reservoirs are used for each mixture. When the next mixture is ready, it is let to flow through the line via an application of pressure with a different syringe, until the volume flowed is approximately 10 times the volume of the line. The new reservoir is filled with the new mixture and attached to the line via *luer lock* union. The surface tension corresponding to these mixtures is obtained from reference [2] at the temperature of 25°C. The reservoir pressure value is taken from the capillary pressure. We obtain the pressure using camera images of the spherical shape that the meniscus does prior to applying the voltage. The capillary pressure checks with the total gravitational head.

7.2.2 Hypothesis

It is well known in the literature of electrospraying that in general, Taylor cones experience meniscus bifurcation or the breakup of the meniscus into two emission sites at higher electric fields. The hypothesis that we are testing is that:

1. Such **bifurcation of the meniscus could happen at the upper field turning point**, at the $\hat{E}^{II}_{tip_{max}}$ defined in chapter 6.
2. **This bifurcation point may be a more general result for electrospraying** under the assumptions described earlier: we believe it applies for all pure-ion, mixed and pure-droplet electrospraying mode, at the same dimensionless voltage, for the same dimensionless geometry, although we could only simulate it for the pure-ion regime, and experiment it with stable cone-jets.

In this regard, we can compare two aspects of the cone-jet experiments and pure-ion simulations:

1. How close is the dimensionless field of the turning point in the simulations $\hat{E}^{II}_{tip_{max}}$ to the dimensionless electric field of bifurcation for the cone-jet $\hat{E}_{tip_{bif}}$. In other words, we are checking the validity of this equation:

$$\hat{E}_{tip_{bif.}} = \frac{V^{exp}_{bif.}}{A_1 \ln\left(4\hat{d}\right)\sqrt{4\gamma r_0/\varepsilon_0}} = \hat{E}^{II}_{tip_{max}}\left(\hat{d}\right) \tag{7.5}$$

   Where $V^{exp}_{bif.}$ is the experimental voltage at which the meniscus bifurcates. Eq. 7.5 is essentially saying that the dimensionless electric field obtained by the amplification factor described at the beginning of this chapter (eq. 6.3) is equal to the turning point field $\hat{E}^{II}_{tip_{max}}$ that we can simulate for a dimensionless capillary distance $\hat{d}$. $A_1 = 0.37$ is the constant that Ryan suggests for such amplification factor of the capillary geometry [108].

2. How close is the equilibrium shape of the simulations immediately before reaching the turning point to the experimental shape of the cone-jet immediately before bifurcation.

7.2.3 Operation of the experiment

The cone-jet is created using a high-voltage potential bias modulated by a signal generator in the negative mode. The signal generator creates a triangular sawtooth signal of 600-700 s period of specific offset V_{off} and amplitude V_{amp} tuned in such a way that they capture the bifurcation of the cone-jet right at the end of the sawtooth signal. The current signals are amplified and when the bifurcation happens, the current signal experiences a jump that is postprocessed to get the values of V_{bif}^{exp}.

7.2.4 Simulation values

The values for $\hat{V}_{tp.}^{sim}$ are obtained from simulating an [EMIm][BF$_4$] meniscus of $\hat{R} = 69.15$, with the same simulation parameters as described in chapter 6 for the capillary setting, and the dimensionless $\hat{d}$ and $\hat{p}_r$, corresponding to the experiment. Since the turning point that we can predict is independent from the value of the impedance, (as long as the impedance is high enough that flow is impedance dominated) we have taken the arbitrary value of $\hat{Z} = 0.177$.

For the two radii explored in this experiment, the turning point location has been shown before in figure 6-10. We are checking then if $\hat{E}_{tip_{bif.}} \approx 1.34$ for the case $\hat{d} = 8.66$ and $\hat{E}_{tip_{bif.}} \approx 1.35$ for the case $\hat{d} = 13.01$.

7.2.5 Results

In the great majority of our experiments, the cone-jet meniscus starts practically symmetric as in figure 7-1a, and loses its axially symmetric form at higher fields as in figure 7-1b, therefore obscuring any possible comparison of the turning points predicted by our axially-symmetric simulations.

However, when the reservoir pressure is high enough (normally within $p_r \in [\frac{0.3\gamma}{r_0}, \frac{2\gamma}{r_0}]$), the meniscus remains sufficiently axially symmetric to have a meaningful comparison of our simulated observations of the turning point to the experiments with the cone-jet. Only five tests yielded an acceptable axially symmetric cone for the full potential range tested. The experimental details of these tests are shown in table 7.2. In these cases, at the critical voltage prior to bifurcation, we can observe a very flattened Taylor cone, as in figure 7-2a, that diverges into two cones immediately after as in figure 7-2b. From the two last columns of the data in table 7.2, we can mention that the cone-jet bifurcates at an $\hat{E}_{tip_{bif}}$ that is really close to the turning point predicted by the simulations $\hat{E}_{tip_{max}}^{II}$, with less than 3% error for the data that

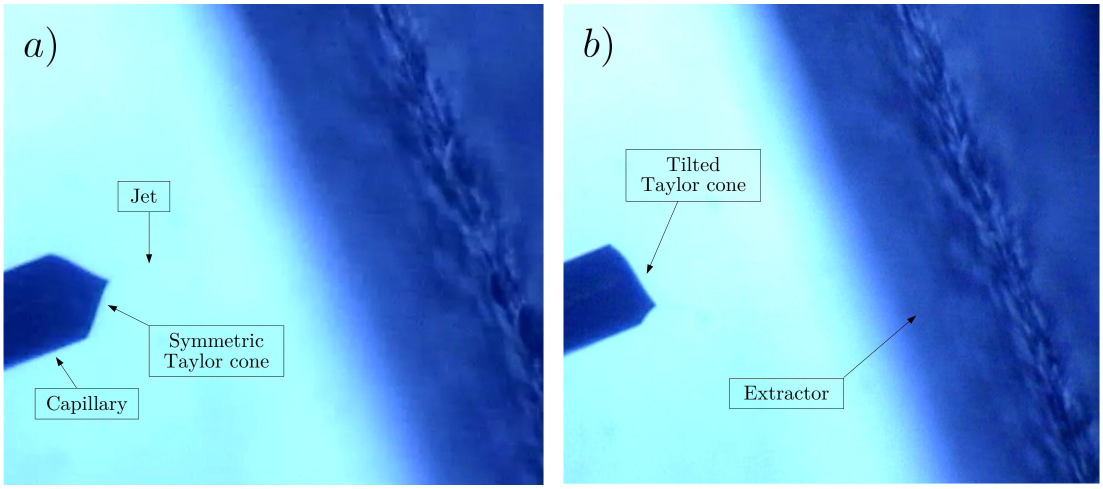

Figure 7-1: a) Stable cone-jet (30% ethanol) operating in the lower field regime. b) cone-jet tilting at higher electric fields. Reservoir pressure is $\hat{p}_r = 0$.

we presented. When we overlap the experimental shape that is obtained from the camera images, to other equilibrium shapes that are very close to the critical shape in figure 7-3 (within 2% difference in electric field), we can certainly notice the resemblance. The details of the jet apex cannot be captured with the resolution of the camera.

Results presented in this section seem to suggest the validity of both of our hypotheses: that the turning point that we observe in our simulations may be a more general result for the bifurcation of electrospray meniscus, under the assumptions of high impedance dominated flow, axially symmetric meniscus and $r_0/r^* \gg 1$, in this case r^* could be taken as the characteristic jet dimension. More future work will be required to quantify where the limit of high impedance dominated flow in this characteristic setup is, and how much deviation there is from this turning point when the cone-jet bifurcates from a tilted configuration. Notwithstanding, we can restate two assumptions and observations that we had to make to perform this analysis, which seem necessary for the impedance-limited regime to apply:

1. Upstream pressure drop is governed by the Darcy equation, which inherently

Ethanol (%)	r_0 (mm)	γ (N/m)	$V_{bif.}^{exp}$ (V)	$\hat{p}_r$	$\hat{d}$	$\hat{E}_{tip_{bif}}$	$\hat{E}_{tip_{max}}^{II}$
30%	0.181	0.0327	-3170 ± 10[a]	0.978	13.01	1.33	1.35
50%	0.181	0.0283	-2970 ± 16.1	0.250	13.01	1.33	1.35
70%	0.283	0.0249	-3245 ± 37.5	0.66	8.66	1.31	1.34
70%	0.181	0.0249	-2843 ± 14.4	0.15	13.01	1.35	1.35
90%	0.181	0.0227	-2686 ± 5.28	0.15	13.01	1.35	1.35

[a] Error computed visually, no oscilloscope data was taken

Table 7.2: Experimental data for the five axially-symmetric cone-jet bifurcations tested. Results shown for increasing values of ethanol percentage. The last column on the right shows the dimensionless turning point location at the simulated distance $\hat{E}_{tip_{max}}^{II}$. The second-to-last column shows the experimental dimensionless field where the cone-jet meniscus bifucates $\hat{E}_{tip_{bif}}$.

means that the flow is in the linear laminar regime (low Reynolds),

$$Re = \frac{\rho u l}{\mu_0} < 1 \tag{7.6}$$

where u is a characteristic velocity of the flow in the substrate with cross-section area A ($u \sim Q/A$), and l is a characteristic length scale of the flow (likely a pore size, or the channel radius r_0).

2. The current is dominated by the impedance. Given our simulation results in chapter 5, this condition seems to be represented by:

$$Z \gg Z_{spch} = \frac{\rho}{\pi r_0^2}\sqrt{2V\frac{q}{m}} \tag{7.7}$$

Given the results in figure 5-9, $\frac{Z}{Z_{spch}} > 5$ seems to be a reasonable reference, where the space charge screening is not larger than 5% of the total current without space charge.

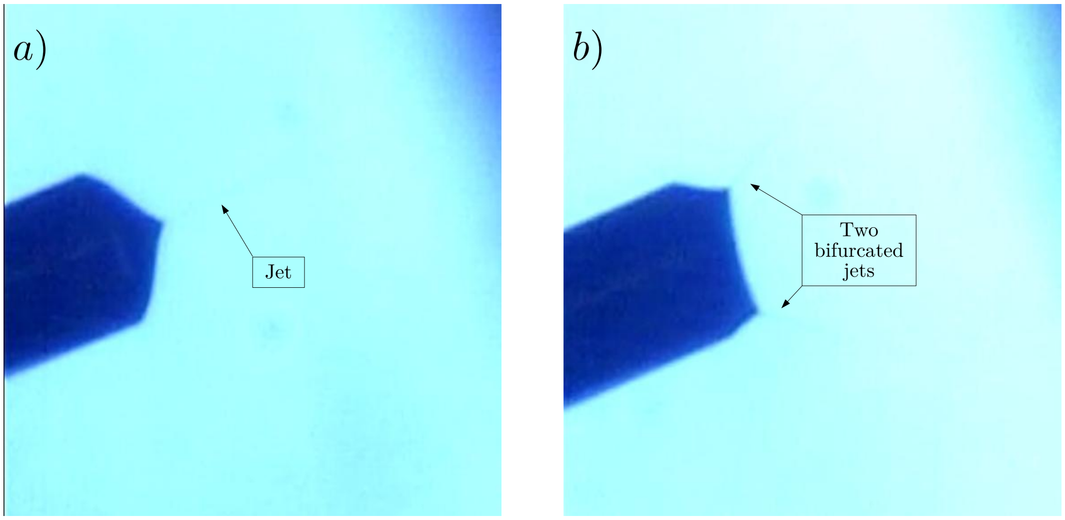

Figure 7-2: a) Stable cone-jet (30% ethanol) operating in the high field regime prior to bifurcation in axially-symmetric configuration. Reservoir pressure is $\hat{p}_r = 0.98$. b) Bifurcation of cone-jet immediately after a).

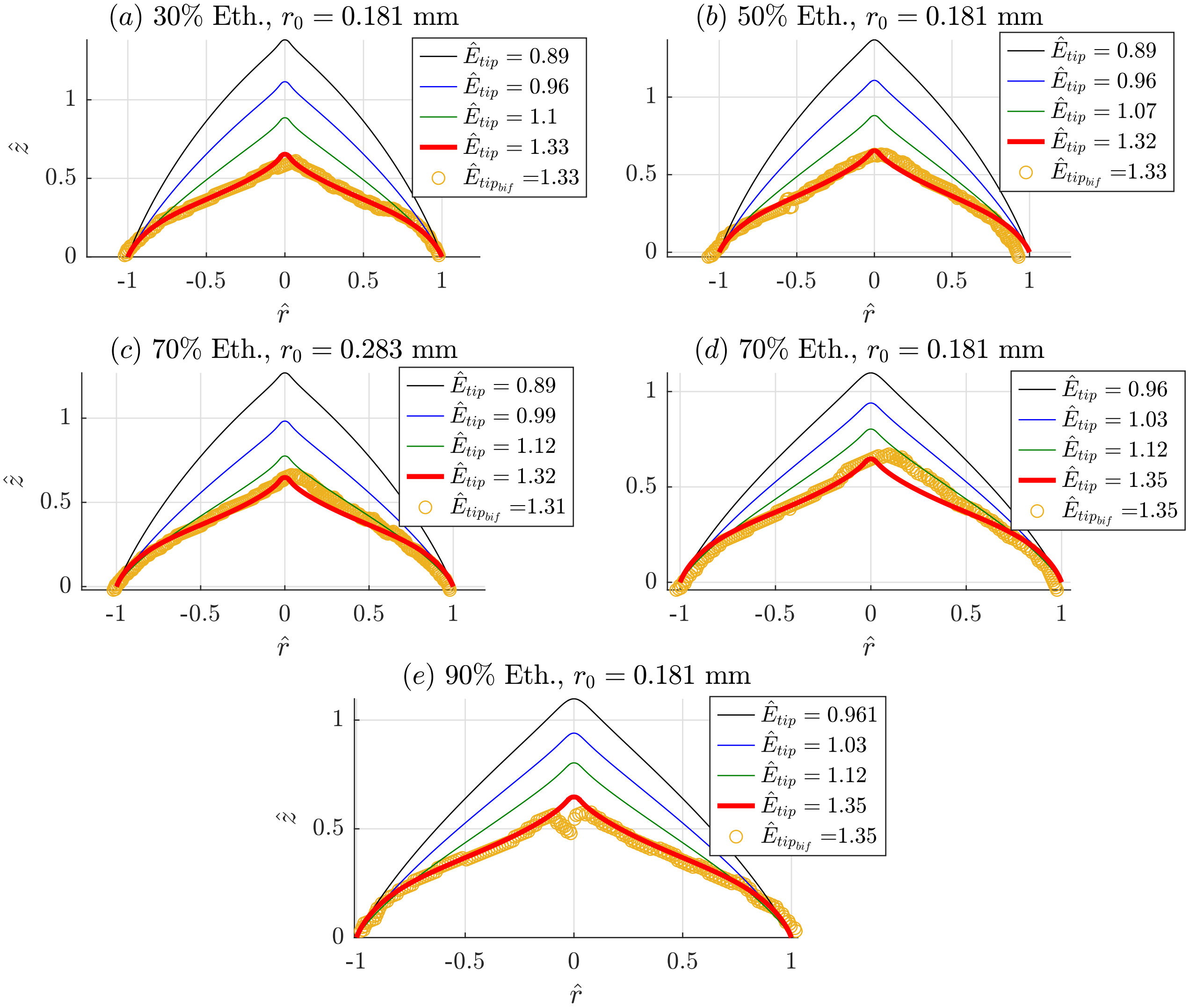

Figure 7-3: Dimensionless simulated equilibrium shapes for an [EMIm][BF$_4$] meniscus in capillary setting for the same experimental conditions as the cone-jet. The experimental cone-jet profile immediately prior to bifurcation is shown with the yellow markers. Simulated solution that best fits the experimental markers is plotted with dark red. This fitted solution corresponds to an $\hat{E}_{tip}$ that deviates less than 3% from the turning point $\hat{E}^{II}_{tip_{max}}$.

Chapter 8

The current-voltage behavior: experiments with porous emitters

In this chapter, we ask the question: can we apply directly equation 6.5 to explain the typical current-voltage obtained in porous emitters? We rewrite equation 6.5 below in dimensional form for ease of reading:

$$I = \frac{2\gamma\rho}{r_0 Z}\frac{q}{m}\left(f\left(\hat{E}_{tip}, \Theta\right) + \frac{p_r r_0}{2\gamma}\right) \tag{8.1}$$

For doing this, we manufactured a single carbon xerogel emitter, similar to the one developed by Pérez-Martínez [96] and tested an ionic liquid: [EMIm][HSO_4].

8.1 Challenges of the applicability of equation 8.1 to the current emitted by porous tips

Equation 8.1 needs as inputs a meniscus radius r_0, a hydraulic impedance Z, and a Laplace pressure p_r. None of these data was directly available to us. It is worth mentioning that precise data for these variables are very challenging to obtain for an experimentalist in a typical vacuum electrospray setting using porous emitters of such small features $R_c \sim 10\ \mu$m. This is the main challenge that we found for the experimental validation of the model in this thesis. We try to discuss each of the items in the points below:

- **The meniscus radius** r_0: The uncertainty of the radius is large: the radius could be a value between the curvature radius of the tip R_c and the pore size

r_p.

- **The Laplace pressure** p_r: The Laplace pressure is dependent on the material contact angle, it also depends on the saturation of the emitter with propellant [126]. A porous structure that is not saturated with liquid may have a negative Laplace pressure that can peak in the perfectly wetting case to the curvature radius on the order of the pore size: $p_r = -\frac{2\gamma}{r_p}$, and in the condition of semi saturation. In such cases the dimensionless reservoir pressure corresponds to $\hat{p}_r \sim -1$, where we have estimated a narrow range of existence of the function $f\left(\hat{E}_{tip}, \Theta\right)$ (see figure 6-8). Previous studies suggest that for the geometry and pore sizes of the tips used in this thesis, if the source is saturated with liquid in such a way that the Laplace pressure is determined by curvature radii lengthscales larger than r_p, it could yield high enough flow rates to lose the pure-ion regime [27]. Knowing the Laplace pressure accurately and saturation in situ, with the geometrical characteristics of our tips requires experimental efforts that are beyond the resources and time available at the point this thesis is written [78].

- **The hydraulic impedance** Z: The hydraulic impedance of an emitter depends on its geometric parameters, such as shape or permeability. Some permeability models have been proposed for porous emitters used in electrospraying [26, 96], in spite of their characteristic uncertainties: for example, the inhomogeneous distribution of pore sizes, which can alter the effective pore radius of the emitter from what is observed in SEM images. Furthermore, operational uncertainties can also make it difficult to accurately determine the impedance. For instance, the meniscus may not be fed by the full emitter's structure if it is too small. Even the location and size of the meniscus could have a leading order impact on what is the impedance predicted by the theoretical models, which typically assume that $r_0 \sim R_c$. Additionally, there may be electrochemical [8] or liquid thin film effects [83] that are rather challenging to quantify experimentally and that may govern the entirety of the impedance.

8.2 The moving meniscus hypothesis: radius reduction during current-voltage excursions

In addition to the uncertainty sources described in section 8.1, we cannot assume that r_0 or Z will remain constant throughout the current-voltage potential curve.

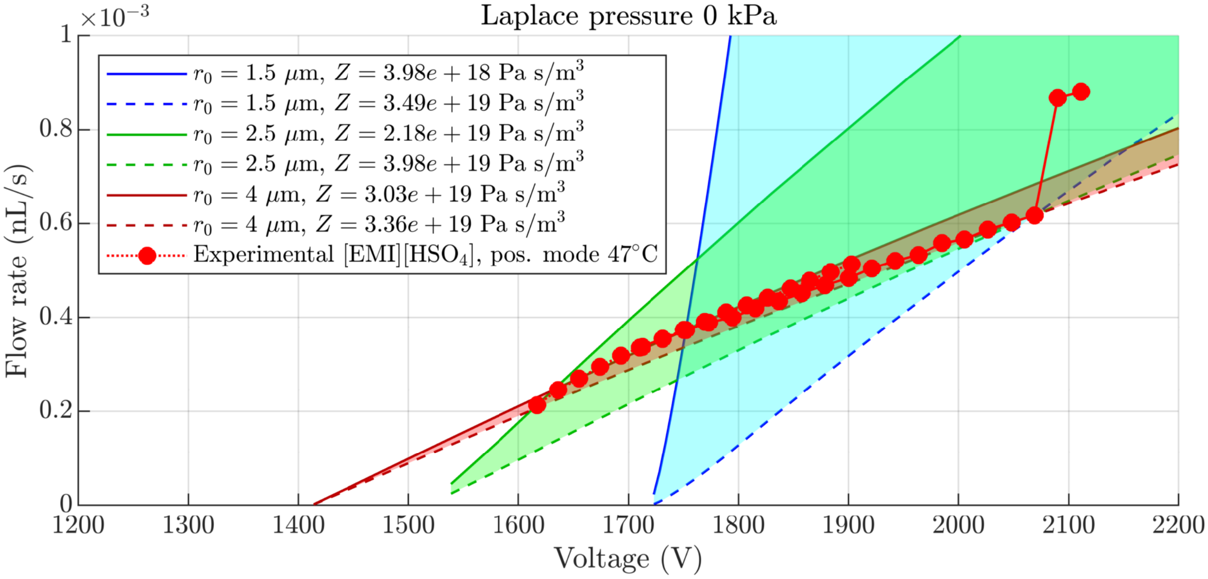

Figure 8-1: Flow rate-voltage curve obtained by simulations (solid, dash-dotted lines) at different radii and impedances. Shaded areas represent which portion of the experimental curves have found simulated static menisci at a specific meniscus radius. Experimental data are shown with red markers.

Figure 8-1 shows an illustrative example of a comparison between the experimental and simulated current-voltage curves obtained in this thesis, if we assume that the meniscus is pinned at some radius r_0 along the profile of a conical porous carbon xerogel tip. The details of how the figure was obtained (experiments and simulations) are described in the next sections of this chapter. The experimental data are scaled by the flow rate, and shown in dotted red. The rest of the green, blue, and red lines are simulated with a constant radius r_0 and hydraulic impedance Z. The simulated radii are in between the radius of curvature of the tip $R_c \sim 10\ \mu$m and the pore radius $r_p \sim 0.4\ \mu$m.

For this particular simulation, we can see that the effect of increasing the meniscus radius r_0 is to reduce the extinction voltage (the blue lines are simulated with radii $r_0 = 1.5\ \mu$m, the green lines are simulated with $r_0 = 2.5\ \mu$m, and the red lines are simulated with $r_0 = 4\ \mu$m). For a given Laplace pressure, if we consider for instance that the meniscus is pinned at $r_0 = 2.5\ \mu$m (green lines in figure 8-1), the interval of feasible impedances that would reproduce the simulated results will go from the one matching the first experimental point (solid green line) to the one matching the last

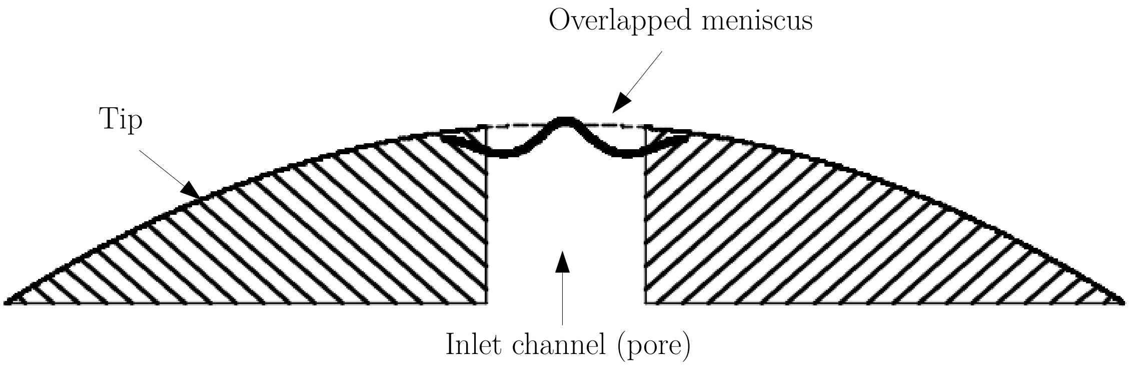

Figure 8-2: Illustration of possible overlap between the meniscus equilibrium profile and tip profiles at higher fields. Before reaching a situation like this shown in the figure, it is reasonable to assume that the meniscus would reduce its radius at increasing values of the voltage until finding a new geometrically compatible configuration.

experimental point before the flow rate jumps (dashed green line).

This range of impedances (or confidence interval) narrows when the radius becomes larger (see solid and dashed red lines for the 4 μm meniscus in figure 8-1). However, we believe that it is improbable to observe a pinned meniscus with a larger radius throughout the entire current-voltage curve. This assertion is supported by the findings discussed in chapter 6, where it was demonstrated that equilibrium shapes associated with higher voltages tend to be drawn into the menisci, resulting in contact angles that could be incompatible with the geometric profile of the tip at higher voltages (see figure 8-2). In other words, the meniscus could overlap with the tip's profile at these voltage levels, especially when the meniscus radius is close to R_c, and its base spans several pores (thus not pinned at the rim of the pore, where it has a full range of movement).

It seems prudent then to take into account the possibility of having a different radius for each of the experimental points (a moving meniscus situation).

Experimental evidence for a moving meniscus

In the experimental realm, it is generally observed that ionic liquid and liquid metal electrospray menisci reduce their radii at higher voltages in porous and externally wetted emitters. For example, direct Transmission Electron Microscopy (TEM) observations of gallium sources unveil smaller menisci at higher voltages [30]. Recent investigations from Huang et al. [65] also report a direct observation of an [EMIm][BF_4] reducing both the film thickness and its radius at higher voltages in a porous emitter, which is consistent with the charts presented in this thesis. The reasons why menisci may move by reducing its size along the current-voltage curves can be caused by wetting properties of the ionic liquid with the material, or pure geometrical incompatibility of the equilibrium shapes with the interface profile of the tip (as seen in figure 8-2).

If the meniscus were to travel along the profile of the porous tip and have a smaller size at some point (blue line in figure 8-1), both the range of simulated impedances that would replicate the experimental results, and the value of these impedances will be larger. The reason why the impedance would increase in this situation is that for a smaller meniscus, the volume of the emitter involved in the transport of ionic liquid fed to the meniscus is smaller, if we assume that the ionic liquid is fully transported to the meniscus base via the internal network of pores (e.g, no external flow).

In summary, the figure shows that experimental results cannot generally be explained by simulations at constant radius or impedance, unless the radius is large enough (on the order of $r_0 \sim R_c$) but this situation could originate meniscus overlapping at higher fields. Therefore, we need to define a *band* of impedances that would be able to reproduce the experimental results for each radius and Laplace pressure.

8.3 Chapter objectives

Due to the limitations described above, and the assumption of a possibly moving meniscus, the objective of this chapter is to find sets of simulated (r_0, p_r, Z) that can fit the experimental data, rather than a full validation of the model.

8.4 Simulation settings

Finding this *band* of impedances compatible with each experimental point directly requires solving the inverse problem implemented in this thesis (e.g, finding r_0, p_r, Z that reproduces *each* experimental point). We have taken advantage of the relationship of eq. 8.1, where we only need the value of $f\left(\hat{E}_{tip}, \Theta\right)$ for the particular geometry. We enumerate the simulation steps taken below:

1. Capture the profile of the tip from SEM images, approximate the axis of symmetry of the tip and compute an axially symmetric average of the tip profile

Ionic liquid	R_c (μm)	ϑ (°)	h (μm)
[EMIm][HSO]$_4$	10	4	290

Table 8.1: Approximate geometrical details of the tips as given by SEM images (corrected by imaging angle). R_c is the radius of curvature, ϑ is the tip conical angle, h is the tip height.

using the distance of each tip point to the guessed symmetry axis (figure 8-3).

2. Truncate the tip profile with a channel of radius equal to the meniscus radius of our choice r_0.
3. Mesh the truncated tip profile and the full axially-symmetric geometrical details used in the experiment (figure 8-4).
4. Choose an arbitrary value of the impedance, a reservoir pressure of $p_r = 0$, and the physical parameters of the liquid referenced in the annex tables A.1, A.2, A.3 and A.4.
5. Extract the value of $f\left(\hat{E}_{tip}, \Theta\right)$ from the simulated curves at the radius r_0. The space charge problem is not solved in this section, since we only want estimations of $f\left(\hat{E}_{tip}, \Theta\right)$. $\beta = 1$ in eq. 3.38 and $\hat{\rho}^v_{sch} = 0$.
6. For each experimental datapoint, find what is the combination of Z and p_r that would yield such experimental value, using $f\left(\hat{E}_{tip}, \Theta\right)$ at the correspondent radius.

8.4.1 Simulation geometrical dimensions and dimensionless numbers

The geometrical lengths of the simulation (figure 3-1 for diagram, figure 8-4 for mesh render) are the following: $z_{up} = 1340$ μm, $z_{el} = 630$ μm, $r_h = 394$ μm, $\alpha = 54°$, $d = 330$ μm for the simulations with [EMIm][HSO$_4$]. The reference temperature and charge-to-mass ratio values for the simulation are $T_0 = 47.8$°C, and $q/m = 4.81 \cdot 10^5$ C/kg. Tables 8.2 and 8.3 show the dimensionless numbers and reference velocities originated from the physical constants described in the annex section A. Some

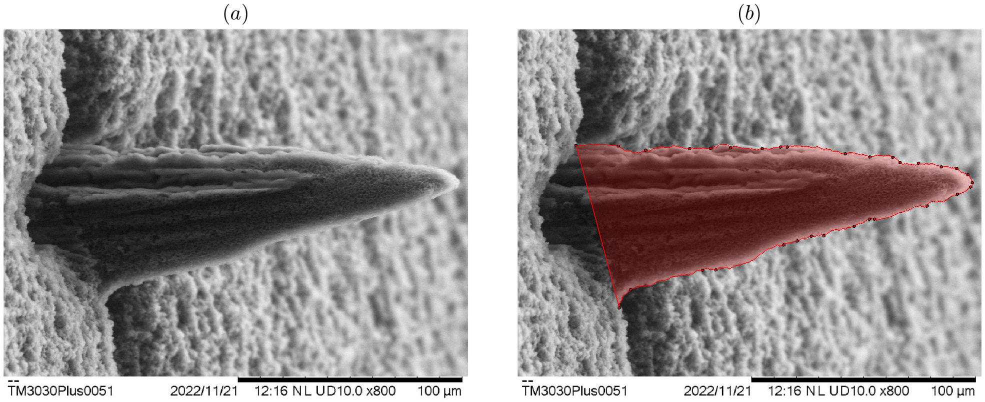

Figure 8-3: Example of tip profile captured by edge detecting MATLAB routines from SEM images.

parameters were not found in the literature and arbitrary values are chosen, therefore some of the values in tables 8.2 and 8.3 are arbitrary. It is worth mentioning that the only experimental variable that we compare in this chapter is the current, which is only dependent on the parameters of eq. 8.1: $f\left(\hat{E}_{tip}, \Theta\right)$, γ, r_0, p_r, q/m, ρ, and Z. In this sense, $f\left(\hat{E}_{tip}, \Theta\right)$ is independent of any parameter in tables 8.2 and 8.3, and the rest of parameters are inferred (r_0, p_r and Z) or obtained from the experimental work in this chapter (γ, q/m).

8.5 Experimental settings

8.5.1 Source elements

The emitter source is composed of the following elements:

- A stainless steel tube (type 304) with 9.53 mm outer diameter, 6.22 mm inner diameter, 25 mm long (purchased from McMaster-Carr, brought to desired height by in-house machining).

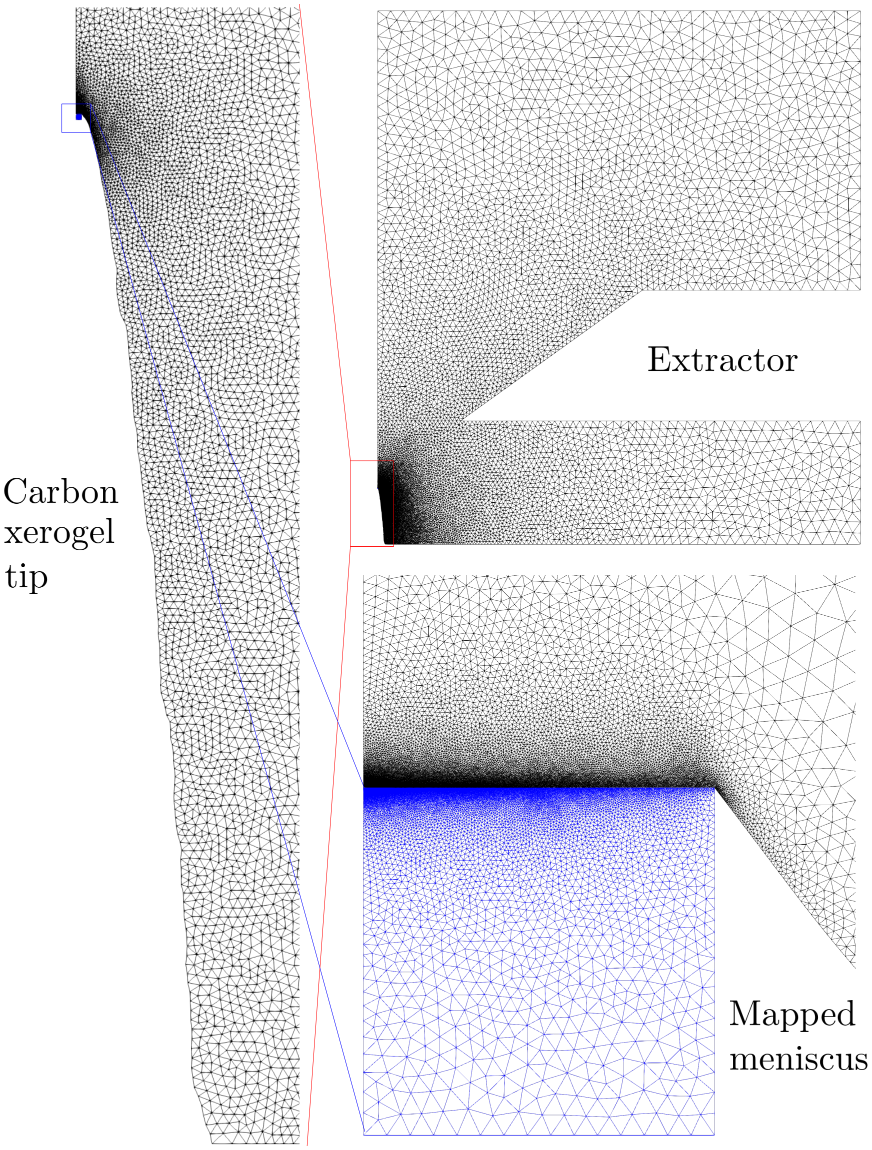

Figure 8-4: Axially symmetric mesh profile. Meniscus map is shown in blue. Detailed geometrical dimensions are described in section 8.4.1.

Number	Value	Default [EMIm][HSO$_4$] (ΔG[a] = 1.15 eV)
ψ	$\frac{\Delta G}{k_B T_0}$	41.6
C_β	$\frac{2\kappa_0^2}{\rho\varepsilon_0\left(\frac{q}{m}\right)^2}$	$6.81 \cdot 10^{-5}$
Pe	$\frac{\kappa_T}{u_c r^* \rho c_p}$	18.26
Oh	$\frac{\mu_0}{\sqrt{\rho\gamma_0 r^*}}$	230.7
C_m	$\frac{u^*}{u_c}$	0.146
Θ	$\frac{u_{ion}^2}{u_c^2}$	No space charge
β	$\frac{\rho^v}{\rho}$	1 (No space charge)
$\hat{l}_H$	$\frac{l_H}{c_p T_0}$	1.61
$\hat{T}_{out}$	$\frac{T_{out}}{T_0}$	1.17

[a] Arbitrary value

Table 8.2: Dimensionless numbers used in the simulations for [EMIm][HSO$_4$].

Reference symbol	Reference value	Default [EMIm][HSO$_4$] (ΔG[a] = 1.15 eV)
u_c	$\frac{\gamma_0}{\mu_0}$	0.161 m/s
u^*	$\frac{\kappa_0 E^*}{\varepsilon_r \rho \frac{q}{m}}$	0.0235 m/s
t_c	$\frac{r^*}{u_c} = \frac{r^* \mu_0}{\gamma_0}$	$1.90 \cdot 10^{-7}$ s
t_e	$\frac{\varepsilon_0 \varepsilon_r}{\kappa_0}$	$5.29 \cdot 10^{-10}$ s
t_μ	$\frac{4\mu_0}{\rho c_p T_0}$	$2.03 \cdot 10^{-9}$ s
t_m	$\frac{h}{k_B T_0}$	$1.50 \cdot 10^{-13}$ s
Z^*	$\frac{2\gamma_0 \rho \frac{q}{m}}{\kappa_0 E^* {r^*}^3}$	$9.27 \cdot 10^{21}$ Pa·s/m^3

[a] Arbitrary value

Table 8.3: Reference times, velocities, and impedance used in the simulations for [EMIm][HSO$_4$].

- A porous PTFE tube 6.22 mm outer diameter, 3.17 inner diameter (purchased from Scientific Commodities Inc.). A 4.55 mm diameter hole, 9 mm tall is machined on the teflon cylinder to acommodate carbon xerogel monolith. The porous PTFE allows the evacuation of possible dissolved gas in the ionic liquid, while keeping the liquid in place.
- In-house manufactured carbon xerogel monolith containing laser micromachined tip on top (details in the section below).
- Stainless steel washer, 4.55 mm outer diameter, 3.17 mm inner diameter (purchased from McMaster-Carr). A stainless steel wire is spot-welded on top to provide electrical contact.
- Fiberglass fill (1 mm tall approximately, 4.55 mm diameter, cut from VWR 691 Microfibre disks). The fiberglass fill wetted with the ionic liquid provides the distal contact between the carbon xerogel monolith with the etched tip and carbon chip.
- In-house manufactured carbon xerogel chip, 4.55 mm diameter, 1.5 mm tall. The chip is in contact with the fiberglass to provide the distal electrical connection of the same material as electrode.

8.5.2 Assembly of the elements

The assembly of the materials can be seen in figure 8-5, all elements in section 8.5.1 are pressure fit. The stainless steel cylinder with the source assembly is mounted on a machined PEEK base held by a x-y-z linear stage to assist in the alignment to the extractor plate. The PEEK mount contains a hole to accommodate the stainless steel source assembly. The mount on the PEEK is done using a set screw, to keep the modularity of the source, and ease the change of the ionic liquid. Different source stainless steel assemblies are used for each ionic liquid tested. A heater is constructed of the same diameter as the stainless steel cylinder by attaching a 12 Ω flat resistor to a boron nitride jacket with thermally conducting epoxy resin.

8.5.3 Carbon xerogel monolith and chip development

Carbon xerogel tips were made of carbon monoliths from pyrolyzed resorcinol formaldehyde resin. The monoliths were built following the steps in [105], with the only difference being the mold where the resin is poured before curing. The mold is made by milling a Teflon block with cylinders of 4.6 mm diameter and 10 mm tall. Once the carbon xerogel monoliths are obtained from the curation and pyrolization of the resin, the following steps are followed to bring the monoliths at the desired geometry:

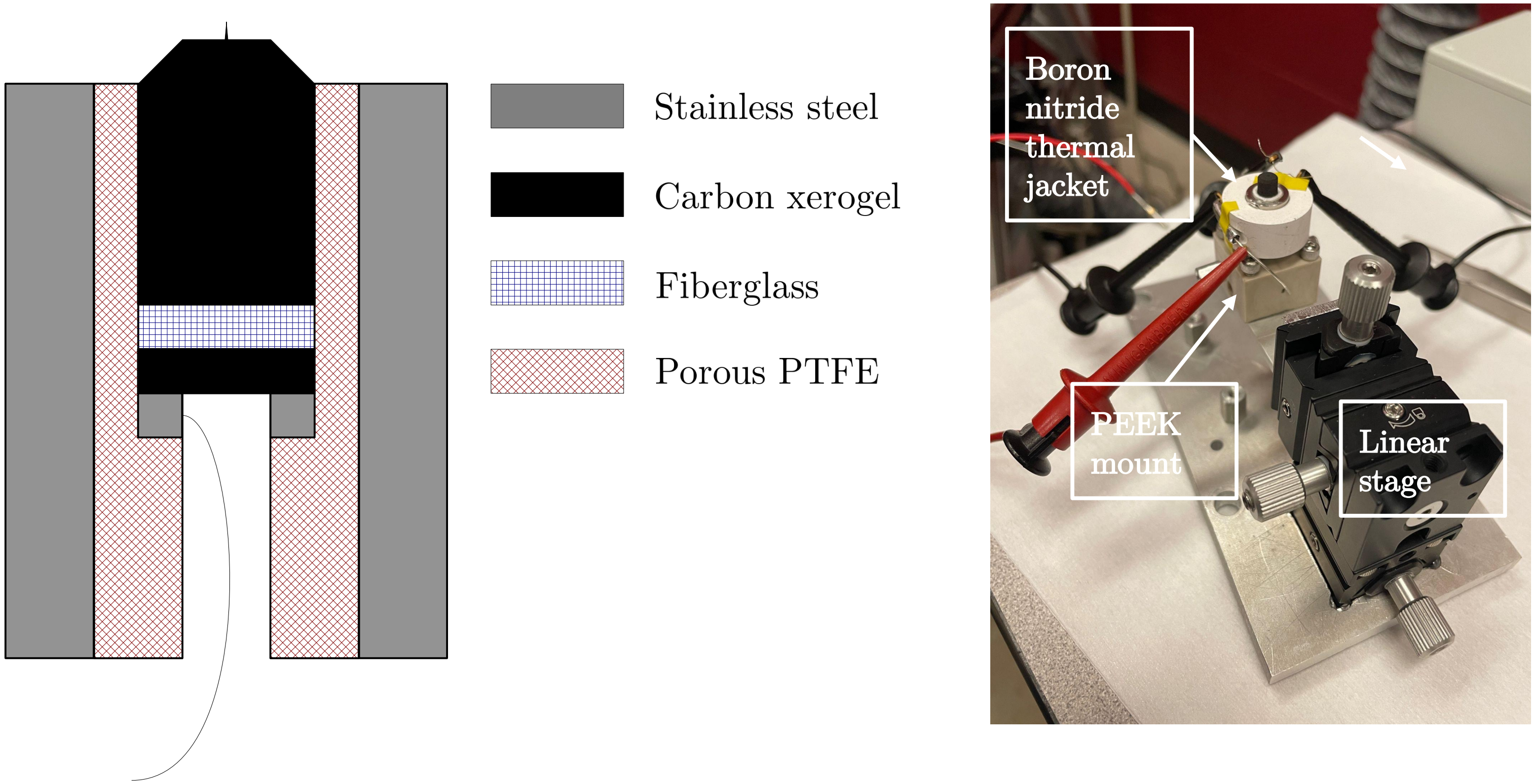

Figure 8-5: Assembly of the source (left) and experimental handler (right).

1. Removal of the carbon skin ($\sim 100\ \mu$m) by slightly rolling the monolith in a 1500 grit sandpaper.
2. Bring monolith to 7 mm height, keeping both flat ends using sandpaper grits of 300, 1500 and 2500 sequentially.
3. Make 45° rounded chamfer at one monolith face end using 1500 sandpaper grit against the monolith rolling on a lathe. The rounded chamfer is made to prevent electrospraying from the carbon monolith edges.
4. Remove remanining debris by blowing pressurized air on the monolith.

8.5.4 Laser etching

The etching of the carbon monolith was performed with a 355 nm ultraviolet, solid-state laser located at Photomachining, Inc.(PMI) facility in New Hampshire. The beam settings are: 2 Watt focused (10 μm between etching lines), with pulse frequency of 200 kHz, 1500 mm/s translational velocity. The 10 μm etching line pattern was specifically stopped by forming a 32 μm square to profile the tip. The line pattern was provided to the manufacturer via .dxf CAD capability and was run 24 times. The laser etching is performed *after* the elements are assembled in the stainless steel cylinder.

8.5.5 Wetting of the source

Once the carbon monolith is etched with the tip, the source is wetted from the porous PTFE orifice situated at the bottom of the assembled stainless steel cylinder. Ionic liquids are degassed prior to wetting in the porous carbon. The wetting is performed in a glove box under a CO_2 atmosphere (below 9 % relative humidity) to reduce the dissolution of air and water vapor particles in the ionic liquid as much as possible and prevent possible chaotic outgassing of the liquid while testing. The wetting is also performed on a copper device explicitly machined to heat the source. Heating the source while wetting reduces the viscosity of the ionic liquid and ensures timely saturation of the pores with the liquid. The device is a hollow thermal jacket with four legs attached where the stainless cylinder fits through. The cylinder is held with a set screw upside down with the legs contacting a hot plate at 70° C.

Droplets of ionic liquid up to approximately 100 μL are carefully deposited from the back of the device and the device is left for approximately 1h on the hot plate. To remove excess liquid, fiberglass is used to absorb the liquid through the bottom hole of the source until no more liquid is observed at the bottom of the device under the microscope. This step was found to be very important to ensure that the Laplace pressure is determined by curvature length scales on the order of the pore size radius, in order to enhance the pure ionic nature of the source.

8.5.6 Operation of the tip

The current-voltage characteristics of the tip were performed using both voltage ramps of 500-700 seconds period, and alternate square waves of potential at a period of alternation between 15-25 seconds. Raw signal data of the current-voltage curves are displayed in section 8.6.2.

8.5.7 The charge-to-mass ratio

The charge-to-mass ratio of the ions was tested using time-of-flight (TOF) spectroscopy using a channeltron electron multiplier detector. The TOF curve was taken at the center of the beam. Details of the standard operation of TOF [87, 94]. The mass flow rate of species up to trimers was computed as:

$$\dot{m}_i = \frac{f_i I}{q_i/m_i} \tag{8.2}$$

Where f_i is the fraction of the beam composied by the i-th ion, I is the current of the beam, and $\frac{q_i}{m_i}$ is the charge-to-mass ratio of each ion. The fraction of each species of the beam f_i was inferred by running Prof. Jia-Richards ensemble Kalman update estimator [68] from the normalized time-of-flight curves, the operating voltage V is the traveling distance of the ions from the deflection gate to the channeltron electron multiplier detector L. The mass flow rate of higher-order species was estimated by smoothing the upper part of the normalized TOF curve (Savitzky-Golay filter) and using the following equation [46]:

$$\dot{m}_H = \frac{2V}{L^2} I \int_{t_{n>3}} t^2 \frac{d\bar{I}}{dt} dt \tag{8.3}$$

Where $\bar{I}$ is the normalized time-of-flight curve.

Finally, the average charge-to-mass ratio was inferred from individual mass flow rates of the ions as and higher order clusters as:

$$\frac{\bar{q}}{m} = \frac{I}{\dot{m}_H + \dot{m}_1 + \dot{m}_2 + \dot{m}_3} \tag{8.4}$$

8.5.8 Geometrical details of the tips and theoretical predictions for the hydraulic impedance Z

The total hydraulic impedance of the porous emitters used in this thesis can be interpreted as having two impedances in parallel, one governing the external flow Z_{ext}, and one for the porous internal flow Z_{pore}:

$$Z = \frac{Z_{pore}}{1 + \frac{Z_{pore}}{Z_{ext}}} \tag{8.5}$$

Mair [83] develops an equation for the value of Z_{ext} as a function of the geometry of the tip (conical semiangle ϑ), and the film thickness δ:

$$Z_{ext} = \frac{6\mu}{\pi^2 \delta^3} \frac{\ln\left(1 + h \tan\vartheta / r_0\right)}{\tan\vartheta} \tag{8.6}$$

As seen in eq. 8.6, the film thickness is a critical parameter (to the third exponential power), it is not generally available in conventional externally wetted electrospraying, and it may have different local values along the emitter. Mair argues that flow saturation usually occurs in externally wetted emitters due to average film thickness decrease, which means that the impedance may also not be constant when increasing the flow demand (for instance by increasing voltage). A porous emitter that is overwetted with propellant may favor large film thicknesses, bringing up the denominator in eq. 8.6, and dramatically reducing Z. Since the film thickness is an arbitrary parameter, we treat Z_{ext} as a whole integrated parameter.
The value of Z_{pore} can be estimated using Darcy law [138]:

$$\mathbf{q} = -\frac{k}{\mu} \nabla P \tag{8.7}$$

Where $\mathbf{q}$ is the volumetric flow rate per unit surface area and k is the permeability of the medium. For a porous material, the permeability can be estimated using the Kozeny-Carman formula [12]:

$$k = \frac{D_{eff}^2}{180} \frac{\phi_p^3}{\left(1 - \phi_p\right)^2} \tag{8.8}$$

Where ϕ_p is the porosity of the material and D_{eff} is an effective particle diameter. Glover [55] estimates $D_{eff} = 1.74 r_p \phi_p^{3/2}$ for porous substrates formed by spherical particles, and r_p is the average hole size in between the spheres. Using this approximation, eq. 8.8 yields:

$$k = \frac{r_p^2}{60\left(1-\phi_p\right)^2} \tag{8.9}$$

In the case of an axially-symmetric conical tip, assuming that the flow is perfectly spherical, that the meniscus pins at the curvature radius R_c whose field lines coincide locally with the tip profile we can integrate 8.7 as:

$$\Delta P \approx \frac{\mu}{k}\int_{r_b}^{R_c} \frac{Q}{2\pi r^2\left(1-\cos\vartheta\right)} dr \tag{8.10}$$

Where, r is the distance of the tip conical apex to any point of the conical tip; $r = r_b$ at the base of the tip. For a set of points describing an arbitrary axially symmetric tip profile as a function of the tip height h, $R_{tip}\left(h\right)$ then we can substitute r with $R_{tip}(h)$ in eq. 8.10 as:

$$r\left(h\right) = \frac{R_{tip}\left(h\right)}{\sin\vartheta\left(h\right)} \tag{8.11}$$

Together with the fact that:

$$dr = \frac{dh}{\cos\vartheta} \tag{8.12}$$

The component of the impedance describing the porous flow is then:

$$Z_{pore} = \frac{\Delta P}{Q} = \frac{\mu}{k}\int_0^{h_{r_0}} \frac{\sin^2\vartheta\left(h\right)}{2\pi R_{tip}^2(h)\left(1-\cos\vartheta\left(h\right)\right)\cos\vartheta\left(h\right)} dh \tag{8.13}$$

With the axisymmetric average of the tip profile from the SEM described in section 8.4 $R_{tip}\left(h\right)$, we can integrate 8.13 numerically by also knowing that:

$$\frac{dR_{tip}}{dh} = \tan\vartheta\left(h\right) \tag{8.14}$$

8.6 Results with [EMIm][HSO$_4$]

8.6.1 Time-of- flight mass spectroscopy

The time of flight curves can be seen in figures 8-6 and 8-7 for the $T = 47$°C and the $T = 40$°C datasets. The compositions inferred from the ensemble Kalman update (see section 8.5.7) are shown in tables 8.7, 8.5, 8.6, and 8.4. We notice a slight decrease in the average charge-to-mass ratios of the ions at higher voltages. The

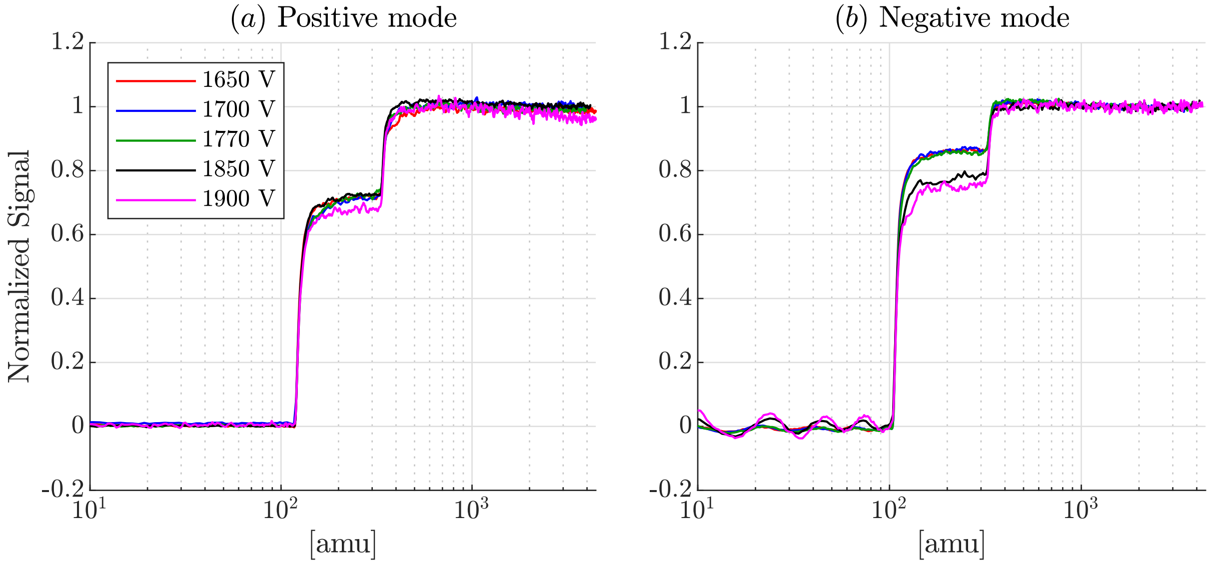

Figure 8-6: [EMIm][HSO$_4$] $T = 47°$C. TOF mass spectrum at different voltages for the positive (a) and negative (b).

population of the beam is "less monomeric" at higher voltages. This fact is observed in pure-ion beams with other ionic liquids [86]. We notice a significant disparity between the charge-to-mass ratios in the positive and negative modes that will be discussed in section 8.6.3.

8.6.2 Current-voltage and flow rate characteristics

Figure 8-8 shows the experimental current-voltage curve characteristics obtained with the carbon emitter wetted with [EMIm][HSO$_4$]. The curves were obtained by averaging the last 5 seconds of the square signal prior to the polarity switch. The raw current-voltage curves with the voltage signal ramps can be seen in figures 8-9 for $T = 47.8°$C and 8-10 for $T = 40°C$.

We also notice a significant disparity of current emitted in the positive and negative modes. This fact is exacerbated when looking at the estimated flow rate from the TOF curves, if we consider the higher average charge-to-mass ratio in the negative mode.

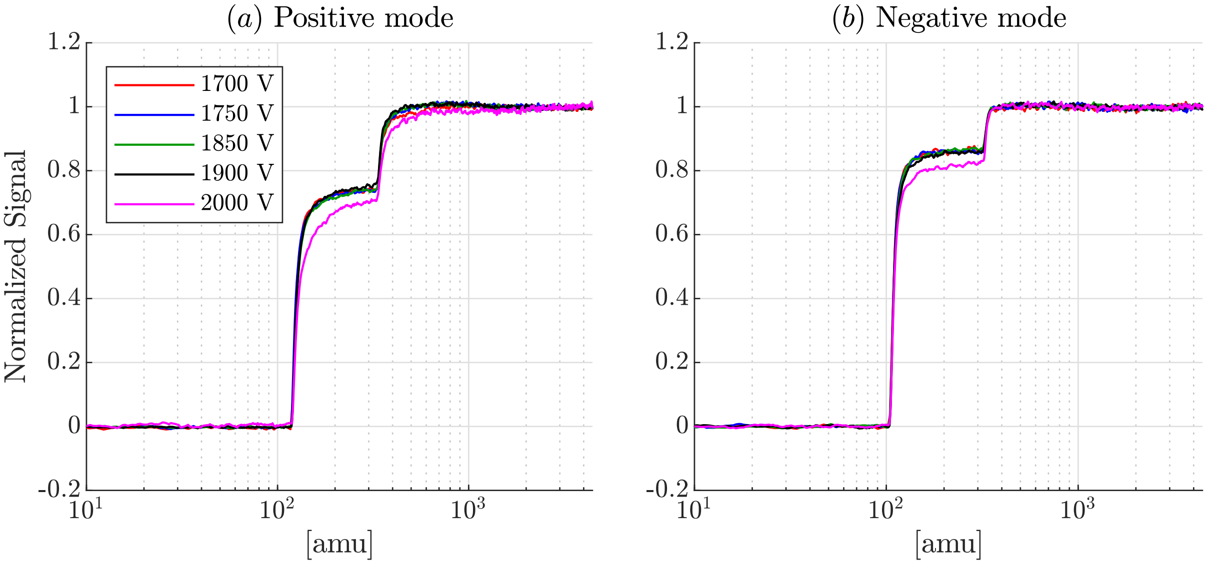

Figure 8-7: [EMIm][HSO$_4$] $T = 40°$C. TOF mass spectrum at different voltages for the positive (subfigure a) and negative (subfigure b).

Species	1650 V	1700 V	1770 V	1850 V	1900 V
[EMIm]$^+$	66	63	62	66	63
[EMIm]$^+$ ([EMIm] [HSO$_4$])	24	29	32	30	33
[EMIm]$^+$ ([EMIm] [HSO$_4$])$_2$	10	8	6	4	5
Higher order clusters	~ 0	~ 0	~ 0	~ 0	~ 0
Average q/m (C/kg)	$4.76 \cdot 10^5$	$4.73 \cdot 10^5$	$4.77 \cdot 10^5$	$4.73 \cdot 10^5$	$4.63 \cdot 10^5$

Table 8.4: [EMIm][HSO$_4$] TOF beam composition for positive mode $T =$ 47°C.

Species	1650 V	1700 V	1770 V	1850 V	1900 V
$[HSO_4]^-$	81	80	78	72	69
$[HSO_4]^-$ ([EMIm] $[HSO_4]$)	18	20	21	26	28
$[HSO_4]^-$ ([EMIm] $[HSO_4])_2$	1	~ 0	1	2	3
Higher order clusters	~ 0	~ 0	~ 0	~ 0	~ 0
Average q/m (C/kg)	$6.79 \cdot 10^5$	$6.65 \cdot 10^5$	$6.65 \cdot 10^5$	$6.11 \cdot 10^5$	$6.01 \cdot 10^5$

Table 8.5: [EMIm]$[HSO_4]$ TOF beam composition for negative mode $T =$ 47°C.

Species	1700 V	1770 V	1850 V	1900 V	2000 V
$[EMIm]^+$	69	65	64	65	53
$[EMIm]^+$ ([EMIm] $[HSO_4]$)	25	26	28	29	34
$[EMIm]^+$ ([EMIm] $[HSO_4])_2$	6	8	8	6	11
Higher order clusters	~ 0	~ 0	~ 0	~ 0	2
Average q/m (C/kg)	$5.15 \cdot 10^5$	$4.80 \cdot 10^5$	$4.75 \cdot 10^5$	$4.89 \cdot 10^5$	$4.26 \cdot 10^5$

Table 8.6: [EMIm]$[HSO_4]$ TOF beam composition for positive mode $T =$ 40°C.

Species	1700 V	1770 V	1850 V	1900 V	2000 V
$[HSO_4]^-$	82	82	80	80	75
$[HSO_4]^-$ ([EMIm] $[HSO_4]$)	17	17	19	20	24
$[HSO_4]^-$ ([EMIm] $[HSO_4])_2$	1	1	1	~ 0	1
Higher order clusters	~ 0	~ 0	~ 0	~ 0	~ 0
Average q/m (C/kg)	$7.17 \cdot 10^5$	$7.13 \cdot 10^5$	$6.82 \cdot 10^5$	$6.94 \cdot 10^5$	$6.43 \cdot 10^5$

Table 8.7: [EMIm]$[HSO_4]$ TOF beam composition for negative mode $T =$ 40°C.

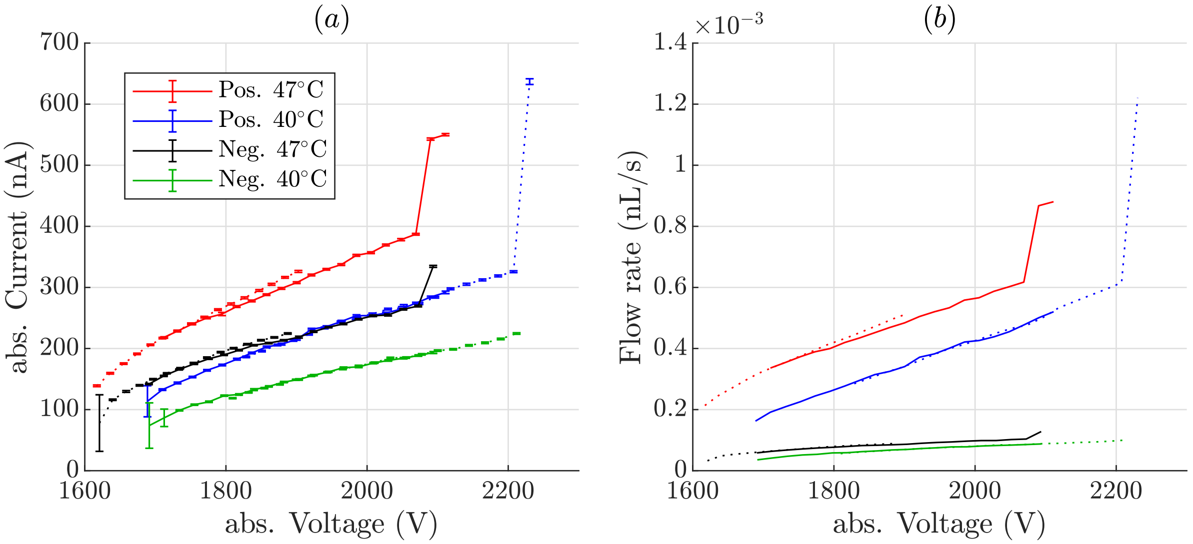

Figure 8-8: (a) experimental current-voltage characteristics obtained with [EMIm][HSO$_4$] at two different temperatures. Solid lines and dotted lines correspond to two different passes of the same source. (b) inferred flow rates by dividing the average data on the left figure by a linear regression fit of the $\frac{\bar{q}}{m}$ as a function of the voltage from data in tables 8.4, 8.5, 8.6, and 8.7.

(a) 1st pass $T = 47.8°\text{C}$

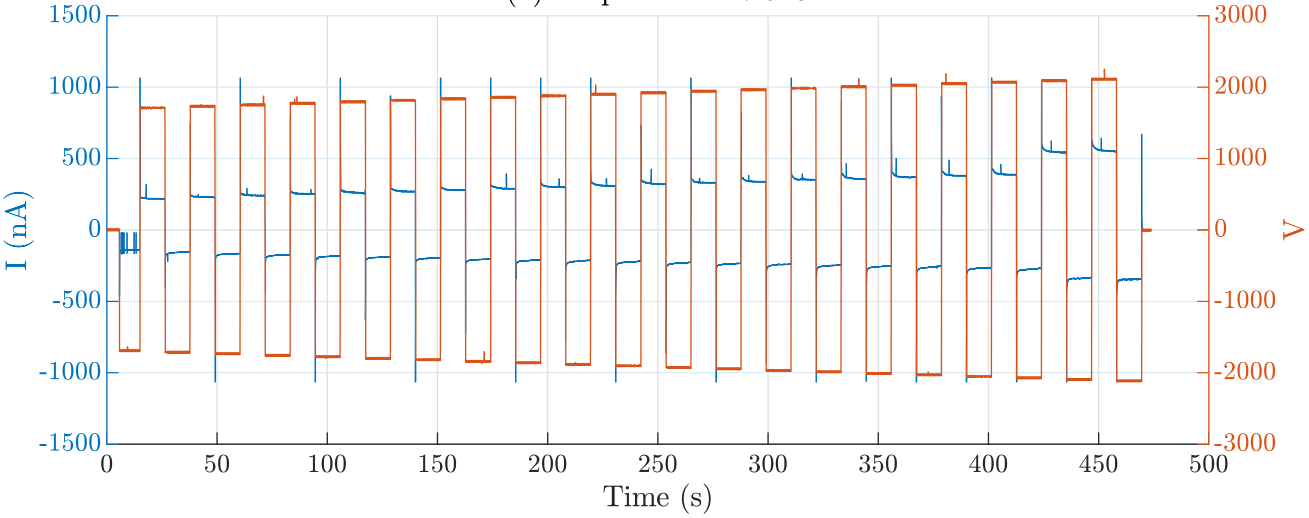

(b) 2nd pass $T = 47.8°\text{C}$

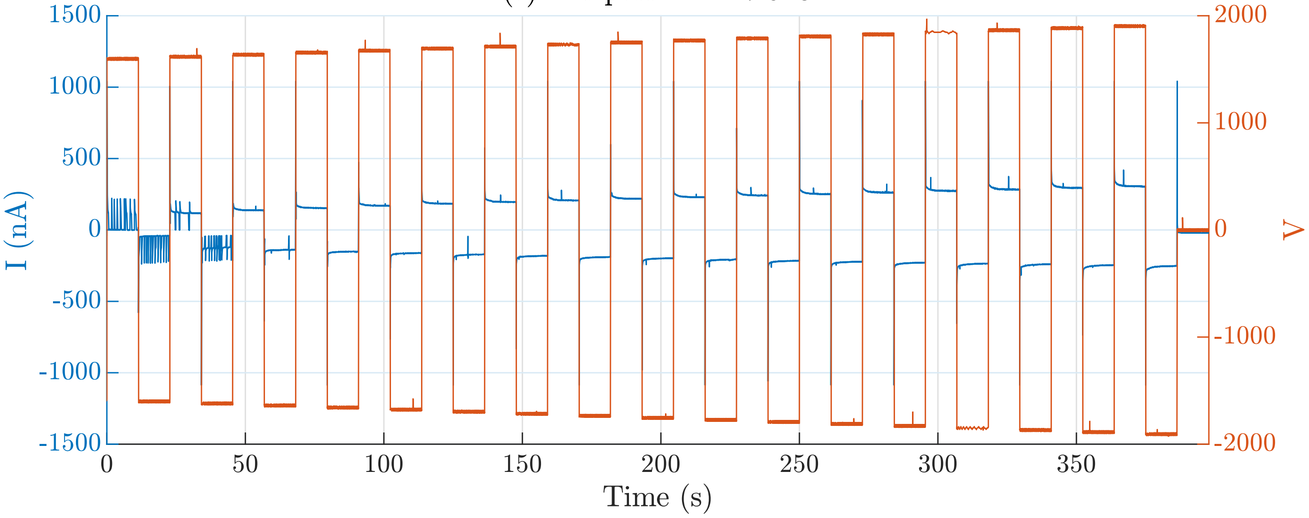

Figure 8-9: Voltage (orange, right vertical axis) and current (blue, left vertical axis) for the two different passes considered in figure 8-8 for [EMIm][HSO$_4$] at $T = 47.8°\text{C}$.

(a) 1st pass $T = 40°\mathrm{C}$

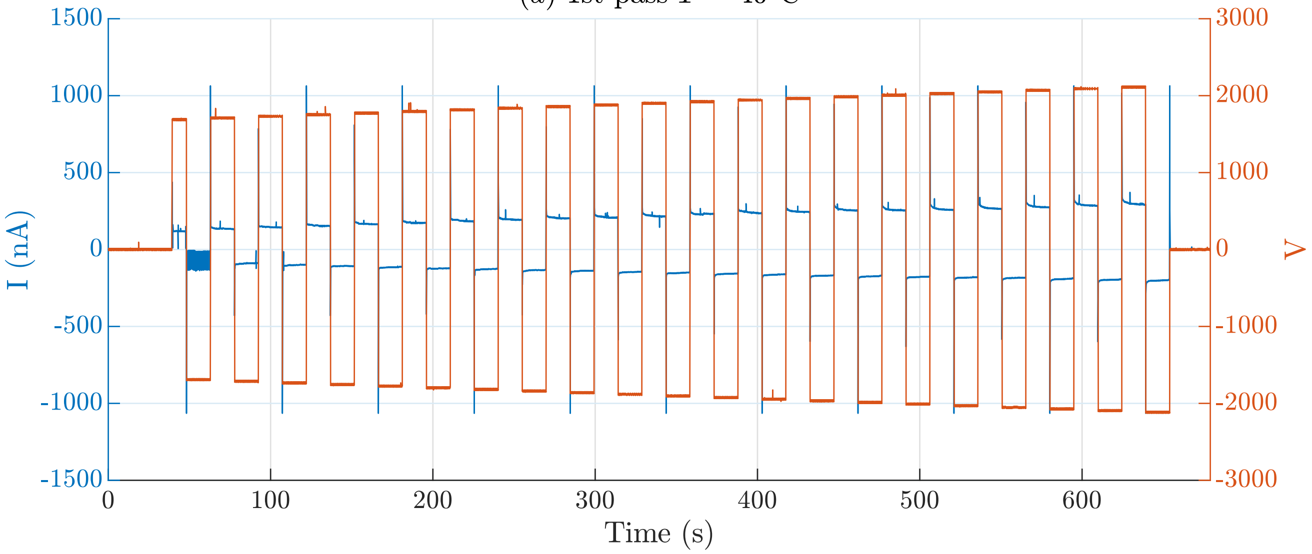

(b) 2nd pass $T = 40°\mathrm{C}$

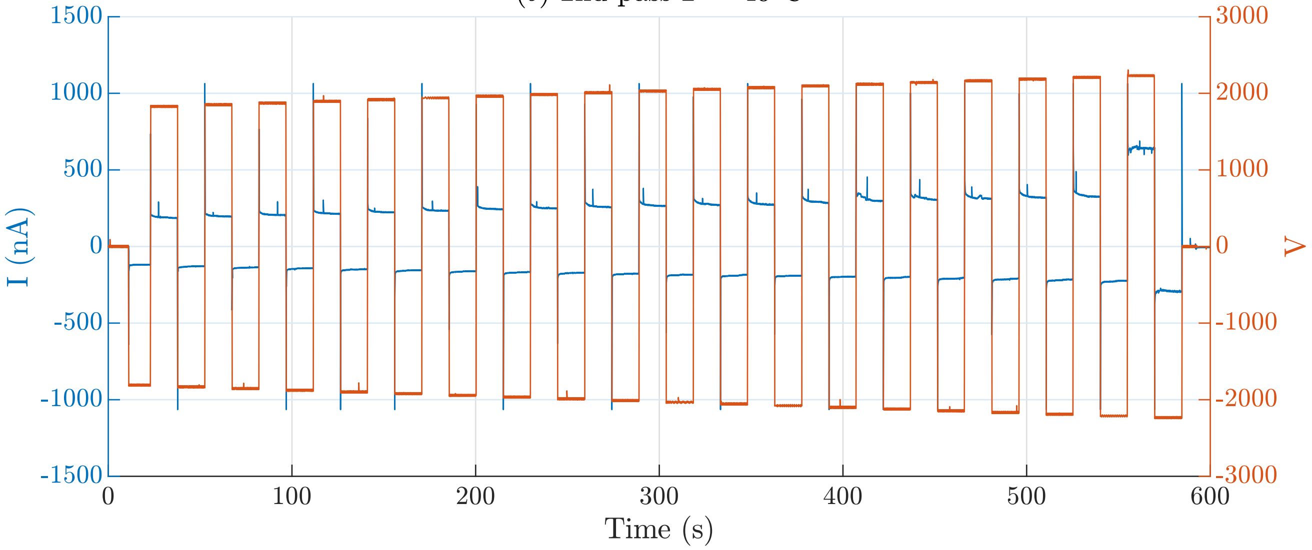

Figure 8-10: Voltage (orange, right vertical axis) and current (blue, left vertical axis) for the two different passes considered in figure 8-8 for [EMIm][HSO$_4$] at $T = 40°\mathrm{C}$.

8.6.3 Discussion

Possible meniscus trajectories

For each of the radii simulated r_0, we can build a map of what impedance Z would reproduce the experimental current-voltage curve in figure 8-11 at different Laplace pressures. Each experimental point is reported in the legend by its voltage and corresponding current. Dotted lines correspond to data belonging to the first dataset, solid lines correspond to data from the second dataset. To ease the readability of the plot, only a few experimental points are plotted.

By looking at the graphs in figure 8-11, we can see how the range of feasible impedances that would reproduce the experimental results expands at smaller radii. A similar expansion of this range of impedances is observed when increasing the negative Laplace pressure (see subfigures 8-11a and b for two different values of the Laplace pressure). The intuition for this observation is that both a negative Laplace pressure and a smaller radius increase the extinction voltage, therefore generally needing a larger span of impedances that could reproduce the experimental results (this was already explained in section 8.2, see for instance red vs. blue lines in figure 8-1).

Another interesting observation when the negative Laplace pressure is increased is that the absolute value of the feasible impedances is generally smaller. The intuition for this observation is that a higher negative Laplace pressure decreases the flow rate, therefore, a less impedance is required to reproduce the experimental results.

Given the charts in figure 8-11 we can hypothesize possible meniscus trajectories along an example current-voltage potential curve (positive mode 47°C). There could be infinite trajectories given the uncertainty of the experimental results. Acknowledging this fact, we consider three example trajectories to illustrate how these charts could be useful. The charts are built for a meniscus that has a specific radius at the first experimental point with less voltage and current (dotted black line, 1617 V, 139 nA), and ends at the last experimental point before the appearance of another emission site (brown solid line, 2069 V, 387 nA). Unless external flow is relevant, according to the theoretical impedance models described in section 8.5.8, the impedance will always grow when the meniscus radius becomes smaller. This is taken into account when proposing feasible trajectories on the charts.

- **Slide** trajectory (magenta arrowed line in 8-11b): The meniscus starts at $r_0 = 4\ \mu\text{m}$ in between the pore size ($r_p \sim 0.4\ \mu\text{m}$) and radius of curvature of the tip ($R_c \sim 10\ \mu\text{m}$), then it can slide slightly along the electrode profile by reducing its size and consequently increasing the impedance.

- **Slide and pin** trajectory (green arrowed line in 8-11a): Similar to the previous one, but in this trajectory, the meniscus may find an edge along the tip profile and pin. It is worth mentioning that when a meniscus pins and there is no external flow (the impedance is solely governed by the porous structure), the impedance should not change significantly. In other words, the meniscus can only pin in regions of the chart that have "packed" lines, or that concentrate a lot of experimental points in a narrow range of feasible impedances.

- **Film decrease and slide** trajectory (blue arrowed line in 8-11a). In this trajectory, the meniscus starts with some radius close to the curvature radius of the tip R_c. Notice that for this case, the lower voltage experimental point is predicted at a higher impedance. At such low Laplace pressures, the liquid film thickness may be large enough to originate $Z_{ext} \sim Z_{pore}$. This film thickness may decrease at higher voltages, boosting Z_{ext}, but effectively decreasing the global Z through eq. 8.5. The meniscus may remain pinned close to the curvature radius until the film thickness is decreased enough for the impedance to be dominated by Z_{pore}, before it starts decreasing its size.

Theoretical impedance matching

We can also note that the theoretical impedance as computed by eq. 8.13 when the permeability is computed as in eq. 8.9 with porosity $\phi_p = 0.4$ and pore size $r_p = 0.4$ μm lies within the predicted impedance-radius band that we simulated when the Laplace pressure is $p_r = -5.7$ kPa (subfigure 8-11b, black line). For a given simulated Laplace pressure of -5.7 kPa, we can plot this radius-impedance feasibility region for the four experimental curves in figure 8-12 (positive and negative modes at 47°C and 40°C). Figure 8-12 also shows the value of the theoretical Z_{pore} impedance obtained by equation 8.13 as a function of the meniscus radius for the viscosities of [EMIm][HSO$_4$] at the two temperatures tested ($\mu(40°C) = 0.533$ Pa s, $\mu(47°C) = 0.355$, $\phi_p = 0.4$, $r_p = 0.4$ μm). We can see that the feasibility region is in agreement with the predicted by Z_{pore} for the positive mode curves.

Flow rate asymmetry and possible explanations

There is a considerable disparity between the set of impedances and radius predicted for the negative mode. We may need almost 3 times more impedance to fit the negative current-voltage curve data, due to the significant low flow rates observed.

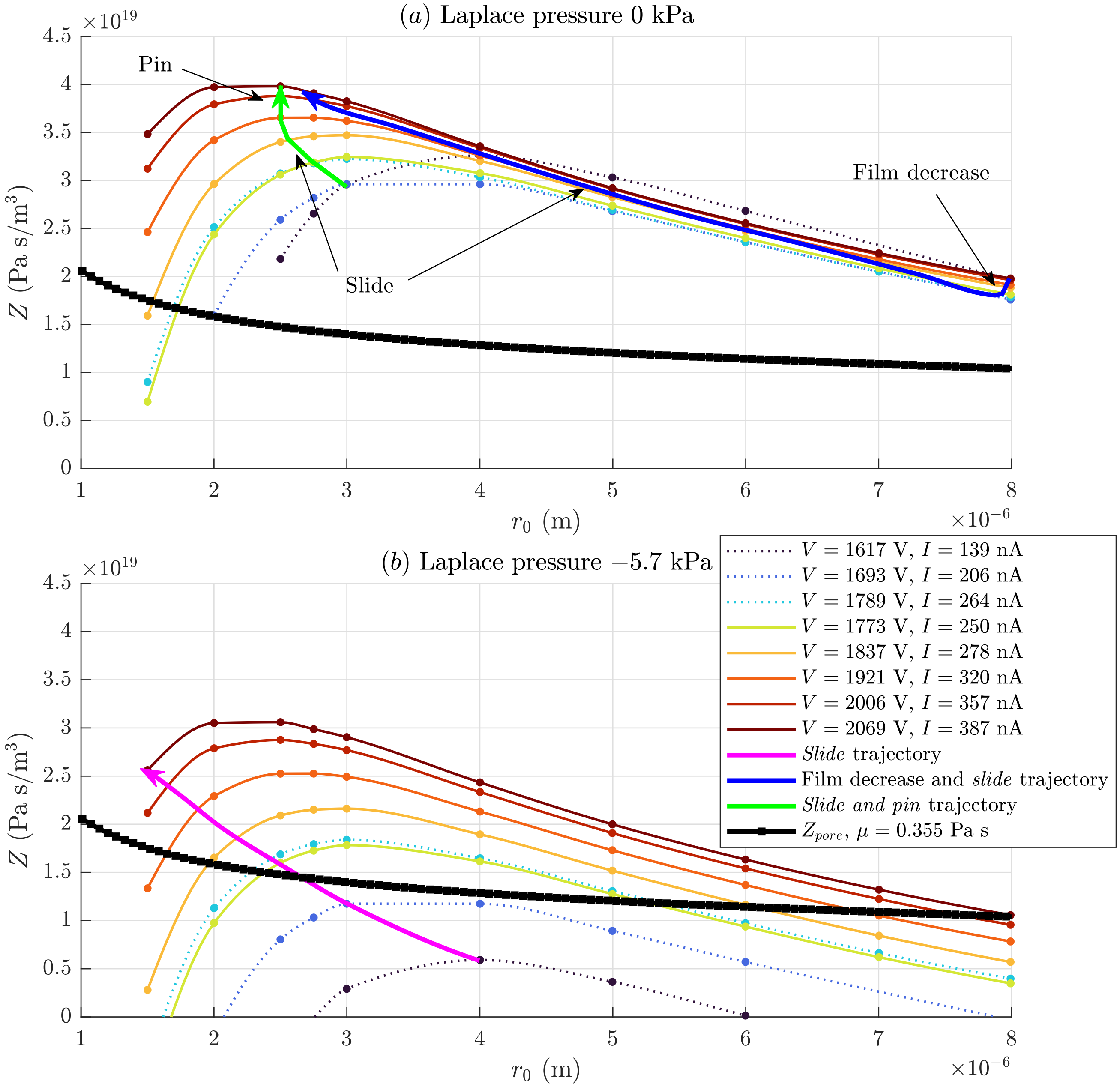

Figure 8-11: Simulated radius-impedance feasibility region that reproduces the experimental data for the positive mode at 47°C for [EMIm][HSO_4].

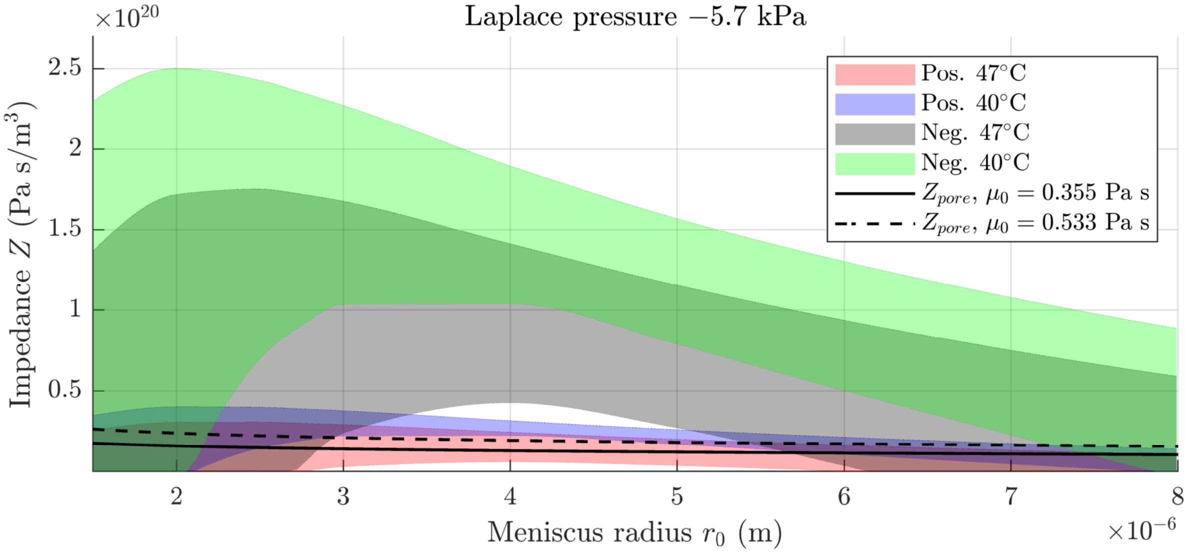

Figure 8-12: Impedance-radius feasibility region for the four experimental curves of [EMIm][HSO$_4$]. The theoretical Z_{pore} agrees well with the positive mode estimations.

The model implemented in this thesis provides a closed current-voltage equation (eq. 8.1), which can be put as a function of the flow rate:

$$Q = \frac{2\gamma}{r_0 Z}\left(f\left(\hat{E}_{tip}, \Theta\right) + \frac{p_r r_0}{2\gamma}\right) \tag{8.15}$$

If the model was validated, the flow rate should be the same at the same positive or negative voltage ($\hat{E}_{tip}$ does not change), geometry, Laplace pressure, meniscus radius, and impedance. This fact has not been observed with this liquid, given the disparity of the flow rates between the positive and negative modes at the same voltage magnitude.

1. **Possibility 1**. There could be a significant portion of the beam in the negative mode that is composed of higher-order ion clusters and is **rapidly fragmenting** into monomers: essentially, this might happen immediately after emission. In such cases, only the monomer byproduct of these fragmentations can be seen in the time of flight curves. These monomers are hardly differentiable from unfragmented monomers emitted by the meniscus, at least with the resolution of our TOF setup. This would bring the effective charge-to-mass ratio that is observed significantly down and would increase the flow rate that we have

estimated from these curves.

2. **Possibility 2**. **Parameters of eq 8.15 change between the positive and negative modes**. We have seen that a change in either the surface tension, radius and Laplace pressure has an effect on the extinction voltage: either by changing $\hat{E}_{tip}$, or by changing $\frac{p_r r_0}{2\gamma}$ in eq. 8.15. By looking at the data from figure 8-8 we hypothesize that this situation is unlikely. Instead, the model suggests that what could be changing for different polarities is the hydraulic impedance Z.
   Flow rate disparity is a phenomenon that has been observed for some ionic liquids. Experimental evidence suggests that this asymmetry is very sensitive to the material of the emitter, and it seems to be exacerbated for some dielectrics [40, 57]. The permeability models that are typically used to compute the impedance of porous emitters are purely geometrical (effective pore size, and porosity), they assume Darcy flow and are insensitive to how the boundary layer of the flow changes with the floating potential of the ionic liquid. Even when there is distal contact far away from the tip that keeps electrochemical reactions away from the tip, where the impedance is actually relevant, there is a potential drop between the ionic liquid, and the floating potential of the carbon monolith across the double layer. In this sense, effects related to ionic liquid electroviscosity [8] may play a significant role, and may differ significantly under different liquid polarities.

   In addition, we may argue that while small, an electric field inside the liquid could exist: it is necessary to transport charge via conduction towards the emission region of the meniscus. Charges can also be transported via convection through the double layer (slip velocity).

   In either case, the idea of an impedance depending on the polarity of operation through the physics of the double layer may be worth investigating. The interaction of this double-layer charge with the electric field inside the liquid could be dependent on the material properties, and its floating charge, and could also modify significantly how the boundary layer of the fluid behaves with the porous structure, for instance by inducing what is known as electroosmotic motion [136]. Electroosmotic flow is known to alter the effective impedance of porous media [103].

How small is the electric field inside the liquid? Could it be relevant to induce electroosmotic motion?

As an example, consider a modified version of Darcy's law for a capillary emitter of the same radius of the meniscus r_0, with a fully relaxed Hagen-Poiseuille flow modified to include the effects of an electric field inside the liquid parallel to the core flow E_{in} [143]:

$$Q = \frac{-r_0^2 A}{8\mu}\nabla p + \frac{\varepsilon_0 \varepsilon_r \psi_0 E_{in} A}{\mu}\left(\frac{2I_1\left(\frac{r_0}{\lambda_d}\right)}{\frac{r_0}{\lambda_d}I_0\left(\frac{r_0}{\lambda_d}\right)} - 1\right) \tag{8.16}$$

A is the area of the capillary, I_0 and I_1 are the modified Bessel functions of the first kind of orders 0 and 1 respectively, λ_d is the Debye length, and ψ_0 is the Zeta potential, or the potential across the double layer at which charges are not adsorbed to the walls of the capillary, therefore are mobile. The Zeta potential is highly dependent on the charged state of the electrode, the material, and the adsorption characteristics of the ions on the porous electrode, which may significantly change during voltage alternation. An estimation of the electric field inside the liquid can be done by considering a pure bulk conduction charge transport as:

$$E_{in} \sim \frac{j}{\kappa} = \frac{I}{A\kappa} = \frac{Q\rho\frac{q}{m}}{A\kappa} \tag{8.17}$$

Substituting 8.17 in 8.16, and introducing the capillary hydraulic impedance as $Z = \frac{r_0^2 A}{8\mu}$ yields:

$$ZQ\left(1 - \frac{\varepsilon_0\varepsilon_r\psi_0\rho\frac{q}{m}}{\Lambda}\left(\frac{2I_1\left(\frac{r_c}{\lambda_d}\right)}{\frac{r_c}{\lambda_d}I_0\left(\frac{r_c}{\lambda_d}\right)} - 1\right)\right) = -\nabla p \tag{8.18}$$

Where $\Lambda = \kappa\mu$ is the Walden constant of the ionic liquid.

For porous emitters of $r_0 \sim 1$ μm, then the ratio $r_c/\lambda_d \to \infty$, and equation 8.18 yields an "effective impedance" Z_E:

$$Z_E = Z\left(1 - \frac{\varepsilon_0\varepsilon_r\psi_0\rho\frac{q}{m}}{\Lambda}\right) \tag{8.19}$$

Considering $q/m \sim 6 \cdot 10^5$ C/kg, $\varepsilon_r \sim 15$, $\rho \sim 1250$ kg/m^3, Walden constant of $\Lambda \sim 0.025$ S/m Pa s, and Zeta potential around $\psi_0 \sim -90$ mV, the effective impedance $Z_E \sim 1.45Z$ is almost 50% more than the one considered without electroosmotic flow. While this is a very crude estimation, it could serve as a motivation for future studies on double layer effects on the impedance.

Chapter 9

Existence of static solutions and small perturbation dynamics: axially symmetric linear stability analysis of the meniscus

In this chapter, we have a look at:

1. Limits to the existence of static solutions, including the space charge problem. For doing this we explore selected values of the parameter space (electrical conductivity κ, critical field through ΔG, meniscus radius r_0 and hydraulic impedance Z).

2. Unstable perturbations of the static solutions in the low-frequency domain. For doing this, we use an eigenvalue decomposition of the problem dynamics.

9.1 Limitations for the claims about the stability of the meniscus

Prior to discussing any results on this section it is necessary to establish the limitations for any of the stability observations that we report in this chapter.

9.1.1 Limitations for the static stability problem

We are discussing sets of parameters where we could not find any static solution **with the numerical scheme that we present in this thesis**. Solutions to the static problem may exist, but may not be capturable with the scheme that we considered in this thesis, namely, with our specific laplacian shape of the numerical meniscus map (see eq. B.17 in the annex: $\hat{\nabla}^2_{(\eta,\xi)}\hat{y} = 0$), or the detailed resolution of our mesh. For example, we were able to obtain static solutions to this problem that were thought to not exist at lower fields [20] by only changing the numerical approach (the existence of a hysteresis region).

9.1.2 Limitations to the dynamic stability problem

There are two main limitations:

1. We are computing unstable growth rates of solutions based on **linearized** dynamics of the problem. For example, the fact that we find a perturbation that grows in time or deviates the solution from its steady state value does it up to a very narrow window of time ahead. More future work will be needed to characterize the nature of such growth (i.e, jet development, pulsation, dripping, etc).

2. We are restricting ourselves to the **low frequency perturbation range** for two reasons. The first one, is that eigenvalue problems are very expensive computationally and only a narrow region of the dynamic modal decomposition can be explored and saved with our computational resources. The second one is that high frequency perturbations could have physics that we may not be taking into account with the electrohydrodynamic model presented in this thesis, for instance assuming that the electric field is conservative (e.g, neglecting possible magnetic effects, exacerbated at high frequencies).

9.2 Existence of static solutions

For this analysis, we use the reduced computational domain 3-2, with the same dimensionless numbers described in chapter 5 (tables 5.1 and 5.2), except in parameters that we explicitly vary to analyze their study. The criterion for not finding a solution is that the residual, or $\|\mathbf{F}\left(\mathbf{x}_i, \mathbf{x}_T, \hat{\rho}^v_{sch}\right)\|_2$ (eqs. 4.19, 4.20) gets stuck or even diverges along the iterative process for a close enough initial guess (see algorithm 1 in chapter 4).

9.2.1 Effect of the hydraulic impedance

For a given radius of $r_0 = 2.5$ μm, we have computed the range of $\hat{E}_{tip}$ where we found solutions at several hydraulic impedances and two different ΔG values: 1.1 and 1.2 eV. In dimensionless terms, the simulated radius is $\hat{R} = 81.4$ for $\Delta G = 1.1$ eV, and $\hat{R} = 115.3$ for $\Delta G = 1.2$ eV. Results are shown in figure 9-1 where the correspondent dimensionless flow rate $\hat{Q}$ at the simulated impedance is shown in the y-axis. The flow rate is made dimensionless $\left(\hat{Q} = \frac{Q}{Q_0}\right)$ by the characteristic capillary velocity $u_c = \frac{\gamma_0}{\mu_0}$[1]:

$$Q_0 = \frac{\gamma_0}{\mu_0} r_0^2 \tag{9.2}$$

Since the reference impedance Z^* depends on ΔG through r^*, it is more convenient to show the results as a function of the dimensional impedance Z. Solutions for the $\Delta G = 1.2$ eV only exist in the dashed part of the colored lines. If ΔG is decreased to 1.1 eV, the set of values of $\hat{E}_{tip}$ and $\hat{Q}$ for which there is a solution are represented by both the dashed and solid section of the line.

For impedances smaller than $Z = 2 \cdot 10^{19}$ Pa s/m^3, the range of $\hat{E}_{tip}$ where our algorithm converges is very limited (especially for the $\Delta G = 1.2$ eV case), and concentrated in the vicinity of the extinction voltage. We can see how generally speaking, increasing the hydraulic impedance for a given field reduces the total flow rate (or current) output, yet the range of electric fields where a static solution to the problem is found becomes larger. At higher hydraulic impedances, it appears that the maximum dimensionless flow rate $\hat{Q}$ at which a solution is found tends to increase. When the impedance is further increased, the dimensionless range of electric fields keeps increasing, until it cannot increase anymore: it finds the turning point of higher fields in region **III**, which is likely associated with the bifurcation of the meniscus, as we saw in chapter 6 and will show experimentally in chapter 7 for the cone-jet regime. The results of figure 9-1 suggest the existence of a *sweet spot* of impedance for the computed radius, or the impedance whose maximum flow rate $\hat{Q}_{max}$ is found at exactly the dimensionless field of presumable bifurcation. In the figure 9-1, this *sweet spot* impedance is found for $\Delta G = 1.1$ eV in between those

---

[1] We prefer to present the results as a function to $\hat{Q}$, because in the dimensionless framework that we chose for this problem, $\hat{Q}$ does not change when we change the reference conductivity κ_0, unlike $\hat{I}$. The relationship between $\hat{I}$ and $\hat{Q}$ is up to a constant depending on the simulation parameters

$$\hat{Q} = \frac{\kappa_0 E_c \mu_0}{\rho \frac{q}{m} \gamma_0} \hat{I} \tag{9.1}$$

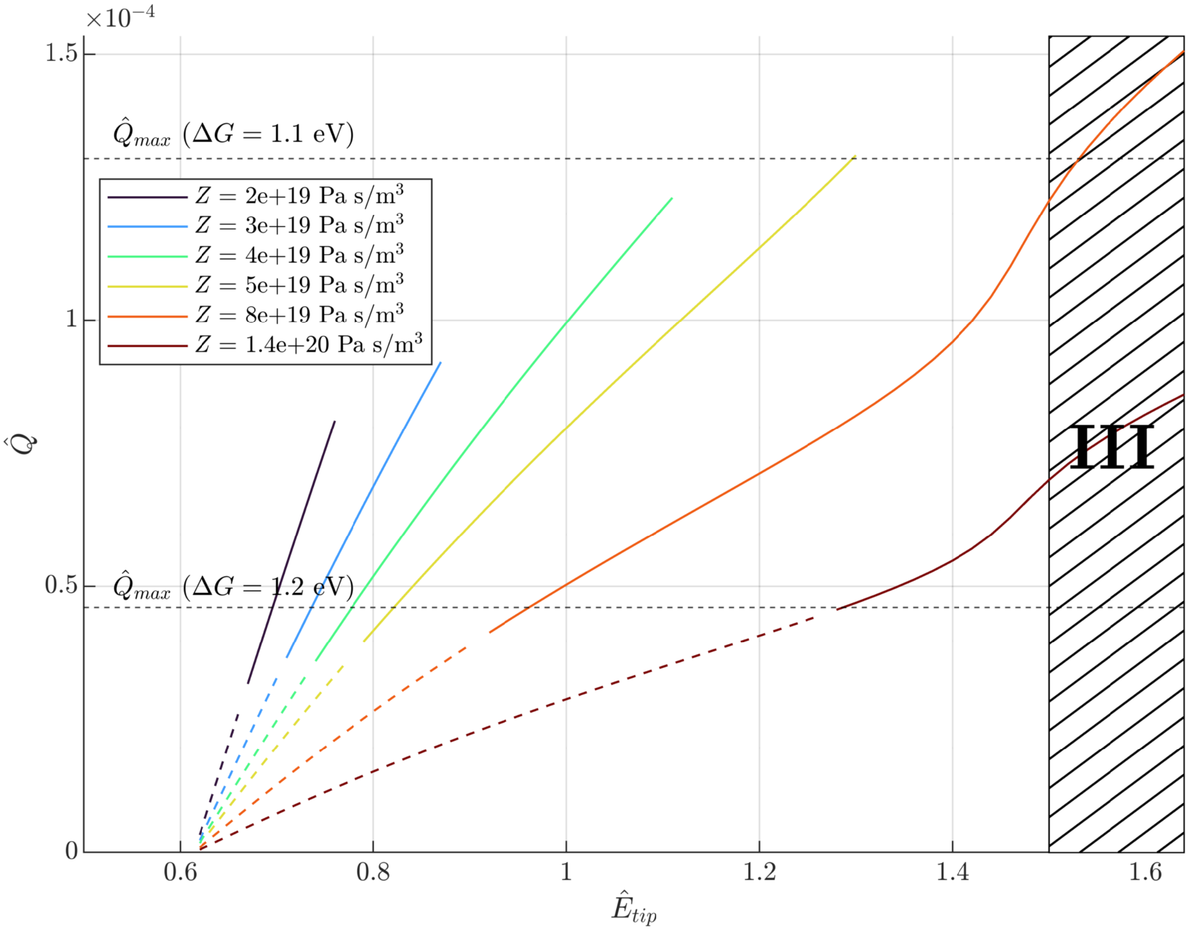

Figure 9-1: Flow rate-field curves for different hydraulic impedances. The unstable region III after the turning point where the meniscus presumably bifurcates is shown as the shaded area to the right. Results shown for two different values of ΔG. The range of $\hat{Q}$ and $\hat{E}_{tip}$ where we found stable solutions for the smaller value $\Delta G = 1.1$ eV are solid and dashed lines, whereas for $\Delta G = 1.2$ eV, solutions were only found at the dashed lines.

corresponding to the yellow and orange lines ($Z_{opt} \in [5 \cdot 10^{19}, 8 \cdot 10^{19}]$ Pa s/m^3). Impedances lower than Z_{opt} would reach dimensionless pure ionic flow rates that 1) are lower than $\hat{Q}_{max}$ at such radius, and 2) are stable within a smaller range of $\hat{E}_{tip}$. Any impedance greater than Z_{opt} would yield stable solutions within the full range of $\hat{E}_{tip}$, but will find the presumably bifurcation region (region **III**) before reaching their maximum current.

9.2.2 Effect of ΔG

From the results of figure 9-1 we observe that as shown in chapter 5, the ΔG does not affect the magnitude of the current, but it decreases the range of $\hat{E}_{tip}$ and $\hat{Q}$ where the algorithm converges. If the difficulty of converging is a symptom of decreasing stability as assumed in this section, then, for the conditions simulated in this analysis, we can envision a maximum ΔG above which the pure-ion regime is not possible. This fact would support Romero-Sanz hypothesis [107] of why general organic solvents with electrical conductivities higher than ionic liquids have never reached the pure ionic regime: they have higher solvation energies, and would need a high enough critical field to trigger ion emission. High enough that the surface tension and hydrodynamic stress cannot stabilize the emission region, and the interface may not be stable in the pure-ion regime.

9.2.3 Effect of electrical conductivity

Similar to the critical field for emission in the previous subsection, increasing the conductivity does not change the magnitude of the current or flow rate, but it increases the ranges of both $\hat{E}_{tip}$ and $\hat{Q}$ where the algorithm converges. Due to our limited computation capabilities, figure 9-2 illustrates this fact with only one flow rate-voltage curve. The values of $\hat{Q}_{max}$ at each κ_0 are an approximate lower bound, since they could vary slightly with the impedance, as seen in figure 9-1.

9.2.4 Effect of the meniscus radius r_0

Figure 9-3 shows the combination of meniscus radius r_0 and E_{tip} where we found solutions to the meniscus equilibrium problem for $\Delta G = 1.1$ eV. We changed the reference field in figure 9-3 for the non-dimensionalization to E^* for ease of understanding, since the nominal one $E_c = \sqrt{\frac{4\gamma_0}{r_0\varepsilon_0}}$ used in this thesis also depends on the radius r_0. The radius of the meniscus in the y-axis of figure 9-3 is non-dimensionalized by the curvature radius ($R_c = 10$ μm). The non-emitting region **I** is separated from

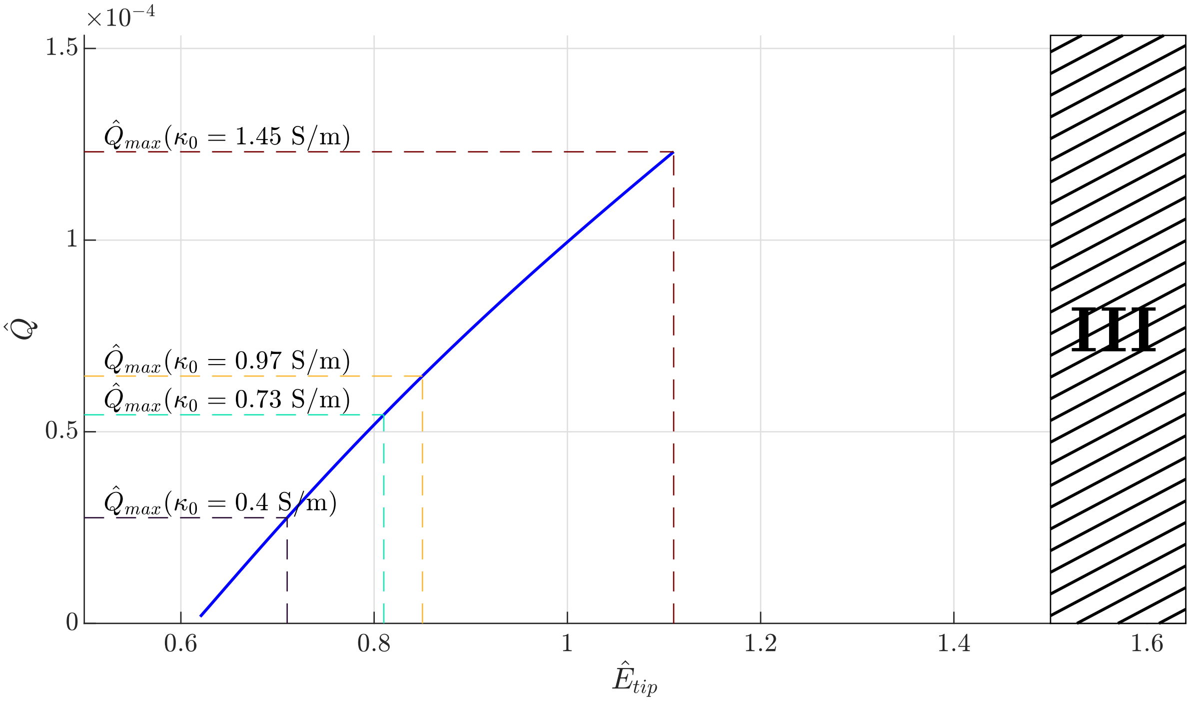

Figure 9-2: Flow rate-field curve at different electrical conductivities. Results shown for the same example parameters as in the previous section, with $\Delta G = 1.1$ eV, and $Z = 4 \cdot 10^{19}$ ($\hat{Z} = 0.021$).

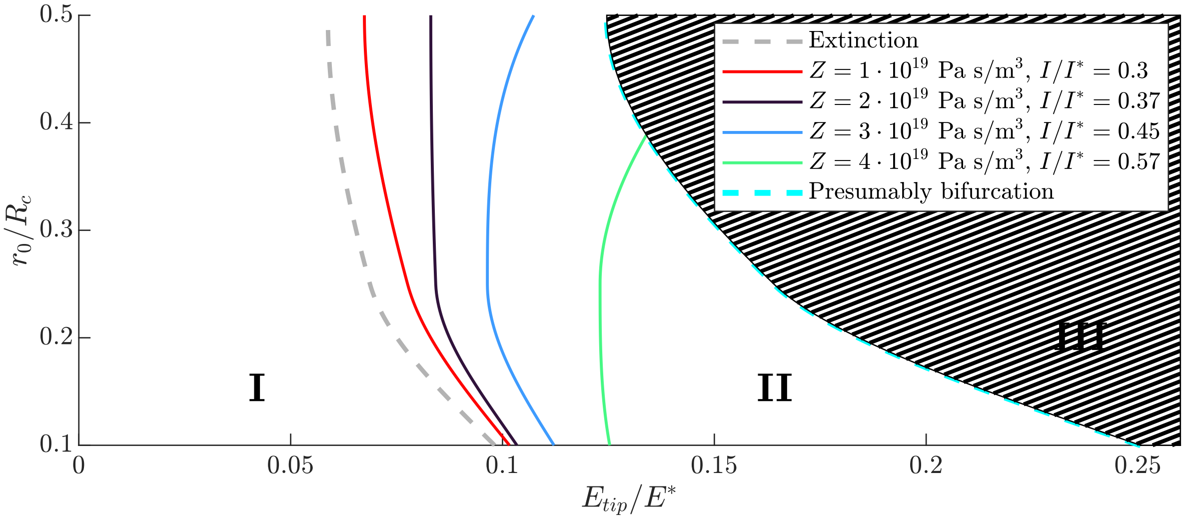

Figure 9-3: Static stability diagram for different hydraulic impedances and $\Delta G = 1.1$ eV. The range of electric fields and radii where solutions were found is located to the left of the curves at selected impedance values.

the emitting region **II** by the grey dashed line. The overlap region is small enough to be ignored. We could only find solutions at the left of the colored lines. The colored lines are at fixed impedance. The model shows that such lines also very approximately correspond to an iso-current/flow rate line in *dimensional* terms. Since our reference value for the flow rate Q_0 also depends on the radius, the dimensionless value $\hat{Q}$ would change depending on the radius. As a consequence, it is convenient to show the correspondent approximate iso-current/flow rate line in the legend of figure 9-3 non-dimensionalized with the I^* defined in eq. 1.9, which does not depend on r_0, but on r^* (constant for all the data shown in figure 9-3). The relationship to $\hat{Q}$ is:

$$\hat{Q} = \frac{\mu_0 I^*}{\rho \frac{q}{m} \gamma_0 r_0^2} \left(\frac{I}{I^*} \right) \tag{9.3}$$

and to $\hat{I}$:

$$\hat{I} = \frac{32\pi \gamma_0^2 \varepsilon_r}{r_0^2 E_c \varepsilon_0^2 E^{*3} \left(\varepsilon_r - 1\right)^2} \left(\frac{I}{I^*} \right) \tag{9.4}$$

We can see how generally speaking, when the impedance is increased, the range of r_0/R_c and E_{tip}/E^* expands. It cannot expand without limit: as also shown in the previous figure 9-1, the stability ends at region **III** after the turning point of presumable bifurcation (shown in cyan in figure 9-3). An interesting observation of figure 9-3 is that higher currents/flow rates are only accessible when the radius is sufficiently small. For larger radii and a fixed impedance, the meniscus presumably bifurcates before reaching the limit iso-current/flow rate line.

9.2.5 Discussion

Both a lower ΔG and higher κ have a common effect on the meniscus, which is to decrease the electric field at the apex of the meniscus.

The decrease in ΔG is more intuitive as it lowers the critical field required for ion emission. This means that the meniscus can emit ions at a lower electric field at the apex. The effect of conductivity may be less immediately noticeable, but we can refer the reader to figure 5-5c in chapter 5 for a better understanding. In the Iribarne and Thomson model implemented in this thesis [67], the current density is influenced by the interfacial charge density on the meniscus interface (σ), the interface temperature (T), and a term that exponentially affects the current density based on the deviation of the normal electric field from the critical field of emission.

A higher conductivity of the meniscus results in a more relaxed interfacial charge distribution, or in other words, a higher value of σ. If a meniscus with higher conductivity emits a certain current determined by the upstream conditions of the flow (such as impedance and reservoir pressure), it would require less temperature and electric field at the apex to satisfy these upstream conditions compared to a meniscus with lower conductivity simply because the interfacial charge σ is higher.

The dimensionless electric field at the emission region being higher may potentially play a significant role in triggering an instability that leads to the breaking of the meniscus apex. This situation goes beyond the capabilities of the static model to predict. However, it appears that the emitting apex tends to be more stable when the current demand is distributed over a larger area within the emission region, resulting in a larger effective emission area instead of having larger electric fields with more current density concentrated at the apex.

Another insight could stem from the need for the meniscus to compensate for the increased electric stress by curving the apex further. This adjustment, while addressing the higher stress, comes at the cost of reducing the total available emission area. Consequently, this trade-off could impose a limit on the amount of current that can be extracted from the meniscus, particularly when the electric field at the vacuum is higher. A simplified lumped parameter model is presented as follows to better explain this. We can start with the interfacial charge jump condition in eq.

3.8:

$$\sigma = \varepsilon_0 E_n^v - \varepsilon_0 \varepsilon_r j_n^e / \kappa \tag{9.5}$$

where in the last identity we have substituted the electric field in the liquid with the Ohmic conductivity model. We can substitute σ in eq. 9.5 using the kinetic law for ion evaporation (eq. 1.6) to give a dimensionless expression for the current density normal to the meniscus interface as:

$$j_n^e = \frac{\varepsilon_0 \kappa}{\varepsilon_r} \frac{E_n^v}{\frac{h\kappa}{\varepsilon_0 \varepsilon_r k_B T} \exp \frac{\Delta G}{k_B T} \left(1 - \sqrt{\frac{E_n^v}{E^*}}\right) + 1} \tag{9.6}$$

If the emission region is modeled as a spherical cap, and neglecting the electric field in the liquid and tangential stress, then the balance of normal stresses 3.38 yields:

$$\frac{1}{2} \varepsilon_0 E_n^{v^2} = \frac{2\gamma}{r_c} \tag{9.7}$$

where r_c is the radius of curvature of the spherical cap emission region. The total current emitted in this lumped parameter model $I^L = 2\pi r_c^2 j_n^e$, can be used to substitute the radius of curvature in equation 9.7:

$$\begin{aligned} I^L &= \frac{32\pi\gamma^2}{\varepsilon_0 \varepsilon_r E_n^{v^3}} \frac{\kappa}{\frac{h\kappa}{\varepsilon_0 \varepsilon_r k_B T} \exp \frac{\Delta G}{k_B T} \left(1 - \sqrt{\frac{E_n^v}{E^*}}\right) + 1} \\ &= \frac{32\pi\gamma^2}{t_e E^{*^3} \frac{E_n^{v^3}}{E^{*^3}}} \frac{1}{\frac{t_m}{t_e} \exp \psi \left(1 - \sqrt{\frac{E_n^v}{E^*}}\right) + 1} \end{aligned} \tag{9.8}$$

where the superscript L indicates "lumped parameter model", $\psi = \frac{\Delta G}{k_B T}$, $t_e = \frac{\varepsilon_0 \varepsilon_r}{\kappa}$ is the electrical relaxation time, and $t_m = \frac{h}{k_B T}$ is the characteristic ion emission time; all of them evaluated in the emission region (e.g, with the extra temperature originated due to Ohmic heating in the emission region). Interestingly, eq. 9.8 shows a maximum current. The value of this maximum is not available with an exact analytic closed form, but we have found an asymptotic solution that can be expressed as:

$$I_{max}^L \approx \frac{192\pi}{7} \frac{\gamma^2}{t_e E^{*^3}} \left(\frac{1}{1 + \ln\left(6 \frac{t_m}{t_e}\right) / \psi} \right)^6 \tag{9.9}$$

If we make eq. 9.9 dimensionless with the I^* defined in eq. 1.9 when $\varepsilon_r \gg 1$ then:

$$\left(\frac{I}{I^*}\right)^L_{max} \approx \frac{6}{7}\left(\frac{1}{1+\ln\left(6\frac{t_m}{t_e}\right)/\psi}\right)^6 \tag{9.10}$$

In terms of the dimensionless flow rate:

$$\hat{Q}^L_{max} \approx \frac{I^L_{max}}{\rho\frac{q}{m}Q_0} \approx \frac{192\pi}{7}\frac{\gamma\mu_0 r_0^2}{t_e {E^*}^3 \rho\frac{q}{m}}\left(\frac{1}{1+\ln\left(6\frac{t_m}{t_e}\right)/\psi}\right)^6 \tag{9.11}$$

The derivation of equation 9.9 can be found in the annex. Although the physics underlying equation 9.9 are far from complete, this simple equation captures all the experimentally observed factors that enhance the maximum current achievable by a pure-ion ionic liquid source. These factors include a higher surface tension (γ), a lower critical field for emission (E^*), and a shorter charge relaxation time facilitated by a high conductivity (t_e) [54]. E^* and κ were explicitly studied in this section[2]. The effect of a heated emission region expanding the maximum flow rate or current that can be emitted by the meniscus [42] seems to also be represented by I^L_{max} in eq. 9.9, through the power-6 coefficient: higher emission region temperature leads to a lower ψ, which decreases the denominator of the power-6 term[3] and enhances the maximum current allowed in the pure-ion regime according to this model I^L_{max}.

Temperature also decreases the term t_m inside the logarithm, but this dependency dominates less than ψ.

It is important to emphasize that equation 9.9 would represent an *upper bound* for the maximum attainable current in the pure-ionic regime or flow rate. However, it does not address the mechanism by which this flow rate is achieved. According to this model, the key to reaching the maximum current or flow rate lies in the upstream conditions of the flow, as discussed in chapter 6.

9.2.6 Summary and connection to the cone-jet regime

The findings from chapter 6 suggest that the flow rate (or current) in the pure-ion regime is governed by simple hydrodynamics, specifically the reservoir pressure p_r, hydraulic impedance Z and dimensionless extracting field $\hat{E}_{tip}$, together with two

---

[2] E^* was studied through ΔG.

[3] The term inside the logarithm is usually $\frac{6t_m}{t_e} < 1$, for typical values of ionic liquids, thus the logarithm is negative.

parameters of the meniscus (γ and r_0). Comparisons with existing literature in chapter 7 suggest that under steady conditions, the control of this flow rate through the external field E_{tip}, Z, p_r, r_0 and γ could be universally applicable for all electrospraying, given certain assumptions like impedance-dominated flow with Darcy's law and negligible space charge effects. We represented this universal steady flow rate with a dimensionless equation (eq. 6.31 in chapter 6):

$$Q = \frac{2\gamma}{Zr_0}\left(f\left(\hat{E}_{tip}, \Theta\right) + \frac{p_r r_0}{2\gamma}\right) \tag{9.12}$$

A significant implication of this finding is that details such as conductivity (κ) and critical field for emission (E^* or ΔG) do not affect the total flow rate emitted. Instead, these details only influence the structure of the apex of the electrospray. The apex structure adapts itself to the flow rate dictated by eq. 9.12. When the flow rate is very high, the apex breaks, and the emission region forms a thin jet. The shape of the base cone remains relatively unchanged, provided the emission region is much smaller than the meniscus base. As a result, despite our simulations having a closed emission region interface, we could accurately reproduce the most axially-symmetric shapes of the cone-jet (see figure 7-3).

The next question is to determine the flow rate beyond which the pure-ion regime is no longer sustainable. Conductivity κ and ΔG play a crucial role here; they increase the range of $\hat{Q}$ in which the pure-ion regime is stable. In other words, they determine the limits of the existence of the pure-ion regime or the ability of the emission region to be stable in a **closed configuration** while emitting ions in steady state.

For clarity, we can summarize these findings in a flow rate-current framework commonly used in the experimental literature of electrospraying (figure 9-4). At low flow rates, the pure-ionic regime holds, and the current scales proportionally to the flow rate according to the continuity equation:

$$I/I_Q = \rho\frac{q_i}{m_i}\frac{Q}{I_Q} = \hat{Q} \tag{9.13}$$

Here, $I_Q = \rho\frac{q_i}{m_i}Q_0$ is a characteristic current made dimensionless with constants independent of conductivity and ΔG. The term q_i/m_i represents the characteristic charge-to-mass ratio of the spray in the pure-ion mode[4]. On the other hand, at higher flow rates, the droplet mode prevails, and the dimensionless current follows

---

[4] The subscript i is included in q_i/m_i to reference exclusively to the average charge-to-mass ratio of the molecular ions (not to be confused with the general q/m of the electrospray.)

Prof. Fernández de la Mora's scaling:

$$I/I_Q = \frac{f_{FdM}\left(\varepsilon_r\right)}{r_0^2\rho}\frac{m_i}{q_i}\sqrt{\frac{\gamma\kappa\hat{Q}}{\varepsilon Q_0}} \tag{9.14}$$

The higher conductivity and lower ΔG expand the range of $\hat{Q}$ where the pure-ion regime is sustainable, increasing $\hat{Q}_{max}$. Beyond $\hat{Q}_{max}$, our algorithm fails to converge to a steady solution. It is hypothesized, under the limitations stated at the beginning of this chapter in section 9.1.2, that if no steady solution exists, a dynamic oscillatory regime may dominate the apex of the meniscus before the apex develops a jet, marking the beginning of the mixed mode [62].

Notably, Romero-Sanz *et al.* [107] report the nature of this transition for [EMIm][BF$_4$]. Romero-Sanz *et al.* data has been added to figure 9-4 in blue dots. We use the reference parameters I_Q and Q_0 with a charge-to-mass ratio $q_i/m_i = 4.8$ C/kg, and $r_0 = 10\ \mu$m (same as the internal radius of the capillary used in [107]) to present the data. When approached from the pure droplet mode, ion emission starts earlier at higher conductivities κ and lower ΔG, consistent with experimental observations and the scalings proposed by Prof. Gamero [45]:

$$Q_{min}^{droplet} \propto \frac{f_{FdM}^2\left(\varepsilon_r\right)\gamma^3}{E^{*6}}\frac{\kappa}{\varepsilon_r} \propto \frac{f_{FdM}^2\left(\varepsilon_r\right)\gamma^3\kappa\, q^{18}}{\Delta G^{12}\varepsilon_0^6\varepsilon_r} \tag{9.15}$$

Here, $\hat{Q}_{min}^{droplet} = Q_{min}^{droplet}/Q_0$. Since Romero-Sanz *et al.* [107] only provide data in the mixed mode, except for the first data point in the pure-ion regime, we made an estimation of the end of the pure-droplet mode when approached from the right. It is important to note that the illustrative plots depicting the increase in κ and decrease in ΔG are purely qualitative.

9.3 Dynamic stability, axially-symmetric linear stability analysis

9.3.1 Numerics

Derivation of the temporal terms in the finite element framework

Consider the full electrohydrodynamic problem described earlier in chapter 3, including the dynamic terms (that is, $\frac{\partial \mathbf{u}}{\partial t}$, $\frac{\partial \rho_{sch}}{\partial t}$, $\frac{\partial T}{\partial t}$, etc). As stated in chapter 4, the static problem can be expressed as a system of equations represented by function $\mathbf{F}$.

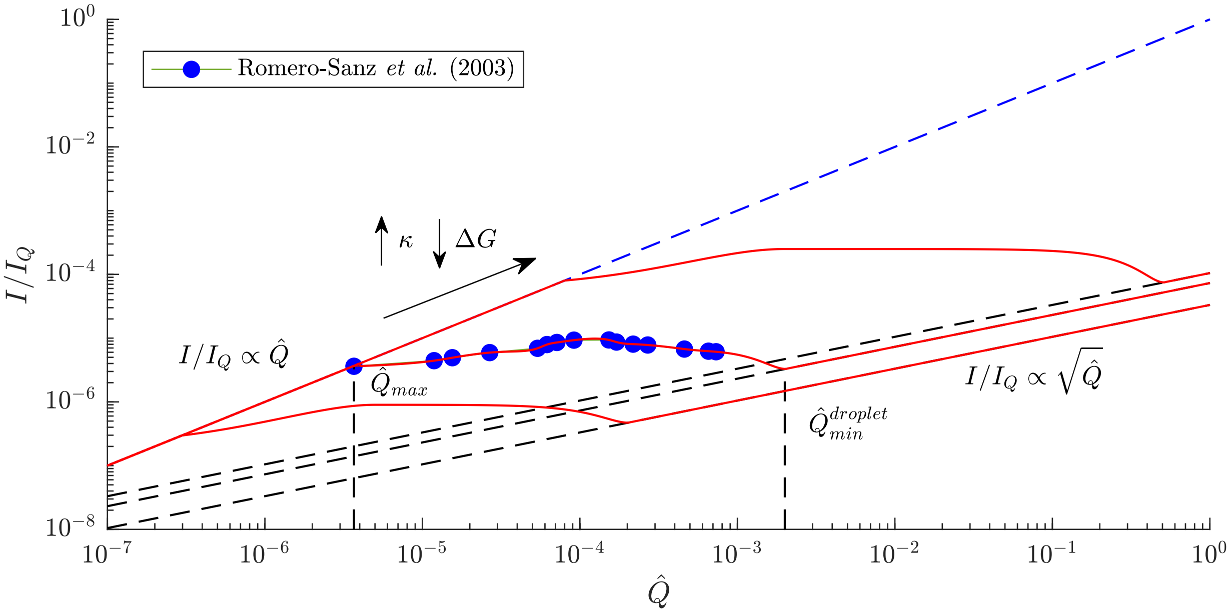

Figure 9-4: Illustrating the transition between the pure ion and the cone-jet regimes. Conductivity κ and ΔG increase the range of I/I_Q where solutions were found for this problem. The I/I_Q mixed mode regime transition curves are matched to the pure-ion regime and pure-droplet regime curves following the trends found by Romero-Sanz *et al.* [107].

If we add the dynamic terms to the system of equations we can express the whole problem as:

$$\mathbf{G}\left(\mathbf{x}\left(\eta,\xi,\Upsilon\right);\mathbf{x}_{\mathcal{T}}\right)=\mathbf{F}_{\Upsilon}\left(\mathbf{x}\left(\eta,\xi,\Upsilon\right);\mathbf{x}_{\mathcal{T}}\right)+\mathbf{F}\left(\mathbf{x}\left(\eta,\xi,\Upsilon\right);\mathbf{x}_{\mathcal{T}}\right)=0 \tag{9.16}$$

Here $\mathbf{x}_{\mathcal{T}}$ indicates test function, as described in section 4.3 of chapter 4. Notice that the space charge $\hat{\rho}^{v}_{sch}$ is neglected in this section, thus dropped from eq. 9.16. Now, the solution vector depends also on the transformed time Υ, and $\mathbf{F}_{\Upsilon}$ are the terms representing the dynamics in the finite element framework.

The new coordinate transformation with the time dependence is:

$$\begin{pmatrix}\hat{r}\\ \hat{z}\\ \hat{t}\end{pmatrix}=\begin{pmatrix}\eta\\ \hat{y}\left(\eta,\xi,\Upsilon\right)\\ \Upsilon\end{pmatrix} \tag{9.17}$$

Notice how, in this case, the map $\hat{y}$ follows the meniscus over time, thus the coordinate map will be effectively changing over Υ, and $\hat{y}=\hat{y}\left(\eta,\xi,\Upsilon\right)$. All the explicit temporal terms of the electrohydrodynamic problem can be put in the following form:

$$\mathbf{F}_{\Upsilon}\left(\mathbf{x}\left(\eta,\xi,\Upsilon\right);\mathbf{x}_{\mathcal{T}}\right)=\left[f_{1\Upsilon},f_{2\Upsilon},f_{i\Upsilon},...,f_{N\Upsilon}\right] \tag{9.18}$$

For the dynamics considered in this problem, the majority of the temporal dependence of the individual equations are either $f_{i\Upsilon}=0$ (for instance, the momentum balance equations or the Laplace condition for the meniscus map), or

$$f_{i\Upsilon}=\int_{\mathbf{\Omega}}A\frac{\partial x_i}{\partial t}\,x_{i_{\mathcal{T}}}\,d\mathbf{\Omega} \tag{9.19}$$

Where x_i is some variable (for instance T in the temperature equation), $x_{i_{\mathcal{T}}}$ its associated test function, and A is a constant (for instance $A=\rho c_p$ for the same temperature equation). In the transformed domain, eq. 9.19 reads:

$$f_{i\Upsilon}=\int_{\mathbf{\Omega}_{(\eta,\xi)}}A\det\left(\mathbf{K}\right)\left(\frac{\partial x_i}{\partial\Upsilon}+\frac{\partial x_i}{\partial\eta}\frac{\partial\eta}{\partial\hat{t}}+\frac{\partial x_i}{\partial\xi}\frac{\partial\xi}{\partial\hat{t}}\right)\,x_{i_{\mathcal{T}}}\,d\mathbf{\Omega}_{(\eta,\xi)} \tag{9.20}$$

The derivative coefficients can be obtained from the inverse of the three-dimensional

Jacobian transformation matrix (including the temporal terms), namely:

$$\mathbf{K}_\Upsilon = \begin{pmatrix} \frac{\partial \hat{r}}{\partial \eta} & \frac{\partial \hat{r}}{\partial \xi} & \frac{\partial \hat{r}}{\partial \Upsilon} \\ \frac{\partial \hat{z}}{\partial \eta} & \frac{\partial \hat{z}}{\partial \xi} & \frac{\partial \hat{z}}{\partial \Upsilon} \\ \frac{\partial \hat{t}}{\partial \eta} & \frac{\partial \hat{t}}{\partial \xi} & \frac{\partial \hat{t}}{\partial \Upsilon} \end{pmatrix} = \begin{pmatrix} 1 & 0 & 0 \\ \frac{\partial \hat{y}}{\partial \eta} & \frac{\partial \hat{y}}{\partial \xi} & \frac{\partial \hat{y}}{\partial \Upsilon} \\ 0 & 0 & 1 \end{pmatrix} \tag{9.21}$$

And its inverse yields:

$$\mathbf{K}_\Upsilon^{-1} = \begin{pmatrix} \frac{\partial \eta}{\partial \hat{r}} & \frac{\partial \eta}{\partial \hat{z}} & \frac{\partial \eta}{\partial \hat{t}} \\ \frac{\partial \xi}{\partial \hat{r}} & \frac{\partial \xi}{\partial \hat{z}} & \frac{\partial \xi}{\partial \hat{t}} \\ \frac{\partial \Upsilon}{\partial \hat{r}} & \frac{\partial \Upsilon}{\partial \hat{z}} & \frac{\partial \Upsilon}{\partial \hat{t}} \end{pmatrix} = \frac{1}{\frac{\partial \hat{y}}{\partial \xi}} \begin{pmatrix} \frac{\partial \hat{y}}{\partial \xi} & 0 & 0 \\ -\frac{\partial \hat{y}}{\partial \eta} & 1 & -\frac{\partial \hat{y}}{\partial \Upsilon} \\ 0 & 0 & \frac{\partial \hat{y}}{\partial \xi} \end{pmatrix} \tag{9.22}$$

Substituting the coefficients in 9.22 into 9.20 we get:

$$f_{i\Upsilon} = \int_{\mathbf{\Omega}_{(\eta,\xi)}} A \det(\mathbf{K}) \left(\frac{\partial x_i}{\partial \Upsilon} - \frac{\partial x_i}{\partial \xi} \frac{\frac{\partial \hat{y}}{\partial \Upsilon}}{\frac{\partial \hat{y}}{\partial \xi}} \right) x_{i_\mathcal{T}} \, d\mathbf{\Omega}_{(\eta,\xi)} \tag{9.23}$$

Intuitively, looking at the coefficients in 9.23 we have a first term describing the partial derivative with respect to the transformed time Υ. The less intuitive second term includes the fact that the coordinates of the meniscus map change with the meniscus movement. This term is well known in the literature of Arbitrary Lagrangian-Eulerian (ALE) methods [29], where normally an arbitrary mesh velocity is postulated and the equations are formulated with respect to an observer sitting on the moving mesh.
For example, let us take the left-hand side of the temperature equation formulated in an ALE framework [141]:

$$\rho c_p \left(\frac{\partial T}{\partial t} + (\mathbf{u} - \mathbf{u}_{mesh}) \cdot \nabla T \right) = \kappa_T \nabla^2 T + \mathbf{j} \cdot \mathbf{E} + \Phi \tag{9.24}$$

The term $\frac{\partial T}{\partial t}$ is represented by $\frac{\partial x_i}{\partial \Upsilon}$ in eq. 9.23, if $x_i = T$; the term $\mathbf{u} \cdot \nabla T$ is not explicitly dependent on time, and its included in $\mathbf{F}$ (not in $\mathbf{F}_\Upsilon$); the term $\mathbf{u}_{mesh} \cdot \nabla T$ is essentially the second term in 9.23:

$$\mathbf{u}_{mesh} = \begin{pmatrix} 0 \\ \frac{\partial \hat{y}}{\partial \Upsilon} \end{pmatrix} \tag{9.25}$$

that is the velocity of the meniscus map, and the multiplying term $\frac{\frac{\partial x_i}{\partial \xi}}{\frac{\partial \hat{y}}{\partial \xi}}$ in 9.23 is ∇T (if $x_i = T$), but expressed in the coordinates of the transformed domain, thus $\mathbf{K}^{-T} \cdot \hat{\nabla}_{(\eta,\xi)} \hat{T}$ in non dimensional terms (see eq. B.7):

$$\frac{\frac{\partial \hat{T}}{\partial \xi}}{\frac{\partial \hat{y}}{\partial \xi}} = \mathbf{K}^{-T} \cdot \hat{\nabla}_{(\eta,\xi)} \hat{T} \tag{9.26}$$

The equations that depend explicitly on time, and are fulfilled at the interface are the kinematic condition for the interface (eq. 3.17) and the charge conservation equation at the interface (eq. 3.16). In such order, the temporal terms of these equations transform as:

$$f_{\hat{h}\Upsilon} = \int_{\Gamma_{M_{(\eta,\xi)}}} \eta \hat{R} \, \frac{\partial \hat{h}}{\partial \Upsilon} \, \hat{S} \; d\Gamma_{M_{(\eta,\xi)}} \tag{9.27}$$

$$f_{\hat{\sigma}\Upsilon} = \int_{\Gamma_{M_{(\eta,\xi)}}} \eta \left(\frac{\partial \hat{\sigma}}{\partial \Upsilon} - \frac{1}{\hat{S}^2} \frac{\partial \hat{h}}{\partial \Upsilon} \frac{\partial \hat{\sigma}}{\partial \eta} \right) \hat{S} \; d\Gamma_{M_{(\eta,\xi)}} \tag{9.28}$$

In an attempt to compare the interface equations to the bulk equations, we can see that the ALE terms are absent from the transformed kinematic condition 9.27. The kinematic condition is independent of any meniscus map. In fact, the kinematic condition *sets up* the boundary conditions for the meniscus map (see equation B.29 in the annex).

The intuition behind the ALE terms appearing in the charge conservation equation 9.28 is harder to understand. The equation that we presented at the beginning of this thesis for the charge conservation equation at the interface (3.16) is already derived with respect to an observer sitting on the $\hat{r}$ axis, and the ALE term containing $\frac{\partial \hat{h}}{\partial \Upsilon}$ can be identified as the interfacial version of the second term the static case. One can consult [140] for more information about conservation equations at the interface.

Derivation of the perturbation problem

Consider an arbitrary very small perturbation $\delta\mathbf{x}$ to the static equilibrium solution vector $\mathbf{x}_{eq}\left(\eta, \xi, \Upsilon\right)$:

$$\mathbf{x}_{eq}\left(\eta, \xi, \Upsilon\right) = \mathbf{x}_{eq}\left(\eta, \xi\right) + \delta\mathbf{x}\left(\eta, \xi\right) e^{-\omega\Upsilon} \tag{9.29}$$

The perturbation's temporal dependence is modeled as an exponential, where ω is a characteristic frequency of the perturbation. If we force 9.29 to fulfill all the dynamic equations then:

$$\mathbf{F}_{\Upsilon}\left(\mathbf{x}_{eq} + \delta\mathbf{x}e^{-\omega\Upsilon}; \mathbf{x}_{\mathcal{T}}\right) + \mathbf{F}\left(\mathbf{x}_{eq} + \delta\mathbf{x}e^{-\omega\Upsilon}; \mathbf{x}_{\mathcal{T}}\right) = 0 \tag{9.30}$$

We can expand the terms in eq. 9.30. In the case of $\mathbf{F}_{\Upsilon}\left(\mathbf{x}_{eq} + \delta\mathbf{x}e^{-\omega\Upsilon}, \mathbf{x}_{\mathcal{T}}\right)$, we can see how this expansion would look element-wise:

$$\begin{aligned} f_{i\Upsilon} &= \int_{\mathbf{\Omega}_{(\eta,\xi)}} A \det\left(\mathbf{K}\right) \left(\frac{\partial x_i}{\partial \Upsilon} - \frac{\partial x_i}{\partial \xi} \frac{\frac{\partial \hat{y}}{\partial \Upsilon}}{\frac{\partial \hat{y}}{\partial \xi}} \right) x_{i_{\mathcal{T}}} \, d\mathbf{\Omega}_{(\eta,\xi)} \\ &\approx -\omega e^{-\omega\Upsilon} \int_{\mathbf{\Omega}_{(\eta,\xi)}} A \det\left(\mathbf{K}_{eq}\right) \left(\delta x_i - \frac{\partial x_{i_{eq}}}{\partial \xi} \frac{\delta \hat{y}}{\frac{\partial \hat{y}_{eq}}{\partial \xi}} \right) x_{i_{\mathcal{T}}} \, d\mathbf{\Omega}_{(\eta,\xi)} \end{aligned} \tag{9.31}$$

Equation 9.31 has been obtained by a Taylor expansion keeping only terms of order O(δx_i, $\delta \hat{y}$). Notice how $f_{i\Upsilon}\left(\mathbf{x}_{eq} + \delta\mathbf{x}e^{-\omega\Upsilon}, \mathbf{x}_{\mathcal{T}}\right)$ is approximated as a scaled value of the same integral evaluated at the base solution except the temporal differentials with respect to Υ, which are substituted by the perturbation terms δx_i, $\delta \hat{y}$. The scale factor is $-\omega e^{-\omega\Upsilon}$. The meniscus interface terms in $\mathbf{F}_{\Upsilon}$ are derived in the same way as 9.31. The final discretized version of $\mathbf{F}_{\Upsilon}$ yields:

$$\mathbf{F}_{\Upsilon}\left(\mathbf{x}_{eq} + \delta\mathbf{x}e^{-\omega\Upsilon}; \mathbf{x}_{\mathcal{T}}\right) \approx -\omega e^{-\omega\Upsilon} \mathcal{B}\left(\mathbf{x}_{eq}; \mathbf{x}_{\mathcal{T}}, \delta\mathbf{x}_i\right) \tag{9.32}$$

Where the assembled $\mathcal{B}$ in matrix form contains all the information from the linearized dynamics. Notice that $\mathcal{B}$ is a singular matrix since many of the $f_{i\Upsilon}$ are 0, and from 9.18:

$$\begin{aligned} \mathbf{F}_{\Upsilon}\left(\mathbf{x}_{eq} + \delta\mathbf{x}e^{-\omega\Upsilon}; \mathbf{x}_{\mathcal{T}}\right) &= \left[f_{1\Upsilon}, f_{2\Upsilon}, f_{i\Upsilon}, ..., f_{N\Upsilon}\right]\Bigg|_{\mathbf{x}_{eq} + \delta\mathbf{x}e^{-\omega\Upsilon}} \\ &\approx -\omega e^{-\omega\Upsilon} \mathcal{B}\left(\mathbf{x}_{eq}; \mathbf{x}_{\mathcal{T}}, \delta\mathbf{x}_i\right) \end{aligned} \tag{9.33}$$

For $\mathbf{F}\left(\mathbf{x}_{eq} + \delta\mathbf{x}e^{-\omega\Upsilon}; \mathbf{x}_{\mathcal{T}}\right)$ we can also Taylor expand as:

$$\begin{aligned} \mathbf{F}\left(\mathbf{x}_{eq} + \delta\mathbf{x}e^{-\omega\Upsilon}; \mathbf{x}_{\mathcal{T}}\right) &\approx \mathbf{F}\left(\mathbf{x}_{eq}; \mathbf{x}_{\mathcal{T}}\right) + \mathcal{J}\left(\mathbf{x}_{eq}; \mathbf{x}_{\mathcal{T}}, \delta\mathbf{x}_i\right) e^{-\omega\Upsilon} + O\left(\delta\mathbf{x}^2\right) \\ &\approx \mathcal{J}\left(\mathbf{x}_{eq}; \mathbf{x}_{\mathcal{T}}, \delta\mathbf{x}_i\right) e^{-\omega\Upsilon} \end{aligned} \tag{9.34}$$

Where $\mathcal{J}\left(\mathbf{x}_{eq}; \mathbf{x}_{\mathcal{T}}, \delta\mathbf{x}_i\right)$ is the same Jacobian that we used for searching the steady solution $\mathbf{x}_{eq}$, and evaluated at that same solution. For the last approximation in

9.34, we have used the fact that $\mathbf{F}\left(\mathbf{x}_{eq};\mathbf{x}_{\mathcal{T}}\right)=0$ by definition. We can use 9.34 and 9.32 to in 9.30:

$$\mathcal{J}\left(\mathbf{x}_{eq};\mathbf{x}_{\mathcal{T}},\delta\mathbf{x}_i\right)=\omega\mathcal{B}\left(\mathbf{x}_{eq};\mathbf{x}_{\mathcal{T}},\delta\mathbf{x}_i\right) \tag{9.35}$$

Equation 9.35 is a generalized eigenvalue problem that can be solved using Krylov-Schur algorithms. These algorithms are efficiently implemented in standard libraries such as SLEPc [58], which we have used for our results.

The solution to problem 9.35 is a set of eigenfrequencies ω and eigenvectors $\delta\mathbf{x}$ that are generally complex numbers. The general solution vector $\mathbf{x}$ in the narrow time window where the dynamics are well represented by the linearized problem is:

$$\mathbf{x}\left(\eta,\xi,\Upsilon\right)\approx\mathbf{x}_{eq}\left(\eta,\xi\right)+\Re\left(\delta\mathbf{x}\left(\eta,\xi\right)e^{-\omega\Upsilon}\right) \tag{9.36}$$

Where $\Re$ indicates real part. If there is *any* eigenfrequency with a real part $\Re\left(\omega_i\right)<0$, then the perturbation described by $\delta\mathbf{x}$ corresponding to ω_i will grow over time thus deviating the meniscus from its steady solution. If on the contrary, *all* eigenfrequencies have positive values, all perturbations will be damped with rates equal to the value of that eigenfrequency.

We believe this analysis could be interesting for electrospray ion source designers since $\min_i\left(\Re\left(\omega_i\right)\right)$ can be a useful metric to **quantify** how stable is a solution under small arbitrary perturbations. The value $\min_i\left(\Re\left(\omega_i\right)\right)$ corresponds to a maximum growth rate of the perturbation if $\min_i\left(\Re\left(\omega_i\right)\right)<0$ ("most negative eigenfrequency") and to a minimum damping rate of the perturbation if $\min_i\left(\Re\left(\omega_i\right)\right)>0$ ("closest eigenfrequency to 0"). The perturbation shapes $\delta\mathbf{x}$ are defined up to an arbitrary constant: what we are finding with this linearization problem is a direction of motion, that grows stably or unstably, according to the rate ω.

Boundary conditions for the perturbation problem

In our analysis, we are examining perturbations to the steady solution $\mathbf{x}_{eq}$ that maintain the steady solution unchanged at the external boundaries (the boundary conditions described in section 3.3). This is achieved by fulfilling the homogeneous boundary conditions, denoted by $\delta\mathbf{x}=0$, in the boundaries where we have prescribed Dirichlet boundary conditions (refer to section 3.3 of this thesis for further details). A similar situation occurs for Neumann boundary conditions. For instance, the boundary conditions for the potential (eqs. 3.53) in dimensionless form yield:

$$\begin{aligned} \hat{\phi} &= \frac{V}{\phi_c} && \text{on} && \Gamma_I \cup \Gamma_D^l \cup \Gamma_D^v \\ \hat{\phi} &= 0 && \text{on} && \Gamma_E \\ -\hat{\nabla}\hat{\phi} \cdot \mathbf{n} &= 0 && \text{on} && \Gamma_L^v \cup \Gamma_L^l \cup \Gamma_{EXT} \end{aligned} \tag{9.37}$$

where $\phi_c = \sqrt{\frac{4\gamma_0}{r_0\varepsilon_0}}\, r_0$ is the reference voltage (see table 3.3). For $\hat{\phi} = \hat{\phi}_{eq} + \delta\hat{\phi}e^{-\omega t}$ we have:

$$\begin{aligned} \hat{\phi}_{eq} + \delta\hat{\phi}e^{-\omega t} &= \frac{V}{\phi_c} && \text{on} && \Gamma_I \cup \Gamma_D^l \cup \Gamma_D^v \\ \hat{\phi}_{eq} + \delta\hat{\phi}e^{-\omega t} &= 0 && \text{on} && \Gamma_E \\ -\hat{\nabla}\left(\hat{\phi}_{eq} + \delta\hat{\phi}e^{-\omega t}\right) \cdot \mathbf{n} &= 0 && \text{on} && \Gamma_L^v \cup \Gamma_L^l \cup \Gamma_{EXT} \end{aligned} \tag{9.38}$$

Since the steady problem already fulfills the boundary conditions (for example $\hat{\phi}_{eq} = \frac{V}{\phi_c}$ on $\Gamma_I \cup \Gamma_D^l \cup \Gamma_D^v$):

$$\begin{aligned} \delta\hat{\phi} &= 0 && \text{on} && \Gamma_I \cup \Gamma_D^l \cup \Gamma_D^v \\ \delta\hat{\phi} &= 0 && \text{on} && \Gamma_E \\ -\hat{\nabla}\delta\hat{\phi} \cdot \mathbf{n} &= 0 && \text{on} && \Gamma_L^v \cup \Gamma_L^l \cup \Gamma_{EXT} \end{aligned} \tag{9.39}$$

The set of boundary conditions in 9.39 can be easily adapted to the fixed domain.

9.3.2 Axially-symmetric stable modes of a benchmark current-voltage curve

For this analysis, we use the same configuration and data for the simulation of [EMIm][HSO$_4$] in chapter 8. The simulated radius is $r_0 = 2\ \mu$m. Figure 9-5 displays the perturbation analysis of four selected points on a reference current-voltage plot. In figure 9-5a, we show the equilibrium shapes corresponding to these selected points in solid lines, with a dashed line representing the scaled shape of the most unstable perturbation. We have chosen a sufficiently large scale value to make the perturbation easily noticeable, as its amplitude is arbitrary. A positive scale value corresponds to figure 9-5a1, indicating that the perturbation tries to elongate the equilibrium shapes. In contrast, the perturbation is plotted as negative for figure 9-5a2, where it tries to sink the equilibrium shapes. Figure 9-5b displays the most unstable value of the 40 smallest frequency eigenvalues that we explored due to computational limitations, i.e., $\min_i \Re(\omega_i)$. The eigenfrequencies that are positive (or correspondent to damped perturbations over time) are shown in red, and the negative values are shown in blue. Figure 9-5c shows the dimensionless current $\hat{I}$ with the same stability color code as the eigenfrequencies. Figure 9-5d shows the dimensionless aspect ratio of the equilibrium shapes.

Figure 9-5b reveals that the selected equilibrium shapes A and D have a negative minimum eigenfrequency, indicating that they are dynamically unstable. This finding is intuitive: selected equilibrium shape A is low field, close to the Taylor solution, which is inherently unstable. Such low field instability is well-known in the experimental realm. Selected equilibrium shape D lies precisely in the turning point described in chapter 6, which is also inherently unstable for the same reason. The turning point nature of that instability can be seen from the aspect ratio plot in subfigure d). These observations support the validity of our numerical results. From subfigure b), we also observe a sharp decrease in $\min_i(\Re(\omega_i))$ when the equilibrium shapes approach the Taylor solution. This finding suggests that lower field solutions are only accessible when coming from high to low voltages, as coming from low to high means navigating an abrupt terrain of high instability.

On the high field end prior to the turning point, we observe a small stabilization of the meniscus, where $\min_i(\Re(\omega_i))$ becomes higher before rapidly decreasing again to negative at the turning point.

We also note that the most unstable perturbation in selected equilibrium shape A (the one close to the Taylor solution) appears to be very locally concentrated in the emission region, which may be a symptom of jet development. Similar observations were made in eigenmodal decomposition of cone-jets close to the minimum flow rate [100]. As the external potential increases, this perturbation gains stability and spans a larger region of the meniscus, as shown in figures 9-5a1 and a2. In contrast, the loss of stability in selected shape D appears to affect the entirety of the meniscus, which is consistent with a bifurcating process. The reader may also notice the low differentiability of the least stable eigenfrequency in 9-5d (presence of "kinks"). We believe that the reason for this to happen is the change in the nature of the dominant eigenfrequency, or the eigenfrequency that governs $\min_i(\Re(\omega_i))$ (for instance, by changing the region of the meniscus where the most unstable perturbation lives, or the number of meniscus undulations that characterize such perturbation, etc). If all eigenfrequencies are ordered by such "nature", all of them follow smooth curves, and the kinks appear when another type of perturbation surpasses the currently dominant one, therefore takes its role at that particular value of voltage.

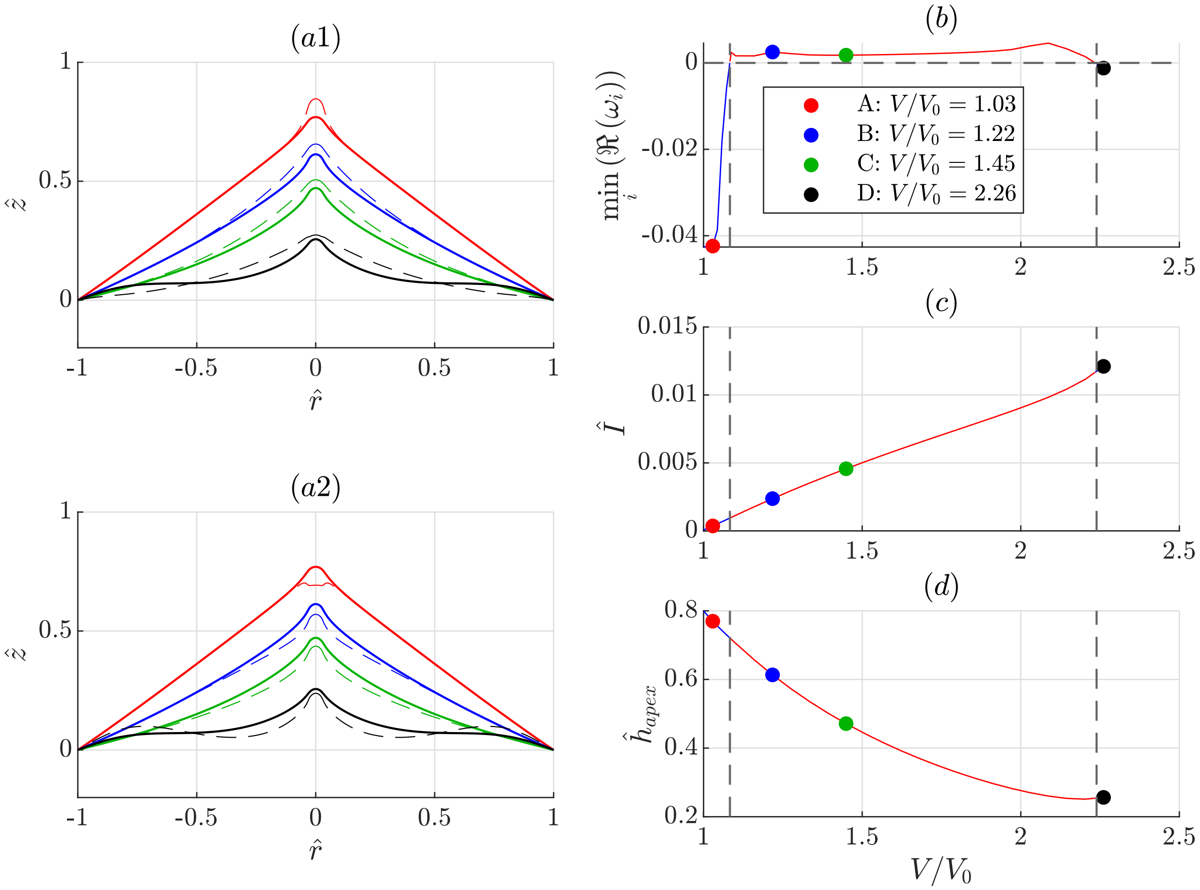

Figure 9-5: Equilibrium shapes (solid) and least stable perturbations (dashed) for four different points in a current-voltage curve. Simulation parameters are $\hat{R} = 65.36$, $\hat{Z} = 0.0081$, $\hat{p}_r = 0$. The perturbation modes are defined up to an arbitrary constant, positive constant is plotted in a1) negative constant in a2). Subfigure b) shows $\min_i (\Re(\omega_i))$. Negative values indicate dynamic instability, therefore dynamically unstable equilibrium shapes are A and D. Subfigure c) shows the dimensionless current, and d) shows the aspect ratio of equilibrium shapes. The value of $\min_i (\Re(\omega_i))$ becomes negative right at the turning point, as discussed in chapter 6.

9.3.3 Preliminary investigation of minimum flow rates: insights from simulations and potential application for Focused Ion Beam technology

Motivation

The utilization of Ionic Liquid Ion Sources (ILIS), which offer lower flow rates or currents compared to Liquid Metal Ion Sources (LMIS), holds potential for enhancing Focused Ion Beam (FIB) technology [94]. In FIB applications, lower current modes could be commonly associated with smaller spot sizes of the ion beams, thereby enabling the achievement of higher resolutions. Moreover, lower currents could offer additional advantages, such as the potential for a beam with reduced polydispersity, which is typically enhanced at lower currents specifically for ILIS. This implies the possibility of generating more monomeric and monochromatic ion beams.

Additionally, the utilization of lower currents in the ion beam can effectively address chromatic aberrations caused by energy dispersity of the ions [31, 123]. By reducing the likelihood of energy exchange resulting from ion collisions, known as the Boersch effect, lower currents have the potential to decrease the energy spread of the beam. Exploring the conditions under which ionic liquid ion sources can consistently emit ions in the lower range of currents, while maintaining stability, could become an area of particular interest.

Objective

The objective of this section is then to analyze preliminary the instability triggered at lower fields, which is characterized by the extincton of the current. Preliminary results indicate that this low field instability responds indeed to a *minimum flow rate or current* that the meniscus can emit. As such, this instability will necessarily occur before the minimum electric field described in chapter 6 ($\hat{E}_{tip_0}$ in dimensionless terms) when reducing the electric field.

Influence of the impedance

We start by analyzing the most unstable perturbation on various impedances while keeping the radius fixed. The simulation conditions included a value of $r_0 = 2$ μm. The results of this analysis are presented in figure 9-6. We consistently observed an unstable mode in the source (below the horizontal dashed line) that suggests a limit on the flow rate that the source can sustain $\hat{Q}_{min}$. The limit seems to be very weakly dependent on the hydraulic impedance, and slightly increases at lower

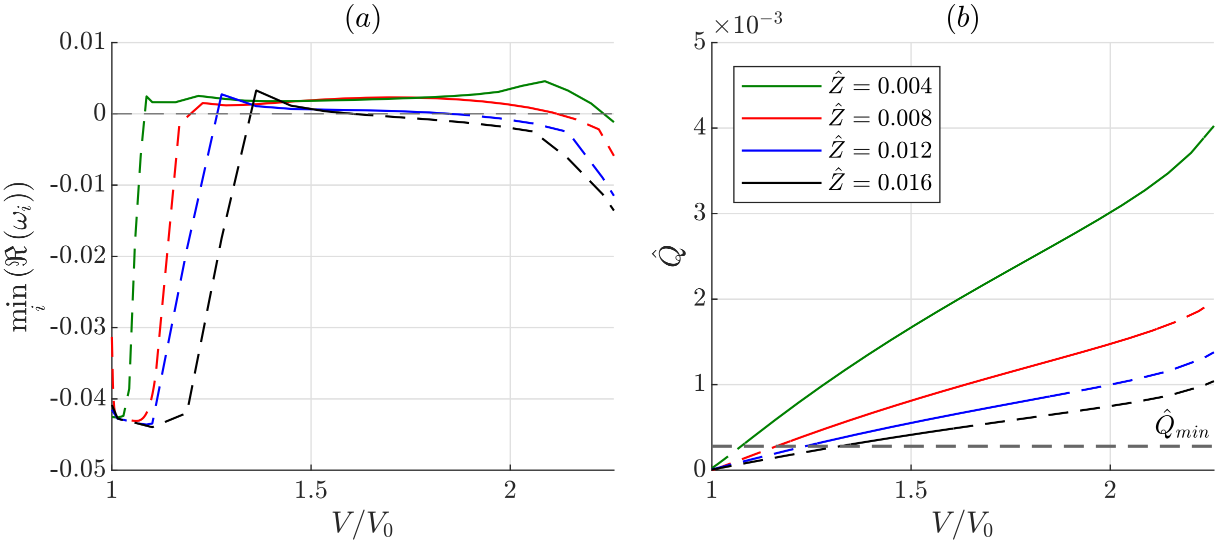

Figure 9-6: Subfigure a) shows $\min_i(\Re(\omega_i))$ and subfigure b) shows dimensionless flow rates for different dimensionless impedances as a function of V/V_0. The simulation parameters are $\hat{R} = 65.36$, $\hat{p}_r = 0$.

hydraulic impedances. Additionally, we observed that higher values of $\hat{Z}$ led to dynamic instabilities before reaching the turning point.

While a thorough investigation of this phenomenon requires a proper temporal integration analysis, we can speculate on its potential causes. It is possible that at higher levels of impedance, where the meniscus pressure sensitivity to changes in flow rate is greater, small perturbations in the meniscus current may have a significant effect on its dynamics, we can envision for instance one of those perturbations causing the meniscus to suddenly sink and then resurface. It is worth noting that the dimensionless growth rate of these unstable perturbations at higher fields and higher $\hat{Z}$ values are approximately an order of magnitude smaller than those present at lower fields. Consequently, these perturbations tend to grow over a longer time scale on the meniscus (refer to figure 9-6a).

Influence of the radius

Figure 9-7 illustrates the minimum $\hat{Q}\hat{R}^2$ as a function of the dimensionless radius $\hat{R}$. The term $\hat{Q}\hat{R}^2 = \frac{Q}{Q_0(r^*/r_0)^2}$ is a different expression for the dimensionless flow rate that eliminates the dependency of the denominator Q_0 on r_0, and substitutes it with

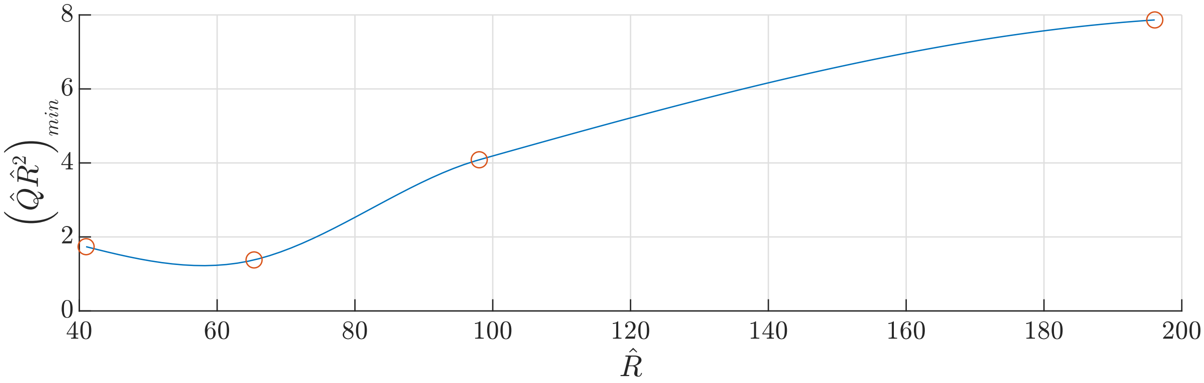

Figure 9-7: Minimum *experimental* flow rate as a function of radius for the experimental [EMIm][HSO$_4$] simulation setup.

r^*, thus the comparison is directly related to the results of the experiment, and not the same r_0.

Figure 9-7 suggests that smaller menisci can sustain lower flow rates without triggering dynamic instabilities. In other words, we found that highly stable solutions are more prevalent at smaller radii. This finding is consistent with previous research on the cone-jet mode, which also suggests that smaller menisci sustaining low flow rates are more stable [100, 111]. These results suggest that the relationship between stability and size of the meniscus in the low field region may be a general phenomenon in electrospraying. Our simulation work reveals dynamically stable solutions characterized by higher flow rates for larger menisci, which appear to be at odds with experimental heuristics, as the pure-ion regime is typically associated with small flow rates and small radii. While such observation warrants at least further investigation within the limitations of our analysis (e.g., low-frequency eigenmode exploration and neglect of space charge effects), one possible explanation may come along with questioning the ability of the meniscus to maintain a high charge-to-mass ratio at larger flow rates, while sustaining the pure ion regime. This phenomenon has been previously reported for many ionic liquids in the literature, where decreasing flow rates correspond to more monomeric behavior (see, for example, figures 8-7 and 8-6). The charge-to-mass ratio is essentially a measure of the efficiency with which current is extracted for a given flow rate ($I = \rho \frac{q}{m} Q$). Therefore, it is reasonable to assume that two liquids capable of ejecting the same flow rate Q, but with different q/m ratios, will exhibit different levels of Ohmic dissipation and heating in the emission region. This heating can enhance the static stability of the meniscus, as reported in previous work [42], and by the logarithmic term in eq. 9.9, if the equation is representative enough for the maximum current limitation of the meniscus.

Given the results of this section (minimum flow rate increases with radius), and the results in section 9.2.4 (maximum flow rates are not attainable at higher radius, because meniscus presumably bifurcates earlier), the model suggests a maximum meniscus radius where these two limits overlap and pure-ion emission is no longer tenable in steady state.

Comparison to experiments

In this section, we present an experimental example of a current-voltage curve for the [EMIm][HSO_4] liquid, obtained close to the minimum flow rate (minimum current) instability limit described in section 9.3.3. The measurements were performed in the positive mode at a temperature of 47.8°C with a decreasing voltage pass. This approach was chosen because menisci tend to be more stable when transitioning from higher to lower voltage near the current extinction, leading to the minimum current typically being found at decreasing voltages. The experimental setup used the same configuration as described in chapter 8, employing a triangular voltage signal with a period of 400 s, an offset voltage of 1800 V, and an amplitude of 350 V. The results are presented in figure 9-8.

For the simulations, we considered a meniscus radius of $r_0 = 2.5\ \mu$m and a Laplace pressure of $p_r = 0$ kPa. We tested four different impedances. In subfigure 9-8a, we show the minimum eigenfrequency $\min_i(\Re(\omega_i))$ as a function of the dimensional voltage V. Notably, at a current value of approximately $I = 130$ nA, the minimum eigenfrequency starts becoming negative for all four tested impedances. This critical point is further highlighted in figure 9-8b. Dashed lines represent the regions in the plot where our simulations yield $\min_i(\Re(\omega_i)) < 0$ for the tested meniscus radius. The yellow and orange solid fine lines represent the experimental curves for two passes. It is evident that the simulation framework closely approximates the minimum current detected when the source is close to its extinction point and exhibits abrupt oscillations.

However, it is essential to acknowledge the presence of uncertainties in the experimental operational parameters (meniscus radius, impedance, Laplace pressure) and some physical parameters of [EMIm][HSO_4] (e.g., ΔG and thermal transport coefficients). As a result, the obtained results are to be regarded as a qualitative evaluation.

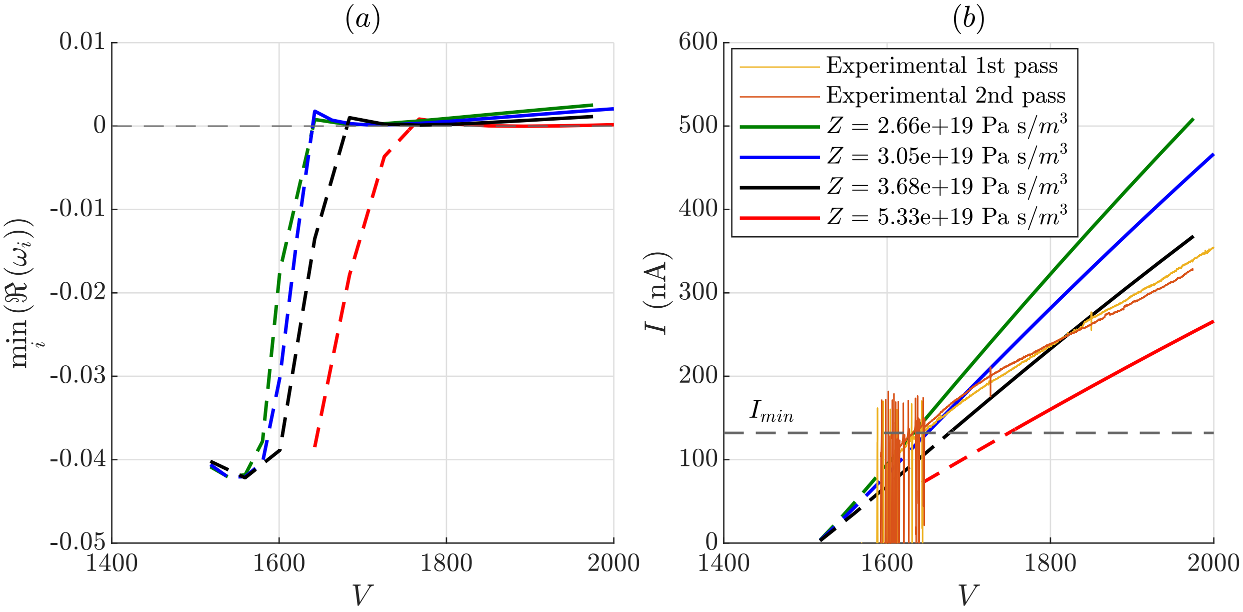

Figure 9-8: Comparison between the simulated minimum current and experimental datasets for [EMIm][HSO$_4$] at $T = 47.8°$C. Subfigure a) shows $\min_i (\Re(\omega_i))$ for four different as a function of the external voltage. Subfigure b) shows experimental current-voltage curves in yellow and orange overlapped with simulated curves at such impedances. Dashed regions have $\min_i (\Re(\omega_i)) < 0$.

Chapter 10

Non-invasive observation of pure-ion emitting menisci: the quenching experiment

10.1 Background

It is believed that pure-ion emission is only achievable at very small meniscus sizes (on the order of 3-5 microns). No direct observation of a macroscopic meniscus operating in the pure ion regime has been reported to the best of our knowledge (amenable to observation with optical wavelengths). This idea of a small meniscus in the pure ion regime is reinforced in chapter 9, where we perform a stability analysis.

Observation of menisci in the pure ionic regime is a crucial validation step for the modeling of pure-ion electrospraying with ionic liquids. There are inherent challenges with imaging such small scales with traditional optical imagery, since these lie on the order of the diffraction limit. Transmission electron microscopy (TEM) has been tried as an imaging tool while emitting *in-situ*. Despite its success for liquid metal ion sources [101, 30], this was proven to be destructive for ionic liquids during the emission process [130]. While emitting, the ionic liquid developed menisci that *a priori* have a flatter structure than Taylor cones as predicted by this thesis effort and by Coffman [20], although usually growing dendritic features that obscured the observation of any meniscus shape, even elongating the presumable menisci to very high aspect ratios ("palm trees"). These dendrites grew quickly only under the combined influence of the imaging electron beam and the extracting voltage potential and stopped growing when the firing potential stops.

10.2 Proposed approach

In this thesis, we tried to observe the meniscus in the pure-ion regime *ex-situ*, by rapidly solidifying them while firing and then observing them in the microscope. In summary, a tungsten emitter was wetted with a mixture of ionic liquids that are solid at room temperature, it was fired under a vacuum on a quenching stage and rapidly solidified with a liquid nitrogen refrigerating pipe while keeping the extracting voltage, and then observed under a Scanning Electron Microscope (SEM). The main idea behind this quenching approach is that solidifying the emitting meniscus *prior* to observation will remove the possible interferences of the firing extracting voltage with the observing electron beam from the SEM, and the features of the meniscus will presumably be much clearer.

10.3 Challenges

This quenching approach was tried in early investigations of liquid metal ion sources, before TEM observations were performed [30], although its success has been reported to be often unpredictable (or in other words, if you are *lucky enough*, the meniscus quenches).
We faced similar repeatability issues with this experiment: the meniscus does not usually quench under similar conditions. The ideal quenching condition would be a fast sharp decay of the current during quenching. The most common failure mode is a slow quench, or a situation where the meniscus would slowly stop emitting or start pulsating "on and off" until the pulsations slowly decay in amplitude and the current extinguishes. We only achieved 1 moderately "successful" (fast enough) quench over more than 20 trials, although experimental conditions were practically identical (to the best of our knowledge). Despite the lack of repeatability of this experiment, we believe that the interesting features of the meniscus that we observed using this quenching approach are worth discussing in this thesis, and are inherently relevant to the modeling efforts that we perform in this thesis. The shortcomings and the procedure reported in this thesis could be useful for addressing the limitations of future designs of similar experiments.

We believe that the key to the repeatability of this experiment is a better understanding of the solidification dynamics of ionic liquids: under normal conditions (no electric field) ionic liquids supercool and do not trigger glass transitions or crystallization until temperatures go way below their melting points (can be more than 40 degrees Celsius difference [73]).

Triggering a rapid solidifying response of the ionic liquid was hard to achieve since homogeneous nucleation of crystals, or glass transition is only achieved at very low temperatures where the viscosity is high enough to stop the defining features of the meniscus (in these cases, presumable menisci appear as little protuberances in the SEM, without a clear emission region, and barely distinguishable from simple pools of ionic liquid). For this reason, we tried to enhance the crystallization of the ionic liquid at a higher temperature, before the homogeneous crystal nucleation point by mixing two ionic liquids that have distinct melting points and operating at a temperature in between these melting points. The two liquids are $[NC_2C_1C_1im][NTF_2]$ (70° C melting point) and $[HCC_2C_1C_1im][NTF_2]$ (approx 40° melting point) [73]. The liquids were specially manufactured by Dr. Spiros Koutsoukos (Imperial College London) to be solid ionic liquids at room temperature that are hydrophobic. This is a very important feature of the ionic liquids used, since in the process of going between the vacuum chamber and the SEM facility in our lab, the solidified meniscus could absorb moisture at a very fast rate, and damage the structure of the quenched meniscus. The reservoir is then a mixture between crystals of one ionic liquid and the other ionic liquid melted. This mixture would hopefully create enough nucleation sites for crystals to grow during the quenching process. In our experience, these two liquids have to be chemically affine (similar structure), so that crystallization apparently can happen fast enough: notice that the anion of both liquids are the same, and the cations only differ in one chain (alkyne vs. nitrile). Details of the experiment are shown in the next section.

10.4 Experimental details

The following steps were taken to achieve a quenched meniscus:

1. Development of a tungsten emitter:

   Emitters were created from a straight tungsten wire (0.5 mm diameter, from Goodfellow), previously brought to a 3 cm tall size with a dremmel tool.

   Spot-weld 2 mm tall tungsten wire 2 mm below tungsten tip, which will act as a holder for the propellant reservoir.

   Submerge the 2 first mm of the tungsten wire in a 2N solution of sodium hydroxide. The solution is placed inside a beaker with enough volume to hold a 4 cm diameter and approximately 10 cm tall electrode. The wire is placed at the center of the beaker electrode and sustained with a floating counterelectrode. 5 V of DC voltage are given between the tungsten emitter and the electrode submerged in sodium hydroxide allowing the portion of the wire submerged in the liquid to dissolve and form a very sharp conical tip at the end of the 2 mm section.

5 V of AC voltage at 60 Hz are given to the electrodes to etch the tungsten wire to the desired curvature radius (30 μm). We want an emitter with a surface as smooth as possible so that the meniscus is clearly distinguishable from any other ripples in the emitter, therefore no acid treatment is done.

2. Heat tungsten with a clean solder gun and emitter with 1st ionic liquid [$NC_2C_1C_1$im][NTF_2] (70° C melting point). The ionic liquid has the form of a puddle on a Petri dish on top of a hot plate at (90°). Lightly touch the tip with the puddle of ionic liquid until the tungsten tip is lightly wet.

3. With the help of a solder gun at 50° lightly touching the tungsten wire, deposit approximately 1 mm^3 of the 2nd ionic liquid [$HCC_2C_1C_1$im][NTF_2] (approx 45° melting point) on the reservoir of the tungsten emitter.

4. Without the solder gun heating the tungsten emitter, deposit small grains of solid [$NC_2C_1C_1$im][NTF_2] on the reservoir until crystalization of the reservoir happens.

5. Test crystalization speed again when lightly touching the emitter with the solder gun at 50°. At that temperature, the reservoir is likely a mixture of crystals from [$NC_2C_1C_1$im][NTF_2] and melted [$HCC_2C_1C_1$im][NTF_2]. When immediately removing the solder gun and the temperature drops below the melting point of [$HCC_2C_1C_1$im][NTF_2], the mixture crystallizes homogeneously.

6. Clamp the tungsten emitter on a quenching stage (2.5 x 2.5 cm wide copper chip, 0.25 cm tall) welded on a copper pipeline (see figure 10-1). The quenching stage contains a heater resistor and a temperature sensor. The copper pipeline is flanged through a vacuum chamber, and connected to a three-way valve that communicates with a cryogenic tank containing liquid nitrogen through a cryogenic hose, and a small pipe end to ambient pressure.

7. Place the extractor plate at 1 mm distance from the quenching stage.

8. Pump down pump. Heat setup to 65° C.

9. Connect high voltage 1500 V with a square wave, 2 Hz alternation period. At the same time, switch the three-way valve so that the outlet of the tank leads to ambient pressure. Open the nitrogen tank to start cooling cryogenic hose.

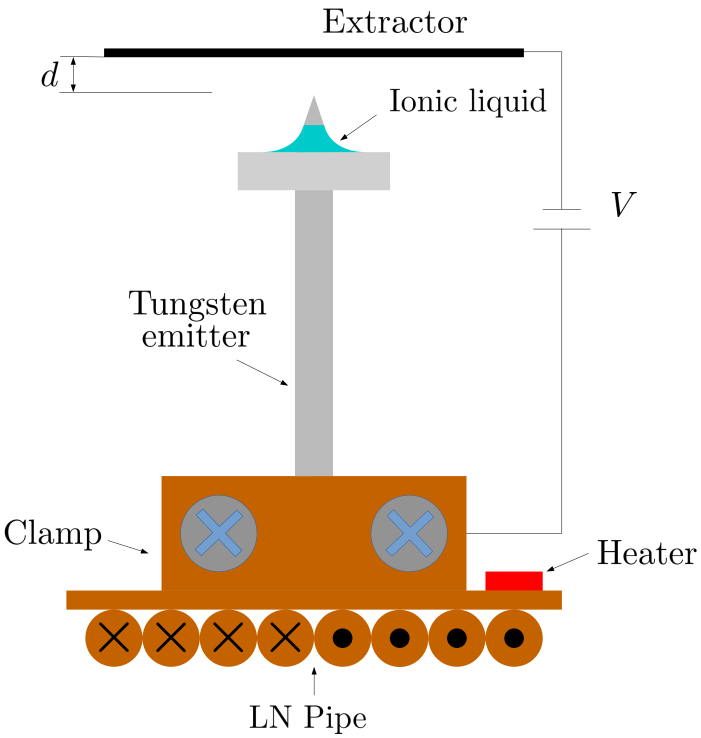

Figure 10-1: Diagram of the copper quenching stage used to solidify the meniscus.

10. Once we can see that the hose is cool enough, and liquid nitrogen (not gas) is coming off the ambient pressure pipe end, stop square voltage and set DC voltage to the same level.

11. Turn heater off, and switch three-way valve so that the nitrogen flows though pipe.

12. Wait until the current detected from the plate extinguishes.

13. Close the nitrogen tank and let the quenching stage come back to ambient temperature while keeping extracting voltage on.

14. Once it heats up to ambient temperature, stop firing voltage, vent chamber, store emitter, and observe possible meniscus features under SEM.

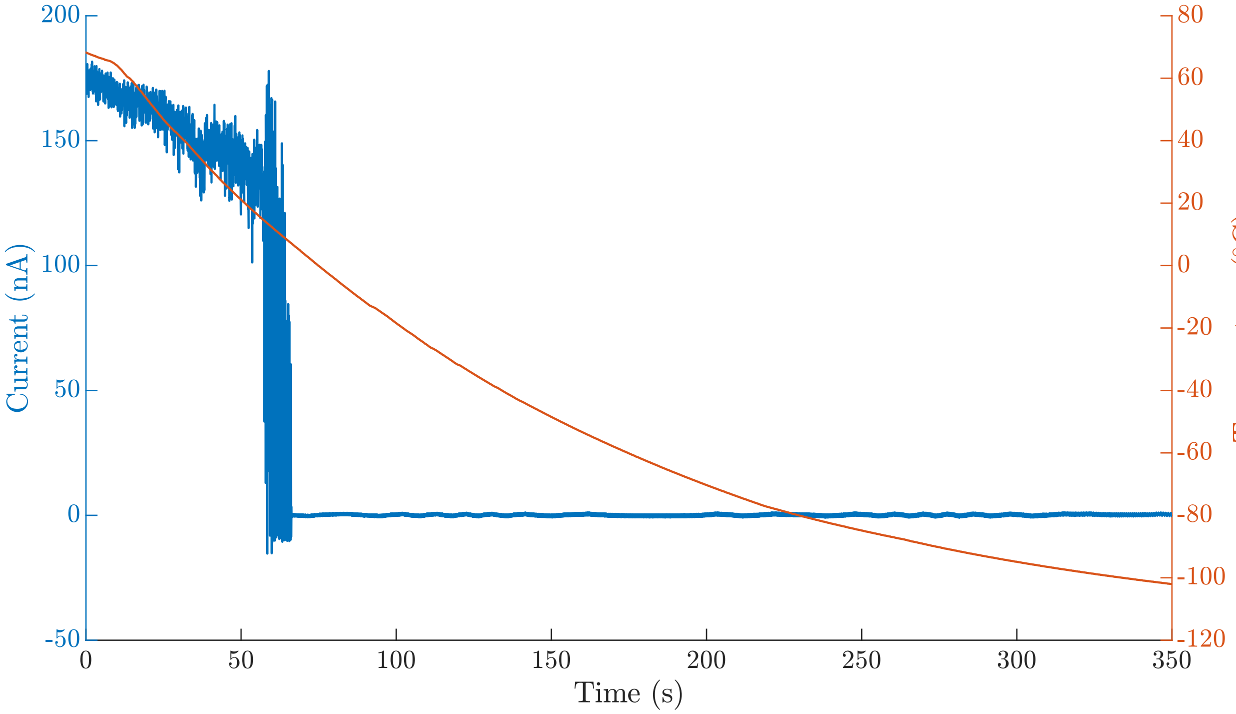

Figure 10-2: Temperature (orange, right vertical axis) and detected current (blue, left vertical axis) during the quenching process.

10.5 Current and temperature decay

The current and temperature decay can be observed in figure 10-2.

10.6 Results and discussion

Results are shown in figure 10-3. There is a major observation: the meniscus is not a Taylor cone. In fact, one can see the close resemblance with the sample meniscus shown in figure 5-7, and with Coffman's menisci [21].

There are other three interesting observations:

1. The meniscus is off-axis. Off-axis emissions with externally wetted emitters are very common, if not the general rule. It is often thought that such off-axis emission is due to the poor supply of liquid at the apex of the emitter, precisely

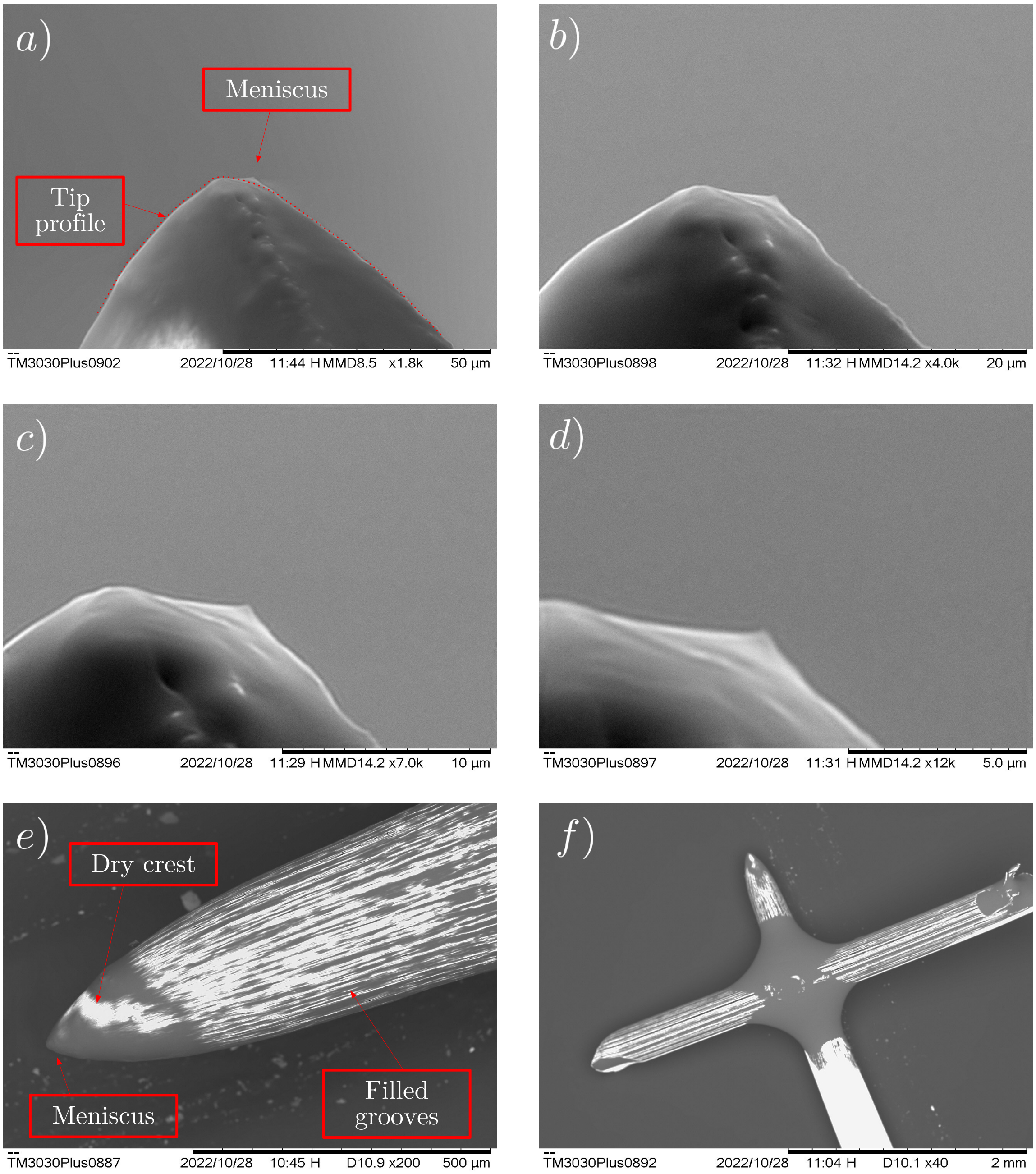

Figure 10-3: SEM results from quenching experiments. Presumable pure ion emitting meniscus appears on the side of the needle.

because of the higher resistance to the flow that such geometrical apexes entail. Yet, the apex of the emitter is *wetted* with ionic liquid. Then we may ask the question of whether off-axis emissions are caused by a preferential pin of the meniscus at the side of the tip, and not by a poor supply of liquid at the apex. What are the key wetting angle and feeding flow structure dynamics that could play a role in setting preferential pins for the meniscus in such a case?

2. Unlike liquid metal ion sources, the meniscus is much smaller $r_0 \sim 5\ \mu$m than the radius of curvature of the tip $R_c \sim 30\ \mu$m, reinforcing the idea that larger ionic liquid menisci in the pure-ion regime are unstable.

3. There is clearly a non-homogeneous flow supply to the meniscus. This is probably due to the smoothness of the conical section of the tip, which seems to restrict the flow from adopting wetting configurations and facilitating access to apex of the tip from all directions (e.g., the flow cannot "imbibe"), and perhaps it further favors its pinning off-axis. This fact is not often contemplated in impedance models of externally wetted emitters, which usually contemplate homogeneous films coating the meniscus.

10.7 Limitations

The controllability of this experiment is limited, we enumerate the most important limitations:

1. The dynamics of the meniscus are not captured with this solidifying approach: the meniscus is not in a steady state, because, at the rates we were quenching, we observed current decrease and oscillatory behavior in the current emitted before quenching caused by the viscosity increase or by the crystallization process. The current drops fast after the oscillations (see figure 10-2), as opposed to the other quenching attempts where the current decays slowly and no menisci were observed after in the SEM.

2. The time-of-flight characteristics were taken before quenching, therefore there is no 100% guarantee that the quenched meniscus is of similar characteristics as the one created during TOF. Figure 10-4 shows the time-of-flight characteristics of the source at 48°C and 2420 V. Notice that the TOF voltage is different than the quenching voltage, due to the fact that the extractors for the TOF and for the quenching have different geometries. The TOF current yields approximately 120 nA.

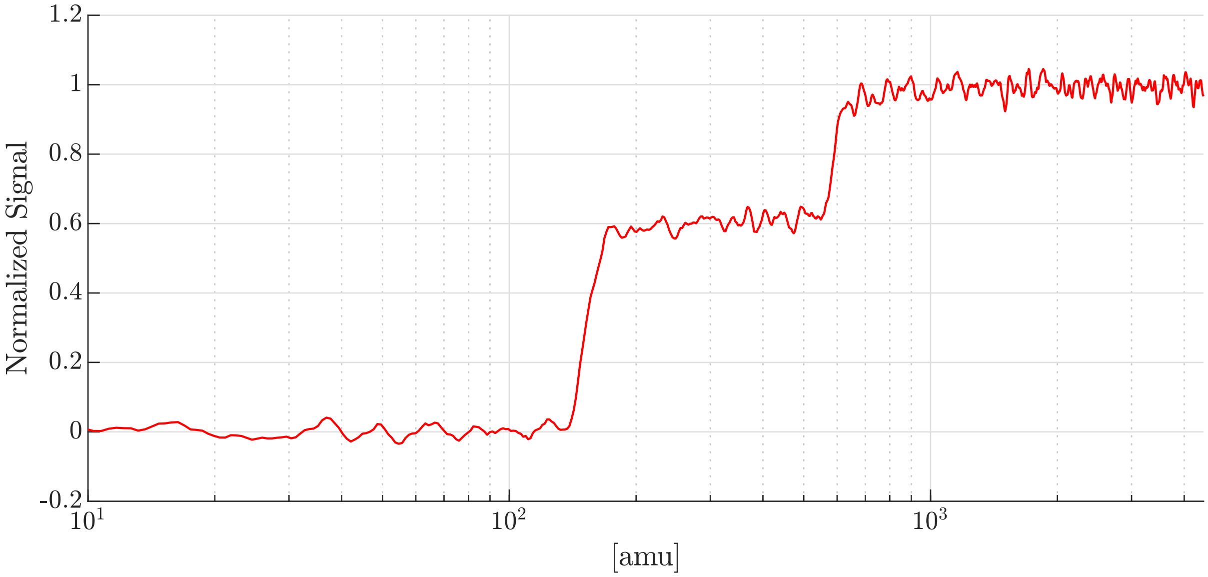

Figure 10-4: Time-of-flight characteristics of quenched meniscus prior to firing.

3. Thirdly, the dynamics of crystalization during quenching are still not fully understood. While we believe that the structure of the quenched meniscus is very suggestive, definitely stands out if compared to other features observed in the SEM, and is clearly supported by our simulation efforts, we cannot completely discard any possible effects of chaotic liquid crystallization that may form similar conical structures, thus obscuring the interpretation that we made of figure 10-3 (see for instance the ripples below the meniscus in subfigures a,b and c).

Chapter 11

Summary of main contributions, conclusions, and future work

11.1 Contribution 1: The approach

This thesis has been centered on the implementation and evaluation of an electrohydrodynamic model of pure-ion electrospray emission. The implementation incorporates **Jacobian-based approaches** that have resulted to be useful for:

- **The fast convergence** of static solutions without space charge effects.
- **A better conditioning** to explore static solutions with space charge effects.
- **A necessary step** to analyze the meniscus stability under small dynamic perturbations.

11.2 Contribution 2: The main results of this thesis

Using this improved numerical method from existent fixed point iterative approaches we have been able to explore:

1. The dependency of the **magnitude of the current** on physical parameters, and its associated **equilibrium shapes**.
2. The range of physical parameters where pure ion menisci may **exist** and are **stable** according to the electrohydrodynamic model.

We have made the following observations:

11.2.1 Ionic liquid ion sources equilibrium shapes depart from the Taylor solution

We have examined the equilibrium shapes of menisci under various geometrical configurations based on planar, infinite hyperboloidal, and capillary emitters and potentially encountered the presence of a meniscus ex-situ through a quenching experiment, where the meniscus shape was sensed. In all these, menisci generally exhibited a different structure from a Taylor cone, usually flatter when the hyperboloidal profile of the electrodes holding the meniscus is not very sharp (e.g., closer to a flat plate). On the other hand, **equilibrium shapes elongate substantially when**:

- Menisci sit on geometries where $r_0 \sim R_c$ (e.g., closer to a capillary).
- **Space charge** effects are important.
- Dimensionless extracting electric fields local to the menisci $\left(E_{tip}/\sqrt{\frac{4\gamma_0}{\varepsilon_0 r_0}}\right)$ are close to the **extinction**.

Other parameters such as E^*, κ, Z, p_r appear to modify the equilibrium shapes, not substantially but **very locally in the emission region.**

11.2.2 Ionic liquid pure-ion emission is only allowed under a bounded range of electric fields and flow rates

The electrohydrodynamic model suggests bounds for the existence of equilibrium solutions. We have **characterized** them in this thesis:

1. **A minimum external field** where the meniscus yields zero current. In the case where the holding electrodes extend the Taylor geometry, and when the boundary conditions are those derived by Taylor, the associated equilibrium shape at this minimum external field bound is **exactly a Taylor cone**, except for the closed interface at the apex. The dimensionless minimum external field **increases** when:
    - $r_0 \sim R_c$
    - At **negative reservoir pressures**.
2. **A maximum external field** where single axially symmetric menisci are not tenable. In the limit where the hydraulic impedance dominates, space charge effects are irrelevant, and $r_0 \gg r^*$ this field is:

  - Practically insensitive to any upstream conditions of the flow, $\hat{p}_r$, Z, and the properties of the ionic liquid, except γ.
  - Possibly **universal** for all (axially-symmetric) electrospraying, including the stable cone-jet. We provided some experimental evidence in chapter 6.
  - The onset of the multi-jet mode, where the **meniscus bifurcates** into two or more emission sites.

  A **closed equation** for this maximum field is provided for the cases investigated in this thesis:

$$\frac{1}{2}\varepsilon_0 E_{tip}^2 = b_0 \left(\frac{2\gamma}{r_0}\right) \tag{11.1}$$

  Where E_{tip} is the electric field that the meniscus sees and has a clearly defined value in idealized geometries (through eqs. 6.1, 6.2, 6.3), and $b_0 \approx 2$ is a constant that is weakly dependent on the geometry of the electrodes for the cases tested, and that has the exact value $b_0 = 2$ in the planar case.

3. **A minimum flow rate** that the meniscus can emit in the pure-ion mode. The minimum flow rate emerges from the fact that the meniscus is **unstable under small perturbations** at lower flow rates, most commonly found close to the Taylor solution. The minimum flow rate increases with the meniscus radius r_0.

4. **A maximum flow rate** that the meniscus can withstand in the pure ion regime. The maximum flow rate is increased in the model at:

  - High electrical conductivities κ.
  - Low critical field for emission E^*.

11.2.3 The magnitude of the current (flow rate) is independent of electrical conductivity and critical field for emission

This phenomenon was already envisioned by Coffman [20] for observations of ionic liquids with different dielectric permittivity, and Gallud [42] for different temperatures of the liquid at constant impedance Z. We generalized this result in chapter 5 for E^* and κ. The same observation is supported by the liquid metal ion source community with the exception of the space charge. Quoting directly from Forbes [38]:

> ... steady-state LMIS i–V behavior can be explained by a theory based on total-force arguments, the slender-body approximation, and the presence of space-charge, without any need to resort to detailed arguments concerning apex field and current density[1]. Although this may seem counterintuitive, it is characteristic of space-charge-controlled situations that emission details are of limited importance.

Our results seem to show that such condition holds when space charge effects, even though included in our formulation, do not dominate.

Then, what role do the details of the emission region play? The short answer is that according to this electrohydrodynamic model, they may play a role in the stability of the meniscus, its dynamics (e.g, whether or not the meniscus can emit a steady pure ion current without developing a cone-jet, or pulsating) and by modifying the structure of emission region: if a stable pure-ion solution exists for a particular combination of emission region parameters such as κ, ΔG, T, ε_r, any modification of those parameters will modify the emission region size and shape in such a way that the total current emitted does not change.

11.2.4 Space charge effects do not affect the current emitted, unless $Z \approx Z_{spch}$

Mair's characteristic impedance [83],

$$Z_{spch} = \frac{\rho}{\pi r_0^2}\sqrt{2\frac{q}{m}V} \tag{11.2}$$

was found in this thesis to be correlated to how much space charge affects current. The main takeaway from eq. 11.2 is that Z_{spch} **does not refer to any parameter of the emission region (e.g, E^*, r^*, κ, etc.)**. If $Z \gg Z_{spch}$ the meniscus is dominated by the conditions of the flow upstream.

---

[1] Forbes refers here to the field at the apex of the liquid metal meniscus, e.g., emission region.

11.2.5 The current (flow rate) mostly depends on the conditions of the flow upstream (reservoir pressure p_r, hydraulic impedance Z), the geometry, voltage, meniscus radius r_0, and surface tension coefficient γ

This thesis provides an equation for the current that incorporates all of the above observations:

$$I = \frac{2\gamma\rho}{r_0 Z}\frac{q}{m}\left(f\left(\hat{E}_{tip},\Theta\right) + \frac{p_r r_0}{2\gamma}\right) \tag{11.3}$$

Where $f\left(\hat{E}_{tip},\Theta\right)$ is a characteristic function that gives the traditional "shape" of the current-voltage approximately linear behaviour that we observe in the experiments, and $\frac{2\gamma_0\rho}{r_0 Z}\frac{q}{m}$ gives us the "amplitude" of such current.

The function $f\left(\hat{E}_{tip},\Theta\right)$ depends only on two factors, the dimensionless external field $\hat{E}_{tip}$, and parameters describing the geometry of the electrodes Θ. In the class of prolate spheroidal electrodes, these parameters are the dimensionless distance between the tip and extractor d/r_0, and the parameter of slenderness, r_0/R_c. The function $f\left(\hat{E}_{tip},\Theta\right)$ is **order 1**. For the class of prolate spheroidal tips explored in this thesis, $f\left(\hat{E}_{tip},\Theta\right) \in [0,2]$.

Three observations are made:

- The "amplitude" of I in eq. 11.3, $\frac{2\gamma\rho}{r_0 Z}\frac{q}{m}$ is exactly **the same** as the derived for LMIS [83], in the limit of high hydraulic impedance $Z \gg Z_{spch}$.

- The "shape" of I in eq. 11.3, namely the function $f\left(\hat{E}_{tip},\Theta\right)$ **departs** from LMIS theory, since that theory considers a slender body, and fixed contact angle to the electrodes, two assumptions that are **not valid for ILIS**. When the emitter is a capillary (a very slender body), $f\left(\hat{E}_{tip},\Theta\right)$ follows LMIS theory.

- The function $f\left(\hat{E}_{tip},\Theta\right)$ is supported on a range of $\hat{E}_{tip}$ that **decreases** when the slenderness of the electrodes and the meniscus (e.g, r_0/R_c) is higher. For the designer of ILIS, the implications of this are:

$$\left(\frac{V_{bifucation}}{V_{extinction}}\right)_{capillary} < \left(\frac{V_{bifucation}}{V_{extinction}}\right)_{planar\ electrode} \tag{11.4}$$

11.3 Contribution 3: Preliminary validation with porous emitters

We designed, built, and tested a porous carbon xerogel emitter, following the strategy designed by Dr. Pérez-Martínez [96]. The objective was to test the validity of eq. 11.3. We tested the liquid [EMIm][HSO_4] at two different temperatures.

The experiment had limitations: the Laplace pressure p_r, meniscus radius r_0, and impedance Z are not known with accuracy, instead, a range of these parameters that would replicate the experimental results was provided with the assistance of the electrohydrodynamic model, and our best axially-symmetric implementation of the actual experimental geometry. The range is compatible with theoretical estimations of the impedance of the tip in the positive mode (simulated and theoretical impedance agree). For the liquid tested, it is also likely that the meniscus decreases its radius and increases the impedance during the current-voltage curve.

11.4 Suggestions for future work

The electrospray problem with ionic liquids is a rich and challenging research area, encompassing highly coupled multiphysics phenomena that complicate the understanding of fundamental processes. The interactions between fluid dynamics, electrostatics, mass transport, and capillary phenomena make it difficult to unravel these underlying mechanisms. Nonetheless, the efforts in this thesis have yielded promising results, suggesting that the emitted current, a critical parameter for ionic liquid electrospray applications such as space propulsion and Focused Ion Beam technology, can be described by a simple equation dependent on upstream flow conditions: hydraulic impedance, reservoir pressure, surface tension (γ), and meniscus radius (r_0).

In the context of ionic liquid electrospraying, experimental investigations, particularly in the pure-ion regime studied in this thesis, face significant challenges due to the delicate and sensitive nature of the setups. Achieving precise control over operational parameters becomes essential for the validation of the model presented in this thesis, but the small characteristic dimensions of electrospray (a few microns) and limited visual observability pose obstacles. Traditional mechanisms to achieve the pure-ion mode for ionic liquids, like curved porous emitters, do not sufficiently validate the simple current model precisely due to uncertainties in meniscus radius and impedance. Therefore, **characterizing these parameters**, possibly influenced by wetting mechanics over complex porous networks and the double layer characteristics at the electrode walls, becomes crucial for model validation and the predictability of ionic liquid pure-ion electrospray sources.

To further validate the model, **capillary sources** with a small radius and high impedance to sustain the pure-ion regime could be explored. However, achieving the pure-ion regime over extended periods may prove challenging for these capillary sources and could impact the steady-state emission needed for validation.

Moreover, the thesis emphasizes the significance of understanding the physics of the emission region in determining flow rate limits for the pure-ion regime. Addressing the limitations of the Iribarne and Thomson kinetic law for ion evaporation (eq. 3.28) used in the thesis could be critical for an accurate description of the stability of the pure-ion regime. The limitations are numerous: it considers an equilibrium situation with no net charge flux, it is based on a conducting planar meniscus interface, it builds upon image charge arguments for a single ion (e.g., it neglects space charge effects), and neglects any depth or 3D structure of the meniscus interface Debye layer. Two suggestions for future work in this regard are proposed. Firstly, **molecular dynamics** efforts could enhance our understanding of ion evaporation mechanics at the emission region level, leading to improvements in the Iribarne and Thomson equation, the Debye layer structure, and identification of specific characteristics of emitted ions, such as q/m. Secondly, this improved model for charge evaporation could be implemented in a continuum electrohydrodynamic framework with a negligible interfacial thickness, similar to the one described in this thesis. Such a model could provide accurate boundary conditions for energy and mass **interfacial transport**, as recently demonstrated by matching asymptotics for kinetic models and the leaky-dielectric model [88], [112].

Appendix A

Properties of the ionic liquids tested and simulated

Ionic liquid	μ_0 (Pa $\cdot$ s)	B_{μ_0} (K)	T_{μ_0} (K)	$\mu\left(T_{test}\right)$ (Pa $\cdot$ s)
[EMIm][HSO_4]	$1.87 \cdot 10^{-4}$ [53]	1143.6 [53]	184.1 [53]	0.355 (47.8°C)/0.535 (40°C)
[EMIm][BF_4]	$24.82 \cdot 10^{-5}$ [113]	661.6 [113]	165.27 [113]	0.039 (25°C)

Table A.1: Viscosity coefficients of tested ionic liquids. Last column shows viscosity at tested temperatures.

Ionic liquid	κ_0 (S/m)	B_{κ_0} (K)	T_{κ_0} (K)	$\kappa_0\,(T_{test})$ (S/m)
[EMIm][HSO_4]	162.7 [53]	857.42 [53]	169.3 [53]	0.31 (47.8°C)/0.21 (40°C)
[EMIm][BF_4]	142.2 [113]	607.92 [113]	163.23 [113]	1.458 (25°C)

Table A.2: Electrical conductivity coefficients for tested ionic liquids. The last column shows electrical conductivity at tested temperatures.

Ionic liquid	κ_T (W/mK)	c_p (J/kgK)	l_H (J/kg)	ΔG (eV)	T_{out} (K)
[EMIm][HSO_4]	0.195^{a}	1602.0 [118]	$6.05 \cdot 10^{5a}$	1.15^{a}	515
[EMIm][BF_4]	0.195 [131]	1555.5 [135]	$6.36 \cdot 10^{5}$ [28]	$*^{b}$	515

[a] Arbitrary value. No data was found in the literature. [b] Multiple values used in this thesis.

Table A.3: Energy transport properties and ion thermal properties after emission of ionic liquids considered in this thesis. T_{out} is arbitrary.

Ionic liquid	ε_r	ρ (kg/m^3)	γ_0 (N/m)	γ' (N/mK)
[EMIm][HSO_4]	18.4 [66]	1360 [53]	0.057 [69]	~ 0
[EMIm][BF_4]	12.8 [134]	1240 [72]	0.048 [114]	$2.52 \cdot 10^{-5}$[114]

Table A.4: Additional properties of tested ionic liquids.

Appendix B

Further derivations

B.1 Change of coordinates and weak form finite element formulation in the fixed domain

B.1.1 Coordinate transformation

The coordinate transformation is defined as follows:

$$\begin{pmatrix} \hat{r} \\ \hat{z} \end{pmatrix} = \begin{pmatrix} \eta \\ \hat{y}\left(\eta, \xi\right) \end{pmatrix} \tag{B.1}$$

With this coordinate transformation, we can define the domain differentials in the fixed domain:

$$\begin{aligned} d\mathbf{\Omega}^{v} &= \det\left(\mathbf{K}\right)\, d\mathbf{\Omega}^{v}_{(\eta,\xi)} \\ d\mathbf{\Omega}^{l} &= \det\left(\mathbf{K}\right)\, d\mathbf{\Omega}^{l}_{(\eta,\xi)} \end{aligned} \tag{B.2}$$

Where $\mathbf{K}$ is the Jacobian matrix of the transformation, that is:

$$\mathbf{K} = \begin{pmatrix} \frac{\partial \hat{r}}{\partial \eta} & \frac{\partial \hat{r}}{\partial \xi} \\ \frac{\partial \hat{z}}{\partial \eta} & \frac{\partial \hat{z}}{\partial \xi} \end{pmatrix} = \begin{pmatrix} 1 & 0 \\ \frac{\partial \hat{y}}{\partial \eta} & \frac{\partial \hat{y}}{\partial \xi} \end{pmatrix} \tag{B.3}$$

Analogously for the meniscus interface, since it is mapped onto a planar domain, it is practically implemented as $d\eta$:

$$d\Gamma_M = \hat{S}\; d\Gamma_{M_{(\eta,\xi)}} = \hat{S}\; d\eta \tag{B.4}$$

Where the surface differential $\hat{S}$ is:

$$\hat{S} = \sqrt{1 + \left(\frac{d\hat{h}}{d\eta}\right)^2} \tag{B.5}$$

Where $\hat{h}$ is the dimensionless meniscus interface profile (same function h defined in chapter 3). Since the problem solved in this section is steady, we have $\hat{h}\left(\eta, t\right) = \hat{h}\left(\eta\right)$, defined only on $\Gamma_{M_{(\eta,\xi)}}$.

All other boundaries remain the same under this transformation, thus, for any boundary Γ_i:

$$d\Gamma_i = d\Gamma_{i_{(\eta,\xi)}} \tag{B.6}$$

It can be shown that the gradient operator in the meniscus domain transforms as follows to the fixed domain:

$$\hat{\nabla} = \begin{pmatrix} \frac{\partial}{\partial \hat{r}} \\ \frac{\partial}{\partial \hat{z}} \end{pmatrix} = \mathbf{K}^{-T} \hat{\nabla}_{(\eta,\xi)} \tag{B.7}$$

Where,

$$\hat{\nabla}_{(\eta,\xi)} = \begin{pmatrix} \frac{\partial}{\partial \eta} \\ \frac{\partial}{\partial \xi} \end{pmatrix} \tag{B.8}$$

and

$$\mathbf{K}^{-T} = \left(\mathbf{K}^{-1}\right)^T = \frac{1}{\frac{\partial \hat{y}}{\partial \xi}} \begin{pmatrix} \frac{\partial \hat{y}}{\partial \xi} & 0 \\ -\frac{\partial \hat{y}}{\partial \eta} & 1 \end{pmatrix} \tag{B.9}$$

The divergence operator in cylindrical coordinates for a generic vector $\mathbf{a}$ yields:

$$\hat{\nabla} \cdot \mathbf{a} = \frac{1}{\eta \det\left(\mathbf{K}\right)} \hat{\nabla}_{(\eta,\xi)} \cdot \left(\eta \ \det\left(\mathbf{K}\right) \mathbf{K}^{-1} \mathbf{a}\right) \tag{B.10}$$

We define the non-dimensional electric field in the transformed domain as:

$$\hat{\mathbf{E}}_{(\eta,\xi)} = -\mathbf{K}^{-T} \hat{\nabla}_{(\eta,\xi)} \hat{\phi} \tag{B.11}$$

For the vacuum, the normal component of the electric field in the transformed domains is:

$$\hat{E}^v_{n(\eta,\xi)} = \hat{\mathbf{E}}^v_{(\eta,\xi)} \cdot \mathbf{n} \tag{B.12}$$

For the liquid, the normal component of the electric field in the transformed domains is:

$$\hat{E}^l_{n(\eta,\xi)} = \hat{\mathbf{E}}^l_{(\eta,\xi)} \cdot \mathbf{n} \tag{B.13}$$

The tangential component of the electric field is:

$$\hat{E}_{t(\eta,\xi)} = \hat{\mathbf{E}}_{(\eta,\xi)} \cdot \mathbf{t} \tag{B.14}$$

Under this transformation, the normal and tangential vectors yield:

$$\mathbf{n} = \begin{pmatrix} \frac{-d\hat{h}}{d\eta} \\ 1 \end{pmatrix} / \hat{S} \tag{B.15}$$

$$\mathbf{t} = \begin{pmatrix} 1 \\ \frac{d\hat{h}}{d\eta} \end{pmatrix} / \hat{S} \tag{B.16}$$

B.1.2 Equation for the meniscus map and boundary conditions

To account for coordinates of the meniscus in the problem formulation, and to define the numerical map, we need to consider additional equations to the ones summarized in tables 3.1 and 3.2. These are the Laplace equation for the map for both liquid and vacuum domains:

$$\hat{\nabla}^2_{(\eta,\xi)}\, \hat{y} = 0 \qquad \text{in} \qquad \mathbf{\Omega}^l_{(\eta,\xi)} \cup \mathbf{\Omega}^v_{(\eta,\xi)} \tag{B.17}$$

The boundary conditions for eq. B.17 are:

$$\hat{y} = \hat{z} \qquad \text{on} \qquad \Gamma_{EXT} \cup \Gamma^v_D \cup \Gamma^l_D \cup \Gamma_I \cup \Gamma_E \tag{B.18}$$

$$\hat{y} = \hat{h} \qquad \text{on} \qquad \Gamma_{M_{(\eta,\xi)}} \tag{B.19}$$

$$\frac{\partial^2 \hat{y}}{\partial \xi^2} = 0 \qquad \text{on} \qquad \Gamma^v_L \cup \Gamma^l_L \tag{B.20}$$

Eq. B.18 tells us that the map is exactly the physical vertical coordinate $\hat{z}$ at the external boundaries of the domain, as mentioned in section 4.1.1. Through eq. B.19 we enforce that the map is exactly the meniscus height in $\Gamma_{M_{(\eta,\xi)}}$, finally the map adapts to the meniscus physical height by a linear stretch on Γ_L through eq. B.20. This essentially means that whatever the height of the meniscus is, there will be a linear progression of $\hat{y}$ from $\hat{y} = \hat{h}$ at the apex of the meniscus (at the intersection between Γ_L and $\Gamma_{M_{(\eta,\xi)}}$), to the intersection of the left boundary Γ_L to the external domain Γ_{EXT} in $\mathbf{\Omega}^v$, or the inlet Γ_I in $\mathbf{\Omega}^l$.

B.1.3 Dimensionless weak form of the steady problem in the transformed domain (η, ξ)

In this section, we present the dimensionless weak form for the steady problem solved. We assume that we have a given space charge function in the vacuum $\hat{\rho}^v_{sch}$ that we have computed previously. The introduction of dummy variables is convenient to enforce equations in this problem. In such cases, we will explicitly mention it. Trial functions are represented using the same variable symbols. Test functions are represented using a subscript $\mathcal{T}$.

Curvature equation

We have a dummy variable for the dimensionless curvature $\hat{H}$ to use in the balance of stresses equations in the normal direction 3.38 and in eq. 3.26 when we study small dynamic perturbations. Future work could also use this dummy variable to incorporate curvature effects in the energy barrier for ion evaporation.

$$\int_{\Gamma_{M_{(\eta,\xi)}}} \frac{d\hat{h}}{d\eta}\frac{d\left(\eta\hat{h}_{\mathcal{T}}\right)}{d\eta}\, d\Gamma_{M_{(\eta,\xi)}} - \int_{\Gamma_{M_{(\eta,\xi)}}} \left(2\eta\hat{H}\hat{S}^3 + \hat{S}^2\frac{d\hat{h}}{d\eta}\right)\hat{h}_{\mathcal{T}}\, d\Gamma_{M_{(\eta,\xi)}} = 0 \qquad \text{(B.21)}$$

Meniscus height map equation

We use this weak form for eq. B.17. When multiplying eq.B.17 by the test function $\hat{y}_{\mathcal{T}}$, and applying the divergence theorem we get:

$$\begin{aligned}
&\int_{\mathbf{\Omega}^v_{(\eta,\xi)}} \hat{\nabla}_{(\eta,\xi)}\, \hat{y} \cdot\, \hat{\nabla}_{(\eta,\xi)}\, \hat{y}_{\mathcal{T}}\, d\mathbf{\Omega}^v_{(\eta,\xi)} \\
&+ \int_{\mathbf{\Omega}^l_{(\eta,\xi)}} \hat{\nabla}_{(\eta,\xi)}\, \hat{y} \cdot \hat{\nabla}_{(\eta,\xi)}\, \hat{y}_{\mathcal{T}}\, d\mathbf{\Omega}^l_{(\eta,\xi)} - \int_{\Gamma_{M_{(\eta,\xi)}}} \left(\frac{\partial \hat{y}}{\partial \xi}_v - \frac{\partial \hat{y}}{\partial \xi}_l\right)\, \hat{y}_{\mathcal{T}}\, d\Gamma_{M_{(\eta,\xi)}} \\
&+ \int_{\Gamma^l_L} \frac{\partial \hat{y}}{\partial \eta}\, \hat{y}_{\mathcal{T}}\, d\Gamma^l_L + \int_{\Gamma^v_L} \frac{\partial \hat{y}}{\partial \eta}\, \hat{y}_{\mathcal{T}}\, d\Gamma^v_L = 0
\end{aligned} \qquad \text{(B.22)}$$

Where the subscript l or v indicates that the gradient is evaluated at the liquid $\mathbf{\Omega}^l_{(\eta,\xi)}$ or vacuum $\mathbf{\Omega}^v_{(\eta,\xi)}$ side, respectively.

Eq. B.20 is enforced using Lagrange multipliers. We can give a physical interpretation to these as:

$$\lambda_L^l = -\frac{\partial \hat{y}}{\partial \eta} \qquad \text{on} \qquad \Gamma_L^l \tag{B.23}$$

$$\lambda_L^v = -\frac{\partial \hat{y}}{\partial \eta} \qquad \text{on} \qquad \Gamma_L^v \tag{B.24}$$

We can define a dummy variable for the jump in the coordinate map gradient as:

$$\iota = \left(\frac{\partial \hat{y}}{\partial \xi}_v - \frac{\partial \hat{y}}{\partial \xi}_l \right) \tag{B.25}$$

Substituting in eq. B.22 yields finally:

$$\begin{aligned} &\int_{\mathbf{\Omega}^v_{(\eta,\xi)}} \hat{\nabla}_{(\eta,\xi)}\; \hat{y} \cdot\; \hat{\nabla}_{(\eta,\xi)}\; \hat{y}_{\mathcal{T}}\; d\mathbf{\Omega}^v_{(\eta,\xi)} \\ &+ \int_{\mathbf{\Omega}^l_{(\eta,\xi)}} \hat{\nabla}_{(\eta,\xi)}\; \hat{y} \cdot \hat{\nabla}_{(\eta,\xi)}\; \hat{y}_{\mathcal{T}}\; d\mathbf{\Omega}^l_{(\eta,\xi)} - \int_{\Gamma_{M_{(\eta,\xi)}}} \iota\; \hat{y}_{\mathcal{T}}\; d\Gamma_{M_{(\eta,\xi)}} \\ &- \int_{\Gamma^l_L} \lambda^l_L\; \hat{y}_{\mathcal{T}}\; d\Gamma^l_L - \int_{\Gamma^v_L} \lambda^v_L\; \hat{y}_{\mathcal{T}}\; d\Gamma^v_L = 0 \end{aligned} \tag{B.26}$$

Map stretching boundary condition in vacuum

This equation enforces eq. B.20 on Γ_L^v.

$$\int_{\Gamma^v_L} \frac{\partial \hat{y}}{\partial \xi}\; \frac{\partial \lambda^v_{L_{\mathcal{T}}}}{\partial \xi}\; d\Gamma^v_L = 0 \tag{B.27}$$

Map stretching boundary condition in liquid

This equation enforces eq. B.20 on Γ_L^l.

$$\int_{\Gamma^l_L} \frac{\partial \hat{y}}{\partial \xi}\; \frac{\partial \lambda^l_{L_{\mathcal{T}}}}{\partial \xi}\; d\Gamma^l_L = 0 \tag{B.28}$$

Condition for the meniscus height

This equation enforces eq. B.19 on $\Gamma_{M_{(\eta,\xi)}}$.

$$\int_{\Gamma_{M_{(\eta,\xi)}}} \left(\hat{y} - \hat{h} \right) \iota_{\mathcal{T}}\; d\Gamma_{M_{(\eta,\xi)}} = 0 \tag{B.29}$$

Poisson equation

This equation contains the space charge in the vacuum domain $\hat{\rho}^v_{sch}$, which we solve separately.

$$
\begin{aligned}
&\int_{\mathbf{\Omega}^v_{(\eta,\xi)}} \eta \ \det(\mathbf{K}) \ \left(\mathbf{K}^{-T}\hat{\nabla}_{(\eta,\xi)}\hat{\phi}\right)\cdot\left(\mathbf{K}^{-T}\hat{\nabla}_{(\eta,\xi)}\hat{\phi}_{\mathcal{T}}\right) \ d\mathbf{\Omega}^v_{(\eta,\xi)} \\
&+\int_{\mathbf{\Omega}^l_{(\eta,\xi)}} \eta \ \varepsilon_r \ \det(\mathbf{K}) \ \left(\mathbf{K}^{-T}\hat{\nabla}_{(\eta,\xi)} \ \hat{\phi}\right)\cdot\left(\mathbf{K}^{-T}\hat{\nabla}_{(\eta,\xi)}\hat{\phi}_{\mathcal{T}}\right) \ d\mathbf{\Omega}^l_{(\eta,\xi)} \\
&-\int_{\Gamma_{M_{(\eta,\xi)}}} \eta\hat{\sigma}\hat{S}\hat{\phi}_{\mathcal{T}} d\Gamma_{M_{(\eta,\xi)}} - \int_{\mathbf{\Omega}^l_{(\eta,\xi)}} \eta \ \det(\mathbf{K}) \ \hat{\rho}_{sch}\hat{\phi}_{\mathcal{T}} \ d\mathbf{\Omega}^l_{(\eta,\xi)} \\
&-\int_{\mathbf{\Omega}^v_{(\eta,\xi)}} \eta \ \det(\mathbf{K}) \ \hat{\rho}^v_{sch}\hat{\phi}_{\mathcal{T}} \ d\mathbf{\Omega}^v_{(\eta,\xi)} = 0
\end{aligned}
\tag{B.30}
$$

Charge conservation at the interface

We can multiply the convective current density by the test function $\hat{\sigma}_{\mathcal{T}}$ and integrate by parts to get:

$$
\int_{\Gamma_M} -\eta\left(\hat{\kappa}\hat{E}^l_{n(\eta,\xi)} + \varepsilon_r\hat{R}\frac{t_c}{t_e} \ \hat{\sigma} \ \hat{\mathbf{u}}\cdot\mathbf{t}\frac{d\hat{\sigma}_{\mathcal{T}}}{d\eta}/\hat{S} - \hat{j}^e_n\right)\hat{\sigma}_{\mathcal{T}}\hat{S} \ d\Gamma_M = 0 \tag{B.31}
$$

Total current emitted

$$
\int_{\Gamma_{M_{(\eta,\xi)}}} \left(\hat{I} - 2\pi\eta \ \hat{j}^e_n \ \hat{S}\right)\hat{I}_{\mathcal{T}} \ d\Gamma_{M_{(\eta,\xi)}} = 0 \tag{B.32}
$$

Fluid momentum conservation

$$\begin{aligned}
&\int_{\boldsymbol{\Omega}^l_{(\eta,\xi)}} \frac{\hat{R}}{2\,Oh^2}\,\eta\,\det\left(\mathbf{K}\right)\,\hat{\mathbf{u}}^T\cdot\mathbf{K}^{-T}\cdot\left(\hat{\nabla}_{(\eta,\xi)}\hat{\mathbf{u}}^T\right)^T\cdot\hat{\mathbf{u}}_{\mathcal{T}}\,d\boldsymbol{\Omega}^l_{(\eta,\xi)}+\int_{\boldsymbol{\Omega}^l_{(\eta,\xi)}}\eta\det\left(\mathbf{K}\right)\,\hat{\tau}_{f_{(\eta,\xi)}}\\
&:\frac{1}{2}\left(\mathbf{K}^{-T}\cdot\left(\hat{\nabla}_{(\eta,\xi)}\hat{\mathbf{u}}^T_{\mathcal{T}}\right)^T+\left(\hat{\nabla}_{(\eta,\xi)}\hat{\mathbf{u}}^T_{\mathcal{T}}\right)\cdot\mathbf{K}^{-1}\right)\,d\boldsymbol{\Omega}^l_{(\eta,\xi)}+\int_{\boldsymbol{\Omega}^l_{(\eta,\xi)}}\det\,\left(\mathbf{K}\right)\frac{\hat{\mu}\hat{u}_r\hat{u}_{\mathcal{T}_r}}{\eta}\,d\boldsymbol{\Omega}_l\\
&\quad-\int_{\boldsymbol{\Omega}^l_{(\eta,\xi)}}\det\left(\mathbf{K}\right)\,\hat{p}\,\hat{u}_{\mathcal{T}_r}d\boldsymbol{\Omega}^l_{(\eta,\xi)}+\int_{\boldsymbol{\Omega}^l_{(\eta,\xi)}}2\,\eta\,\det\left(\mathbf{K}\right)\hat{\rho}_{sch}\hat{\mathbf{E}}_{(\eta,\xi)}\,d\boldsymbol{\Omega}^l_{(\eta,\xi)}\\
&\quad-\int_{\Gamma_{M_{(\eta,\xi)}}}\eta\,\lambda_{\hat{\tau}_{\mathbf{n}}}\hat{\mathbf{u}}_{\mathcal{T}}\cdot\mathbf{n}\,\hat{S}d\Gamma_{M_{(\eta,\xi)}}-\int_{\Gamma_{M_{(\eta,\xi)}}}\eta\,\lambda_{\hat{\tau}_{\mathbf{t}}}\hat{\mathbf{u}}_{\mathcal{T}}\cdot\mathbf{t}\hat{S}\,d\Gamma_{M_{(\eta,\xi)}}\\
&=0
\end{aligned} \tag{B.33}$$

The transformation of the fluid stress tensor is written below:

$$\begin{aligned}
\hat{\tau}_{f_{(\eta,\xi)}}=-\hat{p}\mathbf{I}_n+\frac{\hat{\mu}}{2}\left(\hat{T}\right)\Bigg(\mathbf{K}^{-T}\cdot\left(\hat{\nabla}_{(\eta,\xi)}\hat{\mathbf{u}}^T\right)^T&\\
+\left(\hat{\nabla}_{(\eta,\xi)}\hat{\mathbf{u}}^T\right)\cdot\mathbf{K}^{-1}\Bigg)&
\end{aligned} \tag{B.34}$$

Analogously to the map functions, we enforce the balance of normal and tangential stresses using Lagrange multipliers, in this case, we give the interpretation for those in eq. B.33 as:

$$\lambda_{\hat{\tau}_{\mathbf{t}}}=\mathbf{t}\cdot\hat{\tau}_{f_{(\eta,\xi)}}\cdot\mathbf{n} \tag{B.35}$$

$$\lambda_{\hat{\tau}_{\mathbf{n}}}=\mathbf{n}\cdot\hat{\tau}_{f_{(\eta,\xi)}}\cdot\mathbf{n} \tag{B.36}$$

The pressure impedance boundary conditions are included in the equilibrium of stresses in the normal direction.

Equilibrium of stresses in the normal direction

$$\begin{aligned}
\int_{\Gamma_{M_{(\eta,\xi)}}}\eta\,\Bigg(&\hat{E}^{v^2}_{n(\eta,\xi)}-\varepsilon_r\hat{E}^{l^2}_{n(\eta,\xi)}+\left(1-\varepsilon_r\right)\hat{E}^2_{t(\eta,\xi)}+\hat{p}_r-\hat{I}\hat{R}^{\frac{5}{2}}\hat{Z}\\
&-\lambda_{\hat{\tau}_{\mathbf{n}}}+C_\beta\,\left(\hat{j}^e_n\right)^2\left(1-\beta\right)-\hat{\gamma}\hat{H}\Bigg)\,\hat{H}_{\mathcal{T}}\,\hat{S}\,d\Gamma_{M_{(\eta,\xi)}}=0
\end{aligned} \tag{B.37}$$

Equilibrium of stresses in the tangential direction

$$\int_{\Gamma_{M_{(\eta,\xi)}}} \eta \left(\lambda_{\hat{\tau}_{\mathbf{t}}} - 2\hat{\sigma}\hat{E}_{t(\eta,\xi)} + \mathbf{t}\cdot\mathbf{K}^{-T}\cdot\hat{\nabla}_{(\eta,\xi)}\hat{\gamma}/2\right)\ \lambda_{\hat{\tau}_{\mathbf{t}_{\mathcal{T}}}}\ \hat{S}\ d\Gamma_{M_{(\eta,\xi)}} \tag{B.38}$$

Mass conservation

$$\int_{\mathbf{\Omega}^l_{(\eta,\xi)}} \hat{\nabla}_{(\eta,\xi)}\cdot\left(\eta\ \det\left(\mathbf{K}\right)\ \mathbf{K}^{-1}\hat{\mathbf{u}}\right)\hat{p}_{\mathcal{T}}\ d\mathbf{\Omega}^l_{(\eta,\xi)} \tag{B.39}$$

Evaporated mass and charge equivalence

$$\int_{\Gamma_{M_{(\eta,\xi)}}} \eta \left(\frac{\varepsilon_r C_m}{\hat{R}^{3/2}}\hat{j}^e_n - \frac{1}{\hat{R}}\hat{\mathbf{u}}\cdot\mathbf{n}\right)\lambda_{\hat{\tau}_{\mathbf{n}_{\mathcal{T}}}}\ \hat{S}d\Gamma_{M_{(\eta,\xi)}} \tag{B.40}$$

Energy transport equation

$$\begin{aligned}
&\int_{\mathbf{\Omega}^l_{(\eta,\xi)}} \eta\ \det(\mathbf{K})\ \frac{1}{Pe\hat{R}^2}\left(\mathbf{K}^{-T}\hat{\nabla}_{(\eta,\xi)}\hat{T}\right)\cdot\left(\mathbf{K}^{-T}\hat{\nabla}_{(\eta,\xi)}\hat{T}_{\mathcal{T}}\right)\ d\mathbf{\Omega}^l_{(\eta,\xi)} \\
&+\int_{\mathbf{\Omega}^l_{(\eta,\xi)}} \eta\ \det(\mathbf{K})\ \frac{1}{\hat{R}}\ \left(\mathbf{K}^{-T}\hat{\nabla}_{(\eta,\xi)}\ \hat{T}\right)\cdot\hat{\mathbf{u}}\ \hat{T}_{\mathcal{T}}\ d\mathbf{\Omega}^l_{(\eta,\xi)} \\
&-\int_{\mathbf{\Omega}^l_{(\eta,\xi)}} \eta\ \det(\mathbf{K})\ \frac{\varepsilon_r t_\mu}{\hat{R}t_e}\ \hat{\kappa}\hat{\mathbf{E}}_{(\eta,\xi)}\cdot\hat{\mathbf{E}}_{(\eta,\xi)}\ \hat{T}_{\mathcal{T}}\ d\mathbf{\Omega}^l_{(\eta,\xi)} \\
&-\int_{\mathbf{\Omega}^l_{(\eta,\xi)}} \eta\ \det(\mathbf{K})\frac{t_\mu\hat{\mu}}{2\hat{R}^2 t_c}\hat{e}^2_{ij}\ \hat{T}_{\mathcal{T}}\ d\mathbf{\Omega}^l_{(\eta,\xi)} \\
&+\int_{\Gamma_{M_{(\eta,\xi)}}} \eta\ \frac{\varepsilon_r C_m}{\hat{R}^{3/2}Pe^2}\hat{j}^e_n\left(\hat{T}_{out} - \hat{T} + \hat{l}_H\right)\ \hat{T}_{\mathcal{T}}d\Gamma_{M_{(\eta,\xi)}} = 0
\end{aligned} \tag{B.41}$$

Charge conservation equation

$$\begin{aligned}
&\int_{\mathbf{\Omega}^l_{(\eta,\xi)}} \eta \det(\mathbf{K}) \frac{t_c}{t_e} \hat{\rho}_{sch} \hat{\kappa}\left(\hat{T}\right)\ \hat{\rho}_{sch_{\mathcal{T}}}\ d\mathbf{\Omega}^l_{(\eta,\xi)} \\
&+ \int_{\mathbf{\Omega}^l_{(\eta,\xi)}} \eta \det(\mathbf{K})\ \varepsilon_r \frac{t_c}{t_e} \hat{\mathbf{E}}_{(\eta,\xi)} \cdot \left(\mathbf{K}^{-T} \hat{\nabla}_{(\eta,\xi)}\ \hat{\kappa}\right)\ \hat{\rho}_{sch_{\mathcal{T}}}\ \ d\mathbf{\Omega}^l_{(\eta,\xi)} \\
&+ \int_{\mathbf{\Omega}^l_{(\eta,\xi)}} \eta \det(\mathbf{K})\ \frac{1}{\hat{R}}\ \left(\mathbf{K}^{-T} \hat{\nabla}_{(\eta,\xi)}\ \hat{\rho}_{sch}\right) \cdot \hat{\mathbf{u}}\ \hat{\rho}_{sch_{\mathcal{T}}}\ d\mathbf{\Omega}^l_{(\eta,\xi)} = 0
\end{aligned} \tag{B.42}$$

Summary

In summary, our solution global variable is:

$$\mathbf{x}\left(\eta,\xi\right) = \{\hat{h}, \hat{y}, \iota, \hat{\phi}, \hat{\sigma}, \hat{I}, \hat{\mathbf{u}}, \hat{p}, \lambda_{\hat{\tau}_{\mathbf{u}}}, \lambda_{\hat{\tau}_{\mathbf{t}}}, \lambda^v_L, \lambda^l_L, \hat{T}, \hat{\rho}_{sch}, \hat{H}\} \tag{B.43}$$

Where $\hat{\rho}_{sch}$ references only the liquid component, which originates mostly from gradients in conductivity.

For each variable, we use a continuous Galerkin discretization with Lagrange basis elements of polynomial order given by table B.1.

B.2 Maximum in lumped parameter equation

We are interested in finding a maximum of a function of the following structure:

$$I = \frac{32\pi\gamma^2}{t_e {E^*}^3 \frac{{E^v_n}^3}{{E^*}^3}} \frac{1}{\frac{t_m}{t_e} \exp\psi \left(1 - \sqrt{\frac{E^v_n}{E^*}}\right) + 1} \tag{B.44}$$

The equation can be made dimensionless as:

$$\bar{I} = \frac{1}{\bar{E}^3} \frac{1}{\chi \exp\psi \left(1 - \sqrt{\bar{E}}\right) + 1} \tag{B.45}$$

Where $\bar{I} = I / \frac{32\pi\gamma^2}{t_e {E^*}^3}$, $\bar{E} = E/E^*$, and $\chi = t_m/t_e$.

Variable	Trial function	Test function	Polynomial order	Equation weighted	Domain
Meniscus interface profile	$\hat{h}$	$\hat{h}_{\mathcal{T}}$	1	B.21	$\Gamma_{M_{(\eta,\xi)}}$
Meniscus coordinate map	$\hat{y}$	$\hat{y}_{\mathcal{T}}$	2	B.22	$\boldsymbol{\Omega}^v \cup \boldsymbol{\Omega}^l$
Map gradient jump	ι	$\iota_{\mathcal{T}}$	1	B.29	$\Gamma_{M_{(\eta,\xi)}}$
Potential	$\hat{\phi}$	$\hat{\phi}_{\mathcal{T}}$	2	B.30	$\boldsymbol{\Omega}^v \cup \boldsymbol{\Omega}^l$
Interfacial charge	$\hat{\sigma}$	$\hat{\sigma}_{\mathcal{T}}$	1	B.31	$\Gamma_{M_{(\eta,\xi)}}$
Total current	$\hat{I}$	$\hat{I}_{\mathcal{T}}$	0	B.32	$\mathbb{R}^+$
Velocity	$\hat{\mathbf{u}}$	$\hat{\mathbf{u}}_{\mathcal{T}}$	2	B.33	$\boldsymbol{\Omega}^l$
Pressure	$\hat{p}$	$\hat{p}_{\mathcal{T}}$	1	B.39	$\boldsymbol{\Omega}^l$
Fluid normal stress	$\lambda_{\hat{\tau}_{\mathbf{n}}}$	$\lambda_{\hat{\tau}_{\mathbf{n}_{\mathcal{T}}}}$	1	B.40	$\Gamma_{M_{(\eta,\xi)}}$
Fluid tangential stress	$\lambda_{\hat{\tau}_{\mathbf{t}}}$	$\lambda_{\hat{\tau}_{\mathbf{t}_{\mathcal{T}}}}$	1	B.38	$\Gamma_{M_{(\eta,\xi)}}$
Vacuum map gradient in radial direction	λ^v_L	$\lambda^v_{L_{\mathbf{t}_{\mathcal{T}}}}$	1	B.27	Γ^v_L
Liquid map gradient in radial direction	λ^l_L	$\lambda^l_{L_{\mathbf{t}_{\mathcal{T}}}}$	1	B.28	Γ^l_L
Temperature	$\hat{T}$	$\hat{T}_{\mathcal{T}}$	2	B.41	$\boldsymbol{\Omega}^l$
Bulk liquid space charge	$\hat{\rho}_{sch}$	$\hat{\rho}_{sch_{\mathcal{T}}}$	1	B.42	$\boldsymbol{\Omega}^l$
Mean curvature	$\hat{H}$	$\hat{H}_{\mathcal{T}}$	1	B.37	$\Gamma_{M_{(\eta,\xi)}}$

Table B.1: Variables included in solution vector x.

We can differentiate B.45 and equate to 0, as usual to find extrema:

$$\frac{d\bar{I}}{d\bar{E}} = \frac{\chi \exp\left(\psi\left(1-\sqrt{\bar{E}}\right)\right)\left(\psi\sqrt{\bar{E}}-6\right)-6}{2\bar{E}^4\left(\chi\exp\left(\psi\left(1-\sqrt{\bar{E}}\right)\right)+1\right)^2} = 0 \tag{B.46}$$

With some algebraic manipulation we can find an implicit form for condition B.46 as:

$$\left(6-\psi\sqrt{\bar{E}}\right)\exp\left(6-\psi\sqrt{\bar{E}}\right) = -\frac{6\exp\left(6-\psi\right)}{\chi} \tag{B.47}$$

For values we expect for $\psi > 30$ and $\chi \sim 10^{-3}$, there are two different solutions for $\bar{E}$ that can be expressed as a function of the branches 0 or -1 of the Lambert W function:

$$6-\psi\sqrt{\bar{E}} = W_i\left(-\frac{6\exp\left(6-\psi\right)}{\chi}\right) \tag{B.48}$$

Where $i = 0, -1$ indicates the branch number. We evaluate branch 0 numerically for the previous ψ and χ values and discard it for being very small, therefore we have a value for $\bar{E}$ that yields a maximum in $\bar{I}$ as:

$$\bar{E} = \frac{\left(6-W_{-1}\left(-\frac{6\exp(6-\psi)}{\chi}\right)\right)^2}{\psi^2} \tag{B.49}$$

At this point we could substitute B.49 in B.45 to yield the exact value for $\bar{I}_{max}$. However, a more convenient and readable expression for $\bar{I}_{max}$ could come along with the fact that the argument inside W_{-1} tends to negative zero for the the typical values we expect $\psi > 30$ and $\chi \sim 10^{-3}$. Under these conditions, namely $x = -\frac{6\exp(6-\psi)}{\chi} \to 0^-$ then $W_{-1}\left(x\right) \approx \ln\left(-x\right) - \ln\left(-\ln\left(-x\right)\right)$ [25]. For the estimations relevant in this thesis only a term suffices, then if we substitute in B.49 yields:

$$\bar{E} \approx \frac{\left(6-\ln\left(\frac{6\exp(6-\psi)}{\chi}\right)\right)^2}{\psi^2} = \left(1+\frac{\ln\left(6\chi\right)}{\psi}\right)^2 \tag{B.50}$$

And substituting in B.45 yields:

$$\bar{I}_{max} \approx \frac{6}{7}\frac{1}{\left(1+\frac{\ln(6\chi)}{\psi}\right)^6} \tag{B.51}$$

Bibliography

[1] K. L. Aitken and Graeme L. R. Mair. Emission characteristics of a liquid caesium ion source. *Journal of Physics D: Applied Physics*, 13(11):2165–2173, 11 1980.

[2] Saeid Azizian and Maryam Hemmati. Surface tension of binary mixtures of ethanol + ethylene glycol from 20 to 50°C. *Journal of Chemical and Engineering Data*, 48(3):662–663, 5 2003.

[3] Francesco Ballarin and Gianluigi Rozza. multiphenicsx - easy prototyping of multiphysics problems in FEniCSx.

[4] Osman A. Basaran and L. E. Scriven. Axisymmetric shapes and stability of charged drops in an external electric field. *Physics of Fluids A*, 1(5):799–809, 5 1989.

[5] Osman A. Basaran and L. E. Scriven. Axisymmetric shapes and stability of isolated charged drops. *Physics of Fluids A*, 1(5):795–798, 5 1989.

[6] Osman A. Basaran and L. E. Scriven. Axisymmetric shapes and stability of pendant and sessile drops in an electric field. *Journal of Colloid And Interface Science*, 140(1):10–30, 1990.

[7] Osman A. Basaran and Fred K. Wohlhuter. Effect of nonlinear polarization on shapes and stability of pendant and sessile drops in an electric (magnetic) field. *Journal of Fluid Mechanics*, 244:1–16, 1992.

[8] Ram P. Bharti, Dalton J.E. Harvie, and Malcolm R. Davidson. Steady flow of ionic liquid through a cylindrical microfluidic contraction-expansion pipe: Electroviscous effects and pressure drop. *Chemical Engineering Science*, 63(14):3593–3604, 7 2008.

[9] M. G. Blyth, H. Luo, and C. Pozrikidis. Stability of axisymmetric core-annular flow in the presence of an insoluble surfactant. *Journal of Fluid Mechanics*, 548:207–235, 2 2006.

[10] John O'M. Bockris and Amulya K. N. Reddy. *Modern Electrochemistry 1*. Springer US, 1998.

[11] J. B. Bostwick and P. H. Steen. Stability of constrained capillary surfaces. *Annual Review of Fluid Mechanics*, 47:539–568, 2015.

[12] W. D. Carrier. Goodbye, Hazen; Hello, Kozeny-Carman. *Journal of Geotechnical and Geoenvironmental Engineering*, 129(11):1054–1056, 11 2003.

[13] S. Castro and J. Fernández de la Mora. Effect of tip curvature on ionic emissions from Taylor cones of ionic liquids from externally wetted tungsten tips. *Journal of Applied Physics*, 105(3), 2009.

[14] S. Castro, C. Larriba, J. Fernandez De La Mora, Paulo C. Lozano, S. Sümer, Y. Yoshida, and G. Saito. Effect of liquid properties on electrosprays from externally wetted ionic liquid ion sources. *Journal of Applied Physics*, 102(9):094310, 11 2007.

[15] S. Castro, C. Larriba, J. Fernandez De La Mora, Paulo C. Lozano, S Sümer, Y Yoshida, and G Saito. Effect of liquid properties on electrosprays from externally wetted ionic liquid ion sources. *Journal of Applied Physics*, 102(9):44104, 2007.

[16] S. Castro, C. Larriba, J. Fernández de la Mora, Paulo C. Lozano, and S. Sumer. Capillary vs. externally wetted ionic liquid ion sources. In *Collection of Technical Papers - AIAA/ASME/SAE/ASEE 42nd Joint Propulsion Conference*, volume 4, pages 3262–3267, 2006.

[17] Yu Hui Chiu and Rainer A. Dressler. Ionic liquids for space propulsion. In *ACS Symposium Series*, volume 975, pages 138–160, 2007.

[18] M. Cloupeau and B. Prunet-Foch. Electrostatic spraying of liquids in cone-jet mode. *Journal of Electrostatics*, 22(2):135–159, 7 1989.

[19] Chase S. Coffman. *Electrically-Assisted Evaporation of Charged Fluids: Fundamental Modeling and Studies on Ionic Liquids*. PhD thesis, Massachusetts Institute of Technology, 2016.

[20] Chase S. Coffman, Manuel Martínez-Sánchez, Francisco J. Higuera, and Paulo C. Lozano. Structure of the menisci of leaky dielectric liquids during electrically-assisted evaporation of ions. *Applied Physics Letters*, 109(23):231602, 12 2016.

[21] Chase S. Coffman, Manuel Martínez-Sánchez, and Paulo C. Lozano. Electrohydrodynamics of an ionic liquid meniscus during evaporation of ions in a regime of high electric field. *Physical Review E*, 99(6):063108, 2019.

[22] Chase S. Coffman, Louis Perna, Hanqing Li, and Paulo C. Lozano. On the manufacturing and emission characteristics of a novel borosilicate electrospray source. In *49th AIAA/ASME/SAE/ASEE Joint Propulsion Conference*, volume 1 PartF, 2013.

[23] Robert T. Collins, Jeremy J. Jones, Michael T. Harris, and Osman A. Basaran. Electrohydrodynamic tip streaming and emission of charged drops from liquid-cones. *Nature Physics*, 2008.

[24] J. J. Connor and C. A. Brebbia. *Finite element techniques for fluid flow.* 1976.

[25] R. M. Corless, G. H. Gonnet, D. E.G. Hare, D. J. Jeffrey, and D. E. Knuth. On the Lambert W function. *Advances in Computational Mathematics*, 5(1):329–359, 1996.

[26] Daniel G. Courtney, Hanqing Q. Li, and Paulo C. Lozano. Emission measurements from planar arrays of porous ionic liquid ion sources. *Journal of Physics D: Applied Physics*, 45(48), 2012.

[27] Daniel G. Courtney and Herbert R. Shea. Influences of porous reservoir Laplace pressure on emissions from passively fed ionic liquid electrospray sources. *Applied Physics Letters*, 107(10):103504, 9 2015.

[28] Alexey Deyko, Kevin R.J. Lovelock, Jo Anne Corfield, Alasdair W. Taylor, Peter N. Gooden, Ignacio J. Villar-Garcia, Peter Licence, Robert G. Jones, Vladimir G. Krasovskiy, Elena A. Chernikova, and Leonid M. Kustov. Measuring and predicting ΔvapH298 values of ionic liquids. *Physical Chemistry Chemical Physics*, 11(38):8544–8555, 9 2009.

[29] J. Donea, A. Huerta, J.-Ph. Ponthot, and A. Rodríguez-Ferran. Arbitrary Lagrangian-Eulerian Methods. In *Encyclopedia of Computational Mechanics.* John Wiley & Sons, Ltd, 11 2004.

[30] W. Driesel, Ch. Dietzsch, H. Niedrig, and B. Praprotnik. HV TEM in situ investigations of the tip shape of a gallium liquid-metal ion/electron emitter. *Ultramicroscopy*, 57(1):45–58, 1 1995.

[31] J.J. Van Es, J. Gierak, R.G. Forbes, V.G. Suvorov, T. Van den Berghe, Ph. Dubuisson, I. Monnet, and A. Septier. An improved gallium liquid metal ion source geometry for nanotechnology. *Microelectronic Engineering*, 73-74:132–138, 6 2004.

[32] J. Fernández de la Mora. The fluid dynamics of Taylor Cones. *Annual Review of Fluid Mechanics*, 39(1):217–243, 1 2007.

[33] J. Fernández de la Mora and I. G. Loscertales. The current emitted by highly conducting Taylor cones. *Journal of Fluid Mechanics*, 260(special issue):155–184, 1994.

[34] Richard G. Forbes. Understanding how the liquid-metal ion source works. *Vacuum*, 48(1):85–97, 1 1997.

[35] Richard G. Forbes, R. K. Biswas, and K. Chibane. Field evaporation theory: A re-analysis of published field sensitivity data. *Surface Science*, 114(2-3):498–514, 2 1982.

[36] Richard G. Forbes, T. Ganetsos, Graeme L. R. Mair, and V. Suvorov. Liquid metal ion sources at Aston in the 1980s and what followed. *Proceedings of the Royal Microscopical Society*, 39:218–226, 2004.

[37] Richard G. Forbes and Neboysha N. Ljepojevic. Liquid-metal ion source theory: electrohydrodynamics and emitter shape. *Surface Science*, 266(1-3):170–175, 4 1992.

[38] Richard G. Forbes and Graeme L. R. Mair. Liquid metal ion sources. In *Handbook of Charged Particle Optics, Second Edition*, pages 29–86. CRC Press, 12 2017.

[39] Richard G. Forbes, Graeme L. R. Mair, Neboysha N. Ljepojevic, and Wenbin Liu. New understandings in the theory of liquid-metal ion sources. *Applied Surface Science*, 87-88(C):99–105, 3 1995.

[40] Dakota S. Freeman. *Design and manufacture of the next generation of ion electrospray thrusters*. PhD thesis, Massachusetts Institute of Technology, 2019.

[41] Michael Freemantle. *An Introduction to Ionic Liquids*. RSC Publishing, 2009.

[42] Ximo Gallud and Paulo C. Lozano. The emission properties, structure and stability of ionic liquid menisci undergoing electrically assisted ion evaporation. *Journal of Fluid Mechanics*, 933, 2 2022.

[43] Ximo Gallud, Paulo C. Lozano, Rafid Bendimerad, Elaine M. Petro, and Sebastian K. Hampl. Modeling and Characterization of Electrospray Propellant-Surface Interactions. In *IEEE Aerospace Conference Proceedings*, volume 2022-March. IEEE Computer Society, 2022.

[44] Manuel Gamero-Castaño. Electric-Field-Induced Ion Evaporation from Dielectric Liquid. *Physical Review Letters*, 89(14), 2002.

[45] Manuel Gamero-Castaño and Juan Fernández de la Mora. Direct measurement of ion evaporation kinetics from electrified liquid surfaces. *Journal of Chemical Physics*, 113(2):815–832, 7 2000.

[46] Manuel Gamero-Castaño and V. Hruby. Electrospray as a source of nanoparticles for efficient colloid thrusters. *Journal of Propulsion and Power*, 17(5):977–987, 5 2001.

[47] Manuel Gamero-Castaño and Marco Magnani. Numerical simulation of electrospraying in the cone-jet mode. *Journal of Fluid Mechanics*, 859:247–267, 1 2019.

[48] Alfonso M. Gañán-Calvo. Cone-jet analytical extension of Taylor's electrostatic solution and the asymptotic universal scaling laws in electrospraying. *Physical Review Letters*, 79(2):217–220, 7 1997.

[49] Alfonso M. Gañán-Calvo. The surface charge in electrospraying: Its nature and its universal scaling laws. *Journal of Aerosol Science*, 30(7):863–872, 8 1999.

[50] Alfonso M. Gañán-Calvo, Jonathan M. Dávila, and Antonio Barrero. Current and droplet size in the electrospraying of liquids. Scaling laws. *Journal of Aerosol Science*, 28(2):249–275, 1997.

[51] Alfonso M. Gañán-Calvo, J. M. López-Herrera, N. Rebollo-Muñoz, and J. M. Montanero. The onset of electrospray: The universal scaling laws of the first ejection. *Scientific Reports*, 6(1):1–9, 9 2016.

[52] Alfonso M. Gañán-Calvo and José M. Montanero. Revision of capillary cone-jet physics: Electrospray and flow focusing. *Physical Review E - Statistical, Nonlinear, and Soft Matter Physics*, 79(6):066305, 6 2009.

[53] S. García-Garabal, J. Vila, E. Rilo, M. Domínguez-Pérez, L. Segade, E. Tojo, P. Verdía, L. M. Varela, and O. Cabeza. TRANSPORT PROPERTIES FOR 1-ETHYL-3-METHYLIMIDAZOLIUM n-ALKYL SULFATES: POSSIBLE EVIDENCE OF GROTTHUSS MECHANISM. *Electrochimica Acta*, 231:94–102, 3 2017.

[54] D. Garoz, C. Bueno, C. Larriba, S. Castro, I. Romero-Sanz, J. Fernandez De La Mora, Y. Yoshida, and G. Saito. Taylor cones of ionic liquids from capillary tubes as sources of pure ions: The role of surface tension and electrical conductivity. *Journal of Applied Physics*, 102(6):064913, 9 2007.

[55] P. W.J. Glover and Emilie Walker. Grain-size to effective pore-size transformation derived from electrokinetic theory. *Geophysics*, 74(1), 12 2009.

[56] William G. Gray, Anton Leijnse, Randall L. Kolar, and Cheryl A. Blain. *Mathematical Tools for Changing Spatial Scales in the Analysis of Physical Systems*. CRC Press, Boca Raton, 1st edition, 2020.

[57] Yuntao Guo, Wei Sun, Zhenning Sun, Zhiwen Wu, Jianwu He, Chao Yang, and Ningfei Wang. Direct thrust test and asymmetric performance of porous ionic liquid electrospray thruster. *Chinese Journal of Aeronautics*, 36(4):120–133, 4 2023.

[58] Vicente Hernández, Jose E. Román, and Vicente Vidal. SLEPc: Scalable library for eigenvalue problem computations. *Lecture Notes in Computer Science (including subseries Lecture Notes in Artificial Intelligence and Lecture Notes in Bioinformatics)*, 2565:377–391, 2003.

[59] Miguel A. Herrada, J. M. López-Herrera, Alfonso M. Gañán-Calvo, E. J. Vega, J. M. Montanero, and S. Popinet. Numerical simulation of electrospray in the cone-jet mode. *Physical Review E - Statistical, Nonlinear, and Soft Matter Physics*, 86(2):247–267, 1 2012.

[60] Miguel A. Herrada and J. M. Montanero. A numerical method to study the dynamics of capillary fluid systems. *Journal of Computational Physics*, 306:137–147, 2 2016.

[61] Francisco J. Higuera. Flow rate and electric current emitted by a Taylor cone. *Journal of Fluid Mechanics*, 484(484):303–327, 6 2003.

[62] Francisco J. Higuera. Liquid flow induced by ion evaporation in an electrified meniscus. *Physical Review E - Statistical Physics, Plasmas, Fluids, and Related Interdisciplinary Topics*, 69(6):10, 2004.

[63] Francisco J. Higuera. Model of the meniscus of an ionic-liquid ion source. *Physical Review E - Statistical, Nonlinear, and Soft Matter Physics*, 77(2), 2008.

[64] Christopher J. Hogan and Juan Fernández De La Mora. Tandem ion mobility-mass spectrometry (IMS-MS) study of ion evaporation from ionic liquid-acetonitrile nanodrops. *Physical Chemistry Chemical Physics*, 11(36):8079–8090, 9 2009.

[65] Chengjin Huang, Jianling Li, Mu Li, Ting Si, Cha Xiong, and Wei Fan. Experimental investigation on current modes of ionic liquid electrospray from a coned porous emitter. *Acta Astronautica*, 183:286–299, 2021.

[66] Mian Mian Huang, Yanping Jiang, Padmanabhan Sasisanker, Gordon W. Driver, and Hermann Weingärtner. Static relative dielectric permittivities of ionic liquids at 25 °c. *Journal of Chemical and Engineering Data*, 56(4):1494–1499, 4 2011.

[67] J. V. Iribarne and B. A. Thomson. On the evaporation of small ions from charged droplets. *The Journal of Chemical Physics*, 64(6):2287, 1976.

[68] Oliver Jia-Richards. Quantification of ionic-liquid ion source beam composition from time-of-flight data. *Journal of Applied Physics*, 132(7):74501, 8 2022.

[69] MA Jianghua, LI Yuping, LI Huiquan, and ZHANG Yi. Synthesis of 1-Ethyl-3-methylimidazolium Hydrogen Sulfate and Its Application in the Electrolysis of Aluminum. *Chinese Journal of Process Engineering*, 7(6):1083–1088, 2007.

[70] George Karapetsas, Kirti Chandra Sahu, and Omar K Matar. Evaporation of Sessile Droplets Laden with Particles and Insoluble Surfactants. *Langmuir*, 32(27):6871–6881, 2016.

[71] D. R. Kingham and L. W. Swanson. Shape of a liquid metal ion source - A dynamic model including fluid flow and space-charge effects. Technical Report 2, 1984.

[72] C. Kolbeck, J. Lehmann, K. R.J. Lovelock, T. Cremer, N. Paape, P. Wasserscheid, A. P. Fröba, F. Maier, and H. P. Steinrück. Density and surface tension of ionic liquids. *Journal of Physical Chemistry B*, 114(51):17025–17036, 12 2010.

[73] Spyridon Koutsoukos, Frederik Philippi, Daniel Rauber, David Pugh, Christopher W.M. Kay, and Tom Welton. Effect of the cation structure on the properties of homobaric imidazolium ionic liquids. *Physical Chemistry Chemical Physics*, 24(11):6453–6468, 3 2022.

[74] Renato Krpoun and Herbert R. Shea. A method to determine the onset voltage of single and arrays of electrospray emitters. *Journal of Applied Physics*, 104(6), 2008.

[75] C. Larriba, S. Castro, J. Fernandez De La Mora, and Paulo C. Lozano. Monoenergetic source of kilodalton ions from Taylor cones of ionic liquids. *Journal of Applied Physics*, 101(8):084303, 4 2007.

[76] Robert S. Legge and Paulo C. Lozano. Electrospray Propulsion Based on Emitters Microfabricated in Porous Metals. *Journal of Propulsion and Power*, 27(2):485–495, 2011.

[77] R. Levi-Setti, G. Crow, and Y. L. Wang. Progress in high resolution scanning ion microscopy and secondary ion mass spectrometry imaging microanalysis. *Scanning Electron Microscopy*, 2(Pt 2):535, 1985.

[78] Qingyang Lin, Branko Bijeljic, Ronny Pini, Martin J. Blunt, and Samuel Krevor. Imaging and Measurement of Pore-Scale Interfacial Curvature to Determine Capillary Pressure Simultaneously With Relative Permeability. *Water Resources Research*, 54(9):7046–7060, 9 2018.

[79] Anders Logg, Kent Andre Mardal, and Garth N. Wells. Automated solution of differential equations by the finite element method. *Lecture Notes in Computational Science and Engineering*, 84 LNCSE:1–736, 2012.

[80] Paulo C. Lozano. Energy properties of an EMI-Im ionic liquid ion source. *Journal of Physics D: Applied Physics*, 39(1):126–134, 2006.

[81] Paulo C. Lozano and Manuel Martínez-Sánchez. Ionic liquid ion sources: Characterization of externally wetted emitters. *Journal of Colloid and Interface Science*, 282(2):415–421, 2005.

[82] Graeme L. R. Mair. Current-voltage curves in liquid metal ion sources. *Vacuum*, 36(11-12):847–850, 1986.

[83] Graeme L.R. Mair. The effects of flow impedance on the current-voltage characteristics of liquid-metal ion sources. *Journal of Physics D: Applied Physics*, 30(13):1945–1950, 7 1997.

[84] K. N. Marsh, J. A. Boxall, and R. Lichtenthaler. Room temperature ionic liquids and their mixtures - A review. In *Fluid Phase Equilibria*, volume 219, pages 93–98. Elsevier, 5 2004.

[85] Manuel Martínez-Sánchez and Paulo C. Lozano. Electrospray Propulsion Notes. *MIT OCW (16.522)*, 2015.

[86] Catherine E. Miller. *Characterization of Ion Cluster Fragmentation in Ionic Liquid Ion Sources*. PhD thesis, Massachusetts Institute of Technology, 2019.

[87] Catherine E. Miller and Paulo C. Lozano. Measurement of the dissociation rates of ion clusters in ionic liquid ion sources. *Applied Physics Letters*, 116(25):254101, 6 2020.

[88] Yoichiro Mori and Y. N. Young. From electrodiffusion theory to the electrohydrodynamics of leaky dielectrics through the weak electrolyte limit. *Journal of Fluid Mechanics*, 855:67–130, 2018.

[89] E. W. Müller and T. T. Tsong. *Field ion microscopy, field ionization and field evaporation*, volume 4. 1974.

[90] Akihiro Noda, Kikuko Hayamizu, and Masayoshi Watanabe. Pulsed-gradient spin-echo 1H and 19F NMR ionic diffusion coefficient, viscosity, and ionic conductivity of non-chloroaluminate room-temperature ionic liquids. *Journal of Physical Chemistry B*, 105(20):4603–4610, 5 2001.

[91] O. O. Okoturo and T. J. VanderNoot. Temperature dependence of viscosity for room temperature ionic liquids. *Journal of Electroanalytical Chemistry*, 568(1-2):167–181, 7 2004.

[92] C. Pantano, Alfonso M. Gañán-Calvo, and A. Barrero. Zeroth-order, electrohydrostatic solution for electrospraying in cone-jet mode. *Journal of Aerosol Science*, 25(6):1065–1077, 9 1994.

[93] Julius Perel, John F Mahoney, R. David Moore, and Arthur Y. Yahiku. Research and development of a charged-particle bipolar thruster. *AIAA Journal*, 7(3):507–511, 1969.

[94] Carla Pérez-Martínez. *Engineering Ionic Liquid Ion Sources for Ion Beam Applications.* PhD thesis, Massachusetts Institute of Technology, 2016.

[95] Carla Pérez-Martínez, Stéphane Guilet, Jacques Gierak, and Paulo C. Lozano. Ionic liquid ion sources as a unique and versatile option in FIB applications. In *Microelectronic Engineering*, volume 88, pages 2088–2091, 2011.

[96] Carla Pérez-Martínez and Paulo C. Lozano. Ion field-evaporation from ionic liquids infusing carbon xerogel microtips. *Applied Physics Letters*, 107(4), 7 2015.

[97] Carla S. Perez-Martinez and Paulo C. Lozano. Visualization of beams from ionic liquid ion sources for focused ion beam applications. *Journal of Vacuum Science & Technology B, Nanotechnology and Microelectronics: Materials, Processing, Measurement, and Phenomena*, 30(6):06F601, 11 2012.

[98] Elaine M. Petro, Ximo Gallud, Sebastian K. Hampl, Madeleine Schroeder, Carl Geiger, and Paulo C. Lozano. Multiscale modeling of electrospray ion emission. *Journal of Applied Physics*, 131(19):193301, 5 2022.

[99] Natalia V. Plechkova and Kenneth R. Seddon. Applications of ionic liquids in the chemical industry. *Chemical Society Reviews*, 37(1):123–150, 2008.

[100] A. Ponce-Torres, N. Rebollo-Muñoz, Miguel A. Herrada, Alfonso M. Gañán-Calvo, and J. M. Montanero. The steady cone-jet mode of electrospraying close to the minimum volume stability limit. *Journal of Fluid Mechanics*, 857:142–172, 12 2018.

[101] B. Praprotnik, W. Driesel, Ch Dietzsch, and H. Niedrig. HV-TEM in-situ investigations of the tip shape of indium liquid metal ion emitter. *Surface Science*, 314(3):353–364, 8 1994.

[102] J. Puretz. *A theoretical and experimental study of liquid metal ion sources and their application to focused ion beam technology.* PhD thesis, Oregon State University, Corvallis, 1988.

[103] A. S. Rathore and Cs Horváth. Capillary electrochromatography: Theories on electroosmotic flow in porous media. In *Journal of Chromatography A*, volume 781, pages 185–195. Elsevier, 9 1997.

[104] Lord Rayleigh. XVI. On the instability of a cylinder of viscous liquid under capillary force. *The London, Edinburgh, and Dublin Philosophical Magazine and Journal of Science*, 34(207):145–154, 1892.

[105] Jimmy Rojas-Herrera and Paulo C. Lozano. Mitigation of anomalous expansion of carbon xerogels and controllability of mean-pore-size by changes in mold geometry. *Journal of Non-Crystalline Solids*, 458:22–27, 2 2017.

[106] I. Romero-Sanz, I. Aguirre de Cárcer, and Juan Fernández de la Mora. Ionic propulsion based on heated Taylor cones of ionic liquids. *Journal of Propulsion and Power*, 21(2):239–242, 2005.

[107] I. Romero-Sanz, R. Bocanegra, Juan Fernández de la Mora, and Manuel Gamero-Castaño. Source of heavy molecular ions based on Taylor cones of ionic liquids operating in the pure ion evaporation regime. *Journal of Applied Physics*, 94(5):3599–3605, 2003.

[108] Charles N. Ryan, Katharine L. Smith, and John P.W. Stark. The flow rate sensitivity to voltage across four electrospray modes. *Applied Physics Letters*, 104(8):084101, 2 2014.

[109] H. Sagan. *Introduction to the Calculus of Variations*. Courier Corporation, 1992.

[110] D. A. Saville. ELECTROHYDRODYNAMICS:The Taylor-Melcher Leaky Dielectric Model. *Annual Review of Fluid Mechanics*, 29(1):27–64, 1 1997.

[111] William J. Scheideler and Chuan Hua Chen. The minimum flow rate scaling of Taylor cone-jets issued from a nozzle. *Applied Physics Letters*, 104(2):24103, 2014.

[112] Ory Schnitzer and Ehud Yariv. The Taylor-Melcher leaky dielectric model as a macroscale electrokinetic description. *Journal of Fluid Mechanics*, 773:1–33, 5 2015.

[113] Christian Schreiner, Sandra Zugmann, Robert Hartl, and Heiner J. Gores. Fractional walden rule for ionic liquids: Examples from recent measurements

and a critique of the so-called ideal KCl line for the walden plot. *Journal of Chemical and Engineering Data*, 55(5):1784–1788, 5 2010.

[114] Mojtaba Shamsipur, Ali Akbar Miran Beigi, Mohammad Teymouri, Sayed Mahdi Pourmortazavi, and Mohsen Irandoust. Physical and electrochemical properties of ionic liquids 1-ethyl-3-methylimidazolium tetrafluoroborate, 1-butyl-3-methylimidazolium trifluoromethanesulfonate and 1-butyl-1-methylpyrrolidinium bis(trifluoromethylsulfonyl)imide. *Journal of Molecular Liquids*, 157(1):43–50, 11 2010.

[115] Katharine L. Smith, Matthew S. Alexander, and John P. W. Stark. The sensitivity of volumetric flow rate to applied voltage in cone-jet mode electrospray and the influence of solution properties and emitter geometry. *Physics of Fluids*, 18(9):92104, 2006.

[116] Katharine L. Smith, Matthew S. Alexander, and John P.W. Stark. Voltage effects on the volumetric flow rate in cone-jet mode electrospraying. *Journal of Applied Physics*, 99(6):064909, 3 2006.

[117] Yoshio Sone. *Kinetic Theory and Fluid Dynamics*. Modeling and Simulation in Science, Engineering and Technology. Birkhäuser Boston, Boston, MA, 2002.

[118] Vojtěch Štejfa, Jan Rohlíček, and Ctirad Červinka. Phase behaviour and heat capacities of selected 1-ethyl-3-methylimidazolium-based ionic liquids. *Journal of Chemical Thermodynamics*, 142:106020, 1 2020.

[119] N. A. Stolwijk and Sh Obeidi. Combined analysis of self-diffusion, conductivity, and viscosity data on room temperature ionic liquids. *Electrochimica Acta*, 54(5):1645–1653, 2 2009.

[120] H. A. Stone. A simple derivation of the time-dependent convective-diffusion equation for surfactant transport along a deforming interface. *Physics of Fluids A*, 2(1):111–112, 6 1990.

[121] Masaaki Sugiyama and Genichi Sigesato. A review of focused ion beam technology and its applications in transmission electron microscopy. *Journal of Electron Microscopy*, 53(5):527–536, 2004.

[122] Yanjun Sun, Clayton J. Radke, Bryan D. McCloskey, and John M. Prausnitz. Wetting behavior of four polar organic solvents containing one of three lithium salts on a lithium-ion-battery separator. *Journal of Colloid and Interface Science*, 529:582–587, 11 2018.

[123] Vasily G. Suvorov and Richard G. Forbes. Theory of minimum emission current for a non-turbulent liquid-metal ion source. *Microelectronic Engineering*, 73-74:126–131, 6 2004.

[124] Vasily G. Suvorov and E. A. Litvinov. Dynamic Taylor cone formation on liquid metal surface: numerical modelling. *Journal of Physics D: Applied Physics*, 33(11):1245–1251, 2000.

[125] L. W. Swanson. Liquid metal ion sources: Mechanism and applications. *Nuclear Instruments and Methods In Physics Research*, 218(1-3):347–353, 1983.

[126] Thomas Sweijen, Hamed Aslannejad, and S. Majid Hassanizadeh. Capillary pressure–saturation relationships for porous granular materials: Pore morphology method vs. pore unit assembly method. *Advances in Water Resources*, 107:22–31, 9 2017.

[127] Mitsuaki Takeuchi, Takuya Hamaguchi, Hiromichi Ryuto, and Gikan H. Takaoka. Development of ionic liquid ion source with porous emitter for surface modification. *Nuclear Instruments and Methods in Physics Research, Section B: Beam Interactions with Materials and Atoms*, 315:345–349, 11 2013.

[128] Geoffrey I. Taylor. Disintegration of water drops in an electric field. *Proceedings of the Royal Society of London. Series A. Mathematical and Physical Sciences*, 280(1382):383–397, 1964.

[129] Geoffrey I. Taylor. Electrically driven jets. *Proceedings of the Royal Society of London. A. Mathematical and Physical Sciences*, 313(1515):453–475, 12 1969.

[130] Kurt J. Terhune, Lyon B. King, Kai He, and John Cumings. Radiation-induced solidification of ionic liquid under extreme electric field. *Nanotechnology*, 27(37), 2016.

[131] Michael E.Van Valkenburg, Robert L. Vaughn, Margaret Williams, and John S. Wilkes. Thermochemistry of ionic liquid heat-transfer fluids. In *Thermochimica Acta*, volume 425, pages 181–188. Elsevier, 1 2005.

[132] R. T. van Gaalen, C. Diddens, H. M.A. Wijshoff, and J. G.M. Kuerten. The evaporation of surfactant-laden droplets: A comparison between contact line models. *Journal of Colloid and Interface Science*, 579:888–897, 11 2020.

[133] R. Verfürth. Finite element approximation of incompressible Navier-Stokes equations with slip boundary condition I. *Numerische Mathematik*, 59(1):615–636, 1986.

[134] Chihiro Wakai, Alla Oleinikova, Magnus Ott, and Hermann Weingärtner. How polar are ionic liquids? Determination of the static dielectric constant of an imidazolium-based ionic liquid by microwave dielectric spectroscopy. *Journal of Physical Chemistry B*, 109(36):17028–30, 2005.

[135] D. Waliszewski, I. Stepniak, H. Piekarski, and A. Lewandowski. Heat capacities of ionic liquids and their heats of solution in molecular liquids. *Thermochimica Acta*, 433(1-2):149–152, 8 2005.

[136] Chao Wang, Jie Bao, Wenxiao Pan, and Xin Sun. Modeling electrokinetics in ionic liquids. *Electrophoresis*, 38(13-14):1693–1705, 7 2017.

[137] Thomas Welton. Room-Temperature Ionic Liquids. Solvents for Synthesis and Catalysis. *Chemical Reviews*, 99(8):2071–2083, 1999.

[138] Stephen Whitaker. Flow in porous media I: A theoretical derivation of Darcy's law. *Transport in Porous Media*, 1(1):3–25, 3 1986.

[139] Christian Wohlfarth. *Surface Tension of Pure Liquids and Binary Liquid Mixtures*. Springer Berlin Heidelberg, 2016.

[140] Harris Wong, David Rumschitzki, and Charles Maldarelli. On the surfactant mass balance at a deforming fluid interface. *Physics of Fluids*, 8(11):3203–3204, 6 1996.

[141] Kai Yang, Fangjun Hong, and Ping Cheng. A fully coupled numerical simulation of sessile droplet evaporation using Arbitrary Lagrangian-Eulerian formulation. *International Journal of Heat and Mass Transfer*, 70:409–420, 3 2014.

[142] John Zeleny. The role of surface instability in electrical discharges from drops of alcohol and water in air at atmospheric pressure. *Journal of the Franklin Institute*, 219(6):659–675, 1935.

[143] Shulin Zeng, Chuan Hua Chen, James C. Mikkelsen, and Juan G Santiago. Fabrication and characterization of electroosmotic micropumps. *Sensors and Actuators, B: Chemical*, 79(2-3):107–114, 2001.

[144] Fei Zhang, Xikai Jiang, Gaofeng Chen, Yadong He, Guoqing Hu, and Rui Qiao. Electric-Field-Driven Ion Emission from the Free Surface of Room Temperature Ionic Liquids. *Journal of Physical Chemistry Letters*, 12(1):711–716, 1 2021.

[145] Anthony N. Zorzos and Paulo C. Lozano. The use of ionic liquid ion sources in focused ion beam applications. *Journal of Vacuum Science & Technology B: Microelectronics and Nanometer Structures*, 26(6):2097–2102, 2008.